AERODYNAMICS OF ACTIVE AND PASSIVE DISPERSAL OF MINIATURE INSECTS WITH BRISTLED WINGS

By

VISHWA TEJA KASOJU

B.E. in Mechanical Engineering
Osmania University
Hyderabad, TG, India
2013

M.S. in Mechanical and Aerospace Engineering
Oklahoma State University
Stillwater, OK, USA
2017

Submitted to the Faculty of the
Graduate College of the
Oklahoma State University
in partial fulfillment of
the requirements for
the Degree of
Doctor of Philosophy Degree
July, 2021

AERODYNAMICS OF ACTIVE AND PASSIVE DISPERSAL OF MINIATURE INSECTS WITH BRISTLED WINGS

Dissertation Approved:

Dr. Arvind Santhanakrishnan

Dissertation Advisor

Dr. Jamey Jacob

Dr. Imraan Faruque

Dr. Daniel Moen

ACKNOWLEDGMENTS

Firstly, I would like to express my sincere thanks to my advisor, mentor Dr. Arvind Santhanakrishnan for his continuous support in this study and related research. I am particularly grateful to him for enlightening me with first glance of research. His motivation and guidance led me to many accomplishments during the course of my Ph.D. and in writing this dissertation.

I would like to thank my dissertation committee: Dr. Jamey Jacob, Dr. Imraan Faruque and Dr. Daniel Moen for their time, insightful comments and encouragement. I am particularly grateful to Dr. Moen for his guidance and help with morphological analysis on bristled wings in tiny insects.

I have benefited greatly from working with past and present members of Dr. Arvind Santhanakrishnan's research group. I would like to acknowledge each member of the group for their support.

Finally, I would express my sincere gratitude to my family and friends for their unwavering support and encouragement throughout the course of my Ph.D.

Acknowledgments reflect the views of the author and are not endorsed by committee members or Oklahoma State University.

Name: VISHWA TEJA KASOJU

Date of Degree: JULY, 2021

Title of Study: AERODYNAMICS OF ACTIVE AND PASSIVE DISPERSAL OF MINIATURE INSECTS WITH BRISTLED WINGS

Major Field: MECHANICAL AND AEROSPACE ENGINEERING

Abstract:

Tiny insects with body lengths under 2 mm, such as thrips, use fringed/bristled wings for active flapping at Reynolds number (*Re*) on the order of 10. Even at such tiny scales these insects were found to fly effectively owing to significant variations in wing kinematics and bristled wing morphology. Very few data is available on these variations at such small scales. Morphological investigation on forewing images of bristled wings revealed large diversity in their wing design. This includes variations in gaping or spacing between pair of bristles (G), bristle diameter (D), number of bristles (n) and wing span (S). In the present study, we quantified these design parameters from forewing images of 59 species of thrips and fairyfly species from previously published data. Physical scaled-up bristled wing models were then fabricated based on these parameters and tested for aerodynamic force generation using a robotic model. Results revealed that tiny insects may experience less biological pressure to optimize n or G/D for a given wingspan. Thrips have been observed to use wing-wing interaction via the clap and fling mechanism to augment lift generation. However, drag was also found to significantly increase. We found that tiny insects use large rotation angle to reduce this drag and proposed that circulatory lift alone cannot explain lift force generation and other lift generating mechanisms such as pressure distribution in the flow field were discussed. Actively flying at such tiny scales demands lot of power and these miniature insects were found to employ two additional strategies that helps in overcoming large power demand. We found that pausing between upstroke and downstroke decrease power required during a cycle with small compromise in lift. In addition to active flight, these insects can intermittently parachute by spreading their bristled wings at a particular inter-wing angle (θ). We found that a dense bristled wing maintains aerodynamic loading relative to leakiness through the bristles for $\theta \geq 100^{\circ}$. Also, we developed a scaled up robotic flapping device that could mimic any flapping flight in a horizontal stroke plane and proposed that pitch rate significantly alters the aerodynamic force generation compared to wing revolution.

TABLE OF CONTENTS

LIST OF TABLES

Table Page

Table Page

LIST OF FIGURES

Figure Page

Figure Page

Figure Page

Figure Page

NOMENCLATURE

A ..... Surface area of rectangular planform wing
A_B ..... Area occupied by bristles of a bristled wing
α ..... Instantaneous angle of the wing relative to the vertical
A_M ..... Area of solid membrane of a bristled wing
AOA .... Angle of attack
A_T ..... Area of solid membrane of a bristled wing
BL ..... Body length
c ..... Wing chord
c_{ave} ..... Average wing chord
$\overline{C}$ ..... Cycle-averaged force coefficient
C_D ..... Drag coefficient
$\overline{C_D}$ ..... Cycle-averaged drag coefficient
$\overline{C_{D,clap}}$ ... Phase-averaged drag coefficient during clap
$\overline{C_{D,fling}}$ ... Phase-averaged drag coefficient during fling
$C_{D,max}$ ... Peak drag coefficient
$\overline{C_{D,net}}$ .... Cycle-averaged net drag coefficient
C_L ..... Lift coefficient
$\overline{C_L}$ ..... Cycle-averaged lift coefficient
$\overline{C_{L,clap}}$ ... Phase-averaged lift coefficient during clap
$\overline{C_{L,fling}}$ ... Phase-averaged lift coefficient during fling
$C_{L,max}$ ... Peak lift coefficient
$\overline{C_{L,net}}$ .... Cycle-averaged net lift coefficient
CMOS ... Complementary metal-oxide-semiconductor
$\overline{C_P}$ (Chapter IV) Spatially averaged coefficient of pressure
$C_{P,max}$ .... Peak power coefficient
$\overline{C_{P,net}}$ (Chapter IV) Cycle-averaged net pressure coefficient
C_P (Chapter V) Power coefficient
$\overline{C_{P,net}}$ (Chapter V) Cycle-averaged net power coefficient
D ..... Bristle diameter
$\overline{V_y}$ ..... Downwash velocity
f ..... Stroke frequency
F_D ..... Drag force
F_L ..... Lift force

F_{N} ..... Normal force on a wing
FOV ..... Field of view
F_{T} ..... Tangential force on a wing
G ..... Inter-bristle spacing (or gap)
$\overline{\Gamma_{\mathrm{net}}}$ ..... Cycle-averaged net circulation
G/D ..... inter-bristle gap to bristle diameter ratio
Γ ..... Circulation of a vortex
Γ_{LEV} .... Circulation of the leading edge vortex
Γ_{TEV} .... Circulation of the trailing edge vortex
HP ..... Horizontal plane
λ ..... Measure of phylogenetic signal
L_{b} ..... Bristle length on either side of the solid membrane of a bristled wing
Le ..... Leakiness
LE ..... Leading edge
Le_{max} .... Peak leakiness
LEV ..... Leading edge vortex
μ ..... Dynamic viscosity of fluid
n ..... Number of bristles
$\overline{P_{\text{-}}}$ ..... Spatially averaged negative pressure
$\overline{N_{\text{-}}}$ ..... Number of grid points of the portion of FOV containing negative pressure
$\overline{N_{+}}$ ..... Number of grid points of the portion of FOV containing positive pressure
ν ..... Kinematic viscosity of fluid
ω ..... Out of plane vorticity
ω_{max} ..... Peak angular velocity
ω_{z} ..... z-component of vorticity
$\overline{P}$ ..... Spatially averaged pressure
PGLS .... Phylogenetic generalized least squares
ϕ ..... Stroke amplitude
PIV ..... Particle image velocimetry
PLA ..... Polylactic acid
PL-PIV .. Phase-locked PIV
$\overline{P_{+}}$ ..... Spatially averaged positive pressure
ψ ..... Pitch angle
ψ^{+} ..... Positive perturbated pitch angle
ψ^{-} ..... Negative perturbated pitch angle
$\dot{\psi}$ ..... Pitch rate
$\dot{\psi}_{\mathrm{max}}$ ..... Maximum pitch rate
Q ..... Volumetric flow rate of fluid
Q_{bristled} .. Q for bristled wing
Q_{inviscid} .. Volumetric flow rate leaked through the bristles under no viscous forces (inviscid flow)
Q_{solid} .... Q for solid wing
Q_{viscous} .. Volumetric flow rate leaked through the bristles under viscous conditions
Q_{wing} .... Volumetric flow rate per unit width
R ..... Radius of the wing from tip to root

Re ..... Reynolds number
Re_b ..... Reynolds number based on bristle diameter
Re_c ..... Reynolds number based on wing chord
Re_S ..... Reynolds number based on wing span
RFC ..... Reverse flow capacity
ρ ..... Fluid density
ROI ..... Region of Interest
S ..... Wingspan of a rectangular wing
S_{max} ..... Maximum wingspan
T ..... Time duration for one cycle of clap-and-fling
t ..... Instantaneous time
τ ..... Dimensionless time
τ_c ..... Dimensionless upstroke (clap stroke)
τ_f ..... Dimensionless downstroke (fling stroke)
TE ..... Trailing edge
TEV ..... Trailing edge vortex
θ ..... Instantaneous angular position of the wing relative to vertical
θ (Chapter VII) Inter-wing angle
θ_r ..... Rotation angle
θ_{rev} ..... Revolution angle
θ_t ..... Translational angle
TR-PIV .. Time-resolved PIV
U ..... Instantaneous wing tip velocity
U_{max} ..... Peak tip velocity
U_{rot} ..... Instantaneous rotational velocity
U_{ST} ..... Steady translational velocity
U_{tip} ..... Wing tip velocity in the direction normal to the instantaneous wing position
U_{trans} .... Instantaneous translational velocity
VP ..... Vertical plane
V' ..... Maximum flow velocity in (x', y') coordinate system
v' ..... local flow velocity in (x', y') coordinate system
w ..... Membrane width
x' ..... x coordinate defined along wing span
y' ..... y coordinate defined perpendicular to bristle array
ζ ..... Overlap percentage

CHAPTER I

Introduction

1 Motivation

Nature comprises of large variety of insects ranging from fairy flies (body size less than 5 mm) to hawkmoth (body size less than 250 mm). Across these lower size scales, these animals were observed to fly with decent speed, control and maneuverability. Most of these insects flap their wings rapidly at about 200 Hz or more and therefore generate necessary lift force required to fly. However, in the past very little was known about how these animals were capable in generating enough lift force to counter their body weight. Thus, it became necessary to understand the force generation during insect flight. During 1930‘s there was large buzz in the research community about how does a bubble bee fly. Conventional aerodynamic theory showed that it is aerodynamically impossible for a bumblebee to fly yet it flies. This finding led to “bumblebee paradox”. This remained an open question till late 1990’s. Later Ellington’s discovery that an increase in aerodynamic lift generation during flapping flight due to formation of stable leading edge vortex looked to solve the puzzle. In addition, several other studies have looked into aerodynamics of flapping flight in insects ((Lighthill, 1973; Dickinson and Gotz, 1993; Dickinson et al., 1999)). However, most of the research have been focused on larger scale insects ((Birch et al., 2004; Willmott et al., 1997)). In addition, some studies have found that the aerodynamic force generation for the smaller scale insects would differ largely from those of larger scale insects. This fascinated many researchers to look into aerodynamics involved in flapping flight of tiny insects.

Tiny insects such as fairy flies, thrips have body lengths less than 5 mm and their wingspan is as low as 0.5 mm. At these small scales, viscous forces becomes dominant

and it would be very difficult to flap their wings thereby resistive forces on their wings increases. However, it is interesting to see these tiny insects to generate enough lift force to fly. Hence, studying the aerodynamics behind the flapping wings will provide us with better understanding on force generation at these smaller scales.

2 Specific aims

Tiny insects of length scales less than 1 mm, such as thrips, fairyflies and parasitoid wasps, are reported to actively fly at Reynolds number (*Re*; defined as ratio of inertial to viscous forces) on the order of 10 (Santhanakrishnan et al., 2014) and use wing-wing interaction via the 'clap and fling' mechanism (Weis-Fogh, 1973) as a part of their flight kinematics. Several researchers (Ellington, 1984*b*; Maxworthy, 1979) have looked into the aerodynamics of solid/flat-plate wing models mimicking clap-fling kinematics and observed the formation of a leading edge vortex at the start of fling, which was attributed to generate lift force required to fly. However, wings of tiny insects show the presence of fringes/bristles or hair-like setae attached to a solid membrane. Few studies (Ford et al., 2019; Kasoju et al., 2018; Santhanakrishnan et al., 2014; Sunada et al., 2002; Jones et al., 2016; Lee and Kim, 2017; Davidi and Weihs, 2012) have investigated the effect of bristles on aerodynamics of flapping flight at low Re and reported predominant decrease in drag force for bristled wings as compared to solid wings. While, the bristled wings reduced lift in smaller proportion in comparision to large drag reduction (Ford et al., 2019; Kasoju et al., 2018), most of these studies assumed a 2D simplified bristled wing model in comparision to a real insect wing which is flexible and not symmetric. Adding three dimensionality to the flow could also alter the results published from the previous studies using a real bristled wing model of tiny insect.From this study, three dimensional clap and fling with bristled wings will be examined for the first time.

In addition to active flight such as discussed above (clap and fling), these tiny insects such as thrips were found to passively fly by floating downwards using their wings wide

open instead of flapping (Santhanakrishnan et al., 2014). This mechanism was termed as 'parachuting', which enables the tiny insects to passively disperse to longer distances with minimum energetic demands. This requires bristled wings of tiny insects to generate more drag to float in air and travel with the wind. But bristled wings were found to decrease drag forces in comparison to solid wings. In this study, bristled wings during parachuting will be examined for the first time.

The central hypothesis of this study is that bristled wings of tiny insects can be employed for drag reduction in active dispersal or drag augmentation in passive dispersal based on insects requirement by varying their wing kinematics at low Re on the orders of 1-10. This hypothesis will be tested using the following specific aims (SAs).

2. 1 SA 1: Inter-species variation in number of bristles on forewings of tiny insects does not impact clap-and-fling aerodynamics

(1) Conduct morphometric analysis of published data of bristled wings in the family of Thysanoptera and Mymaridae to quantify the biological variability in inter-bristled gap (G), bristled diameter (D), number of bristles (n), ratio of inter-wing gap to bristle diameter (G/D) and wing span (S). (2) Use a dynamically scaled robotic clap and fling simulator to quantify the aerodynamic forces and flow structures for a simplified scaled-up bristled wing pair designed based on the morphological estimates for the conditions of varying geometric parameters such as G/D and n at Reynolds number based on chord length Re_c = 10.

Morphological and phylogenetic analysis of published images of bristled wings in the family Thysanoptera and Mymaridae will be conducted using ImageJ software (National Institutes of Health, Bethesda, MD) to quantify the biological variation of inter-bristled gap (G), bristled diameter (D), number of bristles (n), ratio of inter-wing gap to bristle diameter (G/D) and wing span (S). Aerodynamic forces will be measured using strain gauges on physical models of bristled wing pairs incorporated into an existing robotic clap and fling model. 2D time-resolved particle image velocimetry (TR-PIV) will be used to characterize

flow structures along the central chordwise plane, while 2D phase-locked PIV (PL-PIV) will be used to characterize the flow through the bristles along the spanwise direction. TR-PIV data will be used to determine strength (circulation) of the leading edge vortex (LEV) and trailing edge vortex (TEV). PL-PIV data will be used to determine leakiness of flow through the bristled wing model, defined as the ratio of reverse/leaking viscous flow rate through the bristles to the inviscid/ideal flow rate. The results of these analyses will be used to examine how force generation is impacted by: (a) circulation of the LEV and TEV, and (b) leakiness of bristled wing.

2. 2 SA 2: Aerodynamic interaction of bristled wing pairs in fling

A physical bristled wing model will be designed based on the biologically relevant range of number of bristles (n) and ratio of inter-wing gap to bristle diameter (G/D). Using the dynamically scaled model mentioned in specific aim 1, we would test a single and dual bristled wing model for varying rotational angle (θ_r), translational angle (θ_t) and overlap of rotational and translation motion (ζ) at Re=10. Aerodynamic forces will be measured using strain gauges on these wing models. TR-PIV and PL-PIV will be performed along chordwise and spanwise directions, respectively. Analyses of TR-PIV, PL-PIV and force data will be conducted similar to SA1 to examine the implications of varying δ, θ_r, θ_t and ζ on aerodynamic forces, force reduction by a bristled wing, and LEV/TEV circulation. Further, pressure distribution on a single and dual wing in motion will be presented to further examine the implication of variability of δ, θ_r, θ_t and ζ on aerodynamic performance of bristled wings.

2. 3 SA 3: Pausing after clap reduces power required to fling wings apart at low Reynolds number

From high-speed videos of free-flying thrips, we observed that their forewings remain clapped for approximately 10% of the wingbeat cycle before start of fling. We sought

to examine if there are aerodynamic advantages associated with pausing wing motion after clap and before fling at Re_c=10 for both single wing and wing pair configurations. A dynamically scaled robotic clap-and-fling platform will be used to measure lift and drag forces generated by physical models of non-bristled (solid) and bristled wing for pause times ranging between 0% to 41% of the cycle. 2D particle image velocimetry (PIV) measurements were used to examine the evolution and dissipation of flow structures around the wings during the pause following the clap phase.

2. 4 SA 4: Flapping flight with bristled wings at low Reynolds numbers

A dynamically scaled robotic model will be developed to replicate the entire flapping motion relevant to tiny insects for varying pitch and revolution angle in an horizontal stroke plane. An elliptical bristled wing model will be designed from within the biological relevent range of number of bristles (n), inter-wing gap to bristle diameter ratio (G/D) and solid membrane area to total wing area ratio (A_m/A_T). Using this developed dynamically scaled model, we would examine a single and dual bristled wing model performing flapping motion at Re =10-120. As apart of this study, three different wing kinematics will be tested. They will be taken from the previous publishes of actual wing kinematics of thrips, leafminers and fruitfly. For all these studies a constant initial wing-wing gap will be maintained. Similar to SA1 and SA2, aerodynamic forces will be measured using strain gauges on these wing models. PL-PIV would be performed at various instances in time along the plan cutting the wing at mid span. This will help in examining the implications of wing circulation on force generation on a bristled wing model.

2. 5 SA 5: Parachuting with bristled wings

Free takeoff flight recordings of thrips (body length $<$2 mm) show that they can intermittently cease flapping and instead float passively downwards by spreading their bristled wings. Such drag-based parachuting can lower the speed of falling and aid in long distance

dispersal by minimizing energetic demands needed for active flapping flight. However, the role of bristled wings in parachuting remains unclear. In this study, we examine if using bristled wings lowers drag forces in parachuting as compared to solid (non-bristled) wings. Wing angles and settling velocities were obtained from free takeoff flight videos. A solid wing and bristled wing model with bristle spacing to diameter ratio of 11 and number of bristles of 84 were comparatively examined during translational motion . These wing model along with the 3D printed insect body was towed in a 8-foot tank using a linear actuator (Zaber Technologies Inc.,). Aerodynamic force generated under varying wing angle from 20-180 degrees across a Reynolds number (*Re*) range of 5 to 100 will be examined. In addition, numerical simulations using Ansys Fluent software will be conducted for a bristled wing pair at different inter-wing angles under steady flow to understand the inter-bristled flow between the bristles and relate it to the forces acquired using the physical model.

3 Significance

3. 1 Engineering

Places of potential targets are needed to be secured and placed under high security surveillance. While drones are available to complete these tasks, due to their larger size there are possibilities of attracting attention. However, micro air vehicles (MAVs) can serve the purpose without any detection. Micro air vehicles (MAVs) are small unmanned aerial vehicles with overall dimensions not larger than 15 cm and flight speed of 10m/s (Trizila et al., 2011). Designing this small, unmanned, slow flying aerial vehicle is of high importance in the field of military and civilian applications. MAVs equipped with video cameras and sensors could be used for gathering intelligence in hazardous and remote areas performing surveillance and reconnaissance (Percin et al., 2012). In order to accomplish these tasks, MAVs are needed to be easily maneuverable with efficient propulsion to fly onboard with payloads. While conventional methods of lift generation has proved to be inefficient, alternative ways for efficient propulsion of MAVs are of high importance for ongoing research.

Since these MAVs fly at low Re due to their size, inspired by the concept that tiny insects fly at low Reynolds number (Re) and stay aloft using flapping flight, it is safe to consider that flapping wings could provide efficient propulsion compared to conventional propeller mechanisms.

Apart from designing micro air vehicles (MAVs), study on flapping flight of tiny insects is considered to be of large ecological and agricultural importance.

3. 2 Agricultural and ecological

Tiny insects like thrips, were found to play important roles at different circumstances. For example, they act as active pollinators during their feeding process ((Terry, 2001)). They are known to be biological vectors for transmitting plant viruses such as Tospovirus, Ilarvirus, Carmovirus into plants (Jones, 2005). They are also invasive pests of commercially important plants. Some thrips damage the plants by direct feeding. Indications of such affects are leaf silvering (Jones, 2005). In addition, they are also observed to exhibit complex social behavior such as forming allies and group defense (Crespi et al., 1997). Hence, studying the physics behind their flapping flight helps in understanding their strategies, relationship with plants thereby answering various agricultural, ecological and behavioral questions.

CHAPTER II

Background

1 Flapping Flight

The question about how do insects fly practically goes decades back. There have been too many studies on aerodynamics of flapping insect in both experimental and computational worlds. These studies have given a basic idea on flapping flight in insects. However, the question still need precise explanations. Some of the studies will be discussed in coming sections (Sane, 2003; Santhanakrishnan et al., 2014; Jones et al., 2016; Wang, 2005; Sane, 2017). Several researchers in there works have used various flow visualizations techniques to address the correlation between force generation, flow structures and pressure distribution on the insect wings (Dickinson et al., 1999; Santhanakrishnan et al., 2018; Kasoju et al., 2018; Ford et al., 2019). Each of there works has brought us a step closer to finding ways to answer the question. In addition, they also pose more challenges for future works.

1. 1 Steady vs unsteady models

Reviewing the literature on insects have shown that our nature contains large variety of insects ranging from fruit fly, *Drosophila melanogaster* (Dickinson et al., 1999; Dickinson and Gotz, 1993) to hawk moth, *Manduca sexta* (Willmott et al., 1997; Hedrick et al., 2009). However, limited information is available on these insects about how they hop, fly or walk. Early twentieth century was said to be time where scientist started focusing on exploring the physics behind insect flight. The first question asked was can the conventional quasi-steady aerodynamic theory be applied to predict the forces generated by flapping wing? Literature shows that initial attempts in assuming quasi-steady theory on flapping flight was a failure

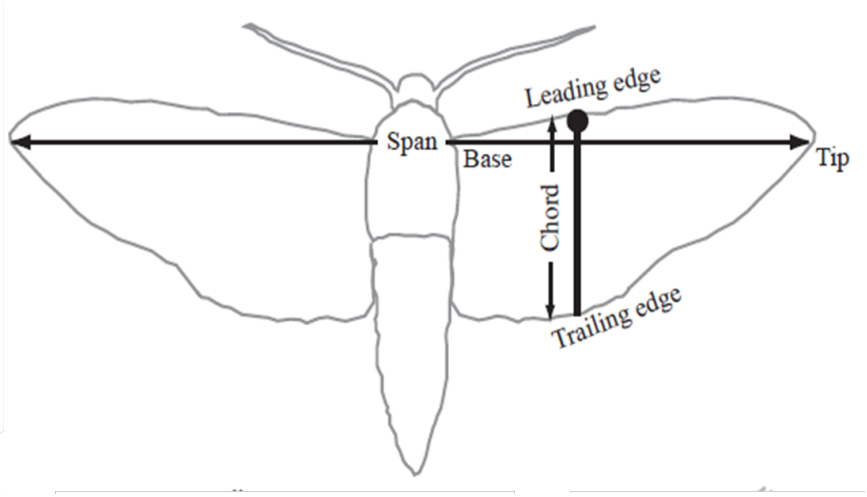

Figure 2.1: Terminology: Sketch of an stretched out insect showing wing tip, wing span, leading edge and trailing edge (Sane, 2003)

and this posed a major challenge to researchers (Sane, 2017, 2003). In addition, there was a feeling among the research community that insects use some unsteady mechanism to generate lift. In order to verify these claims, Weis-Fogh (1975) presented a logical exercise, which was discussed very well in his paper. The results concluded that steady state models were adequate to study the physics behind flapping mechanism for most insects. However, for few insects such as *E. formosa*, the use of steady-state model has failed. This led them to look on to the unsteady fluid mechanics involved in the flapping flight that enables generation of high lift forces. Later Ellington (Ellington, 1975) noticed the flapping flights of various insects and assumed that the unsteady aerodynamics mechanism is characterized based on the kinematics of the wing, wing morphology and flow structures being generated.

2 Terminology

In order to distinguish between fixed wing and flapping flight, a terminology was developed for flapping flight based on the fixed wing aerodynamics. Fig. 2.1 shows the sketch of an insect (Sane, 2003). From the Fig. 2.1, 'wing length' represents the length from base to tip the wing. 'Wing span' represents the length between the tip of the wings when the wings are stretched out laterally. In addition, wing span is also represented as twice the wing length

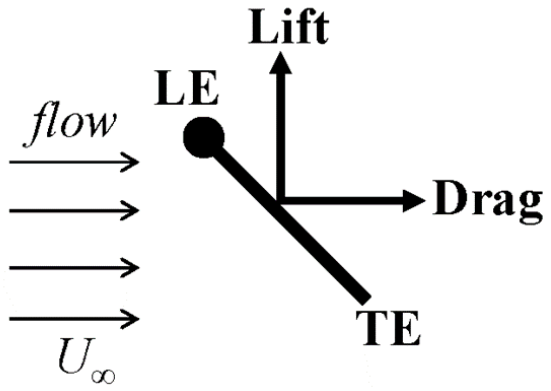

Figure 2.2: Sectional view of an insect wing shown at an angle. The pointed head of the matchstick indicates the leading edge (LE) and the tail indicates the trailing edge (TE). Lift force is represented in vertical direction and drag force in the horizontal direction.

by ignoring the width of the animal. 'Wing chord' represents the vertical distance between leading and trailing edge at any position along the span of the wing. 'Aspect ratio' is defined as the non-dimensional ratio of wing span to wing chord. 'Angle of attack' is defined as the angle that wing chord makes with respect to the free stream velocity direction. The flight of these insects can be categorized based on a non-dimensional quantity, Reynolds number (*Re*). Reynolds number (*Re*) is the measure of viscous forces to inertial forces and given by the equation $Re = \rho LU/\mu$ where ρ is the density of air, μ is the dynamic viscosity of air, L is the chord length of the wing and U is the wing tip velocity. Reynolds number (*Re*) of the insect ranges in the order 10^1-10^4.

3 Characteristics featuring unsteady mechanisms

As discussed in the section 1. 1, unsteady aerodynamics mechanism were characterized based on the kinematics of the wing, wing morphology and flow structures being generated.

3. 1 Flow structures and aerodynamic force generation

Fig. 2.2 shown above represents the sectional view of an insect wing. The matchstick represents the chord line with the pointed head representing the leading edge (LE) and the tail represents the trailing edge (TE). The surrounding fluid is moving in horizontal direction

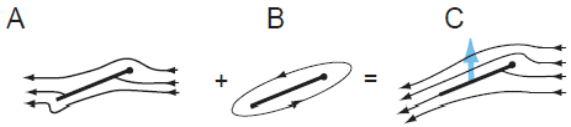

Figure 2.3: Kutta condition. Sum of (A) Ideal flow around an airfoil placed in inviscid fluid, (B) Assumed, circulation around the airfoil under viscous condition (C) Creates a smooth, tangential flow at trailing edge (Sane, 2003).

with a velocity U_∞, thereby imparting horizontal, vertical force which represents as drag, lift force respectively. When a wing translates in an inviscid fluid at particular angle of attack, it is assumed that the fluid gets slightly deflected but would move in the same direction as the surrounding flow. Hence the stagnation point is somewhere on the top surface of the wing section. While under viscous conditions, the flow was observed to be attached in the direction of trailing edge, thereby creating stagnation point at the trailing edge. In addition, there was net force generated in the direction perpendicular to fluid flow. Considering this, Martin Wilhelm Kutta developed a theory, which states that there was a bound circulation on the wing, which was causing the fluid to flow tangentially from the trailing edge. Thereby generating the lift force. This theory was named as 'Kutta condition' (Sane, 2003). When Kutta condition for a wing is satisfied, the vorticity generated at the trailing edge is zero.

In addition, as the wing increases the angle of attack, the fluid flow was observed to separate from the leading edge but it reattaches before reaching the trailing edge, thus satisfying the kutta condition and also creating a huge vortex. This vortex was called Leading edge vortex. There was an intuition that increasing the angle of attack of a wing could impart greater downward momentum to the fluid, thereby enhancing the lift force. Several computational and experimental studies have identified leading edge vortex to be important for insect wings in generating the forces thereby supporting the intuition.

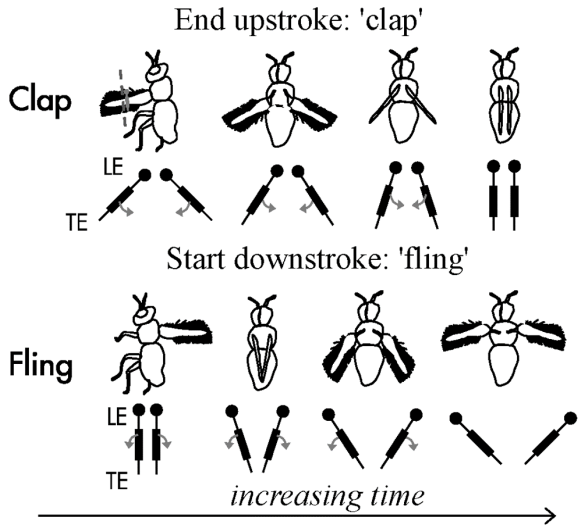

Figure 2.4: Clap and fling mechanism: (A) Clap: At the beginning of the upstroke, the wings rotate together with respect to leading edges and bring the wings close to each other. (B) Fling: At the beginning of down stroke, the wings rotate with respect to trailing edges and peel them apart.

3. 2 Wing kinematics

The aerodynamics associated with flapping insect flight features unsteady motions throughout its wing stroke such as clap and fling mechanism, Wagner effect, delayed stall. Each of them are described briefly below.

3. 2.1 Clap and fling mechanism

After observing flapping flight of insects such as *E. Formosa*, Weis-Fogh (Weis-Fogh, 1973) proposed an idea that insects employ a common flapping mechanism called as 'clap and fling' during their flapping cycle (Fig. 2.4). Later many other researchers (Lighthill, 1973) reported to observe clap and fling in other tiny insects like greenhouse whitefly *Trialeurodes vaporariorum* (Weis-Fogh, 1975) , Thrips *physapus* (Ellington, 1980), parasitoid wasps *Muscidifurax raptor* and the jewel wasp *Nasonia vitripennis* (Miller and Peskin, 2009). Clap and fling mechanism is sometimes referred as 'Weis-Fogh mechanism'. During end of upstroke of a flapping flight, insects are noticed to rotate their wings with respect to leading edge and come close together. This is termed as 'clap'. Some insects were ob-

served to touch their wings each other at the end of clap. While at the start of upstroke, insects were observed to rotate their wings with respect to trailing edge and fling the wings apart. Hence, this is termed as 'fling'. This mechanism was proposed as one of the reason for augmentation in lift force generation during flapping flight.

3. 2.2 Wagner effect

Aerodynamic forces acting on a wing that started impulsively from rest at an inclination are lower than the values predicted by quasi-steady models. There was a delay before the forces reach the steady-state value. This was first proposed by Wagner (1925) and later studied experimentally by Walker (1931) (Sane, 2003). As discussed in the previous section circulation around the airfoil generate the necessary lift force required for the insects to fly. So describing 'Wagner effect' in terms of circulation around an airfoil helps in understanding the consequences of this effect. As an inclined wing starts impulsively from rest, the circulation around it takes some time to attain a steady-state value. Therefore as shown in the Fig. 2.5 (Sane, 2003) any wing must travel several chord-lengths before steady-state circulation is reached. However, the experiments of Dickinson and Gotz (1993) showed that the delay in lift generation is less noticeable at lower Reynolds numbers.

3. 2.3 Delayed stall

In a 2D study, the wings generate an attached leading edge vortex at higher angle of attach. However, if the wings continue to translate at these high angles, the separation of the leading edge vortex takes place. This result in creating trailing edge vortex (from Kutta condition) thereby decreasing the lift force generation. At this stage, the wings are said to be stalled. While before stalling, the wings generate high lift coefficient due to stronger leading edge formation. This development is termed as 'delayed stall'.

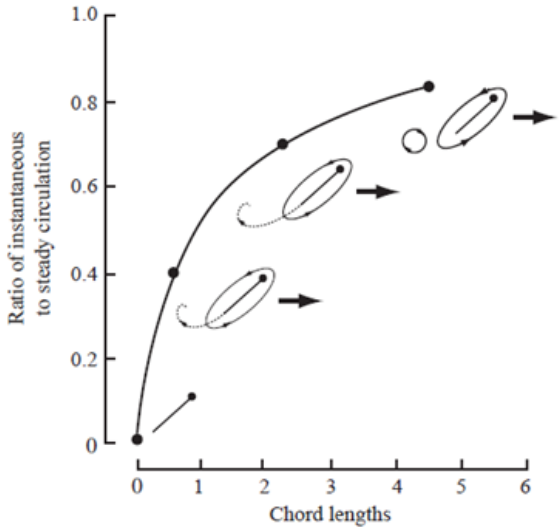

Figure 2.5: Wagner effect: Plot showing ratio of instantaneous to steady circulation versus chord lengths. Dotted line indicates the formation of starting vortex (trailing edge vortex). As the trailing edge vortex sheds, circulation is build up on the wing section. As stated, a flapping wing travels several chord-lengths before reaching steady-state circulation (Sane, 2003)

3. 3 Wing morphology

Different insects have different wing structure, shape, size and weight. These parameters were observed to increase with their body length. However, not all the wings looks alike. Some insect wings have a complete solid wing while some insects have fringes or hair like structures attached to them. Each of them have their own advantages. Bristles on insect wings serve in different ways 1) They reduce the weight of the wing thereby providing aerodynamic benefit. (Santhanakrishnan et al., 2014; Kasoju et al., 2018; Ford et al., 2019; Jones et al., 2016; Sunada et al., 2002), 2) Help to fold and unfold the wings easily (Ellington, 1980), 3) Could help in sensing the surrounding fluid and adjust their flight accordingly.

4 Large vs tiny insects

Many researchers have presented the complex nature involved in kinematics and aerodynamics of insect flight ranging from *Drasophila* to *Manduca* (Spedding and Maxworthy,

1986; Birch et al., 2004; Lehmann and Dickinson, 1998), while the studies on tiny insects like thrips, fairy flies, parasitoid wasps are not well explored. Insects like fruit flys and hawk moth fly at *Re* range from about 100 to 10000, while the tiny insects fly at *Re* in the order of 10. In fact, the wing span of the insects can help in determining the Re at which its wings operate. One of the main purposes of an insect during its flight is lift augmentation. Previous works have shown that for most of the mechanisms, predominant lift augmentation is observed in insects at higher angles of attack (Sane, 2003; Birch et al., 2004; Santhanakrishnan et al., 2014). While at theses high angles of attack, leading edge vortices was observed to stick on the top surfaces and remains attached until stroke reversal. It is thought that formation of stable leading edge vortices would be the reason for lift augmentation in insects at high angles of attack. In addition, many researchers has identified that the flight kinematics and aerodynamics of small insects may be different from larger insects (Santhanakrishnan et al., 2014; Jones et al., 2015; Wang, 2000; Miller and Peskin, 2004). At low *Re*, drag forces substantially peak, hindering aerodynamic performance of the insects (Wang, 2000; Miller and Peskin, 2004). Filming the flight of free-flying insects is a difficult task due to their small size and high wing beat frequency. Though with the availability of high-speed video camera equipped with macro lens, we have very narrow field of view. Hence, very few video recordings of tiny insects are available to date but these recording have provided lot of information regarding the flight of tiny insects. Most of the insects, in fact all the tiny insects that are filmed were observed to use clap and fling mechanism to fly. A vast amount of research has been carried out on aerodynamics of these insects during clap and fling motion but comparatively most of them were concentrated on larger scale insects ((Spedding and Maxworthy, 1986; Dickinson et al., 1999; Lighthill, 1973; Maxworthy, 1979; Srygley and Thomas, 2002; Shyy and Liu, 2007). Although handful of research was done on the tiny insects like thrips (Liu and Aono, 2009; Ellington, 1980) there is lot more to understand. It was reported that there are over 5000 different species of thrips alone (Jones et al., 2016; Ellington, 1980; Morse and Hoddle,

2006). From the snapshots taken during free take off flight of thrips (Santhanakrishnan et al., 2014), it was observed that they flap their wings at about 200 Hz and their wingspan is as low as 0.5 mm. It was also observed that the wings of many of these tiny insects have fringes or bristles attached to a solid membrane rather than complete solid wings. The aerodynamics benefits behind the use of bristled wings were not clear exactly. However, Sunada et al. (2002) and others (Kasoju et al., 2018; Ford et al., 2019) constructed a dynamically scaled bristled wing model and tested them under pure translation and rotation motion. Results show that lift and drag forces are scaled automatically and they did not find any aerodynamic benefit with single wing kinematics. While computational study on bristled wing models during wing-wing interaction showed that the force required to fling the wing apart or clap the wings together decreases (Jones et al., 2016). But the limitations on this steady is the assumption of 2D flow around the airfoil which is not true in real conditions.

CHAPTER III

SA 1: Aerodynamic performance of simplified bristled wing models based on morphological estimates

1 Introduction

The wings of flying insects show tremendous diversity in shape, size and function. Curiously, the wings of several families of flight-capable insects smaller than fruit flies have independently evolved ptiloptery (Polilov, 2015; Sane, 2017), meaning wings with long setae at the fringes. Though their extremely small sizes (body length < 2 mm) make visual observation difficult, tiny flying insects are not limited to just a few outlying examples. Rather, more than 5,500 species of thrips (Thysanoptera; Morse and Hoddle 2006, as well as several hundred species of bristle-winged wasps (Trichogrammatidae, Mymaridae, Mymarommatidae; Heraty et al. 2013), have been identified to date. Despite their importance as biological vectors of plant viruses and as invasive pests of commercially important plants (Ullman et al., 2002; Jones, 2005), we still understand little of the flight mechanics of tiny insects. Due to the difficulty in acquiring free-flight recordings of tiny insects, several studies have used physical and computational modeling to examine the functional significance of wing bristles (Santhanakrishnan et al., 2014; Jones et al., 2016; Lee and Kim, 2017; Kasoju et al., 2018). While these studies have shown that having bristles aids flight at such small sizes, little is known about the extent of variation in bristled wing morphology among different species of tiny insects. Moreover, it remains unclear whether tiny insects experience selective pressure to optimize the mechanical design of their bristled wings, particularly given the extreme challenges of flight at miniature body sizes.

Pronounced viscous dissipation of kinetic energy occurs at wing length scales on the

order of 1 mm, making it difficult for tiny insects to stay aloft. The relative importance of inertial to viscous forces in a fluid flow is characterized using the dimensionless Reynolds number ($Re = \rho VL/\mu$), where ρ and μ are the density and dynamic viscosity of the fluid medium, respectively; V and L are characteristic velocity and length scales, respectively. The length scale has been examined based on wing chord (i.e. $L = c$; Re_c) and bristle diameter ($L = D$; Re_b), with Re_c on the orders of 1 to 10 and Re_b ranging between 0.01–0.07 (Ellington, 1975; Kuethe, 1975; Santhanakrishnan et al., 2014; Jones et al., 2016). Despite the difficulty in sustaining flight at such low Re, entomological studies have reported active flight and dispersal of thrips (Morse and Hoddle, 2006; Rodriguez-Saona et al., 2010). Tiny insects use biomechanical adaptations to overcome the fluid dynamic challenges associated with flight at small scales. These insects operate their wings at near-maximum stroke amplitude using the 'clap-and-fling' mechanism, first observed by Weis-Fogh (1973) in *Encarsia formosa* (Hymenoptera). The use of clap-and-fling has been documented in other freely flying tiny insects, including Thrips *physapus* (Thysanoptera; Ellington 1975) and *Muscidifurax raptor* (Hymenoptera; Miller and Peskin 2009). Wing rotation during fling has been noted to augment lift via the generation of a leading edge vortex on the wings (Weis-Fogh, 1973; Lighthill, 1973; Spedding and Maxworthy, 1986; Miller and Peskin, 2005; Lehmann et al., 2005; Lehmann and Pick, 2007; Miller and Peskin, 2009; Arora et al., 2014). However, the concomitant generation of large drag force at the start of fling undermines the advantage of clap-and-fling at Re_c relevant to tiny insect flight (Miller and Peskin, 2005; Arora et al., 2014). Previous studies have thus examined the flow structures and aerodynamic forces generated by bristled wings in comparison with solid wings (Sunada et al., 2002; Santhanakrishnan et al., 2014; Jones et al., 2016; Lee and Kim, 2017; Lee et al., 2018; Kasoju et al., 2018; Ford et al., 2019), showing that bristled areas on the wings can reduce the force required to fling the wings apart.

Despite this focus on modeling, morphological variation of bristled wing design in tiny flying insects is far less documented. Jones et al. (2016) examined the inter-bristle gap

(G), bristle diameter (D), and wing area covered by bristles in the forewings of 23 species of fairyflies (Hymenoptera: Mymaridae and Mymarommatidae). With decreasing body length (BL), they found that G and D decreased and area occupied by bristles increased. Moreover, Ford et al. (2019) found that the ratio of solid membrane area (A_M) to total wing area (A_T) in the forewings of 25 species of thrips (Thysanoptera) ranged from 14% to 27%, as compared to the A_M/A_T range of 11% to 88% in smaller-sized fairyflies examined by Jones et al. (2016). Yet interspecific variation of G, D, wingspan (S), and number of bristles (n), as well as their concomitant effects on clap-and-fling aerodynamics, are currently unknown.

Such variation in wing morphology across species may arise from many factors. Adaptation drives much interspecific variation Futuyma and Kirkpatrick (2017), and many studies have thus focused on the consequences of variation for optimal functional performance. For example, Ford et al. (2019) used physical models to test the aerodynamic consequences of variation in proportion of solid (i.e. compared to bristled) area on wings. They showed that lift-to-drag ratios were largest for bristled wing models with proportions similar to thrips forewings, suggesting that selection may maintain the small range of variation in thrips. Alternatively, variation among species may have little adaptive explanation (Gould and Lewontin, 1979). Contingent factors in evolution may cause distantly related groups to differ, even under the same selective pressures (Gould, 2002; Blount et al., 2018). Thus, high phylogenetic inertia may explain why species from differing clades differ in phenotype (Hansen and Orzack, 2005). Paradoxically, shared evolutionary history can also explain variation among more closely related species. Such species often share factors (e.g. developmental, genetic) that have similar effects on different traits; when one such trait varies among species, the other will likewise vary. For example, shared growth factors underlying different body parts can cause them to covary with body size. If closely related species differ in selection for body size, then they will similarly differ in traits that grow with body size during development. Strong scaling relationships (i.e. allometry) may indi-

cate evolutionary history as a source of interspecific variation (Pélabon et al., 2014). Thus, accounting for phylogenetic relationships and estimating evolutionary inertia can also help explain variation among species.

In this study, we quantified variation in morphology across species of bristle-winged insects and addressed the factors potentially driving this variation. We first measured wing morphology from 59 species of thrips and fairyflies. We then conducted phylogenetic regressions of key variables on body length and we quantified evolutionary inertia. Using the morphological data as a guide for biologically relevant variation, we then fabricated physical bristled wing models varying in G, D, $S_{\max}$, and n. These physical models were comparatively tested using a dynamically scaled robotic platform mimicking the portion of clap-and-fling kinematics where wing-wing interaction occurs. Aerodynamic force measurements and flow field visualization were conducted to identify the functional significance of the above bristled wing design variables. Because of the high variation in n and G/D despite the extreme aerodynamic demands of flight at small size, we hypothesized that at Re relevant to tiny insect flight, dimensionless aerodynamic forces generated by clap-and-fling would be minimally impacted by variation in n and G/D within their biological ranges. If true, tiny flying insects may not experience selective pressure to further functionally optimize the mechanical design of their bristled wings.

2 Materials and Methods

2. 1 Forewing morphology

We measured average BL, A_{T}, S_{max}, n, G and D from published forewing images of thrips and fairyflies, whose size ranged from 0.1 to 2 mm in BL. Our criteria for choosing published forewing images for measurement are shown here. We required that each published forewing image considered for measurements met the following criteria: 1) contained a scale bar; 2) consisted of least one forewing zoomed out with all bristles shown; and 3) had no noticeable damage to any of the forewing bristles. For thrips, we used a different

set of images for measurements of G and D, as we needed to substantially magnify each of these images (as compared to measurements of $S_{\max}$, A_{T} and n). We required that the published forewing images considered for G and D measurements had a spatial resolution of at least 6 pixels per bristle diameter, similar to the criterion used by Jones et al. (2016). As G and D measurements were used to compute non-dimensional G/D ratios, we did not restrict the images selected for G and D measurements to only those that contained a scale bar (i.e., measurements of G and D in pixels sufficed to calculate the dimensionless G/D ratio). However, this resulted in mutually exclusive datasets in thrips for G/D versus the other variables (**Appendix A.1**). We also note that we were unable to ensure bristle position or angle was unaffected during imaging. Thus, while we ensured that there was no visual damage to bristles, it is possible that the measurements of G were somewhat affected by the positioning uncertainty. High-magnification images of free-flying tiny insect wings are needed to address these two measurement uncertainties. Regardless, we expect this effect to be minor, as we measured G at the bristle root, where it attaches to the solid membrane. Rotation should be minimized at this location. Based on these criteria, we selected forewing images of 16 thrips species for measuring $S_{\max}$, A_{T} and n, and of 22 different thrips species for measuring G and D (Mound and Reynaud, 2005; Mound, 2009; Zhang et al., 2010; Riley et al., 2011; *MAF Plant Health & Environment Laboratory*, 2011; Cavalleri and Mound, 2012; Ng and Mound, 2015; Masumoto et al., 2013; Minaei and Aleosfoor, 2013; Zamar et al., 2013; Cavalleri and Mound, 2014; Dang et al., 2014; Cavalleri et al., 2016; Lima and Mound, 2016; Mound and Tree, 2016; Wang and Tong, 2016; Goldaracena and Hance, 2017). The thrips species considered here encompassed three different taxonomic families. In addition, we selected 21 fairyfly species for measuring $S_{\max}$, A_{T} and n (Huber et al., 2006; Huber and Baquero, 2007; Huber and Noyes, 2013*a*; Huber et al., 2008; Huber and Noyes, 2013*b*), largely overlapping those of Jones et al. (2016), who presented data on G and D for 23 species. We measured bristled wing morphological variables from these images using ImageJ software Schindelin et al. (2012). $S_{\max}$ was defined to be

the distance from the center of the wing root to the tip of the bristles, following Fig. 3.1A. Average wing chord (cave) was calculated by measuring AT using the same procedure as in Jones et al. (2016) and Ford et al. (2019), then dividing A_T by S_{max}. G/D ratio was calculated from the measurements of G and D in the forewing images. BL measurements were made either from images (where available) or from the text of the article containing the image. A full list of species, corresponding measurements, and publication sources of the original images are provided as **Appendix A.1**.

We accounted for shared evolutionary history among species in our regressions by using phylogenetic generalized least squares (PGLS; (Hansen and Martins, 1996)). Regressions were fit with the maximum-likelihood value of λ Pagel (1999), the phylogenetic signal of regression residuals. This procedure best balances species similarity due to shared history and shared adaptation Hansen and Orzack (2005), which improves statistical inference Revell (2010). Moreover, λ can be used as a metric of the role of evolutionary history in a fitted relationship Hansen and Orzack (2005).

Phylogenetic data for our study species were scarce. Only 9 of our 59 species of thrips and fairyflies were included in published phylogenies, and these nine are scattered across published trees (Munro et al., 2011; Buckman et al., 2013; Lima and Mound, 2016; Pereyra et al., 2019). Thus, we simulated many possible phylogenies for our study species and conducted comparative analyses across these trees. This procedure allowed for both integration over phylogenetic uncertainty (Martins, 1996) and for assessment of the sensitivity of our results to any specific potential phylogeny (Losos, 1994). Herein we briefly summarize our procedure for simulating phylogenies. We refer readers to the **Appendix A.2** for detailed simulation methods, justification, and discussion of why phylogenetic regressions should be robust to variation or error in phylogeny.

We constrained our simulated trees to fit current taxonomic knowledge, as adding some phylogenetic structure increases accuracy over completely random approaches (Housworth and Martins, 2001; Martins, 1996; Martins and Housworth, 2002; Symonds, 2002). This

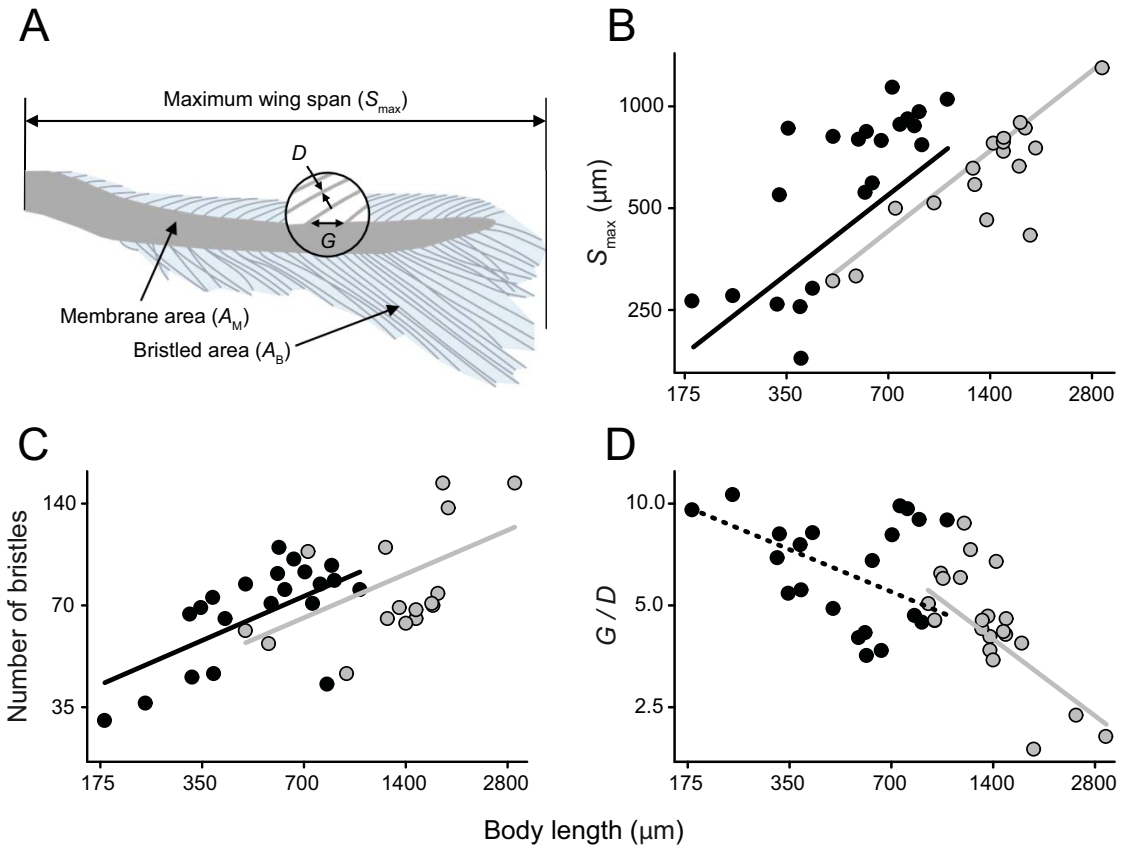

Figure 3.1: Morphological measurements and scaling relationships with body length (BL) in thrips and fairyflies. All scatterplots have data plotted in original units on a logged scale. (A) Forewing of Thrips setosus (BL=1400 μm) redrawn from Riley et al. (2011), with bristled area (A_{B}), membrane area (A_{M}), maximum wingspan (S_{max}), inter-bristle gap (G) and bristle diameter (D) indicated. (B) S_{max} as a function of BL. (C) Number of bristles as a function of BL. (D) G/D as a function of BL. Gray lines and points indicate thrips, while black indicates fairyflies. Solid lines in the same plot indicate that slopes were the same in the most-supported models, while dotted and solid lines indicate statistical support for differing slopes (Tables 3.2, 3.4).

meant, for example, that all species of a given genus were each other's closest relatives in every simulated tree. For thrips, taxonomic information was extracted from the comprehensive Thrips Wiki (https://thrips.info/wiki/; accessed 15 March 2021). Fairyflies are likely a polyphyletic group of two families in two superfamilies of wasps (Mymarommatoidea: Mymarommatidae and Chalcidoidea: Myrmaridae; Huber et al. 1986; Davis et al. 2010; Munro et al. 2011); we assumed these two families to be each other's sister taxon. Genera for these two families were extracted from taxonomic accounts (Gibson et al., 2007; Huber, 2005, 2017; Huber and Noyes, 2013*a*; Poinar Jr and Huber, 2011). Phylogenies were simulated in the package phytools v.0.7-70 (Revell, 2012) in R v.4.0.2 (Team et al., 2013). We simulated 10,000 trees, then pruned each tree to only include the species for which we had phenotypic data, which varied based on the response variable.

Regression analyses were conducted on logged variables, as is standard in body-size scaling analyses (Voje and Hansen, 2013; Pélabon et al., 2014; Glazier, 2021). For each simulated tree, we compared four nested models: (1) a null model with only an intercept; (2) a simple model of regression in which both thrips and fairyflies shared all parameters; (3) a model in which both groups shared a scaling slope but had different intercepts; and (4) a full model in which both groups differed in slope and intercept. These models thus allowed us to estimate scaling relationships between variables and ask whether such relationships differed in thrips and fairyflies (Gartner et al., 2010; Moen et al., 2016). All regressions were estimated in the package *phylolm* v.2.6.2 (Tung Ho and Ané, 2014). We compared models for each tree with AICc and its associated weights (Burnham and Anderson, 2002). We used the model weights to calculate model-averaged regression parameters, adjusted R^2, and λ values (Burnham and Anderson, 2002; Posada and Buckley, 2004). We then averaged these values across trees, as well as the AICc values and model weights. Assuming that each randomly resolved tree is equally likely, such means represent values integrated over phylogenetic uncertainty (Martins, 1996). We also calculated the 95% confidence intervals of slopes, accounting for both estimation and phylogenetic

uncertainty (Martins, 1996). Finally, we calculated the proportion of trees in which a scaling model (i.e. models 2–4) had the highest weight. This proportion reflected the effect of phylogenetic structure on finding a non-zero scaling relationship (Losos, 1994).

Variation in wingspan, bristle number, and G/D at different body lengths motivated our subsequent physical model experiments. However, we designed these models at a chord-based *Re*, rather than body length. Moreover, our experiments held two variables constant (e.g. wingspan and bristle number) while varying a third (e.g. G/D). Thus, we also examined PGLS correlations between these variables, likewise calculating means across the simulated phylogenies, as above. We estimated these correlations using custom R code from Moen et al. (2013), following (Rohle, 2006).

2. 2 Simplified wing models

Our forewing morphological measurements in thrips and fairyflies showed large variation of n (32 to 161). For a bristled wing of rectangular planform with constant w (Fig. 3.2A), G and D, n can be calculated using the following equation:

$$n = \frac{2s}{G+D} \tag{3.1}$$

where n represents the total number of bristles on both sides of a solid membrane. The reason for choosing a rectangular wing planform is because the changes in wing shape are not expected to affect the trend of aerodynamic force generation in time during clap-and-fling, as seen when comparing the lift and drag coefficients of rectangular bristled wing pairs (Kasoju et al., 2018) to approximated elliptical bristled wing pairs (Ford et al., 2019) at chord-based Reynolds number (Re_c) of 10. We designed and fabricated 14 pairs of scaled-up, simplified (rectangular planform) physical wing models to examine effects of changing G, D and S (Table 3.1). In addition, 9 wing pairs were used to examine the variation in non-dimensional geometric variables: (i) n and (ii) G/D (Table 3.1). Note that we rounded n down to a whole number in the physical models. As our wing models were

scaled-up, we were not able to match G, D and S values to be in the range of tiny insects. To achieve geometric similarity, we maintained the relevant non-dimensional geometric variables (n and G/D) to be within their corresponding biological ranges in all the physical models.

The bristled wings tested in this study were simplified to rectangular shape with constant wing chord (c in Fig. 3.2A) to minimize variability in confinement effects along the wingspan from the tank walls. The percentage of A_M/A_T in all the models was maintained at 15%, which is in the range of A_M/A_T of thrips and fairyflies (Ford et al., 2019). Bristle length (L_b, see Fig. 3.2A) and w were maintained as constants on either side of the membrane for all 23 wing models tested. The values of constants c, L_b and w are provided in Table 3.1.

Scaled-up physical models were used in this study to examine the roles of bristled wing geometric variables on clap-and-fling aerodynamics at $Re_c = 10$. We used this approach to overcome the difficulty of resolving the flow around and through a bristled wing on the scale of 1 mm length. As we did not match the values of dimensional geometric variables to those of real insects, we used geometric similarity to match non-dimensional variables (n, G/D) in all the physical models to be in the range of tiny insects. As n depends on G, D and S per 3.1, the choices of non-dimensional variables include n, G/D, G/S and D/S. We chose G/D to match Jones et al. 2016. In addition, to understand the isolated role of each dimensional variable, we tested scaled-up models varying in G, D and S. For each condition, we maintained the 2 other dimensional variables as constants and also matched the non-dimensional variables (n, G/D) to be within their biologically relevant ranges identified from morphological analysis. The 3 mm thick solid membrane used in all the wing models were 3D printed with polylactic acid (PLA) filament using Craftbot printers (CraftUnique LLC, Stillwater, OK, USA). The bristles were made of type 304 stainless steel wires of varying diameter (Table 3.1), glued on top of the membrane. For flow-visualization measurements using particle image velocimetry (PIV), we made new

wing models with the solid membrane laser cut from 3 mm thick acrylic sheets. Also, to avoid reflection in PIV measurements, the bristles were blackened using a blackener kit (Insta-Blak SS-370, Electrochemical Products, Inc., New Berlin, WI, USA).

2. 3 Dynamically scaled robotic model

The dynamically scaled robotic platform used in this study (Fig. 3.3A,B) has been described in previous studies (Kasoju et al., 2018; Ford et al., 2019) and experimentally validated against results in Sunada et al. (2002) corresponding to a single wing in translation at varying angles of attack (in Kasoju et al. 2018). For more details on the robotic platform and justification of our forewing approach, refer to **Appendix A.3**.

2. 4 Kinematics

Free-flight recordings adequate for characterizing instantaneous wing kinematics are unavailable for most species of tiny insects. Thus, we used a modified version of 2D clap-and-fling kinematics developed by Miller and Peskin 2005. The simplified kinematics used here do not capture: (a) 3D flapping translation during the downstroke and upstroke, and (b) wing rotation at the end of the downstroke ('supination'). In real insects, the flapping cycle includes the combination of wing revolution (which we referred as "3D flapping translation" following terminology in Sane 2003), wing rotation, and elevation with respect to the root of the wing. In our study, the wings rotated and translated along a horizontal line with no change in elevation or stroke angle (Fig. 3.3C,D)."Wing rotation at the end of downstroke" refers to the ventral stroke reversal (supination) at the end of downstroke that is observed in 3D flapping flight. In this study, a "stroke cycle" is defined as clap stroke and fling stroke (the latter corresponding to pronation or dorsal stroke reversal) and does not include the ventral stroke reversal occurring towards the end of downstroke. Similar or modified forms of these kinematics have been used in several other studies (Miller and Peskin, 2009; Santhanakrishnan et al., 2014; Arora et al., 2014; Jones et al., 2016; Kasoju

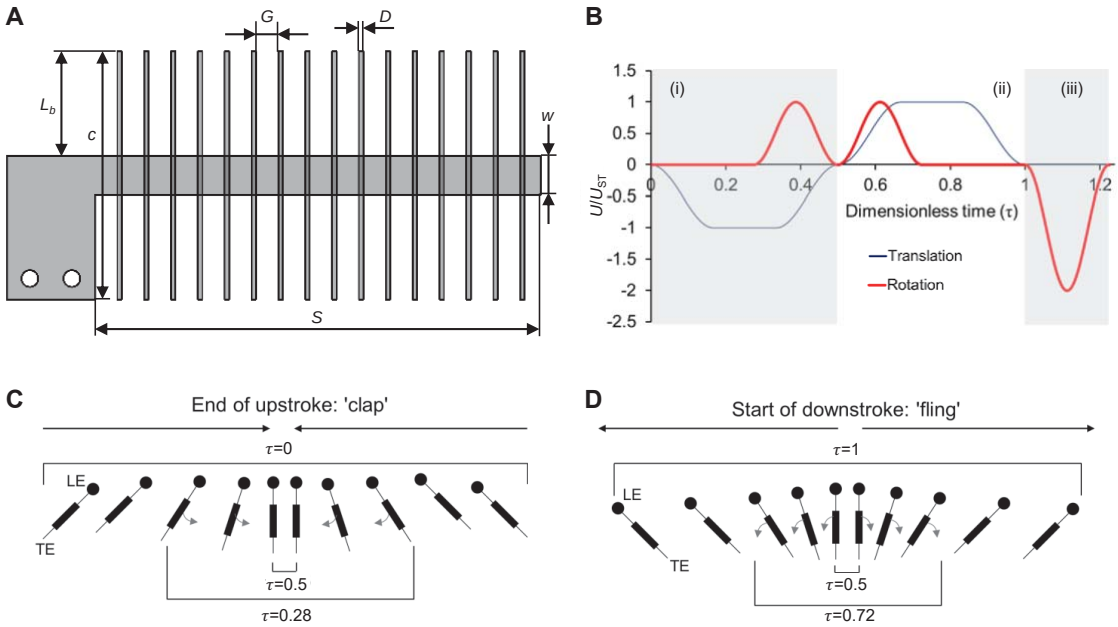

Figure 3.2: Physical bristled wing model and kinematics. (A) Diagram of the simplified bristled wing model with rectangular planform (L_b=bristle length; w=membrane width). See Table 3.2 for the complete list of models tested. (B) Prescribed motion profile of a single wing, based on kinematics developed by Miller and Peskin (2005). Dimensionless velocity (U/U_{ST}), is shown as a function of dimensionless time τ. The wing motion consisted of rotation (thick line) and translation (thin line) along 3 regions: (i) clap (τ = 0-0.5); (ii) fling (τ = 0.5-1); (iii) 90-degrees wing rotation (τ = 1-1.2) to position the wing for the start of the next cycle. During both clap and fling, wing translation was prescribed to occur throughout the wing rotation (100% overlap). The motion profiles prescribed to the other wing was identical in magnitude but opposite in sign, so that the wings would travel in opposite directions. Forces and PIV data were acquired from start of clap to the end of fling. Diagrammatic representation of wing motion during clap (C) and fling (D), where the sectional view along the wing span is shown. $\tau = 0$, $\tau = 0.28$, and $\tau = 0.5$ correspond to start of clap (wings translating toward each other), start of wing rotation and end of clap, respectively. $\tau = 0.5$, $\tau = 0.72$, and $\tau = 1$ correspond to start of fling with wings rotating and translating apart, end of wing rotation and end of fling, respectively. U=instantaneous wing tip velocity; U_{ST}= steady translational velocity; LE=leading edge; TE=trailing edge.

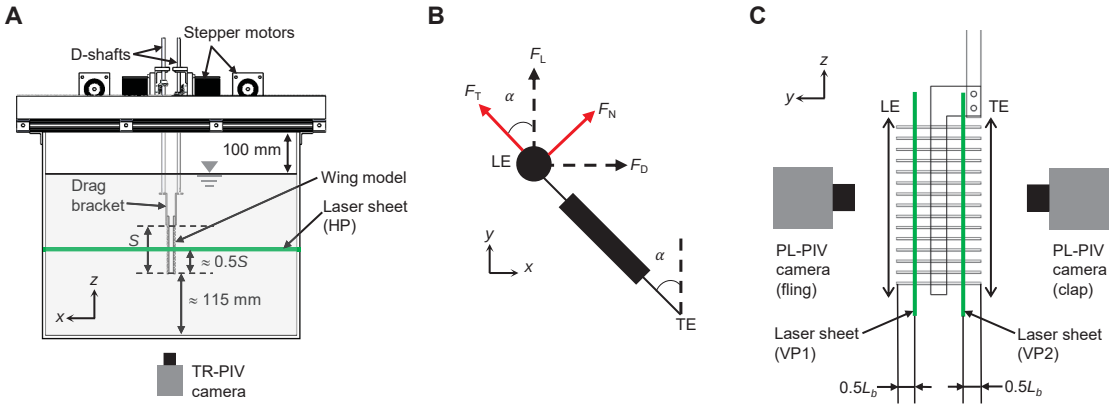

Figure 3.3: Robotic platform and experimental setup. (A) Front view of the robotic platform with bristled wings attached using custom L-brackets with strain gauges to measure the forces generated by a wing during clap and fling phases. The tank measured 510 mm x 510 mm in cross-section and 410 mm in height. 2D TR-PIV was used to visualize the chordwise flow field generated during clap and fling phases, where raw images were acquired using a high-speed camera and illumination was provided with a horizontally oriented laser sheet (horizontal plane, labeled HP) located approximately at mid-span ($0.5S$). (B) Sectional view along spanwise direction for a single bristled wing with directions of measured tangential (F_T) and normal forces (F_N) on a wing during rotation by angle α with respect to the vertical. Lift (F_L) and drag (F_D) forces were measured using a lift and drag bracket, respectively, by taking components of F_T and F_N in the vertical (F_L) and horizontal (F_D) directions. (C) 2D PL-PIV was used to measure the inter-bristle flow for 6 equally spaced time points during clap (τ 0.13 to τ 0.44) using a vertically oriented laser sheet (vertical plane 1, labeled VP1) and 7 equally spaced time points during fling (τ 0.63 to τ 0.94) at laser sheet labeled VP2. Both VP1 and VP2 were located at $0.5L_b$ from the LE and TE, respectively. x,y,z are fixed coordinate definitions.

et al., 2018; Ford et al., 2019; Kasoju and Santhanakrishnan, 2021*a*).Fig. 3.2B shows the motion profiles prescribed for a single wing, where dimensionless velocity (instantaneous wing tip velocity U divided by steady translational velocity U_{ST}) is provided as a function of dimensionless time (τ) during rotational and translational motion. Dimensionless time (τ) was defined as $\tau = t/T$, where t represents instantaneous time and T represents time taken to complete one cycle of clap-and-fling. The motion profile for the other wing was identical in magnitude but opposite in sign, so that the wings would travel in opposite directions. Both wings moved along a straight line (no change in elevation and stroke angles). Schematic diagrams of the clap phase (Fig. 3.2C) and fling phase (Fig. 3.2D) are provided to show the direction of motion and wing position at the start and end of each portion of each half-stroke. The wings were programmed to start from an initial position corresponding to the start of the clap phase, and this was followed by the wings moving toward each other until the start of the fling phase, after which the wings moved apart from each other. The distance between the wings at the end of the clap phase was set to 10% of chord length. The wing separation maintained in this study is similar to those observed in high-speed video recordings of free-flying thrips (Santhanakrishnan et al., 2014) and is also close enough to experience wing-wing interactions, but just far enough apart to prevent the leading and trailing edges of the rigid wing models from colliding during rotation. The variation in wing separation at the end of clap and start of fling is considered in our recent study (Kasoju and Santhanakrishnan, 2021*a*), where we found that our smallest tested gap of 10% chord length between the wings augmented the aerodynamic force generation significantly. This occurred because the pressure distribution varied in the gap between the wings. Due to design limitations of our test facility, we were unable to test the case where the opposing wings come in full contact. More generally, if most species deviate the same way from our models, our results will apply equally to all of them. In other words, while our force measurements may underestimate the actual magnitudes, such an underestimation should equally apply to all species, and thus our results on the effects of different variables

	Wing models tested	S [mm]	G [mm]	D [mm]	n	G/D
Varying G	4	81	1– 2.1	0.2	70–132	5–10
Varying D	5	81	1.4	0.13–0.64	78–106	2–11
Varying S	5	67.5– 94.5	1.3–1.8	0.25– 0.36	88	5
Varying n	8	81	1–19	0.2– 3.81	6–132	5
Varying G/D	4	81	1.2– 1.8	0.15– 0.6	88	2 –11

Table 3.1: Experimental conditions and physical wing models used in this study. Each row represents the specific geometric variable or ratio that was controllably changed. Wing chord (c)=45 mm, membrane width (w)=7 mm, and bristle length (L_b)=19 mm were maintained constant across all wing models. G, D, S and n represents inter-bristle gap, bristle diameter, wingspan and number of bristles, respectively. 23 pairs of physical wing models were tested in this study. 3 wing pairs included in the case of varying n overlapped with 3 of the wing pairs considered in varying D, varying S and varying G/D conditions.

(e.g. wingspan, bristle number, G, D) should be robust to this assumption. In addition, the wingbeat kinematics are undescribed for most species of tiny insects and are likely variable across species (Lyu et al., 2019*a*). For the current study, we prescribed 100% overlap between rotation and translation during both clap and fling, meaning that the wings translated during the entire rotational time. This was because previous studies (Arora et al., 2014; Kasoju and Santhanakrishnan, 2021*a*) have shown that high overlap between rotational and translational motions significantly increases the aerodynamic forces (both lift and drag).

2. 5 Test conditions

Each wing model used in this study was tested at a chord-based Reynolds number of 10 (Re_c=10). The kinematic viscosity (μ=$n\nu/\rho$) of the 99% glycerin solution in which wing models were tested was measured using a Cannon-Fenske routine viscometer (size 400, Cannon Instrument Company, State College, PA, USA) to be 860 mm^2 s^{-1} at room temperature. The chord-based Reynolds number was defined using the equation:

$$Re_c = \frac{\rho U_{ST} c}{\mu} = \frac{U_{ST} c}{\nu} \tag{3.2}$$

which we used to solve for U_{ST} at Re_c=10. Time-varying rotational and translational velocities were generated from the solved U_{ST} value using the equations in Miller and Peskin

(2005). The complete duration of a clap and fling cycle (T) was 2,220 ms. As c was invariant across all wing models (Table 3.1), Re_c was constant for all wing models tested using the same motion profile. Keeping Re_c constant, we varied Re_b to ensure that the flow through the bristles of a model would be on the same order of magnitude as those of real insects. Moreover, as we tested a range of other variables in this study (up to 5, including G, D, n, S, G/D), we hesitated to add yet more variation in terms of Re_c.

2. 6 Force measurements

Similar to Kasoju et al. (2018) and Ford et al. (2019), force measurements were performed using L-brackets with strain gauges mounted in half-bridge configuration (drag bracket shown in Fig. 3.3A). The strain gauge conditioner continuously measured the force as voltage, and a data acquisition board (NI USB-6210, National Instruments Corporation, Austin, TX, USA) synchronously acquired the raw voltage data and angular position of the wings once a custom LabVIEW (National Instruments Corporation, Austin, TX, USA) program triggered the recording at the start of a cycle. Force data and angular position of the wings were acquired for complete duration of clap-and-fling motion (τ=0 to 1) at a sample rate of 10 kHz. We used the same processing procedures as in Kasoju et al. (2018), briefly summarized here. The voltage signal was recorded prior to the start of motion for a baseline offset. In this study, a particular experimental test run consisted of 1) upstroke (clap phase), where wings move towards each other, 2) downstroke (fling phase), where wings moved apart from each other and 3) stroke reversal at the end of downstroke for positioning the wing to start the upstroke for the next run. We paused for 30 seconds at the end of each run (after stroke reversal at the end of downstroke) before starting the subsequent run and acquiring the force data. A pause of 30 sec was introduced at the end of each run to remove the influence of wing-wake interaction occurring from the stroke reversal between runs. Another reason for introducing pause between runs is to remove any mechanical disturbance between runs (e.g., sudden bending of L-bracket when the wings come to rest quickly).

However, before commencing multiple runs for data collection (forces, TR-PIV, PL-PIV measurements), we operated the setup for at least 10 runs (without pausing between runs) to establish a periodic steady state in the tank. Operating for at least 10 runs before any data collection has been our standard protocol (Kasoju et al., 2018; Ford et al., 2019; Kasoju and Santhanakrishnan, 2021*a*) to avoid any disturbances (such as sudden motion in a quiescent fluid) in data collection from the first run to the last run of data collection, and we favor it because this procedure helps us to build a similar fluid environment for each run of data collection. In previous studies, this protocol was found to be helpful in maintaining repeatable force data collection between runs at high Reynolds number flows (Re_c¿100). However, at a lower Reynolds number as in this study (Re_c=10), we did not see any noticeable difference from run to run with or without this protocol since we were waiting for 30 seconds between run to run. We acquired the force data for 30 stroke cycles (during clap stroke and fling stroke). The next step was to filter the raw voltage data in MATLAB (The Mathworks Inc., Natick, MA, USA) using a third order low-pass Butterworth filter with a cutoff frequency of 24 Hz. The baseline offset was averaged in time and subtracted from the filtered voltage data. The lift and drag brackets were calibrated manually, and the calibration was applied to the filtered voltage data obtained from the previous step to calculate forces. The forces that were calculated represent tangential (F_T) and normal (F_N) forces (Fig. 3.3B). Lift force (F_L) is defined as the force acting in the vertical direction (y-axis; Fig. 3.3B) and drag force (F_D) is defined as the force acting in the direction opposite to wing motion (positive or negative x-axis depending on the wing motion). Dimensionless lift coefficient (C_L) and drag coefficient (C_D) were calculated using the following relations:

$$C_L = \frac{F_L}{\frac{1}{2}\rho U_{ST}^2 A} = \frac{F_T cos\alpha + F_N sin\alpha}{\frac{1}{2}\rho U_{ST}^2 A} \tag{3.3}$$

$$C_D = \frac{F_D}{\frac{1}{2}\rho U_{ST}^2 A} = \frac{F_N cos\alpha + F_T sin\alpha}{\frac{1}{2}\rho U_{ST}^2 A} \tag{3.4}$$

where F_L and F_D are the lift and drag forces (in Newtons), respectively, α is the angular position of the wing relative to the vertical, recorded from the integrated encoder of the rotational stepper motor, ρ is the fluid density (measured to be 1260 kg m^{-3}), and A is the surface area of the rectangular planform of a wing (A=$S.c$). Standard deviations were calculated across 30 continuous cycles for C_L and C_D, and the force coefficients were phase-averaged across all cycles to obtain time-variation of instantaneous force coefficients within a cycle. In addition, cycle-averaged force coefficients ($\overline{C_L}$,$\overline{C_D}$) were calculated, with standard deviations and averages reported across 30 cycles for $\overline{C_L}$ and $\overline{C_D}$. Note that all forces were only recorded on a single wing, with the assumption that forces generated by the other wing of a wing pair were equal in magnitude, as the motion was symmetric for both wings of a wing pair.

2. 7 Particle Image Velocimetry (PIV)

2D time-resolved PIV (2D TR-PIV) measurements were conducted to characterize the flow generated during clap-and-fling motion by bristle wing pairs along the chordwise plane (data acquired along a horizontal plane (HP) shown in Fig. 3.3A). 2D TR-PIV based two-component velocity vector fields were also used to determine the strength (i.e., circulation) of the leading edge vortex (LEV) and the trailing edge vortex (TEV). 2D phase-locked PIV (2D PL-PIV) measurements were conducted to characterize flow leaked along the span of bristled wings (data acquired along 2 vertical planes (VP1 and VP2) shown in Fig. 3.3C). For more details on validation of 2D flow simplification, the experimental arrangements and processing steps used for 2D TR-PIV and 2D PL-PIV measurements, refer to **Appendix A.4, A.5, A.6, A.7**, respectively.

The processed TR-PIV images were phase-averaged over 5 cycles, and 2D velocity components and their positions were exported for calculating circulation (Γ) of the LEV and TEV. Γ was calculated for 8 equally spaced time points in both clap (from τ=0.05 to 0.4; increments of 5% of τ) and fling (from τ=0.55 to 0.9; increments of 5% of τ). Γ was

calculated from the following equation using a custom MATLAB script:

$$\Gamma = \int\int \omega_z dx dy \tag{3.5}$$

where ω_z represents the out-of-plane (i.e., z) component of vorticity at leading or trailing edge, calculated from exported velocity vectors similar to Ford et al. (2019) and $dx\ dy$ represents the area of the vorticity region selected for either the LEV or TEV. For more details on circulation calculation, refer to **Appendix A.8**.

Cheer and Koehl (1987) proposed the use of a non-dimensional quantity called leakiness (*Le*) to characterize the amount of fluid leaking through bristled appendages. *Le* is defined as the ratio of the volumetric flow rate of fluid (Q) that is leaked through the inter-bristle gaps in the direction opposite to appendage motion under viscous conditions to that under inviscid conditions:

$$Le = \frac{Q_{\text{viscous}}}{Q_{\text{inviscid}}} \tag{3.6}$$

where Q_{viscous} represents the volumetric flow rate leaked through the bristles (i.e., opposite direction to wing motion) under viscous conditions, Q_{inviscid} represents the volumetric flow rate leaked through the bristles under no viscous forces (inviscid flow). Similar to Kasoju et al. (2018), we calculated the inviscid (or ideal) volumetric flow rate leaked through the bristles of a wing as:

$$Q_{\text{inviscid}} = (S - \frac{nD}{2})U_{\text{tip}} \tag{3.7}$$

where U_{tip} represents wing tip velocity in the direction normal to the instantaneous wing position, defined as:

$$U_{\text{tip}} = U_{\text{rot}} \cos\alpha + U_{\text{trans}} \tag{3.8}$$

where U_{trans} and U_{rot} represent instantaneous translational and rotational velocities, respectively, and α represents instantaneous angle of a single wing relative to the vertical

(Fig. 3.3B). U_{rot} was calculated as the product of the wing chord (c) and angular velocity of the wing (ω_{rot}) as in Kasoju et al. (2018).

Q_{viscous} was calculated from 2D PL-PIV velocity field data as the difference in volumetric flow rates of a solid (non-bristled) wing (denoted herein by Q_{solid}) and the bristled wing under consideration, using the same steps as in Kasoju et al. (2018) that is also summarized here. 2D PL-PIV measurements were acquired on a solid wing model of the same c and S as that of the bristled wing under consideration, using identical motion profiles for both solid and bristled wings and at the same time points or 'phase-locked' positions. Horizontal velocity was extracted for the entire length of wingspan along a line 'L' that was oriented parallel to the wingspan and located downstream of the wing (i.e., in the direction of wing motion) at an x-distance of about 5% chord length from the rightmost edge of the wing surface when viewing the wing along the x-z plane. The horizontal component of the 2D PL-PIV velocity fields was in the direction normal to the wing, i.e., velocity component in the direction of wing motion. These velocity profiles were extracted for every wing model tested, at 6 time points in clap and 7 time points in fling. The viscous volumetric flow rate in the direction opposite to the wing motion (i.e., leaky flow) was calculated using the equation:

$$Q_{viscous} = Q_{solid} - Q_{bristled} \tag{3.9}$$

Volumetric flow rates (per unit width) for both solid and bristled wings about line 'L' was calculated by the line integral of the horizontal velocity using the equation below (in a custom MATLAB script):

$$Q_{\text{wing}} = \int_L u \, dz \tag{3.10}$$

In some cases, it may be possible to directly estimate the reverse (i.e. leaky) viscous volumetric flow rate in the direction opposite to bristled wing motion from the 2D PL-PIV data.

Trait	Optimal model	*bThrips*	*bFairyflies*	*R2adj*	*l*	*Propphylo*
Span (Smax)	Same slope, intercept	0.769 (0.577, 0.962)	0.769 (0.577, 0.962)	0.672	0.852	1
Bristle number	Same slope, intercept	0.434 (0.232, 637)	0.434 (0.232, 637)	0.35	0.005	1
G/D	Full	-0.760 (-1.160, -0.360)	-0.418 (-0.819, -0.018)	0.376	0.445	1

Table 3.2: Results of regressions of wing parameters on body length. All analyses were done on logged variables."Optimal model" indicates the model that had the highest mean weight across simulated phylogenies (Table 3.4). Most values indicate mean values across simulated phylogenies. b_{Thrips} and $b_{Fairyflies}$ indicate mean slope estimates and 95% confidence intervals for each group. ${R^2}_{adj}$ is the mean adjusted ${R^2}_{adj}$ is the mean phylogenetic signal of regression residuals; a value of 0 means species similarity in residuals is independent of phylogeny, whereas 1.0 indicates that similarity is directly proportional to shared evolutionary history (Freckleton et al. 2015). $Prop_{phylo}$ = the proportion of simulated phylogenies in which a scaling model (Models 2–4) had the highest AICc weight.

However, we were not able to calculate this flow rate directly because high-magnification images would be needed to resolve flow through inter-bristle gaps (i.e. on the order of a few millimeters). This conflicted with our desire to use lower magnification in order to resolve flow across the entire wingspan (i.e. 10x greater than G) for calculating Q_{viscous} across a bristled wing.

3 Results

3. 1 Forewing morphological analysis

Most variables showed considerable diversity across species. In thrips, S_{max} ranged from 305 to 1301 μm and bristle number (n) ranged from 44 to 161 (see **Appendix A.1**). In fairyflies, S_{max} ranged from 180 to 1140 μm and n ranged from 32 to 104 (see **Appendix A.1**). S_{max} increased with body length with negative allometry, meaning that larger individuals had relatively shorter wings than smaller individuals (Fig. 3.1B, Table 3.2). Most model weight across phylogenies indicated support for a model with the same slope and intercept for thrips and fairyflies (Table 3.4). n increased with body length similarly in both groups (Fig. 3.1C; Table 3.2), though there was nearly equivalent support for similar versus differing intercepts in the groups (Table 3.4). The latter meant more bristles at the same body length in fairyflies (Fig. 3.1C). In both S_{max} and n, however, we found that

	S_{max}	n	G/D
S_{max}	-	0.078	0.211
n	0.431	-	0.133
G/D	-0.378	-0.511	-

Table 3.3: PGLS correlations among wing variables. The correlation between S_{max} and n includes data from thrips and fairyflies. Correlations between S_{max} and G/D, as well as n and G/D, only included fairyflies, as thrips datasets for G/D versus n and S_{max} were mutually exclusive (**Appendix A.1**). Correlations are on the lower diagonal (unshaded) and represent mean values across simulated phylogenies, corrected for bias (Rohle 2006). P-values are on the upper diagonal (shaded) and likewise represent mean values across simulated phylogenies. *P*-values were calculated using *Z*-scores (Sokal and Rohlf 1995).

AICc model weight was concentrated on the two models with the same slopes for the two groups, which suggests similar scaling relationships. In contrast, while the inter-bristle gap to bristle diameter ratio (G/D) decreased with body length across both groups (Fig. 3.1D), the model with the most weight had a different slope and intercept for the two groups (Table 3.4). G/D more strongly decreased with increasing body length for the larger-sized thrips species (Fig. 3.1D, Table 3.2). The model in which both groups shared a slope and intercept also showed high statistical support across trees (Table 3.4). Regardless of the optimal model, these results mean that larger animals have more tightly packed bristles, with less leakage. Phylogenetic signal (λ) was close to 1 in S_{max} (i.e. residual species similarity reflects phylogeny), nearly 0 in n (i.e. similarity is independent of phylogeny), and intermediate in G/D.

Overall, our results suggest that both groups follow shared trends in bristle variables with body length across bristle-winged insects. Yet only BL strongly predicted S_{max}, with ${R^2}_{adj}$ almost two times lower for both n and G/D (Table 3.2). These latter results made us predict that variation in these latter two variables would have less aerodynamic consequences than S_{max}, motivating our robotic model experiments. Given weak correlations among S_{max}, n, and G/D (Table 3.3, Fig. A.9. 1.1), we probed the effect of varying each of these variables while holding the other two constant.

Model	Span (S_{max})			Bristle number			*G/D*		
	AICc	wi	Rank	AICc	wi	Rank	AICc	wi	Rank
Null (same intercept, no slope)	50.95	0.000	4.000	33.93	0.001	4.000	46.26	0.000	4.000
Same slope + intercept	12.23	0.610	1.120	21.75	0.447	1.474	32.60	0.370	1.559
Same slope, different intercept	13.69	0.306	1.889	21.74	0.444	1.526	34.93	0.119	2.984
Full (slope + intercept different)	16.30	0.084	2.992	24.57	0.108	3.000	31.94	0.510	1.458

Figure 3.4: Results of regression model fitting of wing variables on body length in thrips and fairyflies. Models were fit separately for each variable. "Model" refers to parameter independence in thrips and fairyflies; the null model only contained a shared intercept and no slope, whereas the full model allowed a different slope and intercept for both groups. Each numerical value in the table is the mean across simulated phylogenies. AICc is the small-sample Akaike Information Criterion; low value indicates highest statistical support. wi is the AICc weight, the probability that each model is the optimal model relative to the others (Burnham and Anderson 2002). Rank indicates the mean model rank across phylogenies, with 1 indicate the top model and 4 the poorest fit.

3. 2 Force measurements

For all the wing models tested, C_D and C_L were observed to follow the same trend in time during both clap and fling (Fig. 3.5A, B). Peak C_D occurred during fling ($\tau \approx 0.6$) in all wing models (Fig. 3.5A). This time point corresponds to end of rotational acceleration and translational acceleration (Fig. 3.2B), such that the wing pair would experience larger viscous resistance. C_D was found to drop after $\tau \approx 0.6$ until the wing rotation ended ($\tau \approx 0.73$) for all the wing models (Fig. 3.5A). Just before the C_D reached the negative value at the end of fling where the wings decelerate, we observed C_D to plateau from $\tau \approx$ 0.73-0.84 (Fig. 3.5A). This time corresponds to steady translation motion of the wings (Fig. 3.2B), where the wings translate with constant velocity at 45° angle of attack (AOA). Most of the drag during a cycle was generated in fling. Time-variation of C_D was lower during clap half-stroke (τ=0-0.5) as compared to fling (Fig. 3.5A).

Three positive C_L spikes were observed in all the wing models (Fig. 3.5B): 1) $\tau \approx 0.6$ in fling, similar to that of peak C_D; 2) start of clap ($\tau \approx 0.16$); and 3) end of clap ($\tau \approx 0.38$). $\tau \approx 0.16$ corresponds to the end of translational acceleration at 45° AOA and $\tau \approx 0.38$ corresponds

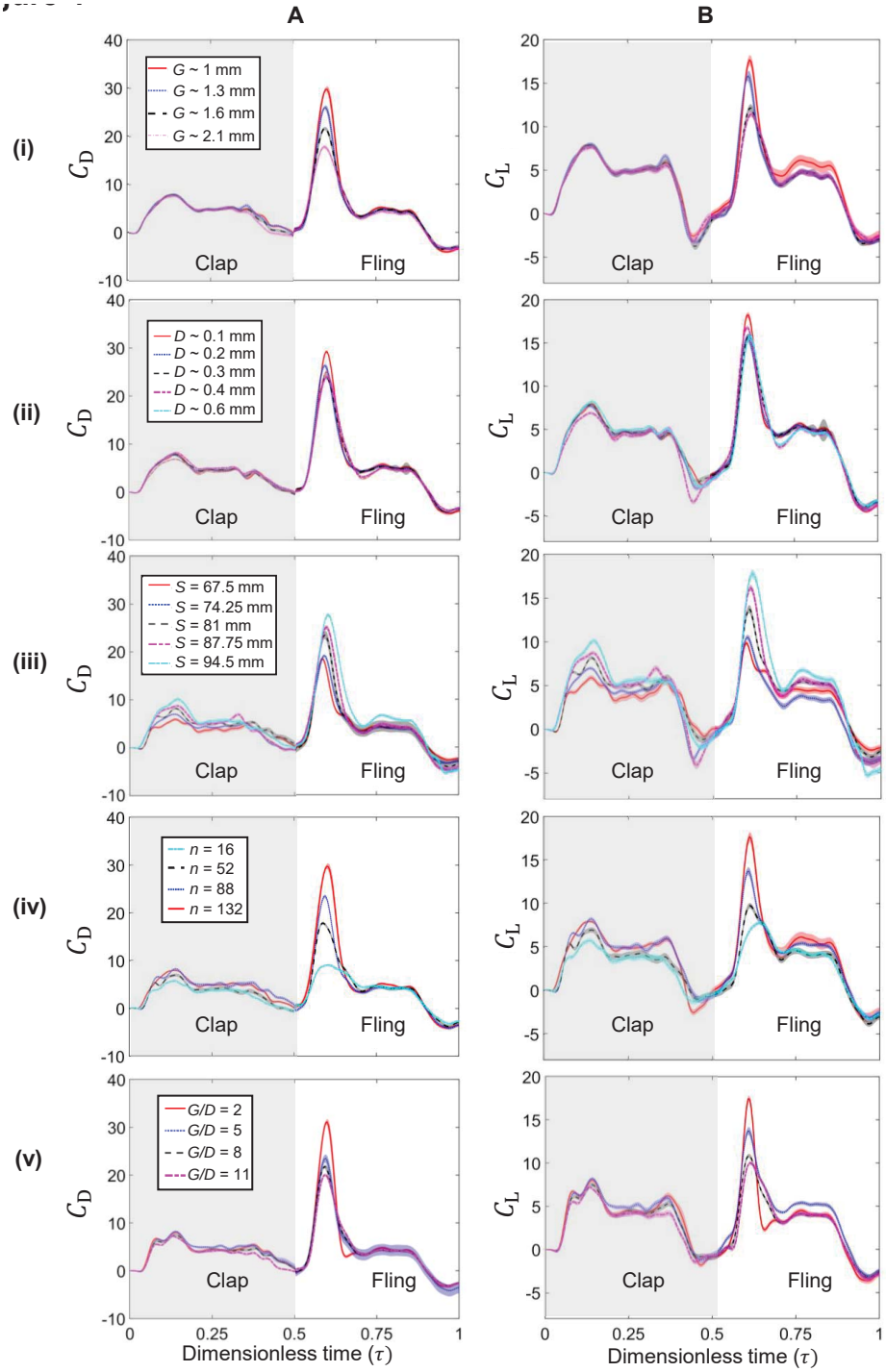

Figure 3.5: Time-varying force coefficients during clap and fling at Re_c=10 with shading around each curve representing range of ± 1 standard deviation (S.D) across 30 cycles. (A) and (B) show time-varying drag coefficient (C_D) and lift coefficient (C_L), respectively. From top to bottom, each row represents varying: (i) G, (ii) D, (iii) S, (iv) n, and (v) G/D. Gray shaded region in each plot represents the clap phase, while unshaded region represents the fling phase.

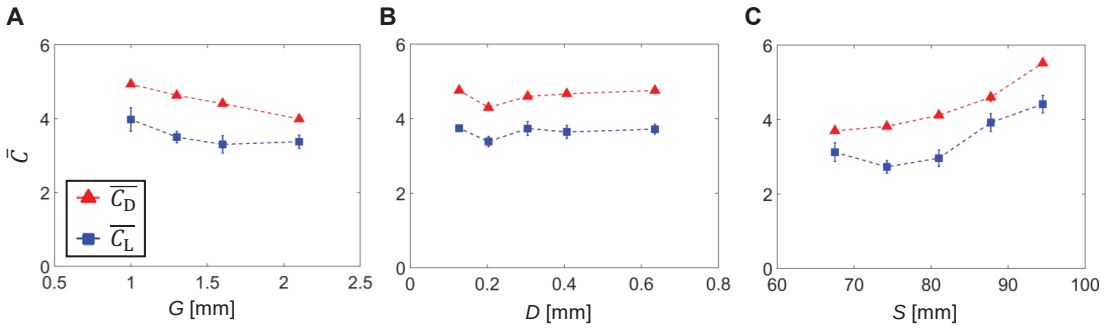

Figure 3.6: Cycle-averaged force coefficients ($\overline{C}$) for varying G, D and S. Error bars corresponding to ± 1 S.D are included for every datapoint. (A, B, C) show average lift coefficient ($\overline{C_L}$) and average drag force coefficient ($\overline{C_D}$) for varying G, D, and S, respectively. S.D estimates for $\overline{C_D}$ and ($\overline{C_L}$) for all conditions were < 0.1 and < 0.32, respectively.

to the end of rotational acceleration during clap (Fig. 3.2B). Peak C_L occurred during fling for all the wing models. Unlike the drag force, both clap and fling half-strokes contributed almost equally to lift generation.

Both C_D and C_L decreased with increasing G and decreasing D (Fig. 3.5(i),(ii)). Increasing S increased both C_D and C_L (Fig. 3.5(iii)). When increasing n for constant G/D, both C_D and C_L were found to increase (Fig. 3.5(iv)), particularly at the beginning of the fling phase. In contrast, increasing G/D for constant n decreased both C_D and C_L (Fig. 3.5(v)). Across all the wing models tested, we observed noticeable negative lift towards the end of fling. This is due to the wings not coming to complete rest and performing stroke reversal to position the wings for clap for the next cycle.

Cycle-averaged force coefficients ($\overline{C}$) were used to examine how each geometric variable impacted aerodynamic forces in a complete cycle (Figs 3.6, 3.7). Individually increasing G and D showed little to no variation in $\overline{C_L}$ when considering the standard deviations (Fig. 3.6A, 3.6B). $\overline{C_D}$ decreased with increasing G and showed little to no variation with increasing D (Fig. 3.6A, 3.6B). Both $\overline{C_L}$ and $\overline{C_D}$ increased with increasing S from intermediate to large values of S (Fig. 3.6C). $\overline{C_D}$ increased with increasing n (Fig. 3.7A). $\overline{C_L}$ increased

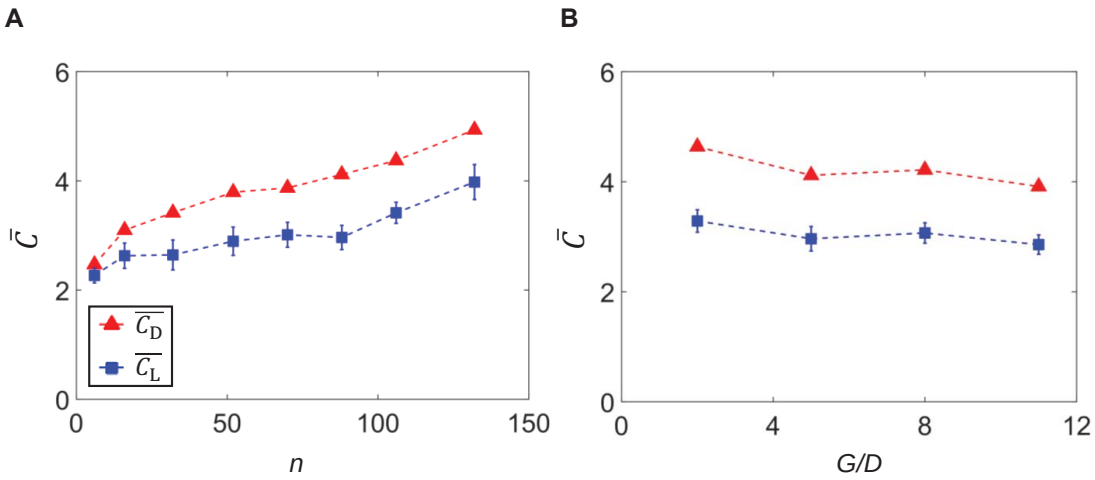

Figure 3.7: Cycle-averaged force coefficients ($\overline{C_L}$,$\overline{C_D}$) as a function of: (A) n and (B) G/D. Error bars corresponding to ± 1 S.D are included. S.D estimates for $\overline{C_D}$ and ($\overline{C_L}$) for all conditions were < 0.1 and < 0.32, respectively.

with n, most notably at $n > 88$, though it plateaued between some consecutive values (Fig. 3.7A). Increasing G/D showed little to no variation in $\overline{C_L}$ and $\overline{C_D}$ when considering the standard deviations (Fig. 3.7B), though extreme values of G/D slightly differed.

3. 3 Inter-bristle flow characteristics

Spanwise distribution of horizontal velocity (u) was examined near the instant of peak C_D ($\tau \approx 0.63$) from 2D PL-PIV velocity fields (Fig. 3.8A). Looking at the extremes of each test condition, u increased with: (i) decreasing G; (ii) increasing D; (iii) increasing S; (iv) increasing n; and (v) decreasing G/D. This reveals how each variable (i.e., G, D, S, n, G/D) differentially affects flow through a bristled wing. Similar to C_D, Le was observed to peak during fling. During the fling half-stroke, Le peaked either at $\tau \approx 0.56$ or $\tau \approx 0.63$ for all the wing models (Fig. 3.8B) where the wings were near the end of rotational acceleration (Fig. 3.2B). Similarly, wing deceleration during fling from $\tau \approx 0.69$ to $\tau \approx 0.88$ resulted in a drop in Le (Fig. 3.8B). During steady wing translation from $\tau \approx 0.75$ to $\tau \approx 0.82$, Le was found to almost plateau in all the wing models.

Le was larger in early clap (τ 12.5) right after the wing pair just started from rest, with

minimal time for boundary layers around each bristle to be well-developed. Thereafter, *Le* decreased with increasing clap duration until τ 0.38 corresponding to end of rotational acceleration (Fig. 3.2B). This latter observation in clap is in direct contrast to the peak in *Le* during fling, which was observed at the end of rotational acceleration. This disparity can be explained by examining the prescribed wing motion. In clap, wings were prescribed to translate first at 45° AOA and then rotate. This provides ample time for the generation of shear layers around the bristles that block inter-bristle flow (see Kasoju et al. (2018) for a detailed discussion). Both rotation and translation started simultaneously in fling, necessitating more time for shear layers to develop around the bristles.

Peak *Le* increased with increasing *G* and decreasing *D* (Fig. 3.8B(i),(ii)). However, changes in *Le* were comparatively small for the range of variation in *G* and *D* tested in this study. Similar to force coefficients (Fig. 3.5(iii)), increasing *S* did not show any particular trend for *Le* (Fig. 3.8B(iii)). However, if we look at the extreme wingspans (67.5 mm and 94.5 mm), *Le* was found to increase with increasing *S*. Increasing *n* for constant G/D was found to decrease *Le*. Changing G/D for constant *n* showed little to no *Le* variation.

3. 4 Chordwise flow characteristics

Velocity vector fields overlaid on out-of-plane vorticity contours (ω_z) showed the formation of LEV and TEV over the wing pair during clap and fling half-strokes (see **Appendix** for supplementary material, Movies A.9. 1.2, A.9. 1.3, A.9. 1.4). Vorticity in the LEV and TEV increased near the end of clap and in early fling, when the wings were in close proximity of each other (Fig. 3.9B,C,D). This suggests that wing-wing interaction plays an important role in LEV and TEV formation, which in turn impacts force generation. Circulation (Γ) of both the LEV and TEV showed little to no variation with changing *G*, *D* and *S*. Peak Γ for both the LEV and TEV occurred in fling (τ=0.65), near the end of both translational and rotational deceleration (Fig. 3.2B). This was followed by decrease in Γ of both LEV and TEV with increasing fling time (Fig. 3.9B,C,D). Γ of the LEV and

TEV increased slowly in time during clap and reached a maximum near the end of the clap (τ=0.35), corresponding to the start of translational deceleration and end of rotational acceleration (latter being identical to the instant where peak Γ occurred in fling).

From the prescribed kinematics (Fig. 3.2B), peak rotational acceleration starts early in fling, while it starts later into the clap. This could be the reason for Γ to peak early in fling and later in clap. This suggests that wing rotation plays a dominant role in LEV and TEV development. Also, both wings are in close proximity during the later stages of clap and early stages of fling, suggesting the importance of wing-wing interaction in in LEV and TEV development. Thus, wing rotation in concert with wing-wing interaction augments LEV and TEV circulation during both clap and fling half-strokes.

4 Discussion

Recent studies have shown that bristled wings provide drag reduction in clap-and-fling at Re_c relevant to tiny insect flight (Santhanakrishnan et al., 2014; Jones et al., 2016; Kasoju et al., 2018; Ford et al., 2019). However, n, S_{max} and G/D have not been measured in different families of tiny insects, and their individual effects on aerodynamic forces are unclear. From our analysis of variation across thrips and fairyflies, we found that S_{max} and n increased with BL in both thrips and fairyflies. We also found that G/D decreased with BL in both groups, but more strongly in thrips. Within the biologically relevant range of n and G/D, we found that: (1) increasing G provides more drag reduction as compared to decreasing D, (2) changing n for constant G/D has little variation on lift generation for n ¡ 100, and (3) changing G/D for constant n minimally impacts aerodynamic forces. The minimal influence of n and G/D on clap-and-fling aerodynamics, despite broad biological variation, suggests that tiny insects may experience lower biological pressure to functionally optimize n and G/D for a given wingspan.

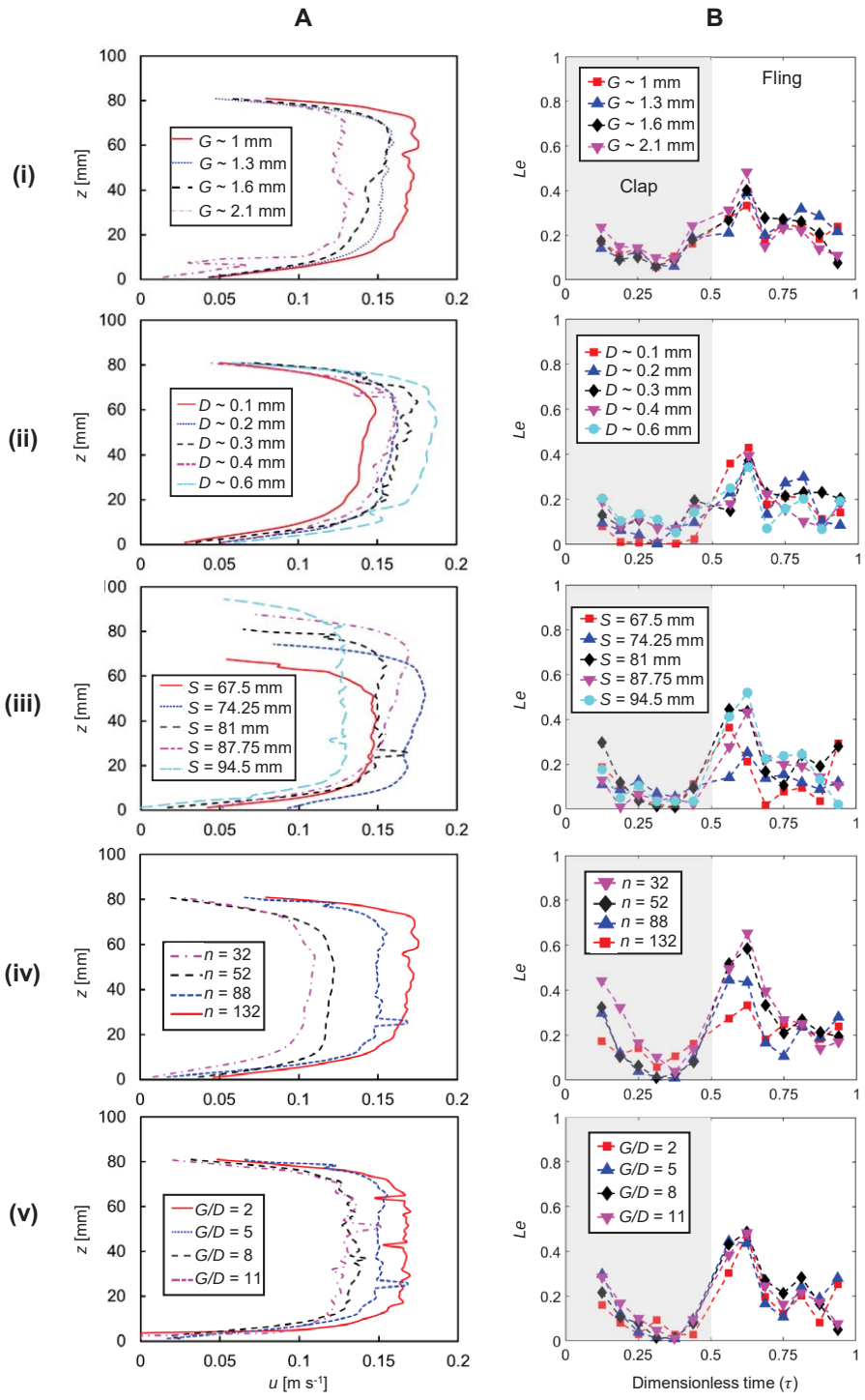

Figure 3.8: Inter-bristle flow characteristics. (A) Horizontal (i.e., x-component) velocity (u) variation along the wing span (z-direction) during fling at τ 0.63. The velocity profile was extracted at a vertical line L oriented parallel to the wing span, located at 5% chord length from the rightmost edge of the wing surface when viewing the wing along the x-z plane. (B) Time-variation of Le. From top to bottom, each row represents varying: (i) G, (ii) D, (iii) S, (iv) n and (v) G/D. Gray shaded region in column B represents the clap phase and unshaded region represents the fling phase.

4. 1 Bristled wing morphology, evolutionary history, and optimization

Variation among related species can stem from many factors: evolutionary history, correlated response in selection to other traits, physical constraints associated with body design and function, and adaptation to variation in body size, ecology, or environment (Gould and Lewontin, 1979; Alexander, 1985; Taylor and Thomas, 2014). In the bristled-wing morphology of tiny insects, most studies have examined physical constraints and adaptation – whether interspecific variation has consequences for flight aerodynamics, possibly driven by variation in body size. For example, Ford et al. (2019) reported a narrow range of A_M/A_T (14%-27%) across 25 thrips species, but much higher variation across fairyflies. In both groups, A_M/A_T showed a strong, positive relationship with body length. At Re_c relevant to tiny insect flight, they found the highest aerodynamic efficiency (lift-to-drag ratio) for A_M/A_T in the range of thrips forewings and lower aerodynamic efficiency outside the range, perhaps facilitating flight in the larger-bodied thrips.

In this study, we found that both S_{max} and n increased with increasing BL in thrips and fairyflies (Fig. 3.1B,C). Interestingly, the ranges of S_{max} largely overlapped across fairyflies and thrips, despite differences in BL (most thrips BL ¿ 1 mm; all fairyfly BL ¡ 1 mm). This suggests that there could be a limit to increasing wingspan in terms of aerodynamic performance. Moreover, we found that phylogenetic signal in the regression residuals (λ) was high for S_{max} on BL (Table 3.2), which explained the high R^2 value despite much scatter about the regression line (i.e. phylogeny explained much of the residual variation in Fig. 3.1B). In other words, closely related species were similar in the way they deviated from the regression line (Revell 2010), which suggests that underlying growth factors in common with body length may be ultimately driving variation in wingspan across closely related species. If selection favors a change in body size, then wingspan may similarly change.

Values of n were concentrated in the range of 60–90 for the species of thrips and fairyflies that we examined, corresponding to a large BL range of 300–1700 μm. More-

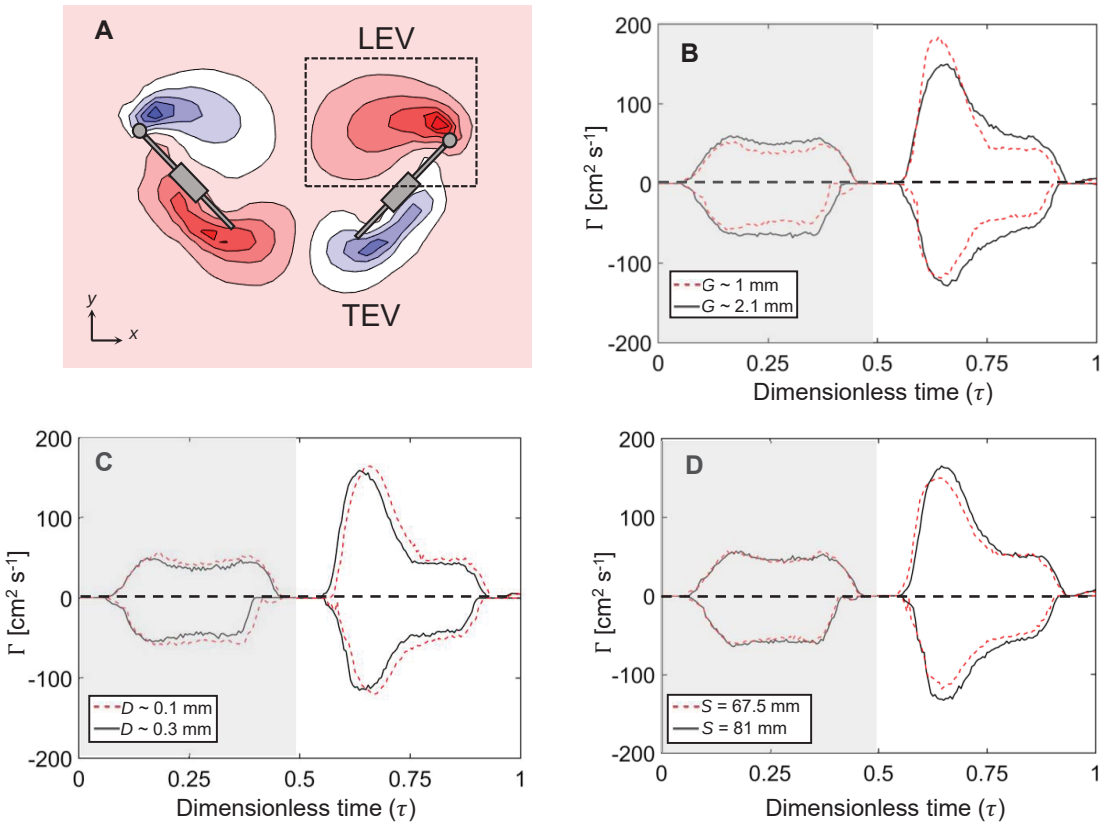

Figure 3.9: Chordwise flow and circulation (Γ). (A) Representative out-of-plane component of vorticity (ω_z) during fling at τ=0.65, obtained from processed TR-PIV data. Γ about the right wing was calculated by drawing a box around the LEV and TEV separately and integrating ω_z of the closed contour within each box. (B), (C) and (D) show Γ during clap and fling for varying G, D and S, respectively. Positive circulation corresponds to TEV during clap and LEV during fling. Negative circulation corresponds to LEV during clap and TEV during fling.

over, the relationship between n and BL was relatively weak (R^2_{adj} = 0.350; Table 3.2). These observations led us to hypothesize that n may not need to be optimized to fall within a narrow range for a given body length toward improving aerodynamic performance. Consistent with this hypothesis, our robotic models showed insensitivity of aerodynamics to this range of n. The weak phylogenetic signal in regression residuals (Table 3.2) suggests little influence of evolutionary history (Hansen and Orzack 2005). Therefore, the factors affecting the evolution of bristle number remain unclear.

Jones et al. (2016) previously showed no relationship between G/D and body length in fairyflies. However, our analyses suggest that there is an overall reduction in G/D with size in bristle-winged insects, with a steeper decline in thrips (Fig. 3.1D; Table 3.2). This difference in our results and those of Jones et al. (2016) stemmed from both our use of phylogenetic analyses and from including the larger thrips, which revealed an overall trend across taxa. That said, this pattern was still relatively weak (R^2_{adj} = 0.376; Table 3.2), with much variation in G/D at a given body length. Previous studies have reported that both lift and drag forces increase with decreasing G/D (Jones et al., 2016; Kasoju et al., 2018). This result could explain the more steeply negative relationship between G/D and BL in thrips, the larger of the two groups: as body mass increases, more lift is necessary to allow flight. Yet the high variation in G/D at long BL in fairyflies raises a question as to whether their G/D needs to be optimized for improving aerodynamic performance. In particular, we currently lack observations of fairyflies in free flight and thus do not know how or to what extent they use flapping flight. An intriguing possibility is that fairyflies facultatively parachute, and their wing structure better reflects the selective demands of that behavior. Thrips have been observed to facultatively parachute (Santhanakrishnan et al. 2014), increasing the probability that fairyflies do so as well.

4. 2 Modeling considerations

Physical model studies of flapping flight match Re_c of the experiments to biological values to achieve dynamic similarity. Specific to the bristled wings of interest to this study, dynamic similarity of inter-bristle flow characteristics also necessitates matching Re_b to be in the range of tiny flying insects. When both Re_c and Re_b are matched between a physical bristled wing model to those of tiny insects, the scale model will produce similar non-dimensional forces to that of real insects. This is the major reason for presenting forces in term of non-dimensional coefficients throughout this study.

It has been reported that thrips (Kuethe 1975) and the wasp *Encarsia formosa* (Ellington 1975) operate at Re_b =10^{-2} and 10^{-1}, respectively, and both at $Re_c \approx 10$. With the exception of Jones et al. (2016), the majority of modeling studies of bristled wing aerodynamics (Sunada et al., 2002; Santhanakrishnan et al., 2014; Lee and Kim, 2017; Lee et al., 2018; Kasoju et al., 2018; Ford et al., 2019) only matched Re_c 10 without matching Re_b to be relevant to tiny insects. Matching Re_b ensures that the flow through bristles of a model (and hence *Le*) would be similar to those of real insects. Considering that lift and drag are known to be impacted by the extent of leaky flow (Kasoju et al. 2018), we matched Re_b to fall within 0.01 to 0.1 in majority of our physical models.

4. 3 Varying G and D for fixed S

Previous studies proposed that the substantial drag reduction realized with bristled wings in clap-and-fling is due to fluid leaking through the bristles (Santhanakrishnan et al., 2014; Jones et al., 2016; Kasoju et al., 2018). We found that *Le* peaked at $\tau \approx 0.56$ or $\tau \approx 0.63$ (Fig. 3.8B) for each condition of varying G and D, corresponding to the beginning of the fling phase. Interestingly, both $C_{D,max}$ and $C_{L,max}$ were observed between the same two time points, showing the importance of *Le* on dimensionless aerodynamic forces.

Previous studies of flow through bristled appendages found that *Le* is a function of both G and D (Cheer and Koehl, 1987; Hansen and Tiselius, 1992; Leonard, 1993; Loudon and

Koehl, 1994). These studies also found that *Le* can be greatly influenced for Re_b between 0.01 to 0.1, which is in the range of Re_b for tiny insects. We calculated Re_b for each wing model using D as the length scale in Eqn 4.4. Within the biological Re_b range (0.01-0.1), average force coefficients ($\overline{C_L}$,$\overline{C_D}$) showed no variation when varying D (Fig. 3.10A,B). For varying G, we maintained D and S as constants. The calculated Re_b for varying G tests was identical and within the biological Re_b range. Therefore for a constant Re_b, $\overline{C_D}$ can be varied significantly by varying G while maintaining minimal changes in $\overline{C_L}$(Fig. 3.10A,B).

Increasing Re_b via varying D showed opposite trends in $C_{D,max}$ and Le_{max} (Fig. 3.10E,G). Within the biological Re_b range, increasing D decreased Le_{max} and increased $C_{D,max}$. Similarly, for a constant Re_b, increasing G increased Le_{max} and decreased $C_{D,max}$. These changes in leakiness for varying G and D are in agreement with previous studies (Cheer and Koehl, 1987; Loudon and Koehl, 1994). Collectively, for Re_b in the range of tiny insects (0.01-0.1), we find that varying G provides drag reduction ($C_{D,max}$ and $\overline{C_D}$) as compared to varying D, by augmenting *Le*. Tiny insects could possibly meet their flight demands by modulating the inter-bristle gap. Ellington (1980) observed that the dandelion thrips (*Thrips physapus*) open their forewing setae prior to takeoff, suggesting modulation of G may be possible when preparing for flight.

Little to no variation in $\overline{C_L}$ for both conditions (varying G and D) is attributed to formation of shear layers around the bristles that lowers the effective gap, resulting in the bristled wing behaving like a solid wing (Lee and Kim, 2017; Kasoju et al., 2018). Miller and Peskin (2005) proposed that LEV-TEV asymmetry plays a critical role in lift generation in clap-and-fling at $Re_c \approx 10$. For varying G and varying D, we observed LEV circulation (Γ_{LEV}) to be larger compared to TEV circulation (Γ_{TEV}) for most of the clap-and-fling cycle (Fig. 3.9B,C). The implication of this asymmetry on lift generation can be seen by examining time-variation of C_L (Fig. 3.5B(i),B(ii)), where positive C_L was observed for most of the cycle. Both Γ_{LEV} and Γ_{TEV} peaked at the same time point where we observed peak C_L.

4. 4 Varying S for fixed n and G/D

Several studies examining the aerodynamic effects of varying S have reported contradictory findings. While some studies found little variation in force coefficients (Usherwood and Ellington, 2002; Luo and Sun, 2005; Garmann and Visbal, 2012), others have postulated that longer wingspans are detrimental for force generation (Harbig et al., 2013; Han et al., 2015; Bhat et al., 2019). All these studies considered solid wings at $Re_c > 100$. Our study is the first to report the effect of varying S on the aerodynamic performance of bristled wings performing clap-and-fling at Re_c=10. Within the biological Re_b range, both $\overline{C_D}$ and $\overline{C_L}$ were found to increase with S (Fig. 3.10A,B). In addition, $C_{D,max}$ and Le_{max} increased with increasing S (Fig. 3.10E,G).

The increase in G when increasing S is expected to increase Le and lower drag. However, we found that increasing S increased both Le and drag. Increasing S increases the wing surface area, which can explain the increase in drag. In addition, increasing G also increases Le. We speculate that the increase in Le with increasing S would minimize the increase in drag that would be expected from increasing wing surface area. Separately, varying S showed little changes in Γ_{LEV} and Γ_{TEV} (Fig. 3.9D) which resulted in small changes in C_L (Fig. 3.5B(iii)). Within the biological range of n, G/D, and Re_b, we postulate that larger S can be particularly beneficial to tiny insects when parachuting (Santhanakrishnan, Robinson, Jones, Low, Gadi, Hedrick and Miller, 2014), as larger drag can slow their descent.

4. 5 Varying n for fixed G/D and S

$\overline{C_D}$ substantially increased with increasing n, while $\overline{C_L}$ showed minimal variations for $n \leq 88$ and then increased with further increase in n (Fig. 3.7A). Wing models with $n \leq 88$ showed better aerodynamic performance in terms of force generation as compared to $n > 88$. Interestingly, forewing morphological analysis showed that values of n were

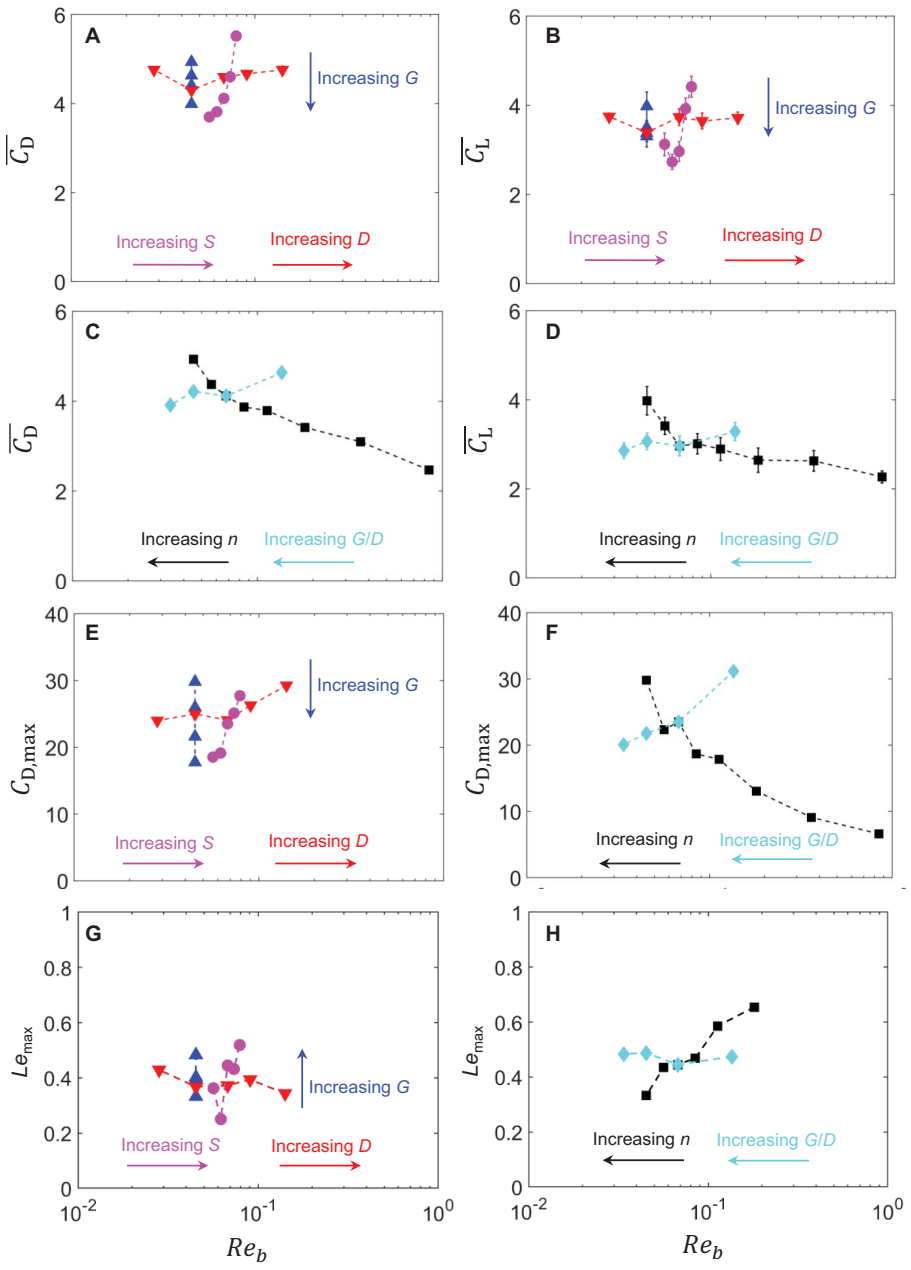

Figure 3.10: Average force coefficients ($\overline{C}$), peak drag coefficient ($C_{\mathrm{D,max}}$) and peak leakiness (Le_{max}) as a function of Re_b. (A) and (B) show $\overline{C_{\mathrm{D}}}$ and $\overline{C_{\mathrm{L}}}$, respectively, for varying G, D and S. (C) and (D) show ($\overline{C_{\mathrm{D}}}$) and ($\overline{C_{\mathrm{L}}}$), respectively, for varying n and varying G/D. (E) $C_{\mathrm{D,max}}$ for varying G, D and S. (F) $C_{\mathrm{D,max}}$ for varying n and G/D. (G) Le_{max} for varying G, D and S. (H) Le_{max} for varying n and G/D. Re_b was calculated from Eqn 3.2 using bristle diameter (D) as the length scale. Trends with increasing geometric variables (G, D, S, n) and ratio (G/D) are indicated.

concentrated in the region 30–90 for thrips and fairyflies. Moreover, $\overline{C_D}$ generated for this dominant range of n was larger than $\overline{C_D}$ generated for n=6 and 16. Thrips have been observed to intermittently parachute (Santhanakrishnan et al. 2014), likely to lower the energetic demands of flapping flight and potentially also during wind-assisted long-distance dispersals. During parachuting, these larger drag forces can assist them in migrating longer distances (Morse and Hoddle 2006). In addition, our morphological measurements showed that n varied from 32–161 across species, so lower n may better assist in generating lift needed for active flight, whereas larger n may better generate drag needed for passive dispersal via parachuting. Currently, it is unknown whether species with larger n tend to parachute more often.

Large variation in $C_{D,max}$ and Le_{max} with n (Fig. 3.10F,H) showed the influence of the number of bristles on aerodynamic performance. Le_{max} decreased with increasing n, while $C_{D,max}$ increased with increasing n. This suggests that changing n can aid or hinder aerodynamic performance by altering the leaky flow through the bristles. However, within the biological range of Re_b and n, only marginal changes in $\overline{C_L}$ in comparison to $\overline{C_D}$ were observed (Fig. 3.10C,D). This suggests that for a fixed S and G/D, tiny insects may experience reduced biological pressure to fit a particular number of bristles for adequate lift generation. This inference is also supported by the broad interspecific variation in n (Fig. 3.1C).

4. 6 Varying G/D for fixed n and S

Within the biological Re_b range, $C_{D,max}$ and Le_{max} were found to minimally change with increasing G/D (Fig. 3.10F,H). Also, varying G/D within the biological Re_b range produced little to no variation in $\overline{C_D}$ and $\overline{C_L}$. Note that for varying G/D within the biological Re_b range, the inter-bristle gap in the corresponding physical models was nearly identical, which likely explains the minimal change in Le_{max}. From these results, we summarize that within the biological range of Re_b, G/D variation for a fixed S, n and G results in little

variation in aerodynamic force generation.

Morphological measurements showed that G/D in thrips decreased with increasing BL, while the relationship was shallower for fairyflies. This dissimilar result in fairyflies and thrips raises a question regarding our use of static wing images for G/D measurements as opposed to free-flight wing images. We were restricted to using static forewing images due to the lack of free-flight wing images of tiny insects with adequate (i.e., high) magnification. It is unknown at present whether tiny insects can modulate G/D during free flight, as such a capability could permit them to tailor aerodynamic forces in relation to ambient conditions (e.g., temperature, humidity, wind speed) and associated energetic costs.

4. 7 Conclusions

Our analysis of forewing morphology in thrips and fairyflies showed similar scaling relationships between the two groups in the variables tested (n, G/D and $S_{\max}$). Within the biologically relevant range of Re_{b} (0.01–0.1) for tiny insects, we observed that increasing the inter-bristle spacing (G) for fixed bristle diameter (D) decreased drag forces significantly. This was supported by a significant increase in leakiness observed during early fling. However, changes in average lift forces were minimal, suggesting that having the capability of increasing the inter-bristle spacing during free flight could help these insects to overcome large drag forces with minimal changes in lift force. We also found that varying bristle diameter (D) had no effect on aerodynamic force generation, and varying the non-dimensional inter-bristle gap to diameter ratio (G/D) showed no significant influence on aerodynamic force generation. Finally, although we found that drag forces significantly decreased with decreasing number of bristles (n), lift force only minimally changed for $n < 100$. At $n > 100$, we observed a significant jump in lift forces. Considering the broad variation of n (32–161) observed across species, the lack of change in lift forces for $n < 100$ suggests that tiny insects may experience less biological pressure to optimize n for a given wingspan. Alternatively, stabilizing selection may maintain species within a range

of values that does not affect flight performance.

CHAPTER IV

SA 2: Flow characterization on aerodynamic force generation during wing-wing interaction for varying wing kinematics

1 Introduction

The smallest insects (body length < 2 mm) such as thrips fly at a chord-based Reynolds number (*Re*) on the order of 10, representing what may be considered as the aerodynamic lower limit of flapping flight. Flight at such low *Re* is challenged by significant viscous dissipation of kinetic energy. To overcome viscous losses, tiny insects have to continuously flap their wings to stay aloft. These insects are observed to flap their wings at high frequencies ($\mathcal{O}$(100 Hz)), likely to increase *Re* by increasing their wing tip velocity. In contrast to larger insects such as hawkmoths and fruit flies, tiny insects are also observed to operate their wings at near-maximal stroke amplitudes (Sane, 2016) and large pitch angles (Cheng and Sun, 2017; Lyu et al., 2019*b*). At large stroke amplitudes, the wings of tiny insects come together in close proximity of each other at the end of upstroke ('clap') and move away from each other at the start of downstroke ('fling'). Since the discovery of 'clap-and-fling' by Weis-Fogh (Weis-Fogh, 1973) in the small chalcid wasp *Encarsia Formosa*, this mechanism has been observed in the free flight of other tiny insects such as the greenhouse whitefly (Weis-Fogh, 1975), thrips (Ellington, 1984*b*; Santhanakrishnan et al., 2014), parasitoid wasps (Miller and Peskin, 2009) and jewel wasps (Miller and Peskin, 2009). A number of studies have explored the fluid dynamics of clap-and-fling experimentally (Maxworthy, 1979; Spedding and Maxworthy, 1986; Lehmann and Pick, 2007), theoretically (Lighthill, 1973; Ellington, 1984*b*; Kolomenskiy et al., 2011), and numerically (Miller and Peskin, 2004; Santhanakrishnan et al., 2014; Jones et al., 2015; Sun and

Yu, 2006; Kolomenskiy et al., 2011; Arora et al., 2014), and have found that wing-wing interaction augments lift force through the generation of bound circulation at the leading edges of the wings during fling (Lighthill, 1973; Maxworthy, 1979; Spedding and Maxworthy, 1986; Miller and Peskin, 2005; Kolomenskiy et al., 2011).

In contrast to larger flying insects where a stable leading edge vortex (LEV) is observed with a shed trailing edge vortex (TEV) (Birch et al., 2004), previous studies of a single wing in linear translation (Miller and Peskin, 2004) and in semi-circular revolution (Santhanakrishnan et al., 2018) have shown that lift generation at $Re \sim 10$ is reduced due to 'vortical symmetry', where both the LEV and TEV remain attached to the wing. Miller and Peskin (Miller and Peskin, 2005) showed that lift enhancement by clap-and-fling is more pronounced for $Re \sim \mathcal{O}(10)$ than at higher Re, as most of the lift lost during the downstroke and upstroke (on account of vortical symmetry) can be recovered by establishing LEV-TEV vortical asymmetry during wing-wing interaction. However, at Re relevant to tiny insect flight, Miller and Peskin (Miller and Peskin, 2005) also showed that large drag penalties (Lyu et al., 2019*a*) are associated with the fling. Subsequent studies have since shown that wing flexibility and the unique bristled structure of tiny insect wings can provide aerodynamic benefits by lowering drag forces needed to fling wings apart and increasing lift over drag ratio (Miller and Peskin, 2009; Santhanakrishnan et al., 2014; Jones et al., 2016; Kasoju et al., 2018; Ford et al., 2019).

Forces generated by biological bristled structures such as tiny insect wings depend on inter-bristle flow that is a function of Reynolds number based on bristle diameter (Re_b). Previous studies (Cheer and Koehl, 1987; Loudon and Koehl, 1994) have shown that an array of bristles can undergo transition from acting as a leaky rake to a solid paddle with decreasing Re_b. Dynamically scaled models of bristled wings during translation and rotation have been reported to show little variation in forces in comparison with a solid wing (Sunada et al., 2002; Kolomenskiy et al., 2020*a*). Further, studies using comb-like wings (Weihs and Barta, 2008; Davidi and Weihs, 2012) were found to generate almost the same amount

of forces as a solid wing, with a 90% drop in wing weight. Recent studies using bristled wings (Lee and Kim, 2017; Lee et al., 2018, 2020*b*) observed the formation of diffused shear layers around the bristles at smaller inter-bristle gaps. These shear layers prevent fluid from leaking through the inter-bristle gaps, resulting in the bristled wing behaving similar to a solid wing. A central limitation of the above studies is the lack of considering clap-and-fling kinematics observed in freely-flying tiny insects, involving aerodynamic interaction of bristled wing pairs. In our recent study (Kasoju et al., 2018) examining clap-and-fling of bristled wing pairs at $Re \sim \mathcal{O}(10)$, we found that leaky flow through the bristles results in large drag reduction and disproportionally lower lift reduction (i.e., improved lift over drag ratio) when compared to forces generated by geometrically equivalent solid wings. These aerodynamic benefits were diminished at *Re*=120 (relevant to larger fruit flies) (Ford et al., 2019), suggesting that the use of clap-and-fling in conjunction with bristled wings is particularly well-suited at *Re* relevant to tiny insect flight.

In terms of wing-wing interaction of bristled wings, our recordings of free-takeoff flight of thrips show that these insects bring the wings close together ($\sim$1/10-1/4 of chord length) at the end of upstroke (clap) before flinging the wings apart (Figure 4.1). Previous studies (Sun and Yu, 2006; Arora et al., 2014) have found that increasing initial inter-wing spacing (δ in Fig. 4.1, expressed non-dimensionally as % of chord length) of interacting solid wings decreases aerodynamic forces. For δ¿80%, interference effects between the wings were found to diminish. A high pressure region was observed to form between the interacting solid wings during the end of the clap phase that generated a sharp peak in forces at the end of clap and start of fling (Cheng and Sun, 2017). However, none of these studies examined how inclusion of wing bristles impacts clap-and-fling aerodynamics under varying δ. The results of these previous studies cannot be expected to be identical for bristled wing pairs performing similar kinematics or for similar δ, due to alterations in flow characteristics expected around and through bristled wings. In addition, the above studies did not examine circulation of LEV and TEV and corresponding effect on lift gen-

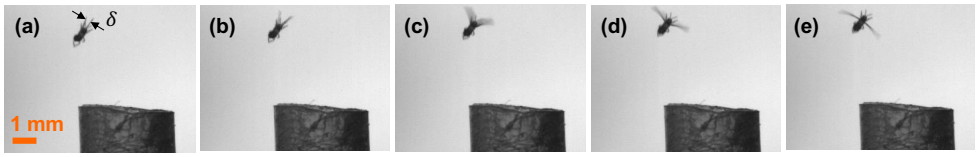

Figure 4.1: Successive snapshots of thrips in free take-off flight. (a) End of upstroke ('clap') where the wings come in close proximity of each other, separated by non-dimensional inter-wing spacing δ. (b) Start of downstroke ('fling') where the wings move apart from each other, followed by the rest of the downstroke from (c) to (e). δ ranges from about 10% to 25% of the wing chord.

eration. In terms of wing motion, a recent study reported the wing kinematics of free-flying thrips (Lyu et al., 2019*b*) and noted large changes in pitch angle for small changes in revolution of the wing. While this indicates that thrips wings may purely rotate at the start of fling before translation, it remains unknown as to whether there are aerodynamic benefits associated with such kinematics.

In this study, we aimed to examine how varying δ and wing kinematics impacts aerodynamic interaction of bristled wings during fling at Re=10. We used a dynamically scaled robotic platform fitted with a pair of physical bristled wing models for investigation. Aerodynamic force measurements and flow visualization were conducted for varying δ in the range of 10% to 50% of wing chord for three different kinematics: 1) wings purely rotating about their trailing edges; 2) linear translation of each wing at a fixed angle relative to the vertical; and 3) overlapping rotation and translation of each wing. In addition to clap-and-fling kinematics, tiny insects have been observed to employ 'rowing' kinematics in three-dimensional flapping flight, where the wings move fast downward and backward (Cheng and Sun, 2018). As Re decreases (e.g., due to size reduction), the planar upstroke that is commonly employed by large scale insects changes to a U-shaped upstroke in tiny insects (Lyu et al., 2019*b*), with large changes in wing deviation from the stroke plane. This mechanism was found to generate 70% of the required vertical force for tiny insects (Cheng and Sun, 2018). It is important to note that changes in deviation are not considered in this study.

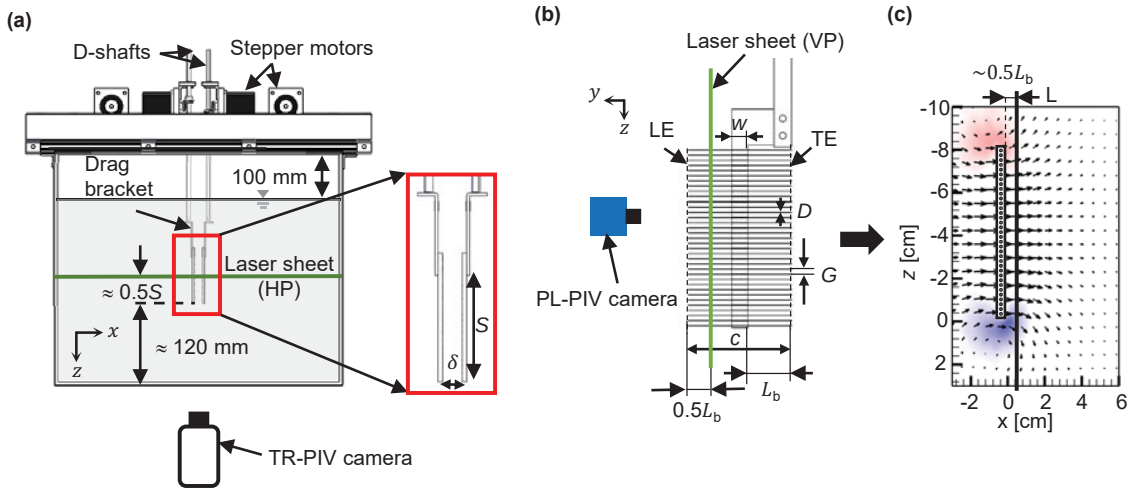

Figure 4.2: Robotic platform and experimental setup used for force and PIV measurements. (a) Front view of the robotic platform with a pair of scaled-up physical bristled wing models separated by initial inter-wing spacing δ expressed non-dimensionally as % of wing chord (c). 2D TR-PIV setup with high-speed camera and laser sheet along a horizontal plane (HP). (b) Magnified view of rectangular bristled wing model showing 2D PL-PIV measurements using an sCMOS camera focused on a laser sheet along a vertical plane (VP). (c) Velocity vector fields obtained from 2D PL-PIV with vorticity contours overlaid on the top. L represents the line along which reverse flow capacity (RFC) was calculated. LE = leading edge; TE = trailing edge; x, y, z are fixed coordinate definitions; c=wing chord=45 mm; S=wing span=81 mm; total number of bristles=70; w=membrane width=7 mm; L_b=bristle length on each side of the membrane=19 mm.

2 Methods

2. 1 Dynamically scaled robotic platform

We comparatively examined the forces and flows generated during the prescribed motion of a pair of bristled wing physical models to those of a single bristled wing. The wing models were driven by a dynamically scaled robotic platform (Fig. 4.2(a)) that has been used in our previous studies (Kasoju et al., 2018; Ford et al., 2019). For more details on the test platform, refer to **Appendix A.3**.

2. 2 Bristled wing models

We fabricated a pair of rectangular scaled-up bristled wing models (Fig. 4.2(b)) with wing span (S) of 81 mm and chord (c) of 45 mm. The bristled wing consisted of a 3 mm thick

solid membrane (laser cut from optically clear acrylic) of length equal to S and 7 mm width (w), with 35 bristles of equal length (L_b=19 mm) attached on two opposite sides along the length of the membrane (70 bristles in total, in the range of tiny insects (Kasoju et al., 2020*a*)). The bristles consisted of approximately 0.20 mm diameter (D) 304 stainless steel wires, each being cut to length L_b. The inter-bristle gap (G) was maintained at 2 mm throughout the wing, to obtain G/D=10 in the range of G/D of tiny insect wings (Jones et al., 2016; Kasoju et al., 2020*a*). An equivalent solid wing pair with the same S and c as the bristled wing was also laser cut from optically clear acrylic for comparative measurements.

2. 3 Kinematics

The robotic platform enabled rotation and linear translation of wing models along a horizontal stroke plane. We examined the isolated and combined roles of rotation and linear translation in this study. Sinusoidal and trapezoidal motion profiles were used for wing rotation and translation, respectively (Fig. 4.3(a)), using equations developed by Miller and Peskin (Miller and Peskin, 2005). The 2D clap-and-fling kinematics developed by Miller and Peskin (Miller and Peskin, 2005) has been used in several previous studies (Miller and Peskin, 2009; Arora et al., 2014; Santhanakrishnan et al., 2014; Jones et al., 2016; Ford et al., 2019). The peak tip velocity (U_{max}) during rotation, linear translation and their combination was maintained constant throughout the study at 0.157 m s^{-1}. For tests examining wing rotation, each wing model was rotated about its trailing edge (TE) from an initial vertical position to an angle θ_r relative to the vertical (Fig. 4.3(b)), reaching their peak angular velocity (ω_{max}) for each θ_r. For the above U_{max}, the peak angular velocity (ω_{max}) was calculated using equation 4.1. The cycle duration (T) thus changed with varying θ_r (Table 4.1). For tests examining linear translation, each wing was preset prior to the start of wing motion to a fixed angle (θ_t) relative to the vertical (Fig. 4.3(c)) and the entire wing moved with the same velocity in a trapezoidal motion profile reaching maximum tip velocity (U_{max}) of 0.157 m s^{-1}.

For tests examining combination of rotation and linear translation, each wing was prescribed to rotate and translate under varying levels of overlap (ζ) that was defined based on the start of wing translation relative to rotation (Fig. 4.3(a)). Note that ζ=0% means that linear translation started at the end of rotation, and ζ=100% means that linear translation started at the same time as start of rotation. θ_r and θ_t of 45° were used for all tests examining combined rotation and linear translation. ω_{max} for each ζ that was tested was equal to ω_{max} used in tests involving only wing rotation. T varied for each tested condition of combined rotation and linear translation (Table 4.1). The wing motion for both the wings were identical but opposite in sign. Also, the motion was strictly two-dimensional (2D) without changes in the stroke plane. At the end of every cycle of each test condition, the wings were programmed to move back to the starting position and were paused for at least 30 seconds before starting the next cycle so as to remove the influence of cycle-to-cycle interactions. This pause time is applicable for all the data collection throughout the study. A description of the mathematical equations used in modeling wing kinematics is provided in **Section 3**.

3 Modeling of wing kinematics

As mentioned in subsection 2. 3, we used the kinematics developed by Miller and Peskin (Miller and Peskin, 2005) in this study. We used a sinusoidal velocity profile for wing rotation. The peak angular velocity (ω_{max}) was maintained constant for each angle of wing rotation (θ_r, in radians) and given by the following equation:

$$\omega_{max} = \frac{2\theta_r U_{max}}{\Delta\tau_{rot} c} \tag{4.1}$$

where $\Delta\tau_{rot}$ represents the dimensionless duration of rotational phase, c is the wing chord length and U_{max} (=0.157 m s^{-1}) is the maximum velocity during wing rotation and linear translation. We maintained the ratio of θ_r to $\Delta\tau_{rot}$ constant at 0.4514 to obtain a constant

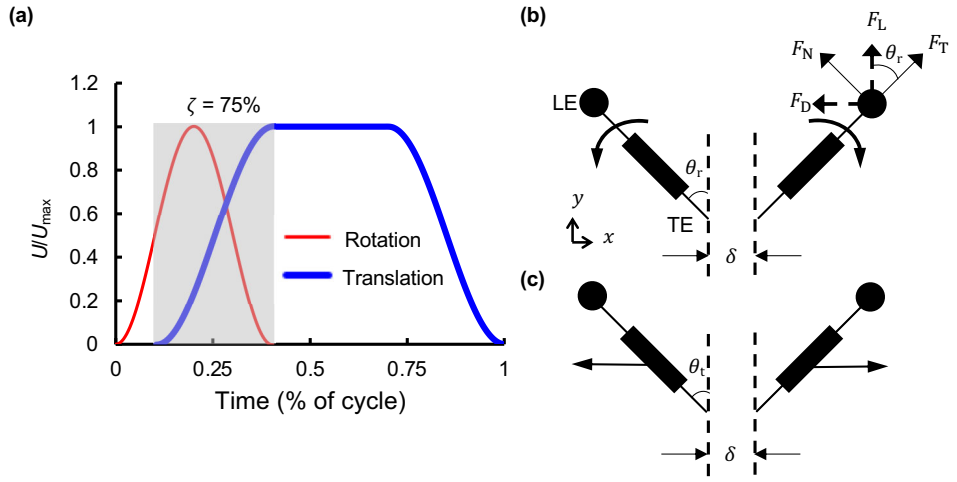

Figure 4.3: Wing kinematics used in this study. (a) Time-varying motion profile for a single wing. Instantaneous wing tip velocity U was non-dimensionalized by peak tip velocity $U_{\max}$. Time is expressed non-dimensionally in terms of percentage of cycle duration T. Thin and thick lines indicate rotational and translational motion, respectively. ζ indicates the percentage of overlap between wing rotation and the start of translation. (b) and (c) show sectional views of a bristled wing pair during wing rotation and linear translation, respectively. θ_r is the angle at the end of wing rotation; θ_t is the translation angle. Lift (F_L) and drag (F_D) forces were calculated by taking components of tangential (F_T) and normal (F_N) forces in the vertical (F_L) and horizontal (F_D) directions.

$\omega_{\max}$. The cycle time (T) for each θ_r was calculated using the following equation (T values provided in Table 4.1):

$$T = \frac{\Delta\tau_{rotc}}{U_{\max}} \tag{4.2}$$

For example, when $\theta_r = 45^\circ = \pi/4$ rad, we obtain $\Delta\tau_{rot}$ = (π/4*0.4514)=1.74. The corresponding cycle time, $T_{\theta_r=45^\circ}$=1.74$\times$0.045$\times$1000)/0.157 m s^{-1}=498 ms. Rounding off to nearest multiple of 10, we obtain 500 ms.

For wing translation at a fixed angle (θ_t, in radians), we employed a trapezoidal velocity profile consisting of an acceleration phase, constant velocity phase and a deceleration phase. The dimensionless duration ($\Delta\tau$) of each of these phases were maintained constant at 1.3. The cycle time (T) for each translation phase was calculated from equation 4.2, using $\Delta\tau$ in place of $\Delta\tau_{rot}$: T=1.3$\times$0.045$\times$1000/0.157=373. Rounding off to nearest multiple of 10, we obtain 370 ms. Total cycle time (T) in translation, for each θ_t, is given by 3$\times$370=1110 ms (T values provided in Table 4.1).

The cycle time (T) for varying levels of overlap (ζ, ranging between 0% and 100%) between rotation (at θ_r=45°) and start of translation (θ_t=45°) was calculated using the following equation:

$$T_\zeta = \left(\frac{100-\zeta}{100}\right) T_{\theta_r=45^\circ} + T_{\theta_T=45^\circ} \tag{4.3}$$

where T_ζ represents cycle time for a specific ζ, $T_{\theta_r=45^\circ}$ and $T_{\theta_T=45^\circ}$ represents cycle time of wing undergoing rotation to θ_r and translation at θ_t=45°. For example, when ζ=25%, we obtain T_ζ = (100-25)/100×500+1110 ms=1485 ms. Rounding off to nearest multiple of 10, we obtain 1490 ms. Similarly, T was calculated for other ζ values (provided in Table 4.1).

3. 1 Test conditions

Bristled wing pairs and a single bristled wing were tested at *Re*=10 for the following kinematics: 1) rotation to θ_r values of 22.5°, 45°, 67.5°; 2) linear translation at θ_t values of 0° (vertically oriented), 22.5°, 45°, 67.5°; and 3) combined rotation and linear translation for ζ=0%, 25%, 50%, 75%, 100%. Each of the above test conditions were repeated for δ=10%, 30%, 50% of wing chord (c) between the bristled wing pairs as well as in a single bristled wing (latter corresponding to $\delta \to \infty$). The wing models being tested were fully immersed in 99% glycerin solution. The kinematic viscosity (ν) of the glycerin used in this study was measured using a Cannon-Fenske routine viscometer (size 400, Cannon Instrument Company, State College, PA, USA) to be 707 mm^2 s^{-1} at room temperature. To obtain *Re*=10, peak velocity (U_{max}) was calculated to be 0.157 m s^{-1} (and maintained constant as mentioned in subsection 2. 3) using the following equation:

$$Re = \frac{U_{max} c}{\nu} \tag{4.4}$$

where c (Fig. 4.2(b)) and ν are constants. Using the kinematics equations provided in Miller and Peskin (Miller and Peskin, 2005), motion profiles were created to drive the stepper motors. Reynolds number based on bristle diameter D (defined as $Re_b = U_{max} D/\nu$)

was also maintained constant at 0.045 throughout the study, which is in the range of thrips (0.01-0.07) (Jones et al., 2016).

3. 2 Force measurements

Similar to our previous studies (Kasoju et al., 2018; Ford et al., 2019), force data were collected using uniaxial strain gauges mounted on both sides of custom L-brackets in half-bridge configuration. The L-brackets were used to couple a wing to the D-shaft (see **Appendix A.3** for details of test platform). A strain gauge conditioner continuously measured the forces in the form of voltage signals based on L-bracket deflection during wing motion. Two different, custom L-brackets were used for non-simultaneous acquisition of normal and tangential forces (Fig. 4.3(b)) that were subsequently used for calculating lift and drag forces. The design of lift and drag L-brackets and validation of the methodology can be found in Kasoju et al. (Kasoju et al., 2018). Normal and tangential forces (and thus lift and drag forces) were only measured on one wing in tests involving a bristled wing pair, with the assumption that the forces generated by the other wing would be equal in magnitude (as the motion was symmetric for both wings of a wing pair). A pause time of 30 seconds was included between one cycle to the next cycle, in order to exclude any mechanical disturbance between cycles (e.g., sudden bending of L-bracket when the wings come to rest quickly). The raw voltage data was acquired using a data acquisition board (NI USB-6210, National Instruments Corporation, Austin, TX, USA) once the LabVIEW program (used for driving the motors) triggered to start the recording. Force data and angular position of the wings were acquired during each cycle at a sample rate of 10 kHz for all the test conditions mentioned in subsection 3. 1. The raw data was processed in the same manner as in our previous studies (Kasoju et al., 2018; Ford et al., 2019) and implemented via a custom MATLAB script. A third order low-pass Butterworth filter with a cutoff frequency of 24 Hz was first applied to the raw voltage data. The baseline offset (obtained with wing at rest) was averaged in time and subtracted from the filtered voltage

data. The lift and drag brackets were calibrated manually, and the calibration was applied to the filtered voltage data obtained from the previous step to calculate tangential (F_T) and normal (F_N) forces (Fig. 4.3(b)). Lift and drag forces were calculated as components of F_T and F_N as described in subsection 3. 4.

3. 3 Flow visualization

We conducted 2D time-resolved particle image velocimetry (2D TR-PIV) measurements to visualize time-varying chordwise flow generated by the motion of a wing pair (or a single wing) at a horizontal plane (HP) located at mid-span (Fig. 4.2(a)). 2D TR-PIV based 2-component velocity vector fields were also used to determine the strength of the LEV and TEV, net circulation on a wing and pressure distribution in the flow field. In addition, 2D phase-locked PIV (2D PL-PIV) measurements were conducted to characterize the inter-bristle flow along the wing span at a vertical plane (VP) located at $0.5L_b$ measured from the leading edge (LE) as shown in Fig. 4.2(b). For more details on 2D TR-PIV, 2D PL-PIV and PIV processing, refer to **Appendices A.5, A.6, A.7**, respectively.

3. 4 Definitions of calculated quantities

3. 4.1 Lift and drag coefficients

Lift force (F_L) and drag force (F_D) were defined along the vertical and horizontal directions, respectively, and calculated using non-simultaneous measurements of tangential (F_T) and normal (F_N) forces (Fig. 4.3(b)). F_T and F_N measurements were phase-averaged over 30 cycles for further analyses of F_L and F_D. We acquired 30 cycles of force data to account for variability in the mechanical operation of our robotic platform, and characterized this variability using standard deviation across the 30 cycles. Dimensionless lift coefficient (C_L) and drag coefficient (C_D) were calculated using components of measured F_N and F_T using

Kinematics	Cycle duration T [ms]	Frame rate [Hz]
Rotation, θ_r [°]		
22.5	250	400
45	500	200
67.5	750	133.33
Translation, θ_t [°]		
0	1110	90
22.5	1110	90
45	1110	90
67.5	1110	90
Overlap, ζ [%]		
0	1610	61.72
25	1490	67.11
50	1360	73.52
75	1240	80.64
100	1110	90.09

Table 4.1: Experimental test conditions, cycle duration and TR-PIV frame rates used for: rotation (θ_r), translation (θ_t), and overlapping rotation and translation (ζ in %). Note that ζ=0% indicates translation starts at the end of rotation, and ζ=100% indicates translation starts at the same time as start of rotation.

the following equations:

$$C_L = \frac{F_L}{0.5\rho U_{max}^2 A} = \frac{F_T \cos\theta + F_N \sin\theta}{0.5\rho U_{max}^2 A} \tag{4.5}$$

$$C_D = \frac{F_D}{0.5\rho U_{max}^2 A} = \frac{F_T \sin\theta + F_N \cos\theta}{0.5\rho U_{max}^2 A} \tag{4.6}$$

where θ is the instantaneous angular position of the wing relative to the vertical and ρ is the density of the fluid medium (ρ of the glycerin solution used in this study was measured to be 1259 kg m^{-3}).

3. 4.2 Circulation

Circulation was calculated to quantify the strength of the LEV and TEV using the z-component of vorticity (ω_z). ω_z was calculated from the exported phase-averaged TR-PIV

velocity fields using the following equation implemented in a custom MATLAB script:

$$\omega_z = \frac{\partial v}{\partial x} - \frac{\partial u}{\partial y}. \tag{4.7}$$

Circulation (Γ) was calculated from ω_z fields at all time instants and test conditions where TR-PIV data were acquired, using the following equation in a custom MATLAB script:

$$\Gamma = \iint_S \omega_z \, ds \tag{4.8}$$

where S is the vorticity region for either the LEV or TEV. For a particular kinematics test condition, the maximum absolute values of ω_z (i.e., $|\omega_z|$) at both LEV and TEV of a bristled wing were identified. A $15\%|\omega_z|$ high-pass cut-off was next applied to isolate the vortex cores on a single bristled wing performing the same kinematics. Alternative cutoff values of 5% and 25% of $|\omega_z|$ were examined for one condition each of rotation (θ_r=22.5°), linear translation (θ_t=22.5°) and combined rotation and translation (ζ=25%). The trend of time-variation of Γ was unaffected when changing cutoff from $15\%|\omega_z|$ (Fig. 4.20) to $25\%|\omega_z|$ (refer **Appendix** for Supplementary material Fig. A.9. 2.1 (b),(d),(f) in (Kasoju and Santhanakrishnan, 2021*a*)), with only small changes in the magnitude. However, for a lower cutoff of $5\%|\omega_z|$, we observed slight variation in the time-variation of Γ at the expense of undesirable high-frequency noise. We thus used $15\%|\omega_z|$ as the cutoff for circulation analyses presented in this study. Γ of LEV or TEV was then calculated by selecting a region of interest (ROI) by drawing a box around a vortex core. A custom MATLAB script was used to automate the process of determining the ROI (Samaee et al., 2020). Essentially, we started with a small square box of 2 mm side and compared the Γ value with that of a bigger square box of 5 mm side. If the circulation values matched between the 2 boxes, then we stopped further iteration. If the circulation values did not match between the 2 boxes, we increased the size of the smaller box by 3 mm and iterated the process. When calculating Γ of a specific vortex (LEV or TEV), we ensured that ω_z of the oppositely-signed vortex was

zeroed out. For example, ω_z of the negatively-signed TEV was zeroed out when calculating the Γ of the positively-signed LEV on the right wing of a wing pair in fling. This allowed us to work with one particular vortex at a time and avoids contamination of the Γ estimation, if the box were to overlap with the region of the oppositely-signed vortex. Γ in this study is presented for left wing only, assuming the following: (a) Γ_{LEV} on the right wing is equivalent to Γ_{LEV} of left wing but oppositely signed; (b) Γ_{TEV} on the right wing is equivalent to Γ_{TEV} of left wing but oppositely signed. It is important to note that asymmetry in Γ_{LEV} and Γ_{TEV} for the *same* wing is to be expected as in previous studies of wing-wing interaction at low *Re* on the order of 10 (Miller and Peskin, 2005; Arora et al., 2014; Ford et al., 2019). Γ at the LEV and TEV for all the test conditions were negative and positive, respectively, for the left wing.

In addition to Γ_{LEV} and Γ_{TEV}, we also calculated cycle-averaged net circulation ($\overline{\Gamma_{\mathrm{net}}}$) on the left wing using the following equation.

$$\overline{\Gamma_{\mathrm{net}}} = \overline{\mid \Gamma_{\mathrm{LEV}} \mid - \mid \Gamma_{\mathrm{TEV}} \mid} \tag{4.9}$$

As 2D, 2-component TR-PIV measurements were used to calculate Γ_{LEV}, Γ_{TEV} and $\overline{\Gamma_{\mathrm{net}}}$, we examined the validity of 2D flow simplification by computing 2D divergence of the TR-PIV based velocity fields along the *x*-*y* plane. We observed small regions of non-zero 2D divergence in the flow field, suggesting that 2D flow simplification was reasonable for this study. For more details, refer to **Appendix A.4**.

3. 4.3 Downwash velocity

Downwash velocity ($\overline{V_{\mathrm{y}}}$) was defined as the spatially-averaged velocity of the flow deflected downward by the motion of a bristled wing pair. $\overline{V_{\mathrm{y}}}$ calculated using the following equation from spatiall-averaged TR-PIV velocity vector fields:

$$\overline{V_y} = \frac{1}{N}\left[\sum_{\mathrm{FOV}} v(x,y)\right] \tag{4.10}$$

where $v(x,y)$ is the vertical component of velocity and N is the total number of grid points within the TR-PIV field of view (FOV).

3. 4.4 Pressure distribution and average pressure coefficient

Using the algorithm developed by Dabiri et al.(Dabiri et al., 2014), unsteady pressure (p) distribution was estimated from TR-PIV velocity vector fields. The pressure distribution presented in this study is calculated using direct integration of the pressure gradient term in the Navier–Stokes equation (for more details, see Dabiri et al.(Dabiri et al., 2014)). The pressure estimation in this study includes the viscous terms in the Navier–Stokes equation. This estimated pressure distribution was visualized in Tecplot software. In addition, we also calculated the spatially-averaged positive and negative pressures across the entire phase-averaged TR-PIV FOV at every time instant using the following equations:

$$\overline{p_+} = \frac{1}{N_+}\left[\sum_{\text{FOV}} p_+(x,y)\right] \tag{4.11}$$

$$\overline{p_-} = \frac{1}{N_-}\left[\sum_{\text{FOV}} p_-(x,y)\right] \tag{4.12}$$

where $\overline{p_+}$ and $\overline{p_-}$ are the spatially-averaged positive pressure and spatially-averaged negative pressure, respectively, estimated in the entire TR-PIV FOV at a particular timepoint. N_+ and N_- are the total number of grid points in (x,y) of the portion of the FOV containing positive and negative pressures, respectively.

Using the spatially-averaged positive and negative pressures, an spatially-averaged coefficient of pressure ($\overline{C_p}$) was calculated using the following equation:

$$\overline{C_p} = \frac{2\,\overline{p}}{\rho U_{\text{max}}^2} \tag{4.13}$$

where $\overline{p}$ is the spatially-averaged positive or negative pressure calculated from equations (4.11) and (4.12).

In addition to the above spatially averaged pressure coefficient ($\overline{C_p}$), we also calculated the cycle-averaged net pressure coefficient ($\overline{C_{p,\text{net}}}$) using the following equation:

$$\overline{C_{p,\text{net}}} = \frac{2\,\overline{|\,|\,\overline{p_+}\,| - |\,\overline{p_-}\,|\,|}}{\rho U_{\text{max}}^2} \tag{4.14}$$

where $\overline{p_+}$ is the spatially averaged positive pressure calculated from equation (4.11), $\overline{p_-}$ is the spatially averaged negative pressure calculated from equation (4.12), ρ is the density of the fluid medium and U_{max} is the maximum tip velocity during translation or rotation (maintained constant throughout the study at 0.157 m s^{-1}.

3. 4.5 Reverse flow capacity (RFC)

Inter-bristle flow along the wing span is influenced by Re_b, G, D and wing inclination relative to the flow. Significant changes can be expected in the Re_b range of tiny insect flight, such that the wing bristles can permit fluid leakage or behave like a solid plate. From the PL-PIV velocity fields, we estimated the capacity of a bristled wing to leak flow (in the direction opposite to wing motion) by comparing the volumetric flow rate (per unit width) along the wing span to that of a geometrically equivalent solid wing undergoing the same wing motion. Reverse flow capacity (RFC) was calculated along a line 'L' parallel to the span and located at a distance of $\sim$50%L_b (Fig. 4.2(b)). Volumetric flow rate per unit width for a particular wing model (Q_{wing}) was calculated using the following equation:

$$Q_{\text{wing}} = \int_L u\, dz \tag{4.15}$$

where u denotes the horizontal component of velocity along line 'L'. RFC was calculated using the following equation:

$$\text{RFC}\ [\%] = \frac{Q_{\text{solid}} - Q_{\text{bristled}}}{Q_{\text{solid}}} \tag{4.16}$$

where Q_{solid} and $Q_{bristled}$ represents the volumetric flow rate per unit width displaced by a solid wing and bristled wing undergoing the same motion, respectively. The reason underlying calculation of reverse flow capacity (RFC) was to understand the ability of a bristled wing to leak the fluid through the gaps by comparing it to a solid wing of identical chord and span when both wing models are undergoing the same wing motion. We expect that reverse flow would be larger closer to the leading edge (LE) of the wing during rotation, when the wing is being rotated with respect to trailing edge (TE). During translation, as the entire wing is translating at the same velocity, the reverse flow through the entire wing at any y-location in x-z plane can be assumed to be the same. Considering the above factors, we chose a laser plane closer to LE of the wing. From our previous study (Kasoju et al., 2018), we observed no flow along the z-direction of a rectangular bristled wing model (Fig. 4.2(b)). We thus expected that using only the x-velocity component would be sufficient to characterize RFC. To verify the lack of z-directional flow in this study, we looked at the velocity vector field (overlaid with vorticity contours) for one condition of rotation, translation and overlap for a single wing and a wing pair with inter-wing spacing (δ) = 10% (see **Appendix** for Supplementary Material, Movies A.9. 2.2, A.9. 2.3, A.9. 2.4). We observed no flow along the z-direction.

4 Results

4. 1 Bristled wings in rotation

Aerodynamic force generation. In general, both C_L and C_D followed the kinematic profile of rotational motion (Fig. 4.4(a)-(d)). When θ_r was increased from 22.5° to 67.5°, C_D and C_L peaks occurred earlier in time (Fig. 4.4(c),(d)). With increasing θ_r, relatively we observed analogous reduction in C_D and C_L. A noticeable drop in C_D was observed with increasing δ for all θ_r. C_L was highest for the lowest initial inter-wing spacing (δ=10%) in both θ_r=22.5° (Fig. 4.4(b)) and θ_r=67.5 ° (Fig. 4.4(d)). Increasing δ from 10% to 30% resulted in a noticeable drop in C_L, following which C_L showed minimal variation for

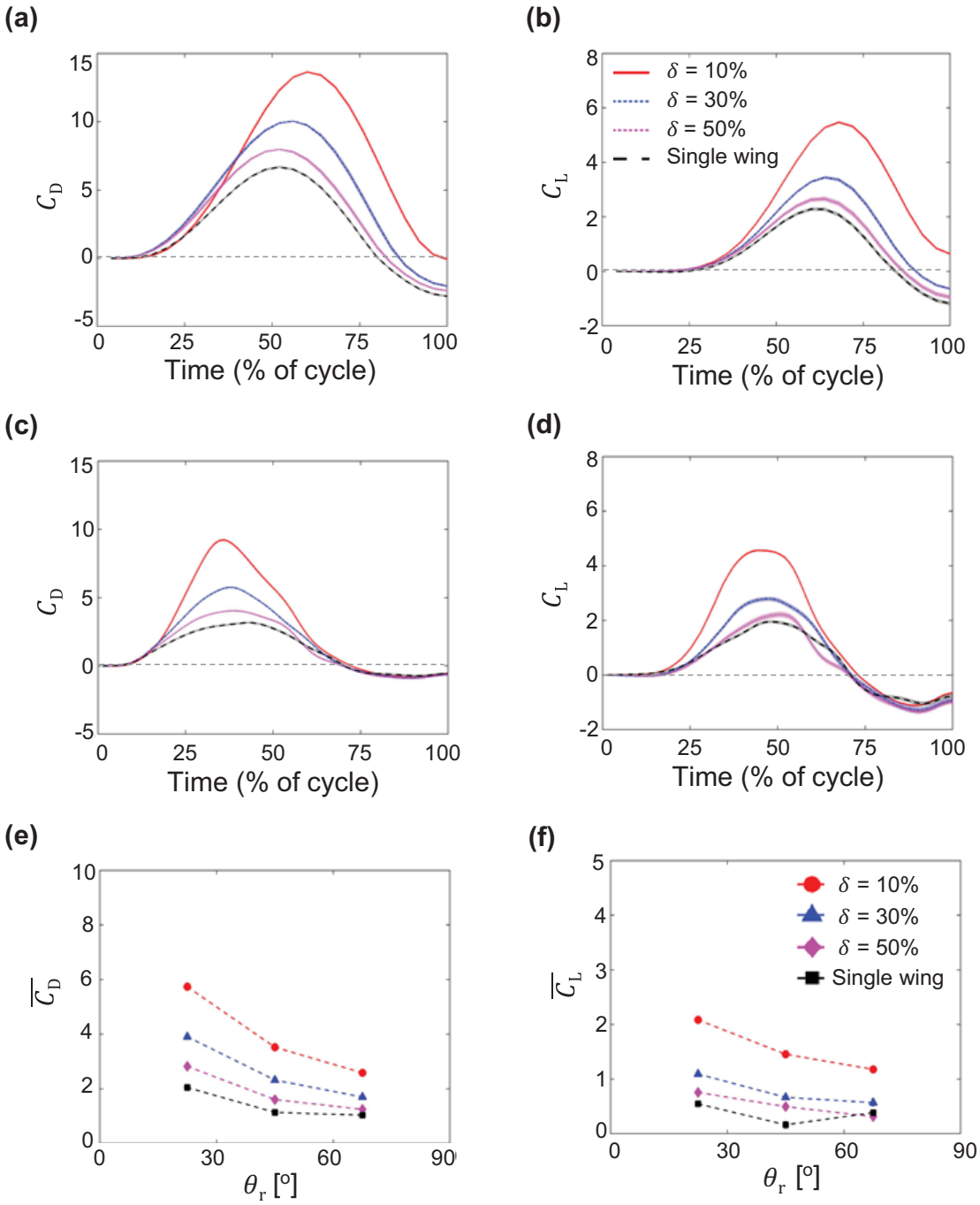

Figure 4.4: Force coefficients during bristled wing rotation at Re=10. Shading around each curve represents ± 1 standard deviation (SD) across 30 cycles. (a) and (b) show time-variation of drag coefficient (C_D) and lift coefficient (C_L), respectively, for θ_r =22.5°. (c) and (d) show time-variation of C_D and C_L, respectively, for θ_r=67.5°. (e) and (f) show cycle-averaged drag coefficient (C_D) and cycle-averaged lift coefficient (C_L), respectively, for varying θ_r. Legend for (a)-(d) is shown in (b); legend for (e)-(f) is shown in (f). The y-axis range for (a) and (c) is -5 to 15, (b) and (d) is -2 to 8, (e) is 0 to 10 and (f) is 0 to 5.

δ=50% as well as the single wing (Fig. 4.4(b),(d)). This insensitivity of C_L for $\delta \geq 30\%$ was in sharp contrast to C_{D} variation with δ (Fig. 4.4(a),(c)). C_{D} dropped below zero toward the end of the cycle for θ_{r}=22.5° (Fig. 4.4(a)), likely due to wing deceleration altering flow around the bristled wing model in a short time span. With increase in θ_{r} to 67.5°, the magnitude of negative drag was decreased (Fig. 4.4(c)).

Cycle-averaged drag coefficient ($\overline{C_{\mathrm{D}}}$) decreased with increasing θ_{r} (Fig. 4.4(e)). Increasing θ_{r} from 22.5° to 67.5° for the single wing showed little to no variation in $\overline{C_{\mathrm{D}}}$. By contrast, the bristled wing pair with lowest δ (=10%) showed substantial decrease in $\overline{C_{\mathrm{D}}}$ with increasing θ_{r}. With further increase in δ, $\overline{C_{\mathrm{D}}}$ decreased with θ_{r} and approached single wing values. Similar to $\overline{C_{\mathrm{D}}}$, $\overline{C_{\mathrm{L}}}$ also decreased with increasing θ_{r}. Increasing δ beyond 10% resulted in little to no variaton in $\overline{C_{\mathrm{L}}}$. Finally, with increasing δ, larger reduction in C_{D} was observed compared to smaller reduction in C_{L} for δ ¿ 10%.

Chordwise flow. Rotation of a single bristled wing generated a pair of counter-rotating vortices at the LE and TE (Fig. 4.5). For the three θ_{r} values that we examined, we observed both the LEV and TEV to be attached to the wing. Increasing θ_{r} promoted earlier development of the LEV and TEV (compare Fig. 4.5(a),(e),(i)). At 50% (Fig. 4.5(b),(f),(j)) and 75% of the cycle (Fig. 4.5(c),(g),(k)), increasing θ_{r} was found to diffuse the vorticity in both the LEV and TEV cores and dissipating at the end of the cycle (Fig. 4.5(d),(h),(l)).

For a bristled wing pair that was rotated to θ_{r}=22.5°, increasing δ from 10% (Fig. 4.6(a)-(d)) to 50% (Fig. 4.6(e)-(h)) diffused the vorticity in both the LEV and TEV. Relative to the LEV for each δ, we observed a weaker TEV (i.e., smaller ω_z) for δ=10% as compared to δ=50% (Fig. 4.6(a)-(d)) . The LEV of the bristled wing pair was stronger and smaller in size for smaller δ compared to the LEV of bristled wing with larger δ (Fig. 4.6(e)-(h)) that was weaker and more diffused. Similar to the single wing, LEV and TEV of the bristled wing pair for both δ=10% and 50% was found to increase in size with increasing cycle duration (T) before dissipating at the end of the cycle (100%T).

Similar to the observations at θ_{r}=22.5°, increasing δ diffused and decreased the strength

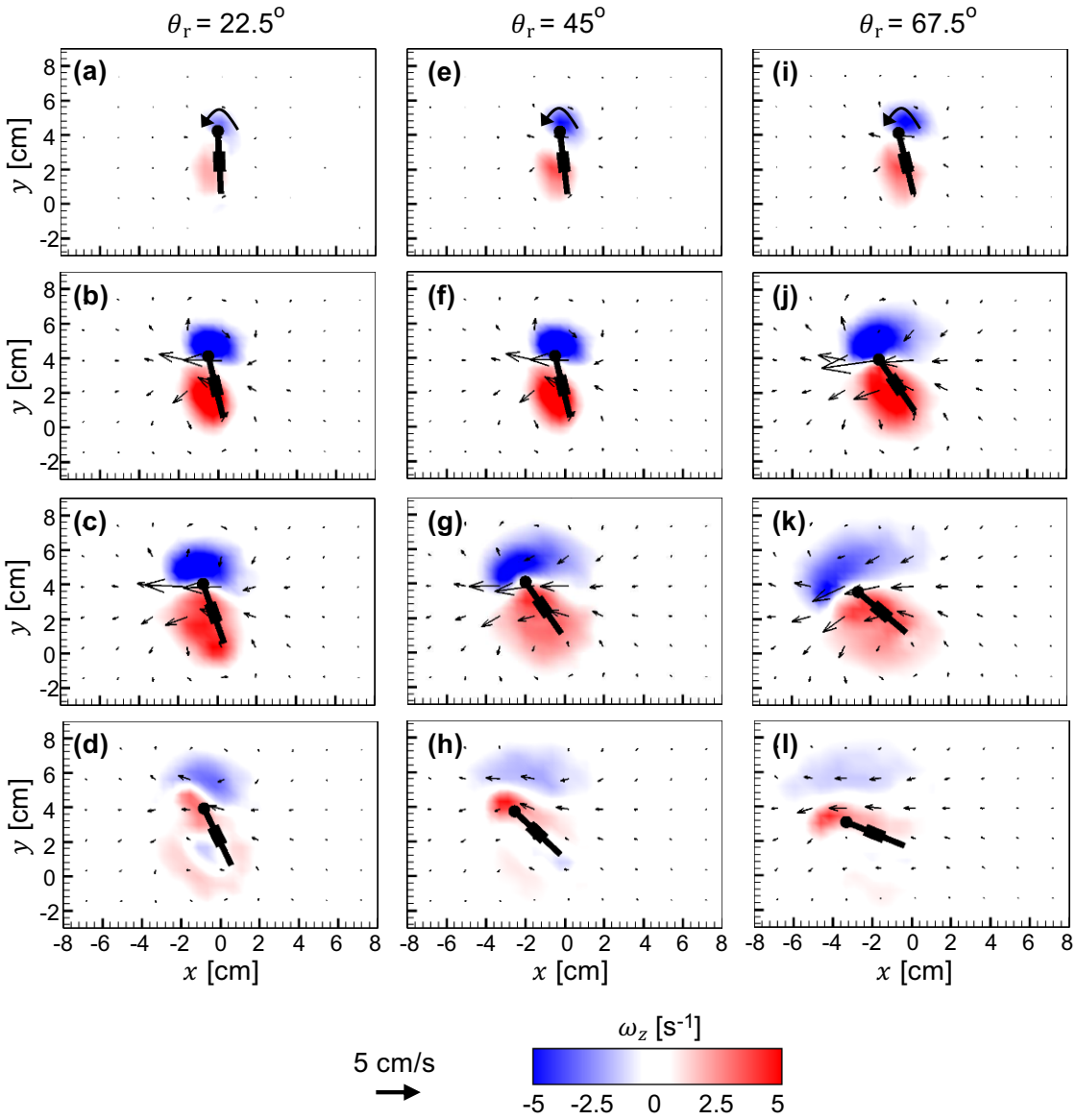

Figure 4.5: Velocity vectors overlaid on out-of-plane z-vorticity (ω_z) contours for a single bristled wing in rotation at Re=10. (a)-(d) θ_r=22.5°; (e)-(h) θ_r=45°; (i)-(l) θ_r=67.5°. For each θ_r, 4 timepoints (25%, 50%, 75% and 100% of cycle time) are shown along each column ((a)-(d); (e)-(h); (i)-(l)) from top to bottom.

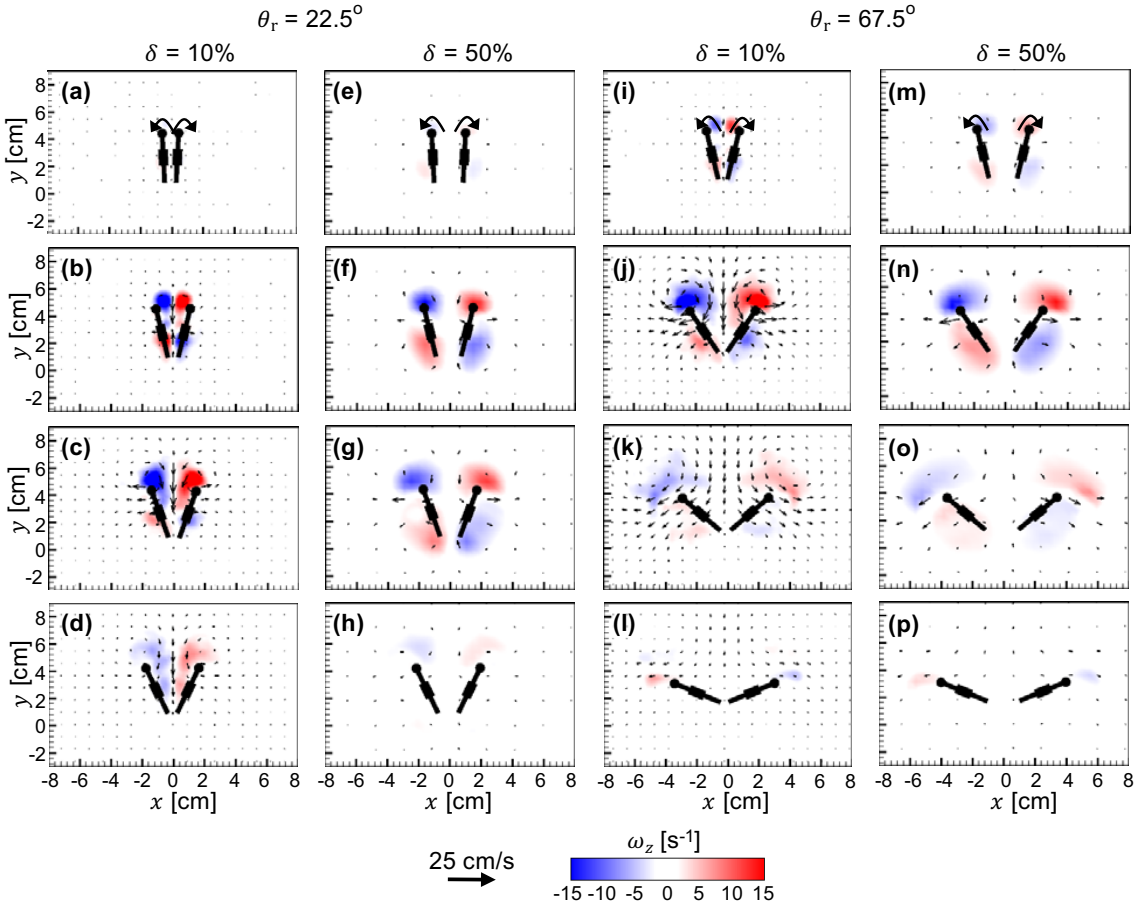

Figure 4.6: Velocity vectors overlaid on out-of-plane z-vorticity (ω_z) contours for a bristled wing pair in rotation at Re=10. θ_r=22.5° is shown for δ=10% in (a)-(d) and for δ=50% in (e)-(h). θ_r=67.5° is shown for δ=10% in (i)-(l) and for δ=50% in (m)-(p). For each θ_r, 4 timepoints (25%, 50%, 75% and 100% of cycle time) are shown along each column ((a)-(d); (e)-(h); (i)-(l); (m)-(p)) from top to bottom.

of both the LEV and TEV when the bristled wing pair was rotated to θ_r = 67.5° (compare Fig. 4.6(i)-(l) and Fig. 4.6(m)-(p)). In contrast to θ_r = 22.5° where LEV and TEV were found to increase in strength from 50%T to 75%T (Fig. 4.6(b),(c)), we observed a drop in strength of both the LEV and TEV for θ_r = 67.5° for both δ=10% and 50% (Fig. 4.6(j),(k)).

Pressure distribution. Positive and negative pressure regions were observed below (i.e., front surface of the wing that first encounters fluid during rotation) and above (back surface of the wing) the single bristled wing in rotation, respectively (Fig. 4.7). Time-variation of pressure distribution around the single rotating wing was similar for all θ_r conditions (22.5°,45°,67.5°). Interestingly, we observed the pressure distribution in all θ_r conditions

to approach zero at 75%T (Fig. 4.7(c),(g),(k)), which corresponds to right after the start of wing deceleration. In addition, the pressure distribution around the wing flipped in sign at the end of the rotation (100%T; Fig. 4.7(d),(h),(l)), so that the positive pressure region was located above the wing and negative pressure region was located below the wing. This pressure reversal was particularly pronounced for the smallest θ_r=22.5° (Fig. 4.7(d)). At 50%T, we observed the pressure distribution to be more diffused for the smallest θ_r=22.5° (Fig. 4.7(b)) as compared to θ_r=67.5° (Fig. 4.7(j)).

Pressure distribution around a bristle wing pair in rotation (Fig. 4.8) was found to be completely different as compared to that of a rotating single wing (Fig. 4.7). During the initial stages of rotational motion, a diffused negative pressure region was observed near the LEs, just above the 'cavity' (i.e., inter-wing space) between the two wings (Fig. 4.8(a),(e),(i),(m)). A weaker negative pressure region was also observed near the TEs, just below the cavity between the two wings. In addition, a diffused region of positive pressure was observed below each wing. For δ = 10% and θ_r=22.5°, we observed a diffused region of positive pressure to be distributed in the cavity between the wing pair at 50%T (Fig. 4.8(b)). The magnitude of positive pressure in the cavity decreased with increasing cycle time. Similar to the single wing model, we observed the positive and negative pressure regions to flip positions at the end of the cycle (100%T; Fig. 4.8(d),(h),(l),(p)). Increasing δ to 50% reduced the positive pressure between the wings and simultaneously increased the magnitude of negative pressure near the TEs (compare Fig. 4.8(b) and Fig. 4.8(f)). At 75%T for θ_r=22.5° and δ=10% (Fig. 4.8(c)), we found both the positive and negative pressure distribution around the wings to substantially decrease in strength.

Time-variation of pressure distribution around a bristled wing pair rotated to θ_r=67.5° resembled that of θ_r=22.5°. However, the positive pressure region in the cavity between the wings for δ=10% and θ_r=22.5° (Fig. 4.8(b)) was essentially absent for δ=10% and θ_r=67.5° (Fig. 4.8(j)). Increasing θ_r to 67.5° allowed the negative pressure region near the LEs (above the cavity) to diffuse over a larger region as compared to θ_r=22.5°. In contrast to

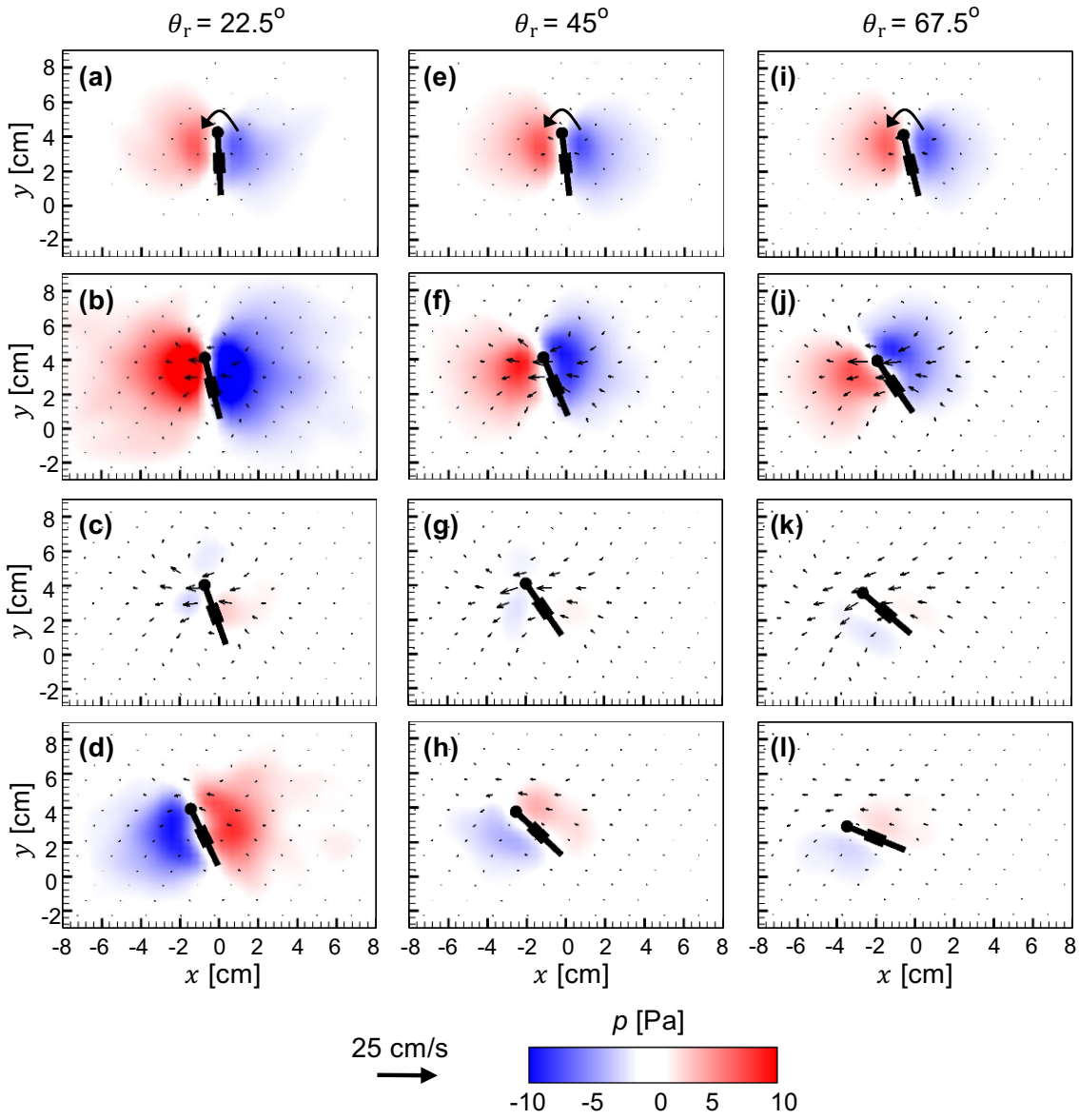

Figure 4.7: Velocity vectors overlaid on pressure (p) contours for a single bristled wing in rotation at Re=10. (a)-(d) θ_r=22.5°; (e)-(h) θ_r=45°; (i)-(l) θ_r=67.5°. For each θ_r, 4 time-points (25%, 50%, 75% and 100% of cycle time) are shown along each column ((a)-(d); (e)-(h); (i)-(l)) from top to bottom. Pressure distribution was calculated from measured velocity fields using the algorithm developed by Dabiri et al.(Dabiri et al., 2014)

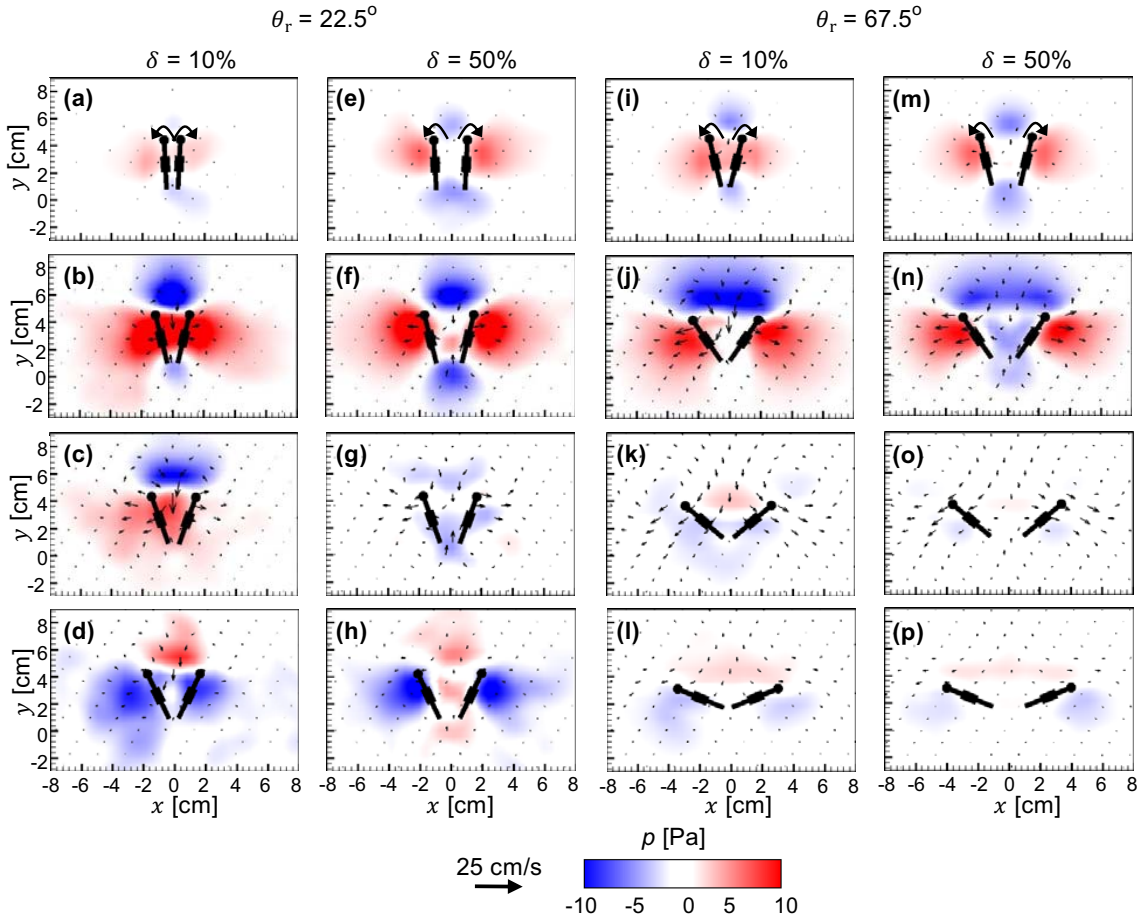

Figure 4.8: Velocity vectors overlaid on pressure (p) contours for a bristled wing pair in rotation at Re=10. θ_r=22.5° is shown for δ=10% in (a)-(d) and for δ=50% in (e)-(h). θ_r=67.5° is shown for δ=10% in (i)-(l) and for δ=50% in (m)-(p). For each θ_r, 4 timepoints (25%, 50%, 75% and 100% of cycle time) are shown along each column ((a)-(d); (e)-(h); (i)-(l); (m)-(p)) from top to bottom.

increasing δ for θ_r=22.5° (Fig. 4.8(f)), increasing δ for θ_r=67.5° resulted in negative pressure distribution in the cavity between the wing at 50% cycle time (Fig. 4.8(n)). Enhanced viscous diffusion of vorticity was observed for $Re \sim \mathcal{O}(10)$ in a previous study (Santhanakrishnan et al., 2018) of a solid elliptical wing (similar aspect ratio as the wings used in this study), undergoing constant velocity revolution at a fixed angle of attack. As the two wings of a bristled wing pair in rotation are in close proximity throughout a cycle (especially for θ_r=22.5° at δ=10%), we speculate that positive pressure is diffused from outside the wings to within the cavity between the wings via the inter-bristle gaps.

4. 2 Bristled wings in linear translation

Aerodynamic force generation. In general, both C_L and C_D were observed to follow similar trends throughout a cycle (Fig. 4.9). For all translational angles (θ_t) that were tested, we observed an increase in C_L and C_D during translational acceleration (see Fig. 4.3(a) for prescribed translation motion profile), followed by C_L and C_D remaining approximately constant during constant velocity translation, and a subsequent drop in C_L and C_D during translational deceleration (Fig. 4.9(a),(b)). When θ_t was increased from 22.5° to 67.5°, we observed large reduction in C_D compared to the small reduction in C_L (compare (Fig. 4.9(a),(b)) and Fig. 4.9(c),(d)). In addition, increasing θ_t decreased peak values of C_L and C_D during translational acceleration by a larger extent as compared to reduction in peak coefficients during constant velocity translation. Similar to wing rotation, we observed C_D and C_L to drop below zero toward the end of the cycle for θ=22.5° (Fig. 4.9(a),(b)). A noticeable drop in C_D and C_L was observed with increasing δ for θ_t=22.5°. Increasing θ_t to 67.5° decreased the drop in C_D and C_L that was observed with increasing δ. Interestingly, changing δ was found to affect C_D and C_L mostly during translational acceleration when the wings were closer to each other, promoting wing-wing interaction. After translational acceleration, when the wings translated further apart, C_L and C_D of the bristled wing pair for all δ values were similar to those generated by a single translating wing.

$\overline{C_D}$ decreased with increasing θ_t, and increasing δ also resulted in decreasing $\overline{C_D}$ for lower values of θ_t. $\overline{C_D}$ was mostly independent of δ for $\theta_t \geq$45°, suggesting that increasing θ_t reduces wing-wing interaction. In sharp contrast to $\overline{C_D}$, $\overline{C_L}$ increased with increasing θ_t until 45° and subsequently decreased for θ_t=67.5° (Fig. 4.9(f)). This suggests substantial changes in flow field likely occur for $45° < \theta_t \leq 67.5°$ to reduce $\overline{C_L}$ in this range. In addition, increasing δ resulted in smaller changes in $\overline{C_L}$ as compared to changes in $\overline{C_D}$.

Vorticity distribution. A single bristled wing in linear translation produced counter-rotating vortices at the LE and TE (Fig. 4.10). Across all θ_t values, we observed a LEV and a TEV that were attached to the wing, and their strength increased in time before dissipating at the

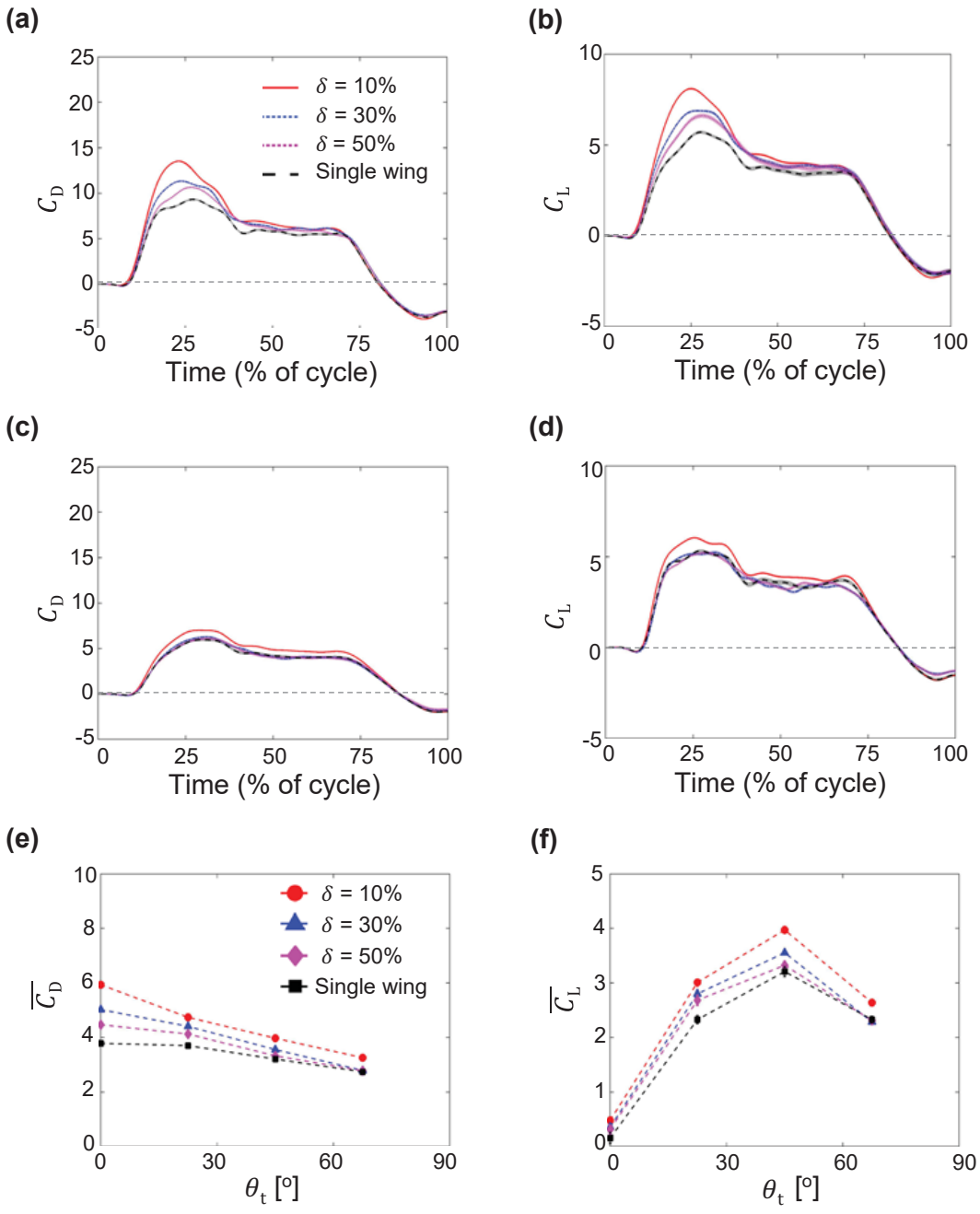

Figure 4.9: Force coefficients during linear translation of bristled wings at *Re*=10. Shading around each curve represents ±1 SD across 30 cycles. (a) and (b) show time-variation of C_D and C_L, respectively, for θ_t=22.5°. (c) and (d) show time-variation of C_D and C_L, respectively, for θ_t=67.5°. (e) and (f) show cycle-averaged coefficients $\overline{C_D}$ and $\overline{C_L}$, respectively, for varying θ_t. Legend for (b)-(d) is shown in (a); legend for (f) is shown in (e). The *y*-axis range for (a) and (c) is -5 to 25, (b) and (d) is -5 to 10, (e) is 0 to 10 and (f) is 0 to 5.

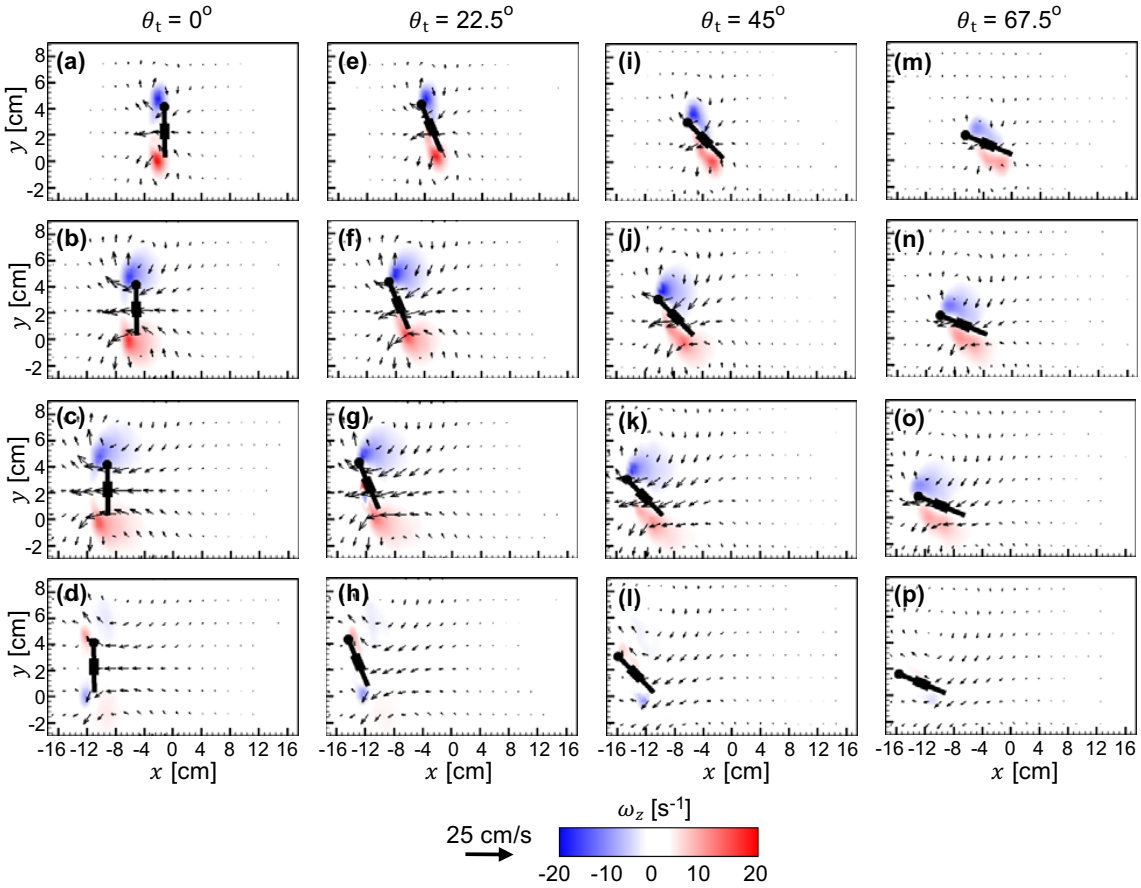

Figure 4.10: Velocity vectors overlaid on out-of-plane z-vorticity (ω_z) contours for a single bristled wing in linear translation at Re=10. (a)-(d) θ_t=0°; (e)-(h) θ_t=22.5°; (i)-(l) θ_t=45°; (m)-(p) θ_t=67.5°. For each θ_t, 4 timepoints (25%, 50%, 75% and 100% of cycle time) are shown along each column ((a)-(d); (e)-(h); (i)-(l); (m)-(p)) from top to bottom.

end of the cycle (100%T). Also, increasing θ_t decreased the strength of both the LEV and TEV during early translation (Fig. 4.10(a),(e),(i),(m)). Minimal variation was observed in the vorticity magnitudes of LEV and TEV cores from 50%T to 75%T across all θ_t values.

For a bristled wing pair in linear translation at θ_t=22.5°, increasing δ from 10% to 50% decreased the strength of both the LEV and TEV (compare Fig. 4.11(a)-(d) and Fig. 4.11(e)-(h)). However, at the end of cycle, vorticity distribution around each wing of the bristled wing pair was similar to that of a single wing in linear translation (compare Fig. 4.10(h) and Fig. 4.11(d),(h)). Similar to the single bristled wing in linear translation, we observed minimal variation in the vorticity magnitudes of the LEV and TEV from

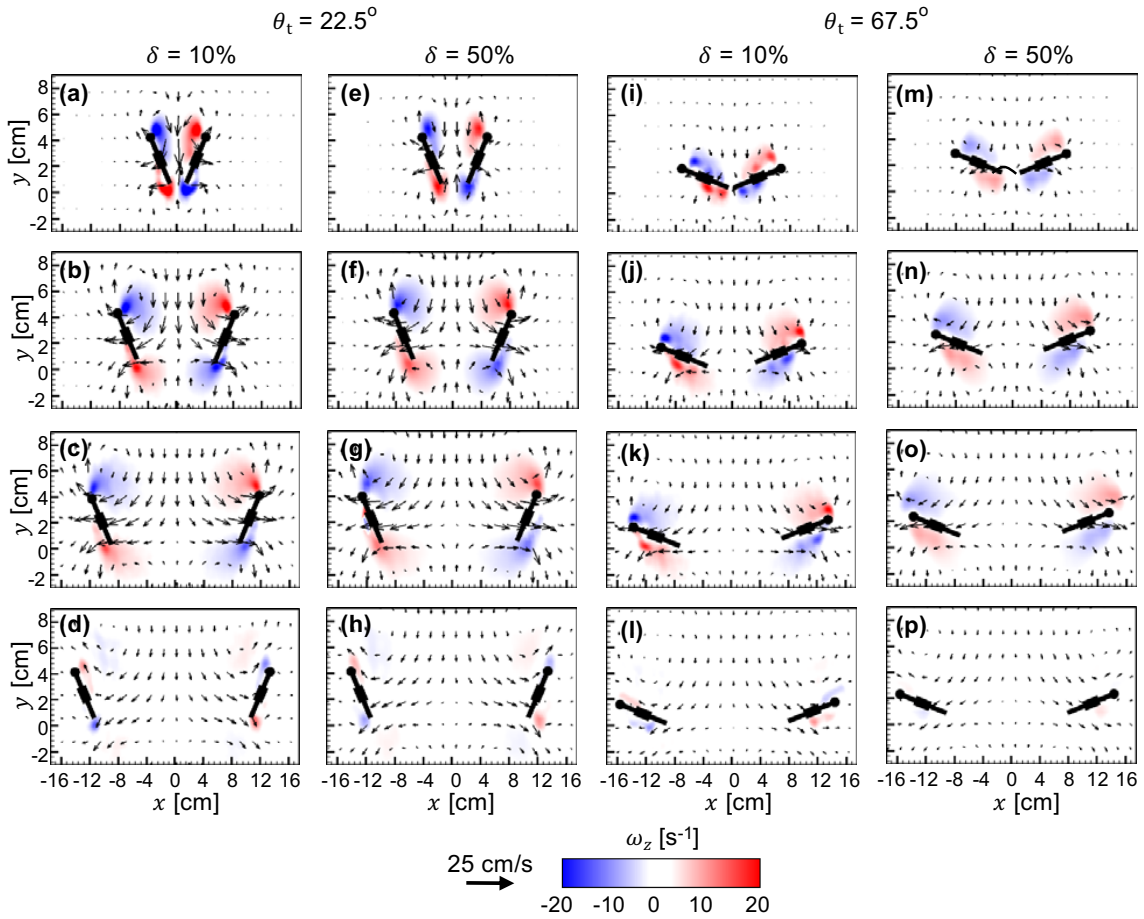

Figure 4.11: Velocity vectors overlaid on out-of-plane z-vorticity (ω_z) contours for a bristled wing pair in linear translation at Re=10. θ_t=22.5° is shown for δ=10% in (a)-(d) and for δ=50% in (e)-(h). θ_t=67.5° is shown for δ=10% in (i)-(l) and for δ=50% in (m)-(p). For each θ_t, 4 timepoints (25%, 50%, 75% and 100% of cycle time) are shown along each column ((a)-(d); (e)-(h); (i)-(l); (m)-(p)) from top to bottom.

50%T to 75%T (Fig. 4.11(b),(c),(f),(g)). Similarly, for the bristled wing pair in linear translation at θ_t=67.5°, increasing δ decreased the strength of both the LEV and TEV (compare Fig. 4.11(i)-(l) and Fig. 4.11(m)-(p)). In contrast to θ_t = 22.5°, LEV and TEV strength for θ_t=67.5° showed larger variation with increasing δ throughout the cycle.

Pressure distribution. Similar to a single rotating wing, a single bristled wing undergoing linear translation showed positive and negative pressure regions below and above the wing, respectively (Fig. 4.12). Time-variation of pressure distribution around the single translating wing was similar for all θ_t conditions.Increasing θ_t weakened the pressure distribution throughout the cycle. In addition, pressure distribution around the wing flipped in sign

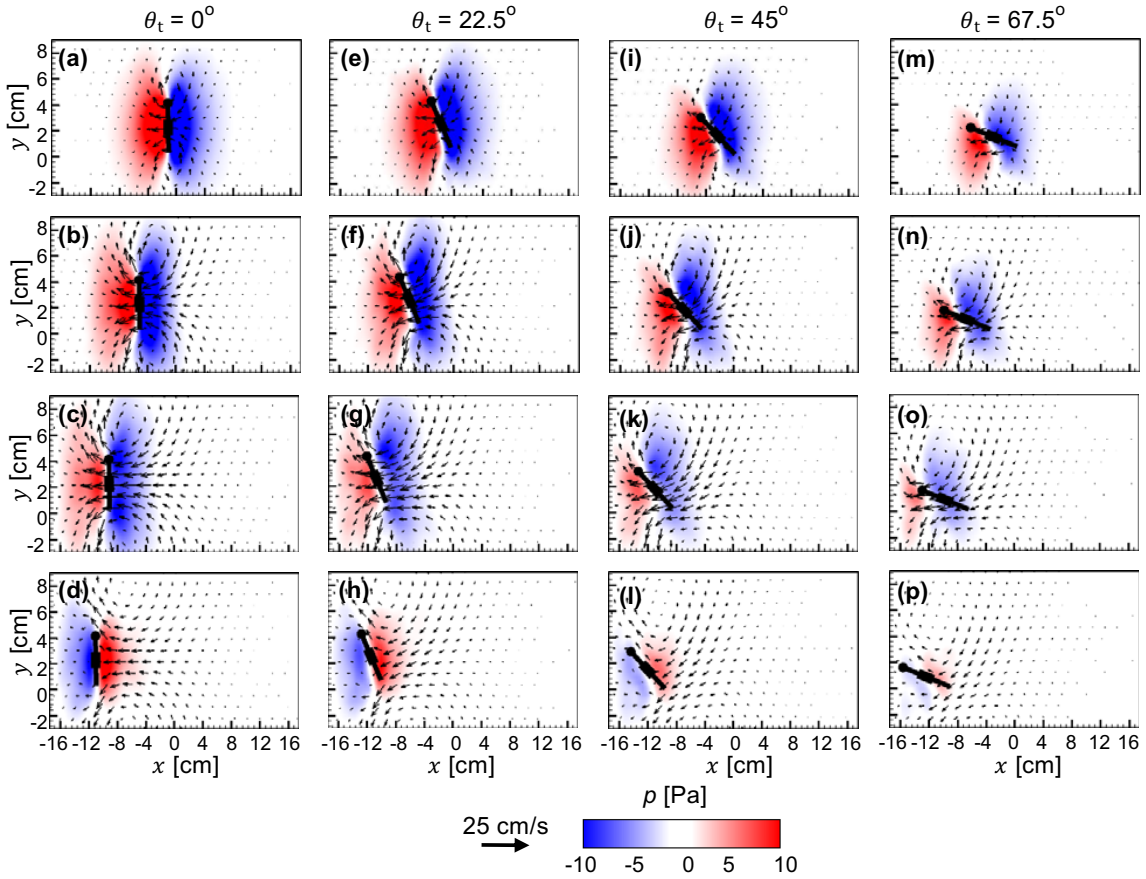

Figure 4.12: Velocity vectors overlaid on pressure (p) contours for a single bristled wing in linear translation at Re=10. (a)-(d) θ_r=0°; (e)-(h) θ_r=22.5°; (i)-(l) θ_r=45°; (m)-(p) θ_t=67.5°. For each θ_t, 4 timepoints (25%, 50%, 75% and 100% of cycle time) are shown along each column ((a)-(d); (e)-(h); (i)-(l); (m)-(p)) from top to bottom.

at the end of the translation (100%T). This pressure reversal was more pronounced for smaller θ_t ($\leq$ 22.5°).

Pressure distribution around a bristle wing pair in linear translation (Fig. 4.13) was found to be different compared to that of a translating single wing (Fig. 4.12) mostly at the start of the cycle on account of wing-wing interaction. During initial stages of linear translation, a diffused negative pressure region was observed near the LEs just above the cavity between the wings and near the TEs (Fig. 4.13(a),(e),(i),(m)). Also, a diffused region of positive pressure was observed below each wing. For δ = 10% and θ_t=22.5°, we observed a diffused region of negative pressure to be distributed in the cavity between the wing pair and near the LE at 50%T (Fig. 4.13(b)). This is in contrast to the positive

pressure region that was observed between the wing pair at the same time point during rotation to θ_r=22.5° (Fig. 4.8(b)). As the wing translates in time, the negative pressure build up in between the wings likely occurs due to increasing inter-wing separation that is not conducive for wing-wing interaction. Similar to the single translating wing, we observed the positive and negative pressure regions to flip positions at the end of the cycle (100%T; Fig. 4.13(d),(h),(l),(p)). Increasing δ to 50% for θ_t=22.5° reduced the negative pressure between the wings (compare Fig. 4.13(b) and Fig. 4.13(f)). From ~50%T onward for θ_t=22.5°, we found both the positive and negative pressure distribution around the wing to be mostly unaffected with increasing δ.

In contrast to θ_t=22.5°, linear translation of the bristled wing pair at θ_t=67.5° showed minimal change in pressure distribution when comparing identical time points at δ=10% (Fig. 4.13(i)-(l)) and δ=50% (Fig. 4.13(m)-(p)). This suggests that there is a limit to θ_t after which wing-wing interaction is unaltered for $\delta \geq$10%. Just after the start of translation at θ_t=67.5°, we found negative pressure to be distributed in between the wing and positive pressure below the wings for both δ=10% and 50%. The magnitudes of negative and positive pressures at θ_t=67.5° were found to be substantially lower than those of θ_t=22.5° throughout the cycle.

4. 3 Bristled wings during combined rotation and linear translation

Aerodynamic force generation. At ζ=25%, both C_L and C_D were found to peak at two timepoints in the cycle (Fig. 4.14(a),(b)). One of the timepoints correspond to where the rotational wing motion reached peak velocity and other time point correspond to the peak translational velocity. With increase in ζ to 100% (Fig. 4.14 (c),(d)), we observed both C_L and C_D to peak at only one time point early in the cycle. In addition, peak values of C_L and C_D increased with increasing ζ. For each ζ, increasing δ decreased peak values of both C_L and C_D. However, during wing translation following overlapping motion, both C_L and C_D showed minimal variation for varying δ. Similar to linear translation, both C_L and C_D

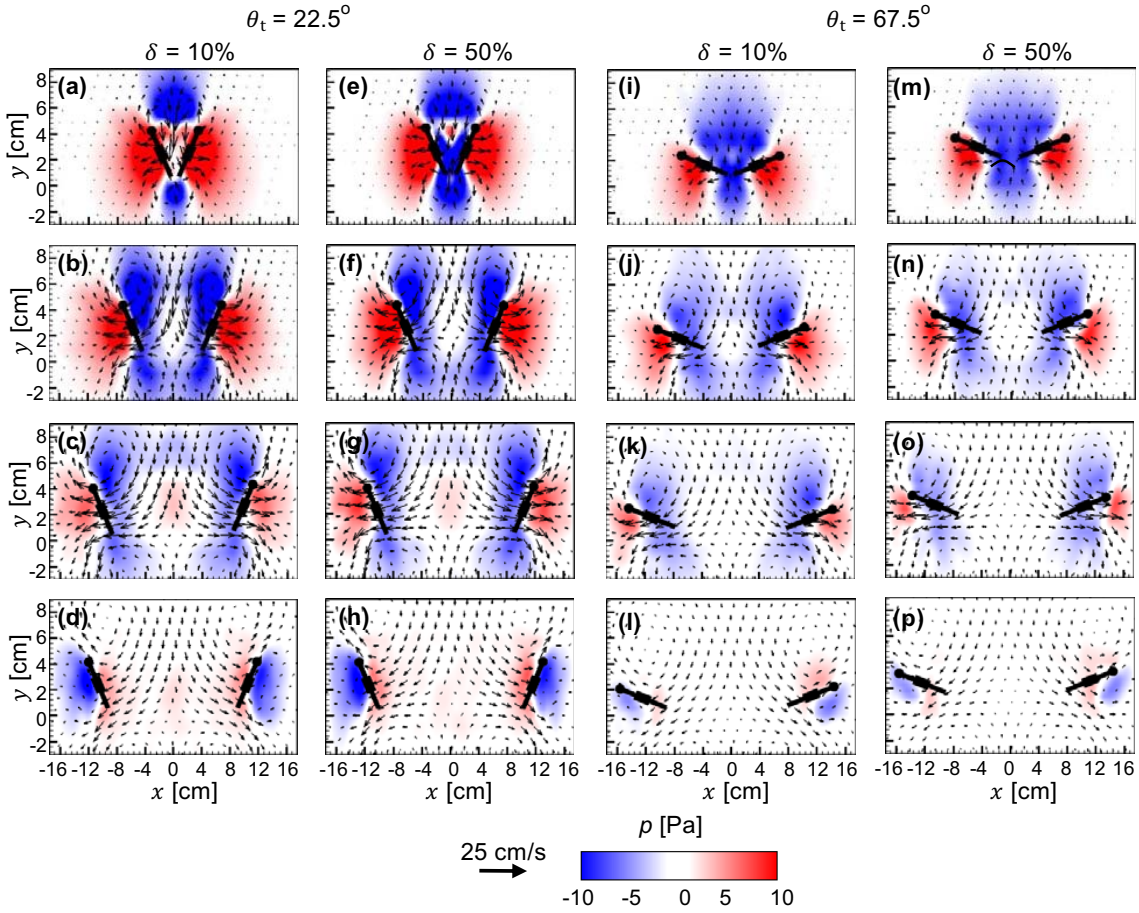

Figure 4.13: Velocity vectors overlaid on pressure (p) contours for a bristled wing pair in linear translation at Re=10. θ_t=22.5° is shown for δ=10% in (a)-(d) and for δ=50% in (e)-(h). θ_t=67.5° is shown for δ=10% in (i)-(l) and for δ=50% in (m)-(p). For each θ_t, 4 timepoints (25%, 50%, 75% and 100% of cycle time) are shown along each column ((a)-(d); (e)-(h); (i)-(l); (m)-(p)) from top to bottom.

dropped below zero close towards the end of the cycle.

In general, cycle-averaged coefficients ($\overline{C_D}$ and $\overline{C_L}$, Fig. 4.14(e),(f)) were observed to increase with increasing ζ. Increasing δ decreased both $\overline{C_D}$ and $\overline{C_L}$. The extent of $\overline{C_L}$ variation with ζ was substantially smaller than that of $\overline{C_D}$.

Vorticity distribution. Fig. 4.15 shows the flow generated by a single bristled wing performing combined rotation and linear translation. With increasing ζ, the strength of both LEV and TEV were found to increase during early stages of wing motion (25%T) This could likely be on account of both wings reaching rotational deceleration phase at 25%T for all ζ. At 75%T, the strength of both LEV and TEV were found to have little to no

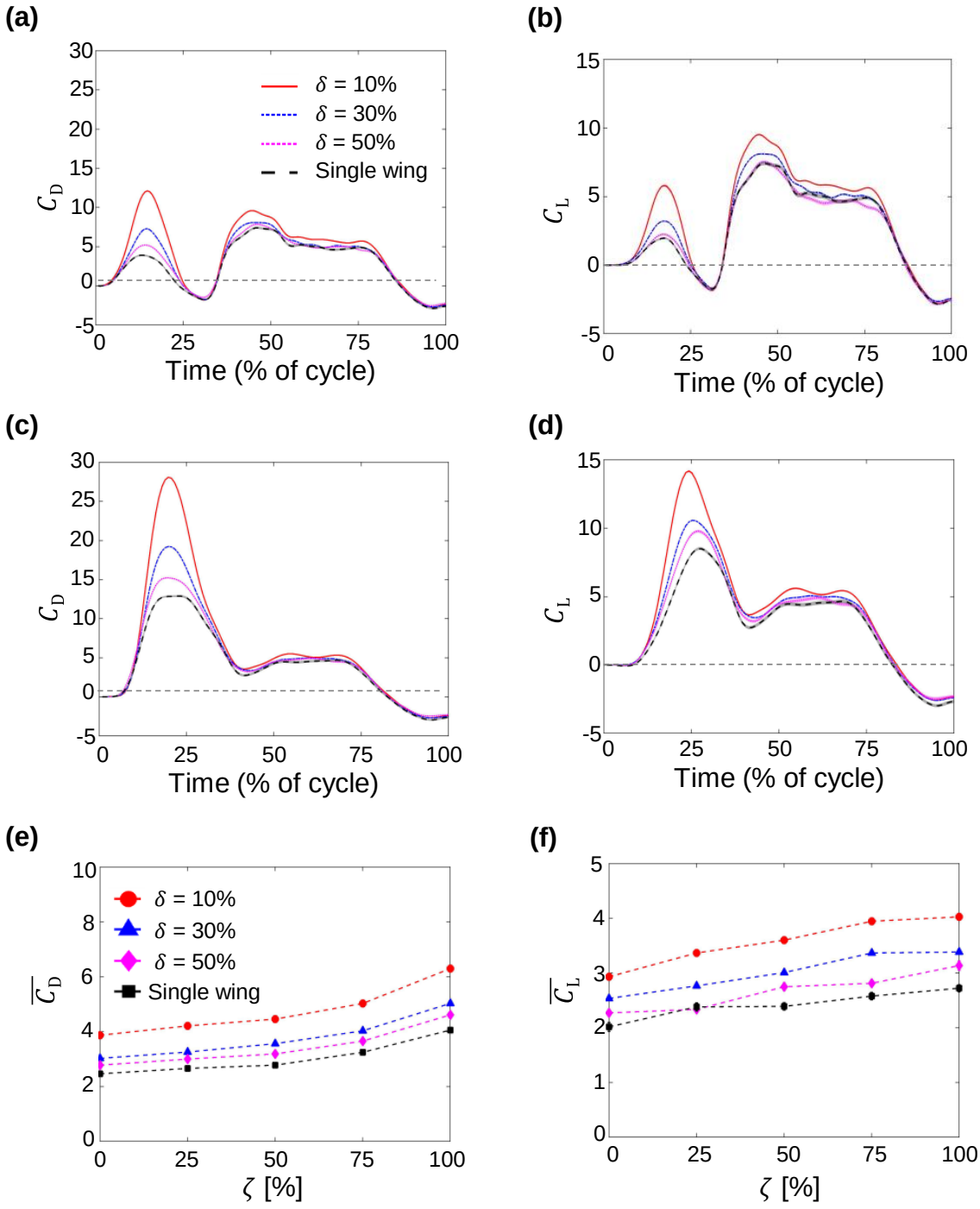

Figure 4.14: Force coefficients during combined rotation and linear translation of bristled wings at *Re*=10. Shading around each curve represents ±1 SD across 30 cycles. (a) and (b) show time-variation of C_D and C_L, respectively, for overlap ζ=25%. (c) and (d) show time-variation of C_D and C_L, respectively, for ζ=100%. (e) and (f) show cycle-averaged coefficients $\overline{C_D}$ and $\overline{C_L}$, respectively, for varying ζ. Legend for (b)-(d) is shown in (a); legend for (f) is shown in (e). The *y*-axis range for (a) and (c) is -5 to 30, (b) and (d) is -5 to 15, (e) is 0 to 10 and (f) is 0 to 5.

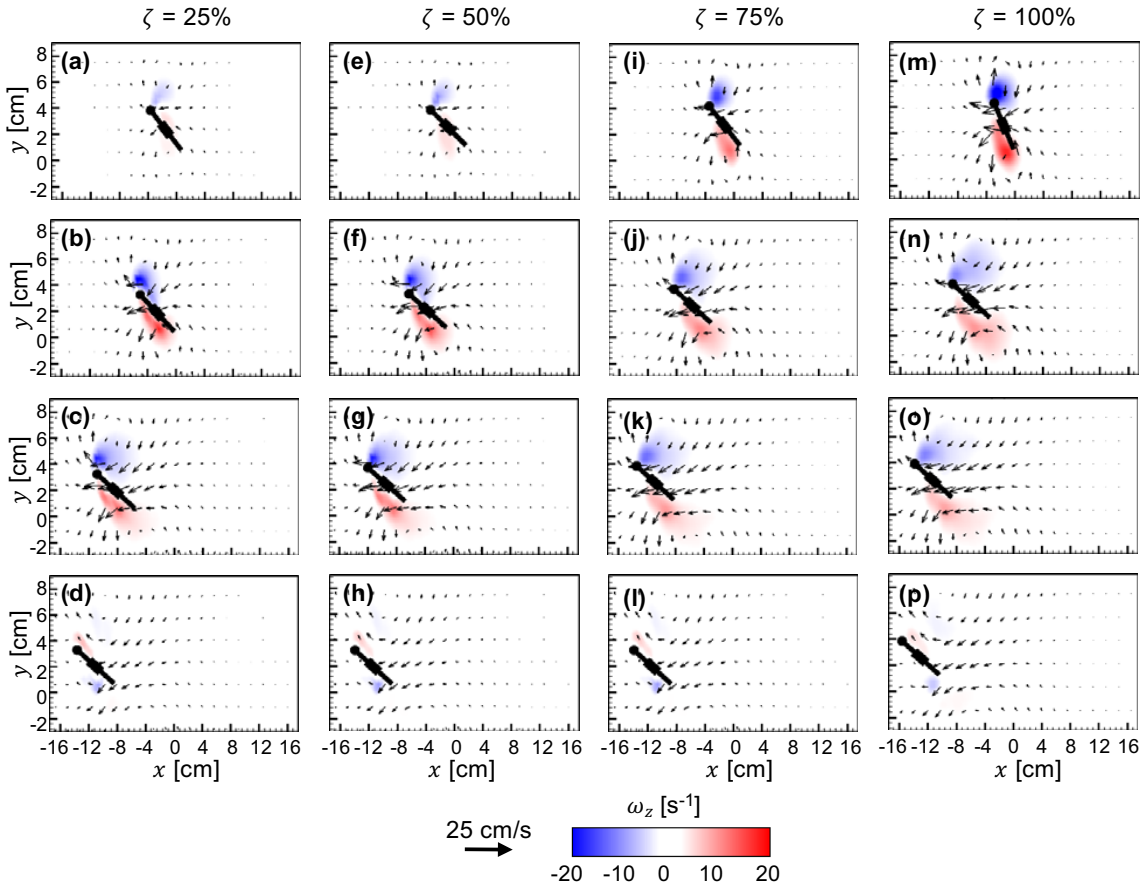

Figure 4.15: Velocity vectors overlaid on out-of-plane z-vorticity (ω_z) contours for combined rotation and linear translation of a single bristled wing at Re=10. (a)-(d) ζ=25%; (e)-(h) ζ=50%; (i)-(l) ζ=75%; (m)-(p) ζ=100%. For each ζ, 4 timepoints (25%, 50%, 75% and 100% of cycle time) are shown along each column ((a)-(d); (e)-(h); (i)-(l); (m)-(p)) from top to bottom.

change with increasing ζ (Fig. 4.14(c),(g),(k),(o)).

For a bristled wing pair performing combined rotation and linear translation at ζ=25% (Fig. 4.16(a)-(h)), increasing δ decreased the strength of both the LEV and TEV during initial stages of wing motion (25%T and 50%T). Towards the end of cycle with increasing δ, there were essentially no changes to the vorticity of the LEV and TEV cores. Similar trends were also observed for ζ=100% (Fig. 4.16(i)-(p)).

Similar to a single wing, increasing the overlap (ζ) for one particular initial inter-wing spacing (δ) increased the strength of both LEV and TEV at 25% and 50% of cycle time. However, LEV and TEV strength showed little to no variations towards the end of cycle

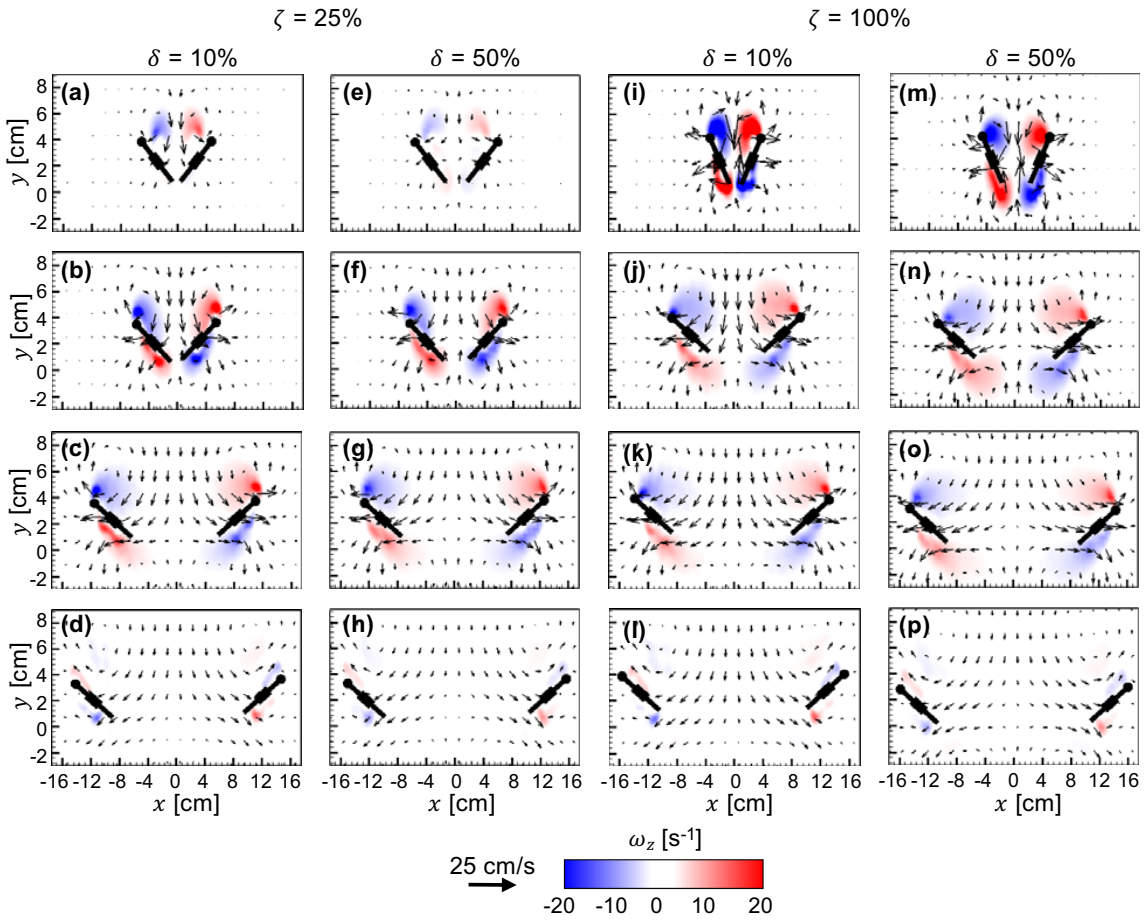

Figure 4.16: Velocity vectors overlaid on out-of-plane z-vorticity (ω_z) contours for combined rotation and linear translation of a bristled wing pair at Re=10. ζ=25% is shown for δ=10% in (a)-(d) and for δ=50% in (e)-(h). ζ=100% is shown for δ=10% in (i)-(l) and for δ=50% in (m)-(p). For each ζ, 4 timepoints (25%, 50%, 75% and 100% of cycle time) are shown along each column ((a)-(d); (e)-(h); (i)-(l); (m)-(p)) from top to bottom.

time for ζ = 25% and 100%.

Pressure distribution. A single bristled wing performing combined rotation and linear translation showed substantial changes in pressure distribution with changing ζ (Figure 4.17). Similar to vorticity distribution, both positive and negative pressure magnitudes increased with increasing overlap during 25%T (Fig. 4.17(a),(e),(i),(m)) and 50%T (Fig. 4.17(b),(f),(j),(n)). At 75%T (Fig. 4.17(c),(g),(k),(o)) and 100%T (Fig. 4.17(d),(h),(l),(p)), increasing ζ resulted in little to no changes to the pressure distribution around the wing.

Pressure distribution around a bristle wing pair (Fig. 4.18) was found to be different compared to that of a single wing (both cases performing rotation and linear translation)

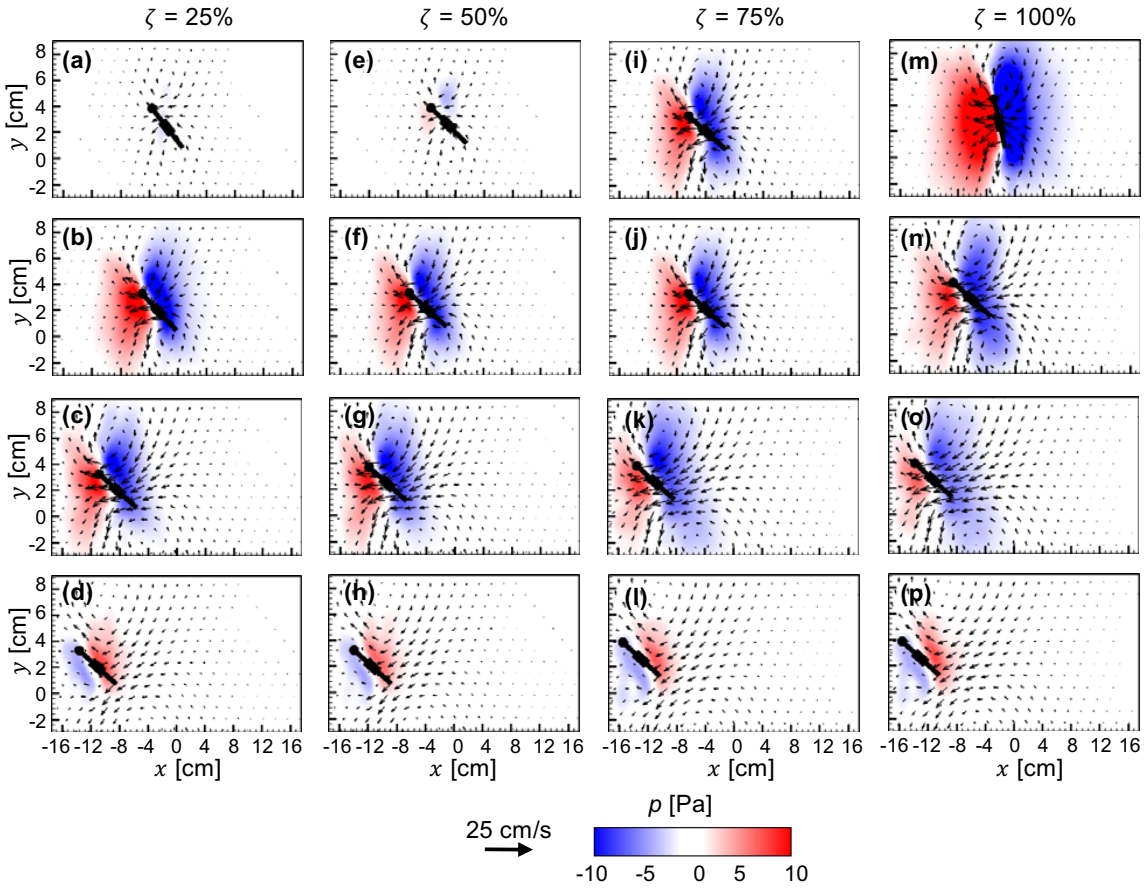

Figure 4.17: Velocity vectors overlaid on pressure (p) contours for combined rotation and linear translation of a single bristled wing at Re=10. (a)-(d) ζ=25%; (e)-(h) ζ=50%; (i)-(l) ζ=75%; (m)-(p) ζ=100%. For each ζ, 4 timepoints (25%, 50%, 75% and 100% of cycle time) are shown along each column ((a)-(d); (e)-(h); (i)-(l); (m)-(p)) from top to bottom.

mostly during early stages of the cycle, where wing-wing interaction appears to have the most influence. During the earlier part of the combined rotation and translation cycle at 50%T and ζ=25% (Fig. 4.18(b),(f)), we observed an increase in negative pressure distribution within the cavity between the wings and positive pressure distributed below each wing. With further increase in time from 75%T (Fig. 4.18(c),(g)) to 100%T (Fig. 4.18(d),(h)), the pressure distribution starts to closely resemble that of a single wing, suggesting diminished influence of wing-wing interaction. Increasing δ at ζ = 25% resulted in a drop in the pressure distribution only during the start of the cycle (25%T; Fig. 4.18(a),(e)), and minimal variation in pressure distribution was observed between δ=10% (Fig. 4.18(b)-(d)) and δ=50% (Fig. 4.18(f)-(h)) for the remainder of the cycle.

Similar trends were observed with increasing δ for ζ=100% (Fig. 4.18(i)-(p)) as compared to those discussed for ζ=25%. However, we observed the development of a strong negative pressure region in the cavity between the wings for δ=50% early into the cycle (25%T; Fig. 4.18(m)). Also, larger negative and positive regions were observed for ζ=100% as compared to ζ=25%. However, we did not observe noticeable differences in the pressure distribution at 75%T and 100%T when changing either ζ or δ.

4. 4 Reverse flow through bristled wings

Reverse flow capacity (RFC) by a bristled wing was quantified using the equation 4.16. RFC gives a dimensionless estimate of the capability of a given bristled wing model to leak fluid through the bristles on a bristled wing model for varying δ, θ_t, θ_r, and ζ (Figure 4.19). For all θ_r, RFC was in the range of 0%-80% (Fig. 4.19(a),(b)). RFC was larger for smaller θ_r of 22.5° as compared to 67.5° at the same % of cycle time. In addition, having the wings closer (δ=10%) showed higher RFC for θ_r=22.5°. This is in agreement with the results of Loudon et al. (Loudon and Koehl, 1994), where the presence of a wall near bristled appendages was observed to promote inter-bristle flow. This increase in RFC can be attributed to net changes in pressure distribution around the wing for δ = 10% at θ_r=22.5°.

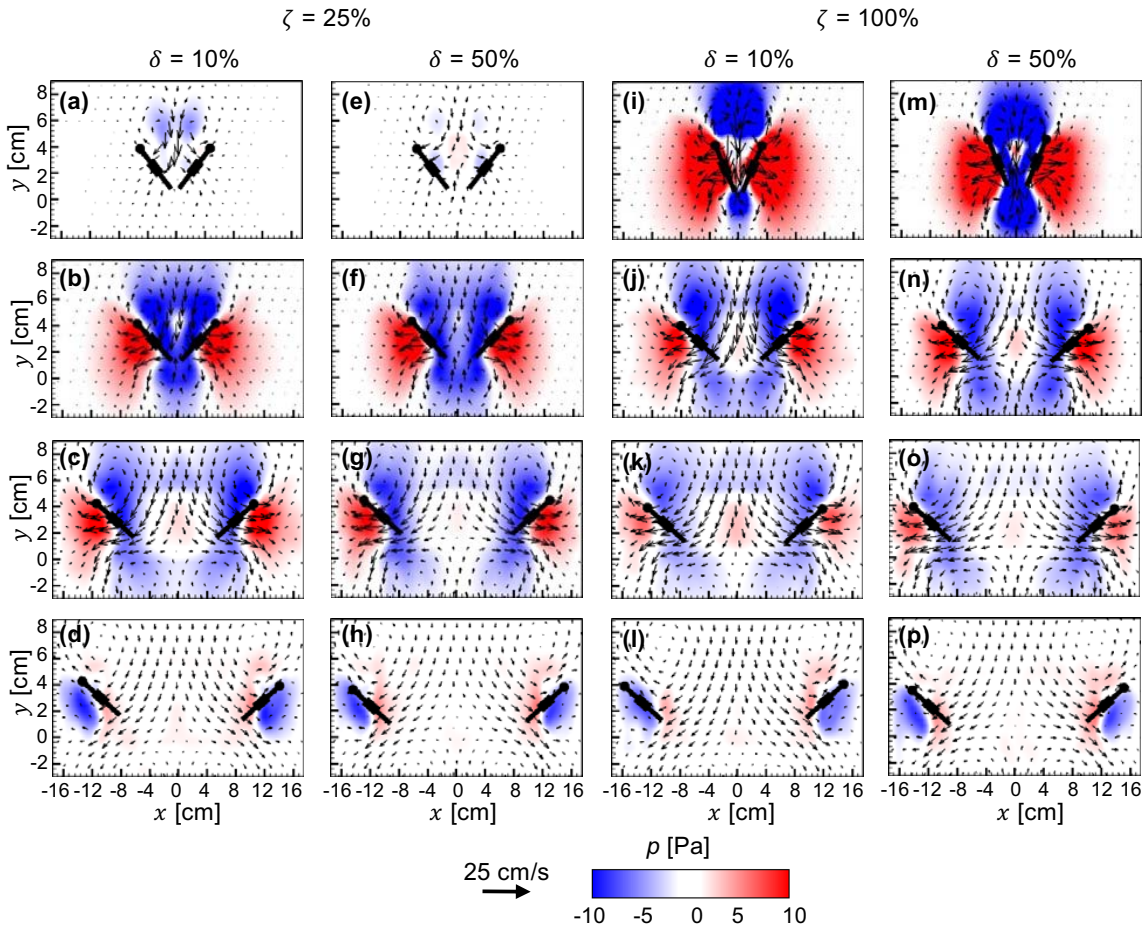

Figure 4.18: Velocity vectors overlaid on pressure (p) contours for combined rotation and linear translation of a bristled wing pair at Re=10. ζ=25% is shown for δ=10% in (a)-(d) and for δ=50% in (e)-(h). ζ=100% is shown for δ=10% in (i)-(l) and for δ=50% in (m)-(p). For each θ_t, 4 timepoints (25%, 50%, 75% and 100% of cycle time) are shown along each column ((a)-(d); (e)-(h); (i)-(l); (m)-(p)) from top to bottom.

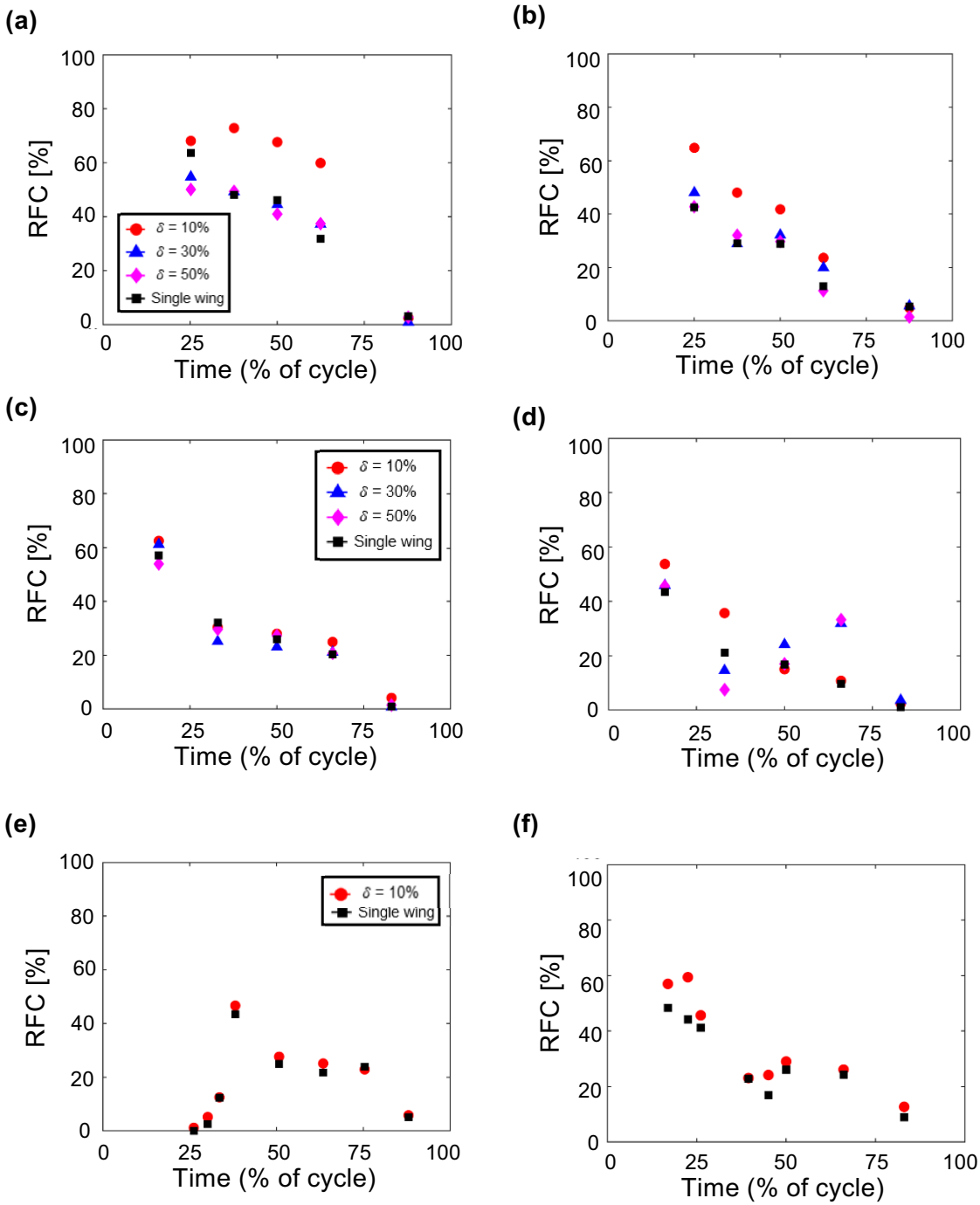

Figure 4.19: Time-variation of reverse flow capacity (RFC), characterizing the reduction in volumetric flow of a bristled wing (or wing pair) with respect to a geometrically equivalent solid wing, as a function of δ and wing kinematics. (a) and (b) show RFC during rotation at θ_r=22.5° and θ_r=67.5°, respectively. (c) and (d) show RFC during linear translation at θ_t=22.5° and θ_t=67.5°, respectively. (e) and (f) show RFC during combined rotation and linear translation at ζ=25% and ζ=100%, respectively. Both single bristled wing and bristled wing pairs are included. See subsection 3. 4 for more details on definition and calculation of RFC.

Increasing δ beyond 10% showed little to no change in RFC. In addition, for changing θ_t (Fig. 4.19(c),(d)) and ζ (Fig. 4.19(e),(f)), we observe very little variation in RFC across all δ values. However, the RFC was found to change in time for each θ_t or ζ (in addition to θ_r). The latter suggests that RFC is largely dependent on wing kinematics and found to be more for smaller δ. Interestingly, higher values of RFC that were observed for lower θ_r and smaller δ were also associated with large C_D. While it is intuitive to expect that a bristled wing with larger capacity to leak flow through the bristles will reduce drag, this counter-intuitive finding suggests that the high drag forces were generated by formation of shear layers around the bristles as has been noted in previous studies (Lee and Kim, 2017; Kasoju et al., 2018).

5 Discussion

While several computational studies (Miller and Peskin, 2005, 2009; Arora et al., 2014; Mao and Xin, 2003; Sun and Yu, 2006) have examined wing-wing interaction in fling at low *Re* for varying δ and ζ, the wings were modeled as solid wings unlike the bristled wings typically seen in tiny flying insects. Further, the few computational studies of wing-wing interaction of bristled wings (Santhanakrishnan et al., 2014; Jones et al., 2016) did not isolate the specific roles of wing rotation from translation. We experimentally examined the flow structures and forces generated by a single bristled wing and a bristled wing pair under varying initial inter-wing distance (δ) at *Re*=10, for the following kinematics: rotation to θ_r about the TE, linear translation at a fixed angle θ_t, and combined rotation and linear translation (overlap duration ζ in %). The central findings for varying wing kinematics are: (1) increasing θ_r decreased both cycle-averaged lift ($\overline{C_L}$) and drag ($\overline{C_D}$) coefficients; (2) increasing θ_t decreased $\overline{C_D}$ and approached $\overline{C_D}$ of a single wing at θ_t=67.5°; (3) $\overline{C_L}$ increased with increasing θ_t, peaking at θ_t=45° and decreasing thereafter at θ_t=45°; and (4) increasing ζ increased both $\overline{C_L}$ and $\overline{C_D}$. For all wing kinematics examined here, δ¿10% resulted in smaller reduction of instantaneous lift coefficient C_L as compared to

larger reduction of instantaneous drag coefficient C_D. We find that peak C_L of a wing pair separated by δ=10% during rotation and during combined rotation and linear translation (ζ=25%) occurs close to the time point where an attached, asymmetric (in size) LEV-TEV pair was observed over the wing. Finally, large values of C_D during rotation of a wing pair with δ=10% resulted from large positive pressure distribution between the wings.

5. 1 Implications of vorticity distribution on lift force generation

Previous studies examining aerodynamic effects of varying δ of solid wing pairs (Arora et al., 2014; Mao and Xin, 2003; Sun and Yu, 2006) and porous wing pairs (Santhanakrishnan et al., 2014) did not elaborate on the physical mechanism(s) responsible for lift augmentation observed with decreasing δ. A stable, attached TEV has been observed in addition to the LEV for a single wing in revolution and in linear translation at $Re \leq 32$ (Miller and Peskin, 2004; Santhanakrishnan et al., 2018), and this LEV-TEV 'vortical symmetry' has been identified as a primary reason for diminished lift generation at this *Re* range (Miller and Peskin, 2004). Miller and Peskin (Miller and Peskin, 2005) identified 'vortical asymmetry' (larger LEV, smaller TEV) during fling of a solid wing pair at $Re \leq 32$ as the mechanism underlying the observed lift augmentation, suggesting that wing-wing interaction can help recover some of the lift lost during the remainder of the cycle (latter attributed to 'vortical symmetry'). We examined circulation (Γ) of the LEV and TEV on a wing of the interacting bristled wing pair to explain the observed changes in lift generation under varying δ and kinematics (Fig. 4.20).

Increasing θ_r from 22.5° to 67.5° increased the peak net circulation on the wing ($|\Gamma_{LEV}|$-$|\Gamma_{TEV}|$) by roughly 2.5 times for δ=10% (Fig. 4.20(a),(b)). Surprisingly, we saw a drop in peak C_L with increasing θ_r (Fig. 4.4(b),(d)). To examine the reason for this discrepancy, we calculated the spatially-averaged downwash velocity ($\overline{V_y}$) (Fig. 4.21). We observed a substantial increase in $\overline{V_y}$ with increased θ_r. An increase in downwash velocity lowers the effective angle of attack (Sane, 2003), which could explain the observed reduction in peak

C_L with increasing θ_r. However, downwash alone cannot be considered as a sole reason for this change. Further analysis such as pressure distribution between the wings would be needed to understand this discrepancy. In addition, increasing θ_r shifted the formation of peak net circulation to occur early in time, similar to what we observed for peak C_L with increasing θ_r (Fig. 4.4(d)) . This was likely on account of the longer time scale for θ_r=67.5° (compared to 22.5°), enabling the LEV and TEV to develop in time. These results suggest that rotational motion continuously change the circulation around the wing by diffusing the LEV and TEV to remain attached in time. Increasing δ above 10% resulted in lower variation of C_L as well as net circulation around the wing. We see wing-wing interaction effects to diminish for $\delta > 50\%$, thereby behaving like a single wing, which is in agreement with previous studies (Sun and Yu, 2006; Arora et al., 2014).

Increasing the translation angle (θ_t) from 22.5° to 67.5° for δ=10% decreased the net circulation by 37% (Fig. 4.20(c),(d)). For the same increase in θ_t, we observed ∼25% drop in peak lift coefficient (Fig. 4.9(b),(d)). In addition, spatially-averaged downwash velocity did not show much variation between θ_t=22.5° and 67.5° (Fig. 4.21(c),(d)). With changing δ for θ_t=22.5°, early stages of translation showed noticeable variation in C_L. However, during constant velocity translation, we observed little to no variation in C_L for δ>30%. A similar trend was observed for net circulation during linear translation with increasing δ, where $\Gamma_{LEV} > \Gamma_{TEV}$ in time and circulation was essentially unchanged during most of constant velocity translation across all δ (Fig. 4.20B(c),(d)). This implies that initial wing motion helps in development of the LEV and TEV around the wing, and increasing δ decreases the strength of both the LEV and TEV. The results further imply that constant velocity translation resulted in constant rate of change of fluid velocity at both LEV and TEV, which resulted in constant circulation of LEV and TEV (Figure 4.20(c),(d)).

Increasing the overlap (ζ) from ζ=25% to 100% for δ=10% increased both Γ_{LEV} and Γ_{TEV}, with peak net circulation being increased by ∼15% (Fig. 4.20(e),(f)). Peak C_L also increased by 49% with increasing ζ=25% to 100% (Fig. 4.14(b),(d)), while $\overline{C_L}$ increased

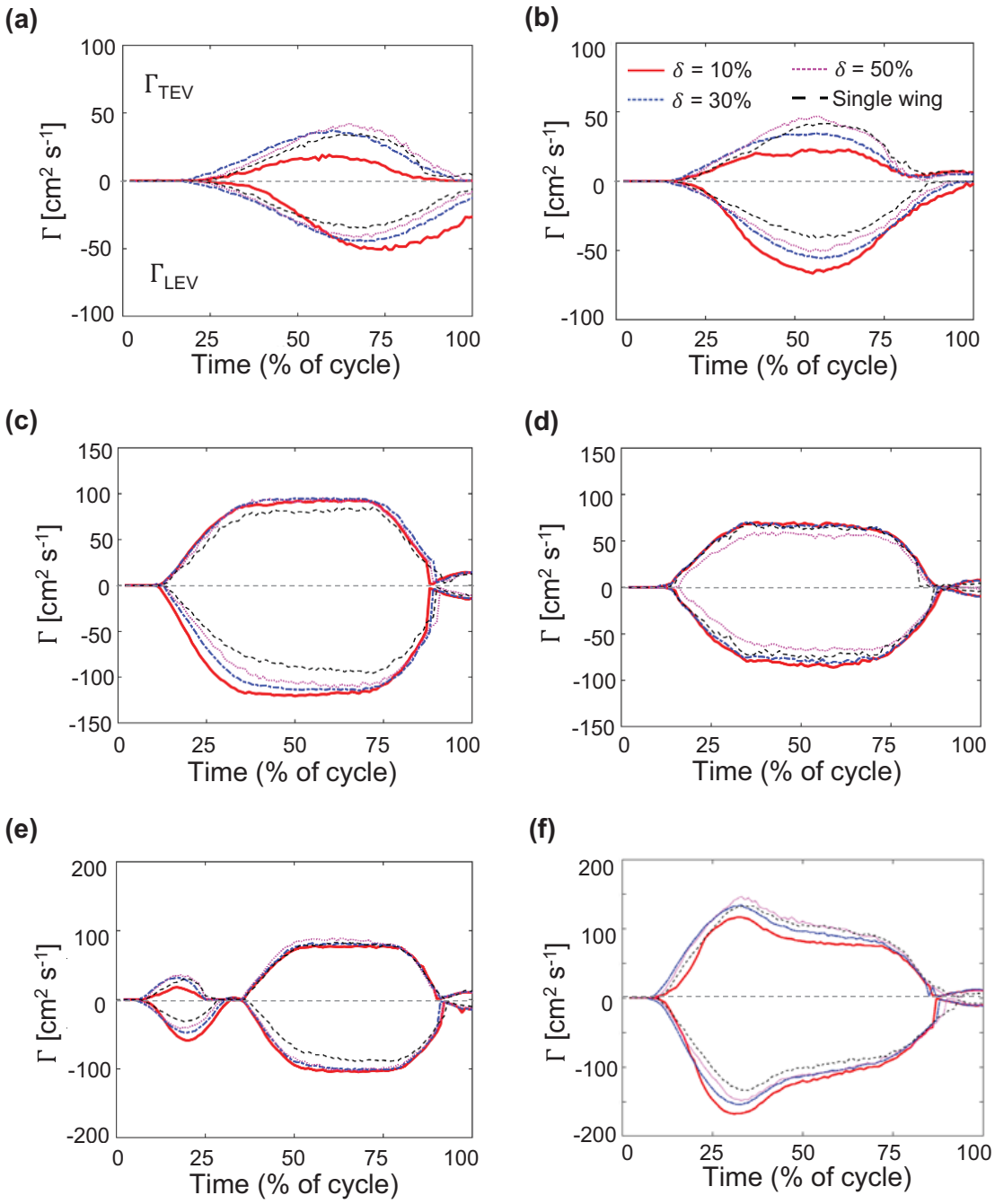

Figure 4.20: Circulation (Γ) of the leading edge vortex (LEV) and the trailing edge vortex (TEV) as a function of δ and wing kinematics. (a) and (b) show Γ during rotation at θ_r=22.5° and θ_r=67.5°, respectively. (c) and (d) show Γ during linear translation at θ_t=22.5° and θ_t=67.5°, respectively. (e) and (f) show Γ during combined rotation and linear translation at ζ= 25% and ζ=100%, respectively. Positive Γ corresponds to TEV and negative Γ corresponds to LEV. Both single bristled wing and bristled wing pairs are included. For bristled wing pairs, Γ was only calculated on the left-wing. See subsection 3. 4 for more details on definition and calculation of Γ. The *y*-axis range for (a) and (b) is -100 to 100, (c) and (d) is -150 to 150, (e) and (f) is -200 to 200.

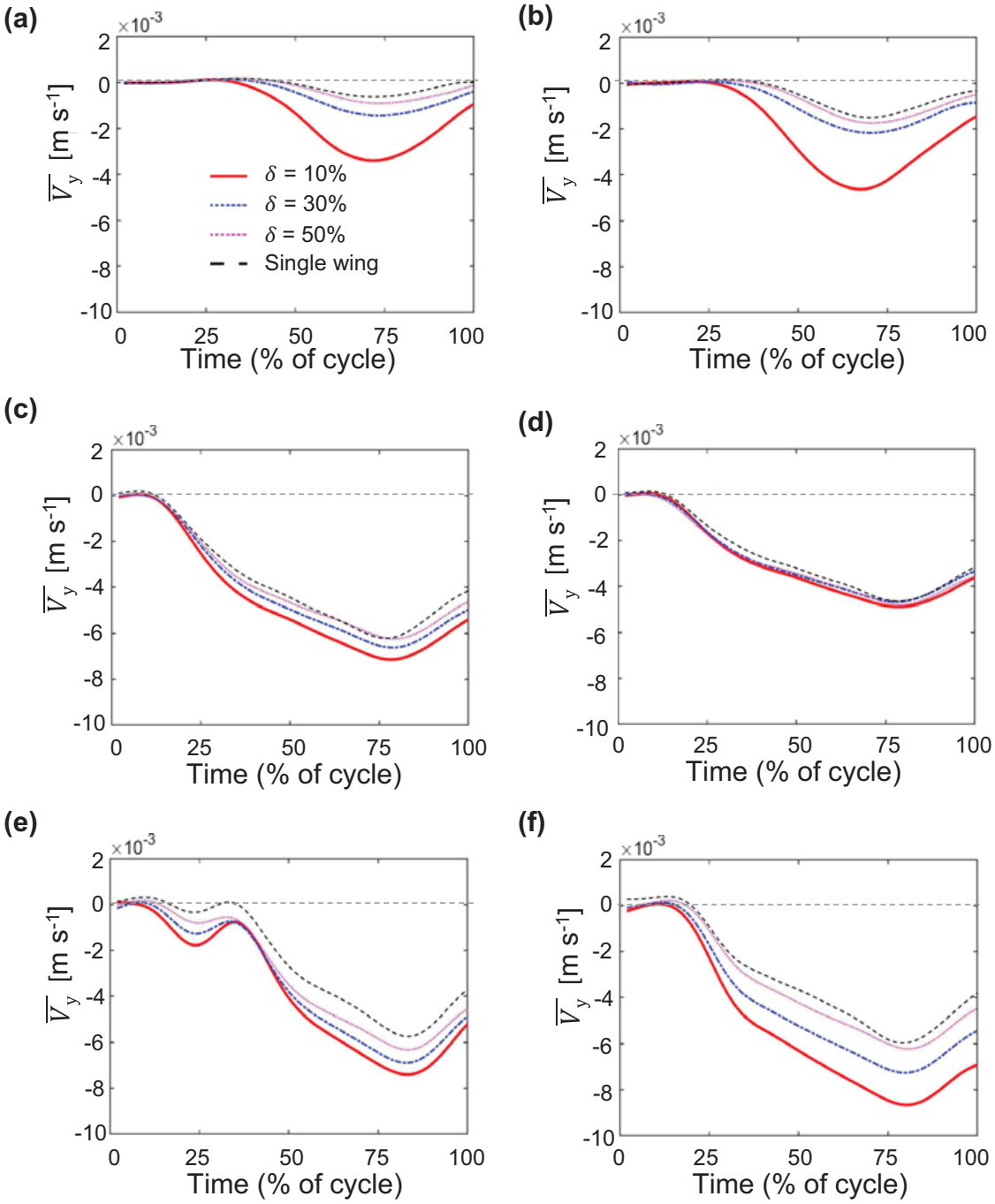

Figure 4.21: Time-variation of downwash ($\overline{V_y}$), defined as the spatially-averaged velocity of the flow displaced vertically downward due to wing motion, as a function of δ and wing kinematics. (a) and (b) show $\overline{V_y}$ during rotation at θ_r=22.5° and θ_r=67.5°, respectively. (c) and (d) show $\overline{V_y}$ during linear translation at θ_t=22.5° and θ_t=67.5°, respectively. (e) and (f) show $\overline{V_y}$ during combined rotation and linear translation at ζ= 25% and ζ=100%, respectively. Both single bristled wing and bristled wing pairs are included. See subsection 3. 4 for more details on definition and calculation of downwash.

by 20% (Fig. 4.14(f)). This substantial increase in lift coefficients is attributed to the generation of stronger LEVs for ζ=100%. This suggests that rotational acceleration during overlapping motion helps in early development of vortices. Additional acceleration from translation allowed vorticity to diffuse at both LE and TE rather than increasing its magnitude. For ζ=100%, right after 25% of cycle time, we see a drop in C_L that can be attributed to increased downwash velocity at the same instant (Fig. 4.21(f)).

5. 2 Implications of pressure distribution on drag force generation

Examining the pressure distribution on a single wing in rotation (Fig. 4.7), we can observe that the formation of a LEV creates a low pressure region on the upper surface of the wing and a positive pressure region on the lower surface. This pressure distribution over a single rotating wing was in agreement with those reported by Cheng and Sun (Cheng and Sun, 2017). For a bristled wing pair in rotation with varying δ (Fig. 4.8), we see a negative pressure region at the top closer to the LEs and positive pressure distribution at the bottom near the TEs. In the cavity between the wings, pressure was zero to start with and becomes positive instead of negative for all δ during rotation. These results are in contrast with those of Cheng and Sun (Cheng and Sun, 2017), where a negative pressure distribution was observed in between the wings at the start of fling. We suspect the positive pressure distribution in the cavity was due to strong viscous forces acting between the plates, which in turn tremendously increase drag.

With increasing time, the positive pressure region diminished with increasing distance between the wings. The inter-wing distance in time decreases with increasing δ. This suggests that smaller δ plays a crucial role in establishing the time-varying pressure field between the wings. The observed time-variation of spatially-averaged positive pressure coefficient ($\overline{C_p}$) was likely influenced by the positive pressure region in the cavity (Fig. 4.22(a)). Increasing θ_r from 22.5° to 67.5° decreased the magnitude of positive pressure inside the cavity which explains the drop in C_D (Fig. 4.22(a),(b)). This drop in C_D could be one of the

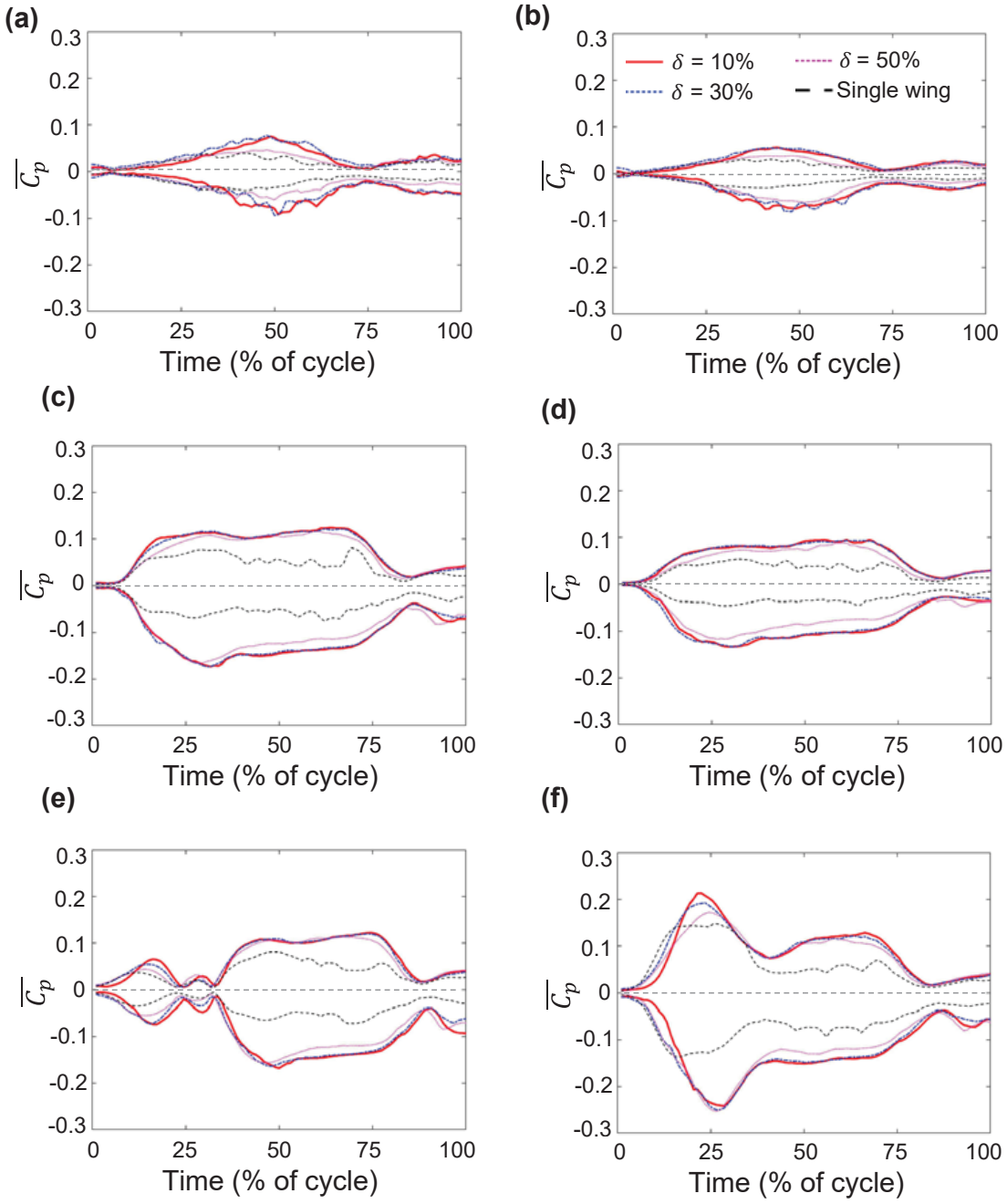

Figure 4.22: Time-variation of spatially-averaged pressure coefficient ($\overline{C_p}$) characterizing the total dimensionless pressure distribution in the flow field, as a function of δ and wing kinematics. (a) and (b) show $\overline{C_p}$ during rotation at θ_r=22.5° and θ_r=67.5°, respectively. (c) and (d) show $\overline{C_p}$ during linear translation at θ_t=22.5° and θ_t=67.5°, respectively. (e) and (f) show $\overline{C_p}$ during combined rotation and linear translation at ζ=25% and ζ=100%, respectively. Both single bristled wing and bristled wing pairs are included. See subsection 3. 4 for more details on definition and calculation of $\overline{C_p}$.

reason for thrips to flap their wings at large rotational angles or low pitch angles (Cheng and Sun, 2017) (about 20°, equivalent to $\theta_r \approx 70°$). Note that pitch angle was defined relative to the horizontal in Cheng and Sun (Cheng and Sun, 2017), unlike how θ_r was defined (relative to the vertical) in this study.

For smaller θ_t and for all δ that was examined here, we observed positive pressure in the cavity between the wings during early stages of linear translation of a bristled wing pair. With time, this positive pressure distribution slowly diminished as the LEs moved apart by $\sim$1.5 chord lengths. A negative pressure distribution was found to develop at the top of the wings. Interestingly, we did not see positive pressure distribution in the cavity for θ_t=67.5° even at smaller δ. We suspect that this could be due to a drop in the viscous forces acting in the cavity. Increasing θ_t was observed to decrease the magnitude of both positive and negative $\overline{C_p}$ (Fig. 4.22(c),(d)), which explains the substantial drop in C_D for larger θ_t. From a recent study examining thrips wing kinematics (Lyu et al., 2019*b*), it was found that they operate at large θ_t values, i.e., they pitch their wings to very low angles (about 30°, equivalent to θ_t= 60°) at the start of translation.

Similar to rotation and linear translation, we observed the formation of positive pressure region in the cavity between the wings during initial stages of wing motion for all ζ and all δ values. This positive pressure was found to diminish once the wings started moving apart. The distance between the wings where positive pressure started to diminish was found to depend on wing velocity and δ. Increasing ζ increased both positive and negative $\overline{C_p}$ (Fig. 4.22(e),(f)), which was also observed in the force coefficients.

5. 3 Cycle-averaged circulation and pressure characteristics: implications on force generation

We next examine cycle-averaged vorticity and pressure distributions for all test conditions and discuss how these factors impact lift generation.

Varying θ_r. Cycle-averaged net circulation on a wing ($\overline{\Gamma_{net}}$) was calculated using equa-

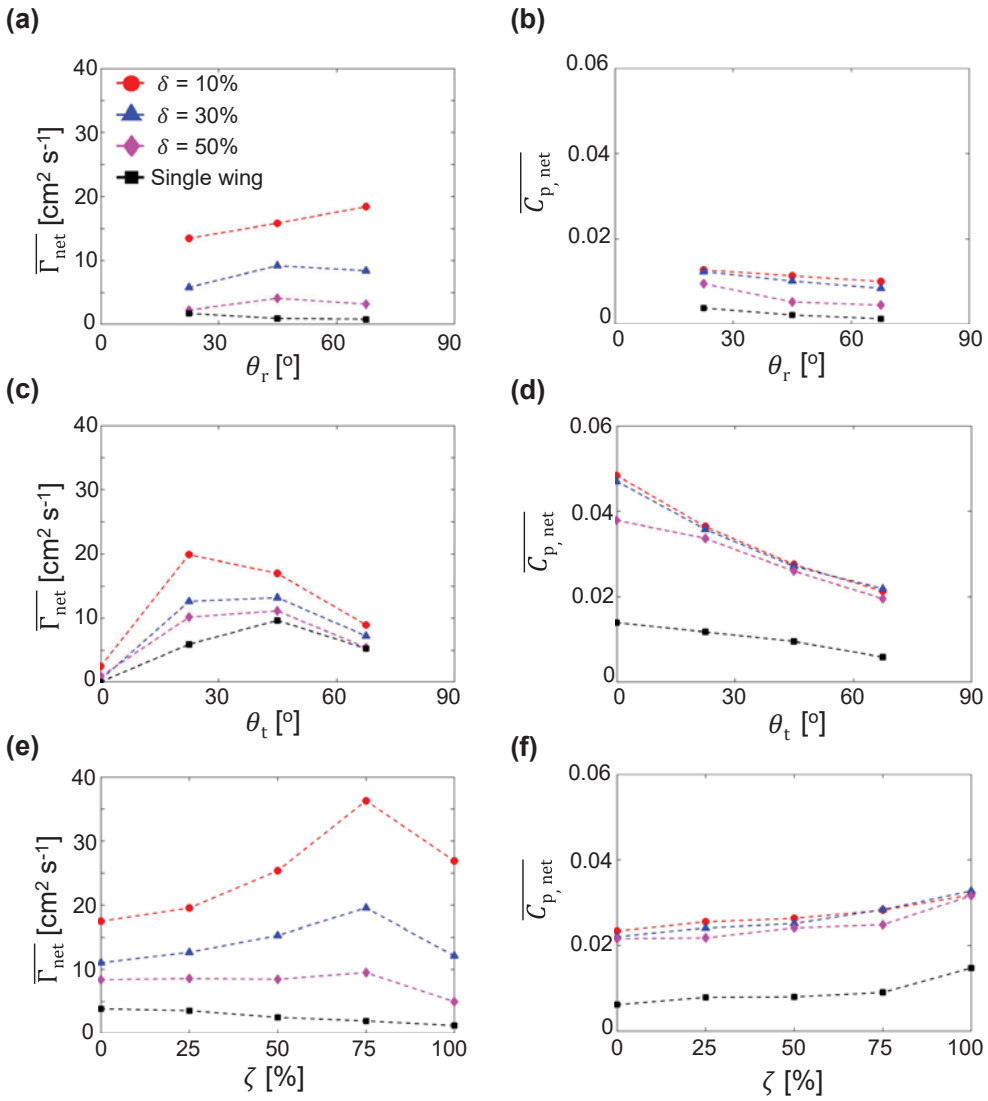

Figure 4.23: Cycle-averaged net circulation ($\overline{\Gamma_{\text{net}}}$) and cycle-averaged net pressure coefficient, $\overline{C_{p,\text{net}}}$ during (a, b) pure rotation (θ_r), (c, d) pure translation (θ_t) and (e, f) overlap (ζ) of bristled wing model at Re = 10. Legends for each plot are shown in (a).

tion (4.9) for interacting bristled wing pairs and a single bristled wing as a function of δ and θ_r (Fig. 4.23(a)). Irrespective of θ_r, increasing δ resulted in decreasing $\overline{\Gamma_{net}}$ on a bristled wing. As the net circulation over a wing is related to lift generation, the loss of $\overline{\Gamma_{net}}$ with increasing δ can explain the observed reduction of cycle-averaged lift coefficient ($\overline{C_L}$) with increasing δ (Fig. 4.4(f)). This association between loss of $\overline{\Gamma_{net}}$ and $\overline{C_L}$ with increasing δ was not established in previous studies of solid wing pairs (Sun and Yu, 2006; Arora et al., 2014; Kolomenskiy et al., 2010). For a bristled wing pair, dissimilar trends were observed when comparing how $\overline{\Gamma_{net}}$ and θ_r (Fig. 4.23(a),(b)) individually affected corresponding $\overline{C_L}$. $\overline{C_L}$ decreased with increasing θ_r (Fig. 4.4(f)), which is in disagreement with how $\overline{\Gamma_{net}}$ changed with increasing θ_r (Fig. 4.23(a)). This suggests that circulatory lift alone cannot be used to explain lift generation during rotation of a bristled wing pair at low *Re*. We need to consider non-circulatory lift mechanisms, including added mass affects, delayed stall at high rotational angles and pressure distribution between the wings during fling.

Cycle-averaged net pressure coefficient ($\overline{C_{p,net}}$) was calculated using equation (4.14)) for each test condition of θ_r (Fig. 4.23(b)). $\overline{C_{p,net}}$ generally decreased with increasing θ_r, which was analogous to the variation in $\overline{C_D}$ with θ_r. It is important to note that the pressure coefficient on the wings is indicative of total force generated rather than only the drag force. Both wings were in close proximity of each other throughout the entire cycle of rotational motion for any δ tested in this study ($\delta \leq 50\%$), which is conducive for aerodynamic interaction. As a consequence, the pressure distribution of one wing is expected to influence the pressure distribution (and thus lift generation) of both wings of the wing pair (Fig. 4.8). Therefore, despite the lack of decrease in $\overline{\Gamma_{net}}$ with increase in θ_r, we conjecture that decrease in $\overline{C_L}$ with increasing θ_r is due to decrease in $\overline{C_{p,net}}$ with increasing θ_r.

Varying θ_t. Similar to varying θ_r, increasing δ resulted in decreasing $\overline{\Gamma_{net}}$ on a bristled wing (Fig. 4.23(c)) for each θ_t examined in this study. Irrespective of δ, mostly similar trends were observed for both $\overline{\Gamma_{net}}$ (Fig. 4.23(b)) and $\overline{C_L}$ (Fig. 4.9(f)) when varying θ_t. However,

peak $\overline{\Gamma_{\text{net}}}$ for δ = 10% was observed at θ_t=22.5°, while peak $\overline{C_L}$ for the same δ occurred at about θ_t=45°. To further explain force generation at δ=10%, we examined the pressure distribution.

$\overline{C_{p,\text{net}}}$ trend for varying θ_t (Fig. 4.23(d)) was analogous to the corresponding trend of $\overline{C_D}$ (Fig. 4.9(e)). As mentioned in the previous paragraph, variation of $\overline{\Gamma_{\text{net}}}$ with θ_t was similar to that of $\overline{C_L}$ for $\delta > 10\%$. Therefore, we focus exclusively on $\overline{C_{p,\text{net}}}$ variation with θ_t for δ=10%. Pronounced wing-wing interaction at δ=10% is expected for θ_t=0° on account of physical proximity of the wings. Both $\overline{C_L}$ (Fig. 4.9(f)) and $\overline{\Gamma_{\text{net}}}$ (Fig. 4.23(c)) for this case (i.e., $\delta = 10\%$ and θ_t=0°) were markedly small. This suggests that circulatory lift can reasonably explain lift generation. The small value of $\overline{C_L}$ for θ_t=0° is expected because of the wings being oriented at 90° angle of attack relative to the horizontal, which promotes LEV-TEV symmetry and has also been reported in previous studies at similar *Re* (Miller and Peskin, 2005; Santhanakrishnan et al., 2018). By contrast, both $\overline{C_{p,\text{net}}}$ (Fig. 4.23(d)) and $\overline{C_D}$ (Fig. 4.9(e)) were large for θ_t=0°, implying that changes in pressure distribution primarily influences $\overline{C_D}$ for θ_t=0°. $\overline{\Gamma_{\text{net}}}$ (Fig. 4.23(c)) increased for θ_t=22.5° with corresponding increase in $\overline{C_L}$ (Fig. 4.9(f)). Similar to θ_t=0°, circulatory lift is adequate to explain lift generation at θ_t=22.5°. We observed a significant drop in $\overline{C_{p,\text{net}}}$ for θ_t=22.5° (Fig. 4.23(d)) corresponding to decrease in $\overline{C_D}$ (Fig. 4.9(e)). Both $\overline{C_{p,\text{net}}}$ and $\overline{\Gamma_{\text{net}}}$ (Fig. 4.23(c),(d)) decreased for θ_t = 45°, unlike the observed increase in $\overline{C_L}$ for θ_t=45° (Fig. 4.9(f)). As wing-wing interaction would be weaker for θ_t=45° as compared to θ_t¡45° due to larger inter-wing separation in the former case, we expect that the pressure distribution on an individual wing would also assist in its lift generation along with circulatory lift. The observed increase in $\overline{C_L}$ at θ_t=45° (Fig. 4.9(f)) can be explained by the contribution of $\overline{C_{p,\text{net}}}$ at this θ_t relative to circulatory lift generation at θ_t=22.5°. With further increase in θ_t (>45°), both $\overline{C_{p,\text{net}}}$ and $\overline{\Gamma_{\text{net}}}$ decreased and these resulted in decreasing $\overline{C_L}$ (Fig. 4.9(f)). Although $\overline{C_{p,\text{net}}}$ and $\overline{\Gamma_{\text{net}}}$ would contribute to lift generation for θ_t¿45°, we suspect the decrease in $\overline{C_L}$ is due to significant decrease in magnitudes of $\overline{C_{p,\text{net}}}$ and $\overline{\Gamma_{\text{net}}}$.

Varying ζ. Similar to varying θ_r and θ_t, increasing δ resulted in decreasing $\overline{\Gamma_{net}}$ on a bristled wing (Fig. 4.23(e)) for each condition of ζ. $\overline{C_L}$ increased with increasing ζ from 0% to 100% (Fig. 4.14(f)), but $\overline{\Gamma_{net}}$ increased until ζ=75% and then decreased with increasing ζ to 100%. Surprisingly, $\overline{\Gamma_{net}}$ decreased with increasing ζ for a single wing. For smaller ζ, wings initially rotate for a period of time before translating away from each other and permit wing-wing interaction due to the wings being in close proximity. However, for ζ=100%, both wings start to translate away from each other from the beginning of the cycle. Therefore, wing-wing interaction is weakest for ζ=100% and could account for the drop in $\overline{\Gamma_{net}}$ for this ζ. As circulatory lift was not adequately able to explain list generation across the entire range of ζ examined here, we examined the pressure distribution.

$\overline{C_{p,net}}$ trend for varying ζ (Fig. 4.23(f)) was analogous to the corresponding trend in $\overline{C_D}$ (Fig. 4.14(e)). However, we observed a sudden increase in $\overline{C_{p,net}}$ for ζ=100% across all of the δ values that we tested. This increase in $\overline{C_{p,net}}$ can explain the increase in $\overline{C_L}$ when ζ is increased from 75% to 100%. Although we observed decrease in $\overline{\Gamma_{net}}$ with increasing ζ for a single wing, $\overline{C_{p,net}}$ increased along with $\overline{C_L}$ and $\overline{C_D}$. Collectively, these results show the importance of considering pressure distribution over the wings to understanding force generation by a bristled wing pair in fling.

5. 4 Limitations

Although we examined aerodynamic performance of bristled wings in fling for varying kinematics, our study is limited to 2D motion. This simplification was justified by considering the phase of flapping motion where wing-wing interaction at smaller δ is observed. An important question that remains to be investigated is whether the trends that we observed using 2D kinematics are retained when examining 3D flapping kinematics at low *Re*. A previous study by Santhanakrishnan et al.(Santhanakrishnan et al., 2018) reported that in the *Re* range relevant to the flight of the smallest insects ($Re \leq 32$), spanwise flow decreased and viscous diffusion increased for a revolving non-bristled elliptical wing (3D motion). It

is unknown how their observations would be affected by the inclusion of wing bristles and when considering realistic (3D) flapping kinematics of tiny insects. Specifically, large deviations from the stroke plane have been reported in free-flight recordings of thrips (Lyu et al., 2019*b*) and shown to be important for vertical force generation in tiny insect flight (Cheng and Sun, 2018). The robotic platform used in this study did not permit evaluating changes in deviation. The above questions will be the subject of our future studies. From the biological standpoint, high-magnification free-flight recordings of tiny insects are needed to identify: (a) the range of δ across different species of tiny flying insects, and (b) whether tiny insects can modulate δ between cycles of flapping flight to tailor their aerodynamic performance.

5. 5 Conclusions

Aerodynamic forces and flow structures generated by a single bristled wing and a bristled wing pair undergoing rotation about the TE(s), linear translation at a fixed angle and their combination were investigated for varying initial inter-wing spacing at Re=10. Irrespective of θ_r, θ_t and ζ, increasing δ in a bristled wing pair decreased drag by a larger extent as compared to lift reduction due to weakening wing-wing interaction, resulting in the wing pair behaving as two single wings. During wing rotation (θ_r) at smaller δ, positive pressure on the leading surface of each interacting wing (ventral surface) diffused through the inter-bristle gaps due to large viscous forces. This resulted in the formation of a strong +ve pressure region in between the wings, necessitating large drag force to move the wings apart. The positive pressure region diminished with increasing θ_r, which in turn reduced drag forces. This finding suggests that a likely reason for tiny insects to employ large rotational angles (relative to vertical) in fling (Cheng and Sun, 2017) is to reduce drag. Finally, we find that rotational acceleration of a bristled wing aids in early development of LEV and TEV. Previous studies (Santhanakrishnan et al., 2014; Jones et al., 2016) have reported δ ranges from 10% to 25% in thrips based on free-flight recordings. Lift was

largest for δ=10% across all wing kinematics that were tested in this study, which also falls within the above observed range of δ in thrips.

CHAPTER V

SA 3: Pausing after clap reduces power required to fling wings apart at low Reynolds number

1 Introduction

Despite the roughly tenfold increase in wing length of a hawk moth compared to that of a fruit fly, the aerodynamic mechanisms underlying their free-flight are surprisingly similar. A vast number of studies examining flight aerodynamics of fruit flies and larger insects have identified the following mechanisms of lift generation: 1) delayed stall via the leading edge vortex (LEV) (Dickinson and Gotz, 1993; Ellington et al., 1996); 2) rotational lift (Dickinson et al., 1999; Sane and Dickinson, 2002); 3) wing-wake interactions (Dickinson et al., 1999); and 4) wing-wing interaction during stroke reversal via clap-and-fling (Weis-Fogh, 1973, 1975; Spedding and Maxworthy, 1986). Far little is known about flight aerodynamics in entire families of miniature insects of body lengths ranging from 0.1 mm to 2 mm, such as thrips and several parasitoid wasps (e.g., *Trichogramma* spp. (Jalali et al., 2016) and fairyflies (Huber et al., 2008)). Miniature insects have been primarily examined by entomologists owing to their ecological and agricultural importance (Crespi et al., 1997; Terry, 2001; Ullman et al., 2002; Whitfield et al., 2005; Jalali et al., 2016). From an engineering standpoint, studies of tiny insect flight can guide the development of biomimetic micro aerial vehicles (Liu et al., 2016).

Viscous dissipation of kinetic energy presents a significant constraint to the flight of tiny insects, where Reynolds number based on wing chord and tip velocity (Re_c) is on the order of 1 to 10 (Santhanakrishnan et al., 2014; Jones et al., 2016; Santhanakrishnan et al., 2018). At such low Re_c, these insects have to continually flap to stay aloft (Sane,

2016). Multifold increase in drag coefficient has been reported for revolving (Santhanakrishnan et al., 2018) and translating (Miller and Peskin, 2004) wings for $Re_c \leq 32$. At $Re_c \geq 120$ corresponding to flight of fruit flies and larger insects, a large LEV is formed at the start of a half-stroke and remains attached to the wing until the end of the half-stroke (Ellington et al., 1996; Birch et al., 2004). The trailing edge vortex (TEV) is detached from the wing and shed in the wake. The attached LEV delays stall and helps in lift generation (Dickinson et al., 1999; Ellington, 1999). In contrast, both the LEV and TEV do not separate from a wing during linear translation (Miller and Peskin, 2004) and revolution for $Re_c \leq 32$ (Santhanakrishnan et al., 2018). This LEV-TEV 'vortical symmetry' has been proposed to decrease lift in tiny insect flight (Miller and Peskin, 2004), due to reduction in the time rate of change of the first moment of vorticity (Wu, 1981).

Many previous studies Miller and Peskin (2004); Sun and Yu (2006); Kolomenskiy et al. (2011) have investigated the effects of clap and fling mechanism using simplified motions and concluded that clap and fling augments lift force generation. Cheng and Sun (2019) computationally investigated biologically-observed wingbeat kinematics of tiny insects and found that drag was reduced by 6 to 10 times as that generated by idealized clap and fling kinematics, with no change in lift generation.

Despite the above aerodynamic challenges, several studies have reported controlled flight of thrips over short distances (Terry, 2001; Whitfield et al., 2005; Morse and Hoddle, 2006; Rodriguez-Saona et al., 2010; Riley et al., 2011). Examining biomechanical adaptations used by tiny insects can help to understand how they are able to overcome fluid dynamic constraints. Two such key adaptations have been examined in several studies, including the presence of long bristles in their wings and obligatory use of wing-wing interaction in free-flight (clap-and-fling). Sunada et al. (2002) used dynamically scaled models undergoing translation and rotation and found little variations in forces between solid (non-bristled) and bristled wing designs. Force coefficients for the bristled wing model were found to be more compared to solid wing model, when using a reduced surface area

to determine the coefficients of the bristled wing. Weihs and Barta (2008) and Davidi and Weihs (2012) found that a comb-like wing could comparatively generate forces similar to that of solid wings of same shape, while saving up to 90% of the wing weight. Recent studies (Lee and Kim, 2017; Lee et al., 2018, 2020*b*) have shown that a comb-like wing can provide aerodynamic benefit at small inter-bristle gaps, owing to the formation of diffused shear layers around the bristles that block flow from leaking through the gaps. However, most of these studies used a single bristled wing model and did not address wing-wing interaction used in free-flight of tiny insects (Lehmann et al., 2005).

Santhanakrishnan et al. (2014) performed 2D computational simulations of clap-and-fling at Re_c corresponding to tiny insect flight. By approximating bristled wings as porous surfaces, this study found that bristled wings can provide substantial drag reduction when compared to solid wings during clap-and-fling. Jones et al. (2016) modeled wing bristles as 2D cylinder arrays and showed that bristled reduce the force required to fling the wings apart during wing-wing interaction. In our recent study (Kasoju et al., 2018), we experimentally examined the inter-bristle flow during clap-and-fling for bristled wing models with varying inter-bristle gap. When compared to a solid wing model, we found that bristled wings provide aerodynamic benefit through larger drag reduction and disproportionally lower lift reduction. Ford et al. (2019) found that thrips wings show a preference for smaller membrane area compared to the total wing area, and that wings with smaller membrane areas provide larger aerodynamic benefit during clap-and-fling at Re_c corresponding to tiny insect flight. Collectively, these studies show that combining biomechanical adaptations in wing kinematics (clap-and-fling) and wing morphology (bristles) can provide aerodynamic benefit to flapping flight at the scale of the smallest insects.

In addition to the obligatory use of clap-and-fling, tiny insects have been observed to use a shorter upstroke duration and a longer downstroke duration (Santhanakrishnan et al., 2014). Such an asymmetric reduction of upstroke duration can lower the time where loss of lift occurs, as most of the lift in flapping flight of insects is generated during the

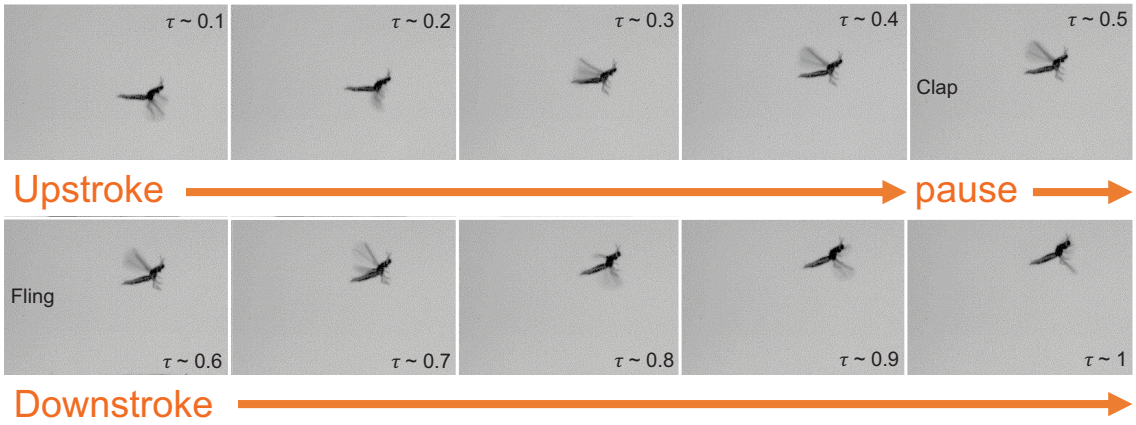

Figure 5.1: Successive snapshots of thrips in free take-off flight during one cycle (τ denotes fraction of cycle time). At the end of upstroke (τ = 0.4-0.5), both fore wings were brought in close proximity of each other ('clap'). The wings paused for approximately 10% of flapping cycle before the start of downstroke ('fling'). See Table 5.1 for more information.

downstroke (Sane, 2003). Ellington (1975) observed that the tiny chalcid wasp *Encarsia formosa* paused wing motion at the end of upstroke (clap) for about 10% of total cycle time (taken here as the sum of upstroke and downstroke time). He proposed that pausing at the end of upstroke (clap stroke) could potentially promote shedding and advection of vortices away from the wing before the start of fling, and reduce the mechanical energy required for fling. These hypotheses were not tested in his study, and the aerodynamic implications of pausing after upstroke (clap stroke) are unknown. In this study, we experimentally examine force generation during clap-and-fling at Re_c=10 across varying pause duration following the upstroke (clap stroke) phase. Our tests were conducted using a dynamically scaled robotic model outfitted with bristled wing and solid wing physical models (Kasoju et al., 2018; Ford et al., 2019). 2D particle image velocimetry (PIV) measurements were used to examine the evolution and dissipation of flow structures around the wings during the pause following the upstroke (clap stroke) phase.

2 Materials and methods

2. 1 Free-flight recordings of thrips

Thrips were collected in Chapel Hill, NC, USA, during early June, 2017 from daylilies, gardenia and Azaleas flowers. The flowers with insects were then brought to recording arena and filmed within few hours of their collection. We used a procedure similar to that described in the study by Santhanakrishnan et al. (2014) for filming free take-off flight. A pipette tip was placed on top of an insect to allow it to crawl inside the tube. A single high-speed camera (Phantom v7.1, Vision Research, Wayne, NJ, USA) was used for filming. The camera was fitted with a 55 mm micro-Nikkor lens, a Nikon PB-5 bellows with variable extension, and a 27.5 mm extension tube. The pipette tip with thrips was placed upside-down in the camera field of view, and we waited for the thrips to crawl out of the tube and take-off from the tip. The field of view was illuminated using a red light emitting diode (LED) array. A white diffuser placed in front of the camera aperture, with the pipette tip located in between camera and the LED array. Free take-off flight of thrips were filmed at different frame rates with a shutter duration ranging between 15–30 μs (Table 5.1).

Five high-speed video recordings (representative snapshots shown in Fig. 5.1) were digitized and analysed in ImageJ (National Institutes of Health, Bethesda, MD, USA) for calculating the pause time between the end of upstroke (clap) and start of downstroke (fling), and the results are provided in Table 5.1. The five raw videos that were used for analysis are within Figshare Digital Repository: https://doi.org/10.6084/m9.figshare.13053056. The average pause time from the five recordings was calculated to be $11\pm2\%$ of the total cycle time. This calculated pause time was close to that of *E. formosa* (10% of cycle time) reported by Ellington (1975).

Video	Sample Rate (fps)	Cycle Time (ms)	% Pause Time
1	3000	4.67	14.3
2	4000	5.25	9.5
3	4000	5.5	9.1
4	4000	4.75	10.5
5	4700	4.04	10.5

Table 5.1: Pause duration analyzed between end of upstroke and start of downstroke for several high speed video recordings.

2. 2 Test facility

The dynamically scaled robotic wing platform used in this study has been used before (Kasoju et al., 2018; Ford et al., 2019) and is described briefly here. The robotic platform consists of four 2-phase hybrid stepper motors with integrated encoders (ST234E, National Instruments Corporation, Austin, TX, USA) mounted on an acrylic tank with 0.51 m x 0.51 m cross-section, and 0.41 m in height. These motors were used to prescribe the motion of 2 physical wing models. The four stepper motors were controlled by a multi-axis controller (PCI-7350, National Instruments Corporation, Austin, TX, USA) via custom programs written in LabVIEW software (National Instruments Corporation, Austin, TX, USA). Two stepper motors were dedicated to each wing to perform rotation and translational motion with help of bevel gear pairs and rack and pinion mechanism, respectively.

2. 3 Physical models

A bristled wing of membrane width 7 mm, with symmetric bristle lengths on either side of a membrane (Fig. 5.2A) was laser cut from an optically clear acrylic sheet of thickness 3.18 mm. The bristles were cut to required length from 304 stainless steel wires of uniform diameter (D) of 0.31 mm and were glued on top of the acrylic membrane with inter-bristle spacing (G) to bristle diameter (D) ratio (i.e., G/D) of 5 (Fig. 5.2A). The commonly observed range of G/D in tiny insects is 4-12 (Jones et al., 2016). In order to fit a biologically relevant number of bristles (n=88) within a fixed span (S) of 81 mm, while also ensuring that Reynolds number based on bristle diameter (Re_{b}) was in the biologically relevant range

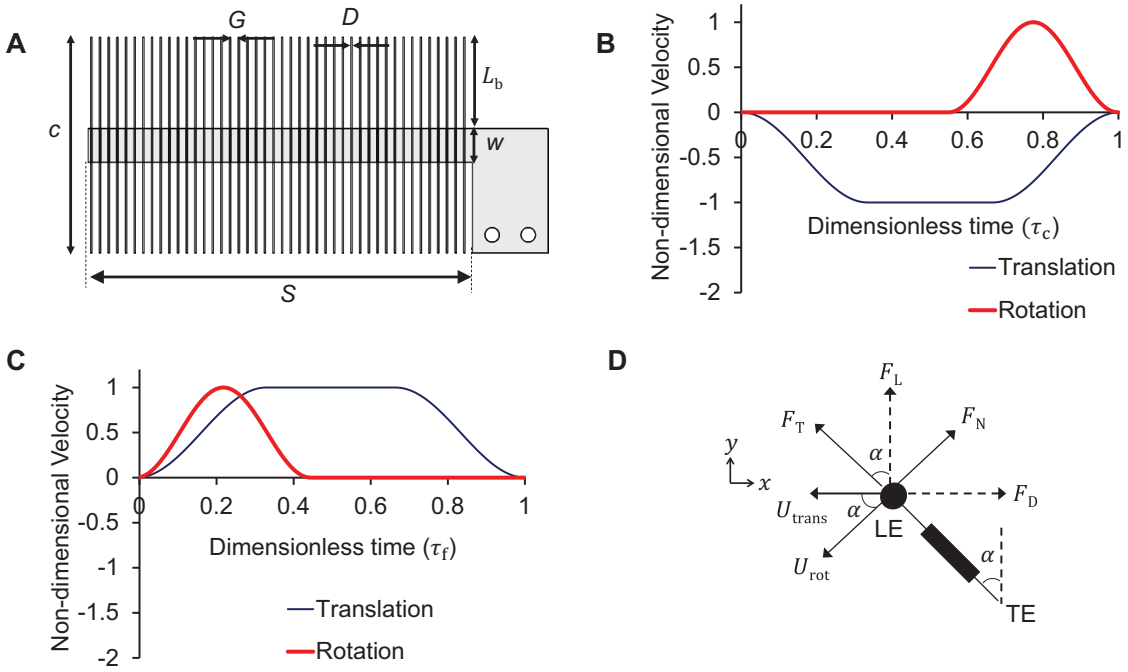

Figure 5.2: (A) Bristled wing model of chord length (c)=45 mm, wing span (S)=81 mm, inter-bristle spacing (G)=1.83 mm, bristle diameter(D)=0.31 mm, length of bristle (L_b)=19 mm and membrane width (w)=7 mm. A solid wing model (without bristles) with the same chord (c) and span (S) lengths as that of the bristled wing was also tested. (B) and (C) show the time-varying motion profile prescribed for motion of a single wing during upstroke (clap stroke) and fling, respectively, based on a previous study by Miller and Peskin (2005). The thin line indicates the wing translational motion while the thick line represents the wing rotation. (D) The sectional view of a bristled wing model (referred here as "chordwise view") with directions of measured tangential (F_T) and normal forces (F_N) experienced during rotation by angle α. Lift (F_L) and drag (F_D) forces were measured by taking components of F_T and F_N in the vertical and horizontal directions, respectively. τ_c=dimensionless upstroke (clap stroke) time; τ_f=dimensionless downstroke (fling stroke) time; LE=leading edge; TE=trailing edge; U_{trans}=translational velocity at wing tip; U_{rot}=rotational velocity at wing tip; x,y are global horizontal and vertical coordinate axes.

of 0.01 to 0.07, we chose bristle diameter (D) of 0.31 mm. For a rectangular bristled wing with symmetric bristle lengths on either side of a solid membrane, G, D, S can be related to the total number of bristles (n, including both sides of a solid membrane) via the relation:

$$\frac{G}{D} = \left(\frac{2S}{nD}\right) - 1 \tag{5.1}$$

We obtained G/D=5 using the above relation, which is in the biologically relevant range. Also, an equivalent solid wing pair with the same chord and span lengths as the bristled wing model was laser cut from a 3.18 mm thick acrylic sheet. Each wing of the wing pair being tested was attached to custom made aluminum L-brackets and completely immersed inside the acrylic tank (described above under test facility) using 6.35 mm diameter stainless steel D-shafts.

Among our physical models, we have not observed the solid wing and the solid membrane of the bristled wing to deform. The solid wings and the membrane of the bristled wings as the wings were fabricated from acrylic sheets. The bristles used in our physical bristled wing models were cut from 304 stainless steel wires, which are thin and have the possibility of bending. However, while performing flow visualization using PIV, we did not observe the bristles to bend during wing motion. This could be due to the high viscosity of the fluid medium (glycerin) not allowing the steel wires to noticeably bend.

2. 4 Wing kinematics

A modified version of 2D clap and fling kinematics that was initially developed by Miller and Peskin (2005) was prescribed for wing motion in the robotic model (Fig. 5.2B,C). The motivation behind using this kinematics is that it provides a simplified representation of the complex three-dimensional wing kinematics of an insect, with particular emphasis on the portion of the wing motion from the end of the upstroke and the start of the downstroke, i.e., the duration of upstroke (clap stroke) and downstroke (fling stroke) motion. However, these kinematics do not account for 3D flapping revolution of a real insect during the

upstroke and downstroke. The rotational velocity profile should be considered as a simplification, and recent studies (Lyu et al., 2019*b*; Cheng and Sun, 2018, 2021) have shown that tiny insects do not employ symmetrical acceleration/deceleration during their wing motion. Similar forms of these kinematics have been used in many previous studies (Santhanakrishnan et al., 2014; Arora et al., 2014; Jones et al., 2016; Kasoju et al., 2018; Ford et al., 2019). The wings were made to rotate and translate simultaneously with 100% overlap prescribed between rotation and translation during both upstroke (clap stroke) and downstroke (fling stroke) phases. Wing rotation during upstroke (clap stroke) was adjusted such that rotation ended exactly when the wings stopped translating, as shown in Fig. 5.2B. During fling, wings were made to start rotation and translation at the same time, as shown in Fig. 5.2C. Arora et al. (2014) previously examined the effects of varying the percentage of overlap between rotation and translation on forces generation, and reported increase in force coefficients with increasing overlap during upstroke (clap stroke) and downstroke (fling stroke). This was the rationale for choosing maximum possible overlap for both upstroke (clap stroke) and downstroke (fling stroke) in this study. Fig. 5.2B,C show prescribed non-dimensional velocities as a function of dimensionless time (τ_c, τ_f) during upstroke (clap stroke) and downstroke (fling stroke), respectively. The dimensionless times for each phase (upstroke (clap stroke) or downstroke (fling stroke)) are indicated as the ratio of instantaneous time to total time of a specific phase (upstroke (clap stroke) or downstroke (fling stroke)). Note that the kinematics presented here are for a single wing performing upstroke (clap stroke) and downstroke (fling stroke). The kinematics for the other wing were identical but in opposite directions. The inter-wing spacing between the wings was set to 10% of chord, which is similar to those observed in free flight recordings of thrips (Santhanakrishnan et al., 2014). While the terms 'clap' and 'fling' are traditionally referred to in the context of wing pairs, we use these terms also for a single wing that is prescribed to move using the same kinematics as that of a wing pair. Comparison of a one-winged upstroke (clap stroke) and downstroke (fling stroke) motion against a two-winged (i.e., traditional)

clap and fling motion has been performed previously for solid wings (Miller and Peskin, 2005), and we employ a similar comparative assessment in this study.

2. 5 Test conditions

Force measurements and flow visualization were conducted on a single wing (solid and bristled) and a wing pair (solid and bristled) for 5 pause times (0%, 9%, 17%, 23%, 41% of the entire cycle time). We included 9% pause time so as to mimic the pause duration observed from high-speed video recordings of the free take-off flight of thrips (Fig. 5.1, Table 5.1). The total cycle time is calculated as sum of upstroke (clap stroke) time, pause time and downstroke (fling stroke) time, in units of milliseconds (ms). Re_c=10 was maintained as a constant across all test conditions, where Re_c was based on steady translational velocity (U_{ST}) of the wing and chord length (c). The acrylic tank described in test facility above was filled with 99% glycerin solution to obtain Re_c=10. The kinematic viscosity (ν) of the 99% glycerin solution used in this study was measured using a Cannon-Feske routine viscometer (size 400, Cannon Instrument Company, State College, PA, USA) to be 706×10^{-6} m^2/s. The density of the 99% glycerin solution was measured to be 1260 kg/m^3. The Reynolds number based on bristle diameter (Re_{b}) was calculated to be 0.067 using the relation:

$$Re_{\mathrm{b}} = \frac{U_{\mathrm{ST}} D}{\nu} \tag{5.2}$$

and is within the biologically relevant range of 0.01-0.07 for tiny insect flight (Jones et al., 2016).

2. 6 Force measurements

Forces on the wings were measured using uniaxial strain gauges bonded to the L-brackets (wing mount). The custom L-brackets were designed to measure forces in perpendicular (i.e., normal) and parallel (i.e., tangential) directions to the wing. The tangential force (F_{T}) and normal force (F_{N}) were then resolved along the global horizontal axis (x-axis) to obtain

drag force (F_{D}) and vertical axis (y-axis) to obtain lift force (F_{L}) (Fig. 5.2D). Separate L-brackets were used for measuring lift and drag as described in a previous study (Kasoju et al., 2018). A data acquisition board (NI USB-6210, National Instruments Corporation, Austin, TX, USA) was used to acquire the strain gauge voltage data and angular position of the wings at a sample rate of 10 kHz throughout the entire cycle (includes upstroke (clap stroke) time, pause time and downstroke (fling stroke) time). We used the same processing procedures as used in Kasoju et al. (2018) and Ford et al. (2019). The raw data was filtered in MATLAB (The Mathworks Inc., Natick, MA, USA) using a third order low-pass Butterworth filter with a cutoff frequency of 24 Hz. The lift and drag brackets were calibrated manually and the calibrations were applied to the filtered voltage data. The forces were then resolved along global horizontal (drag force) and vertical (lift force) directions. We note that forces were only recorded on a single wing of a wing pair, with the assumption that force generation by other wing was symmetrical and equal in magnitude because the motion was symmetrical.

Dimensionless lift (C_{L}) and drag (C_{D}) coefficients were calculated as:

$$C_{\mathrm{L}} = \frac{F_{\mathrm{L}}}{\frac{1}{2}\rho U_{\mathrm{ST}}^2 A} = \frac{F_{\mathrm{T}}\cos\alpha + F_{\mathrm{N}}\sin\alpha}{0.5\rho U_{\mathrm{ST}}^2 A} \tag{5.3}$$

$$C_{\mathrm{D}} = \frac{F_{\mathrm{D}}}{\frac{1}{2}\rho U_{\mathrm{ST}}^2 A} = \frac{F_{\mathrm{T}}\sin\alpha + F_{\mathrm{N}}\cos\alpha}{0.5\rho U_{\mathrm{ST}}^2 A} \tag{5.4}$$

where F_{L} and F_{D} are the lift and drag forces measured along horizontal (in the direction perpendicular to wing motion) and vertical directions, respectively (in Newtons), U_{ST} represents steady translational velocity, ρ is density of the fluid medium and A represents the effective wing surface area (4.05×10^{-3} m^2) for both the solid and bristled wing. The reason for using effective surface area for the bristled wing, as opposed to a reduced surface area (excluding gaps between the bristles), is because a reduced surface area implicitly assumes that flow through the bristles is mostly identical to the ideal/inviscid case without allowing the possibility that flow can incompletely leak through the gaps be-

tween the bristles on account of viscous interactions Kasoju et al. (2018). Standard deviations were calculated across 30 consecutive cycles for C_{L} and C_{D}, and the force coefficients were averaged across all cycles. In addition, phase-averaged force coefficients ($\overline{C_{\mathrm{L,clap}}}$, $\overline{C_{\mathrm{L,fling}}}$, $\overline{C_{\mathrm{D,clap}}}$, $\overline{C_{\mathrm{D,fling}}}$) were calculated in upstroke (clap stroke) and downstroke (fling stroke) phases separately. It is important to note that the term "phase-average" in calculation of $\overline{C_{\mathrm{L,clap}}}$, $\overline{C_{\mathrm{D,clap}}}$, $\overline{C_{\mathrm{L,fling}}}$, $\overline{C_{\mathrm{D,fling}}}$ is referenced in terms of upstroke (clap stroke) and downstroke (fling stroke) phases, so that the averaging was performed in time over the duration of upstroke (clap stroke, τ_{c} in Fig. 5.2B) or downstroke (fling stroke, τ_{f} in Fig. 5.2C). Cycle-averaged force coefficients ($\overline{C_{\mathrm{L,net}}}$, $\overline{C_{\mathrm{D,net}}}$) were calculated by averaging across the time period of the entire cycle, including clap, pause and fling phases. Standard deviations and averages for phase-averaged and cycle-averaged coefficients were calculated across all 30 cycles. Since the direction of drag force acting on the wings were in opposite direction for upstroke (clap stroke) and downstroke (fling stroke) phases, we used absolute values of the sum of C_{D} during upstroke (clap stroke) phase, pause time and downstroke (fling stroke) phase separately. The cycle-averaged net drag coefficient was calculated using trapezoidal rule in MATLAB and is presented here in an integral form as:

$$\overline{C_{\mathrm{D,net}}} = \int_0^1 C_{\mathrm{D}}(\tau)\, d\tau \tag{5.5}$$

and we calculated cycle-averaged net lift coefficient as:

$$\overline{C_{\mathrm{L,net}}} = \int_0^1 C_{\mathrm{L}}(\tau)\, d\tau \tag{5.6}$$

Similar to force coefficients, the power coefficient (C_{P}) was calculated using the equation:

$$C_{\mathrm{P}} = \frac{\text{Power}}{\frac{1}{2}\rho U_{\mathrm{ST}}^2 A} = \frac{F_{\mathrm{D}}\, U_{\mathrm{total}}}{\frac{1}{2}\rho U_{\mathrm{ST}}^3 A} \tag{5.7}$$

where $U_{\text{total}} = U_{\text{trans}} + U_{\text{rot}} \cos\alpha$. U_{trans} and U_{rot} represents the wing tip velocity during translation and rotation, respectively, and α represents the wing rotation angle shown in Fig. 5.2D. Similar to $\overline{C_{\text{L,net}}}$ and $\overline{C_{\text{D,net}}}$, cycle-averaged net power coefficient ($\overline{C_{\text{P,net}}}$) was calculated by averaging across the time period of the entire cycle (including the clap, pause and fling phases) using the equation:

$$\overline{C_{\text{P,net}}} = \int_0^1 C_{\text{P}}(\tau)\, d\tau \tag{5.8}$$

2. 7 Flow visualization

2D time-resolved PIV (2D TR-PIV) were conducted to visualize and measure the flow generated during the upstroke (clap stroke) phase, pause duration and downstroke (fling stroke) phase by the solid and bristled wings (single wing and wing pairs) along chordwise direction at the mid-span location (wings in chordwise view similar to Fig. 5.2D). 2D TR-PIV measurements were acquired for both wing models (solid and bristled) at all test conditions (0%, 9%, 17%, 23%, 41% pause time). A single cavity Nd:YLF laser (Photonics Industries International, Inc., Bohemia, NY, USA) was used for illumination that provided a 0.5 mm diameter beam of 527 nm in wavelength. A thin laser sheet (thickness $\approx$ 3-5 mm) was generated from the beam using a cylindrical lens of 10 mm focal length. A high-speed complementary metal-oxide-semiconductor (CMOS) camera with a spatial resolution of 1280x800 pixels, maximum frame rate of 1630 frames/s, and pixel size of 20x20 microns (Phantom Miro 110, Vision Research Inc., Wayne, NJ, USA) was used for acquiring raw TR-PIV images. This camera was fitted with a 60 mm constant focal length lens (Nikon Micro Nikkor, Nikon Corporation, Tokyo, Japan). Hollow glass spheres of 10-micron diameter (110P8, LaVision GmbH, Göttingen, Germany) were used as seeding particles Kasoju et al. (2018); Ford et al. (2019). 100 evenly spaced images were acquired at a recording rate of 90 Hz during the upstroke (clap stroke) and during the downstroke (fling stroke). The raw im-

ages were processed using DaVis 8.3.0 software (LaVision GmbH, Göttingen, Germany) using the following cross-correlation settings: one pass with an interrogation window of size 64x64 pixels and two subsequent passes with interrogation window of size 32x32 pixels, each with 50% overlap. The processed 2D TR-PIV images were phase-averaged over 5 non-consecutive cycles. We note the distinction in the "phase-average" term used in the context of 2D TR-PIV measurements against those used in the context of force measurements (described previously). With respect to 2D TR-PIV measurements, averaging was performed across 5 non-consecutive cycles at a fixed time instant (unlike "phase-averaging" of force measurements across the time period of the upstroke (clap stroke) or downstroke (fling stroke) phase, as in $\overline{C_{\mathrm{L,clap}}}$, $\overline{C_{\mathrm{D,clap}}}$, $\overline{C_{\mathrm{L,fling}}}$, $\overline{C_{\mathrm{D,fling}}}$). Following phase-averaging, 2D velocity vector fields were exported for calculating circulation (Γ) of the LEV and the TEV on a single wing of the imaged wing pair. Γ was calculated for all time points acquired during upstroke (clap stroke) and downstroke (fling stroke) separately using an in-house MATLAB script using Stokes' equation:

$$\Gamma = \int\int \omega_z dxdy \tag{5.9}$$

where ω_z represents the out-of-plane (z-component) of vorticity at the leading or trailing edges calculated from exported velocity vector fields and $dxdy$ represents the vorticity region for either the LEV or the TEV. For a particular pause condition, the maximum absolute values of ω_z (i.e., $|\omega_z|$) at both LEV and TEV of a bristled wing were identified. Similar to Ford et al. (2019) and Kasoju and Santhanakrishnan (2021*a*), a $10\%|\omega_z|$ high-pass cut-off was next applied to isolate the vortex cores on a solid or a bristled wing model (single wing or wing pair) for that pause condition. Γ of LEV or TEV was then calculated by selecting a region of interest (ROI) by drawing a box around a vortex core. A custom MATLAB script was used to automate the process of determining the ROI (Samaee et al., 2020). Essentially, we started with a small square box of 2 mm side and compared the Γ value with that of a bigger square box of 5 mm side. If the circulation values matched between the 2 boxes,

then we stopped further iteration. If the circulation values did not match between the 2 boxes, we increased the size of the smaller box by 3 mm and iterated the process. When calculating Γ of a specific vortex (LEV or TEV), we ensured that ω_z of the oppositely-signed vortex was zeroed out. For example, ω_z of the negatively-signed TEV was zeroed out when calculating the Γ of the positively-signed LEV on the right wing of a wing pair in downstroke (fling stroke). This allowed us to work with one particular vortex at a time and avoids contamination of the Γ estimation, if the box were to overlap with the region of the oppositely-signed vortex. Γ was determined for the right-hand side wing only, with the assumption that circulation for the left wing will be equivalent in magnitude but oppositely signed. Note that the left wing motion is symmetric to right wing making our assumption justifiable.

2D phase-locked PIV (2D PL-PIV) measurements were acquired for wing models along a spanwise plane (similar to 2D PL-PIV in Kasoju et al. 2018) located at 50% of bristle length (L_b), measured from the membrane to the leading edge of the wing (Fig. 5.2A). A double-pulsed, single-cavity Nd:YAG laser (Gemini 200-15, New Wave Research, Fremont, CA) with wavelength of 532 nm, maximum repetition rate of 15 Hz, and pulse width in the range of 3–5 ns was used for illumination in the PL-PIV measurements. A 10 mm focal length cylindrical lens was used to generate a thin laser sheet (thickness $\approx$ 3-5 mm). Raw PL-PIV images were acquired using a scientific CMOS (sCMOS) camera, with a maximum spatial resolution of 2600x2200 pixels at a frame rate of 50 frames/s, and a maximum pixel size of 6.5x6.5 microns (LaVision Inc., Ypsilanti, MI, USA). The 60 mm lens used in TR-PIV measurements was also used for PL-PIV measurements, and the camera was focused on seeding particles (hollow glass spheres, 10-micron diameter) along the laser plane (Kasoju et al., 2018). Raw image pairs were acquired at 7 time points in downstroke (fling stroke) at equally spaced time steps of 12.5% of stroke times (τ_f). The laser pulse separation between the images of an image pair were estimated based on 6-8 pixels of particle movement from one image to other image. For each wing model tested at Re_c=10,

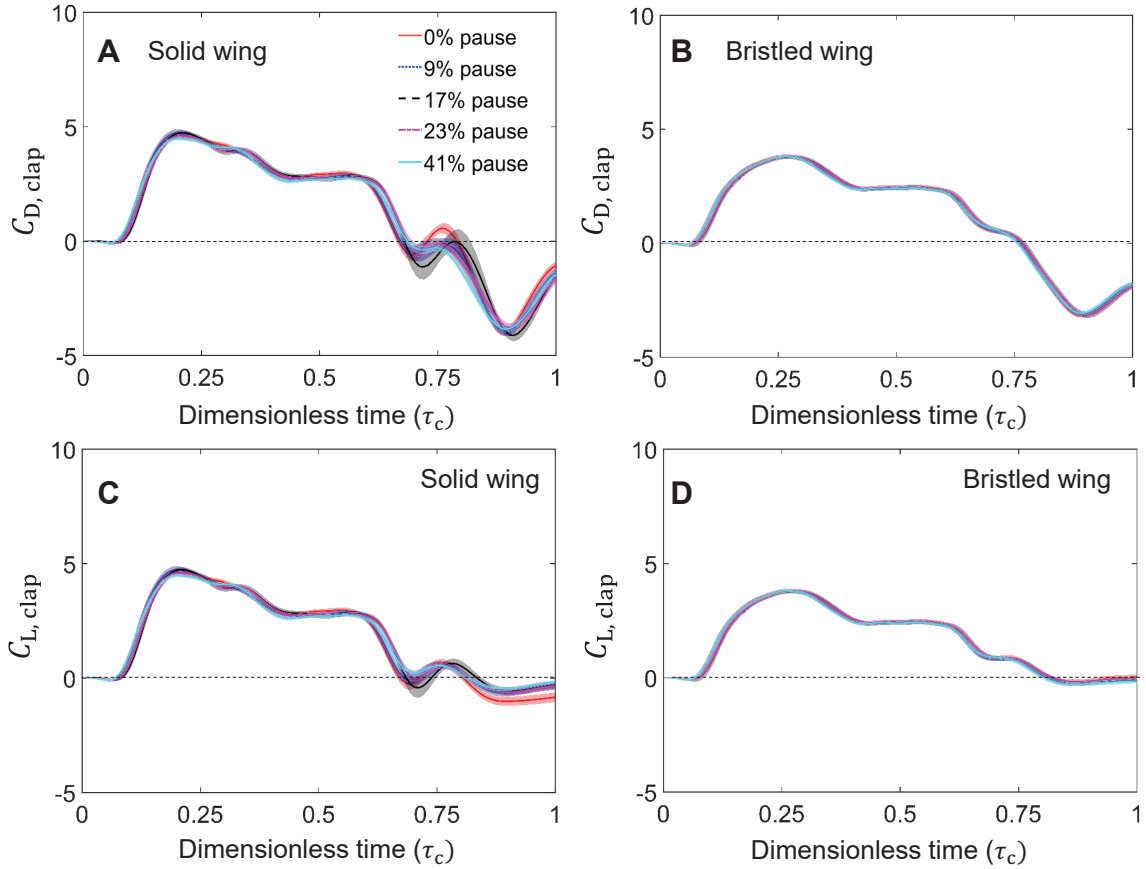

Figure 5.3: Force coefficients during upstroke (clap stroke) for a single wing at Re_c=10 with shading around each curve representing range of ± 1 standard deviation for that particular data (across 30 cycles). (A) and (C) show the drag coefficient (C_D) and lift coefficient (C_L), respectively, during upstroke (clap stroke) (τ_c) for the solid wing model at various pause times. (B) and (D) show the drag coefficient (C_D)and lift coefficient (C_L) respectively during upstroke (clap stroke) (τ_c) for the bristled wing model at various pause times.

5 image pairs were acquired at each time point in downstroke (fling stroke) cycle from 5 cycles of upstroke (clap stroke) and downstroke (fling stroke). These raw image pairs were processed using DaVis 8.3.0 software (LaVision GmbH, Göttingen, Germany) and then averaged for each time point. The post-processing parameters for 2D PL-PIV measurements were the same as those described earlier in 2D TR-PIV. The averaged processed images were exported to quantify the amount of fluid leaked through the bristles along the wing span. Cheer and Koehl (1987) estimated the amount of fluid leaking through a pair of cylinders using a non-dimensional index called leakiness (*Le*). Leakiness (*Le*) is defined as the ratio of the volumetric flow rate of fluid that is leaked through the inter-bristle gaps in

the direction opposite to wing motion under viscous (realistic) conditions to the volumetric flow rate for inviscid conditions, and is given by the equation:

$$Le = \frac{Q_{\text{viscous}}}{Q_{\text{inviscid}}} \tag{5.10}$$

where Q_{viscous} represents the volumetric flow rate leaked through the bristles under viscous condition calculated from the 2D PL-PIV measurements alog wing span, Q_{inviscid} represents the volumetric flow rate leaked through the bristles under no viscous resistance (inviscid flow) calculated based on the assumption that under no viscous resistance, all the flow leaks through the inter-bristle gap (Kasoju et al., 2018).

3 Results

3. 1 Force generation

Single wing during upstroke (clap stroke). For a single wing in upstroke (clap stroke) phase, both lift (C_{L}) and drag (C_{D}) coefficients (Fig. 5.3) were found to increase during early stages of clap, where the wing was made to accelerate during translation. Both the solid and bristled wing models were found to show little variation in force generation (C_{D} and C_{L}) during constant velocity translation (τ_{c}=0.35-0.7). During the end of upstroke (clap stroke) phase (τ_{c}=0.7-1), we observed both C_{L} and C_{D} to vary significantly in time, with change in direction of force generation. C_{L} and C_{D} for the single bristled wing were found to be lower compared to those of the single solid wing throughout the entire upstroke (clap stroke) phase. Interestingly, C_{D} did not reach zero at the end of upstroke (clap stroke) phase when the wings come to rest. This was presumably due to the wing wake not dissipating completely. Changing the pause time, which occurs after upstroke (clap stroke) phase, produced no significant variation in forces generated during the upstroke (clap stroke) phase.

Wing pair during upstroke (clap stroke). For the solid and bristled wing pair in upstroke (clap stroke) phase, the trends for C_{L} and C_{D} (Fig. 5.4) are consistent with previously pub-

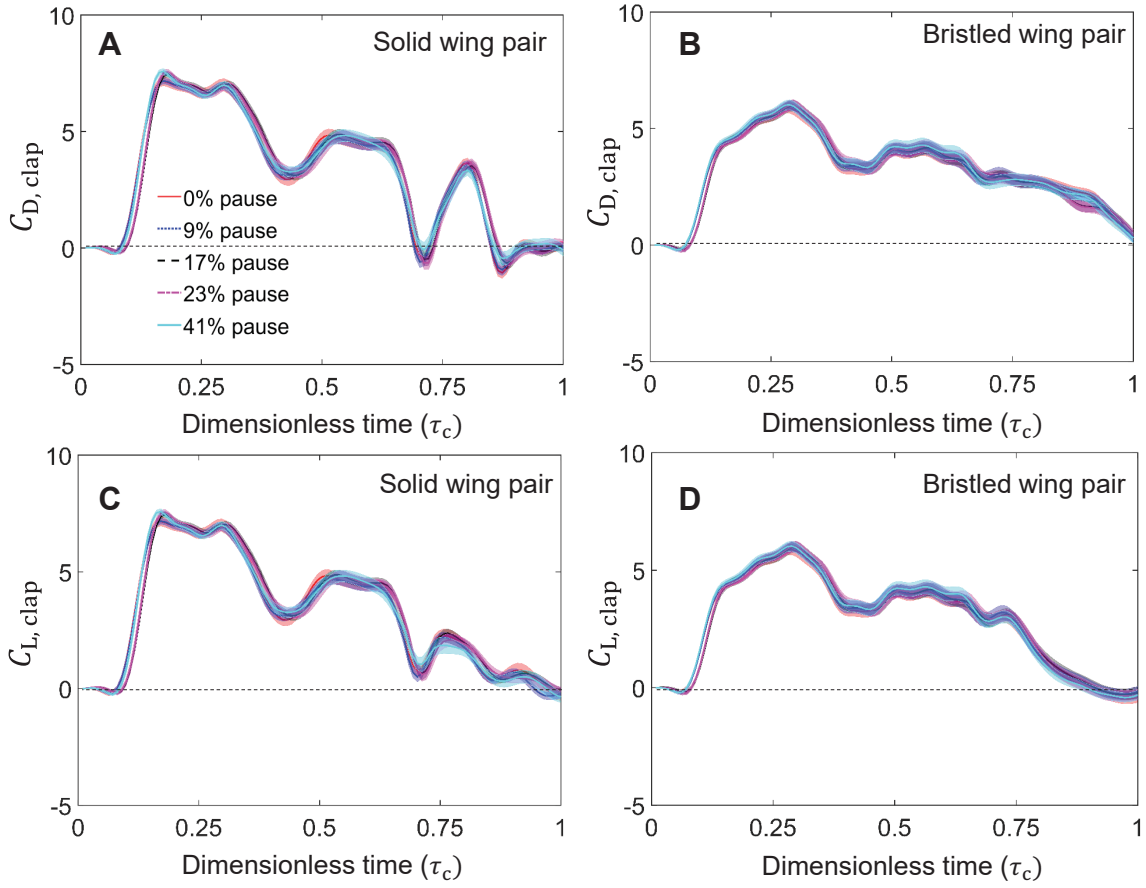

Figure 5.4: Force coefficients during upstroke (clap stroke) for a wing pair at Re_c=10 with shading around each curve representing range of ± 1 standard deviation for that particular data (across 30 cycles). (A) and (C) show the drag coefficient (C_D) and lift coefficient (C_L), respectively, during upstroke (clap stroke) (τ_c) for the solid wing pair at various pause times. (B) and (D) show the drag coefficient (C_D) and lift coefficient (C_L), respectively, during upstroke (clap stroke) (τ_c) for the bristled wing pair at various pause times.

lished data on solid and bristled wings (Santhanakrishnan et al., 2014; Kasoju et al., 2018; Ford et al., 2019). Starting from rest, the two wing-pairs were made to rotate and translate towards each other showing an increase in force coefficients in the initial acceleration phase. This is followed by constant velocity wing translation (τ_c=0.35-0.7), where both solid and bristled wing were found to show little variation in force generation (C_D and C_L) in time. During the end of upstroke (clap stroke) phase (τ_c = 0.7-1), we observed the drag coefficient (C_D) to vary significantly in time for the solid wing (Fig. 5.4A) compared to the bristled wing (Fig. 5.4B). This was presumably due to wing-wing interaction, as the wings approach close to each other at the end of upstroke (clap stroke) phase. However, lift

coefficients (C_L) for both solid and bristled wings (Fig. 5.4C,D) were found to drop during the end of upstroke (clap stroke) phase. Similar to the single wing, changing the pause time produced no variation in force generated during the upstroke (clap stroke) phase (occurring before the pause). Unlike the single wing, we observed both C_L and C_D to reach zero towards the end of upstroke (clap stroke) when the wings come to rest.

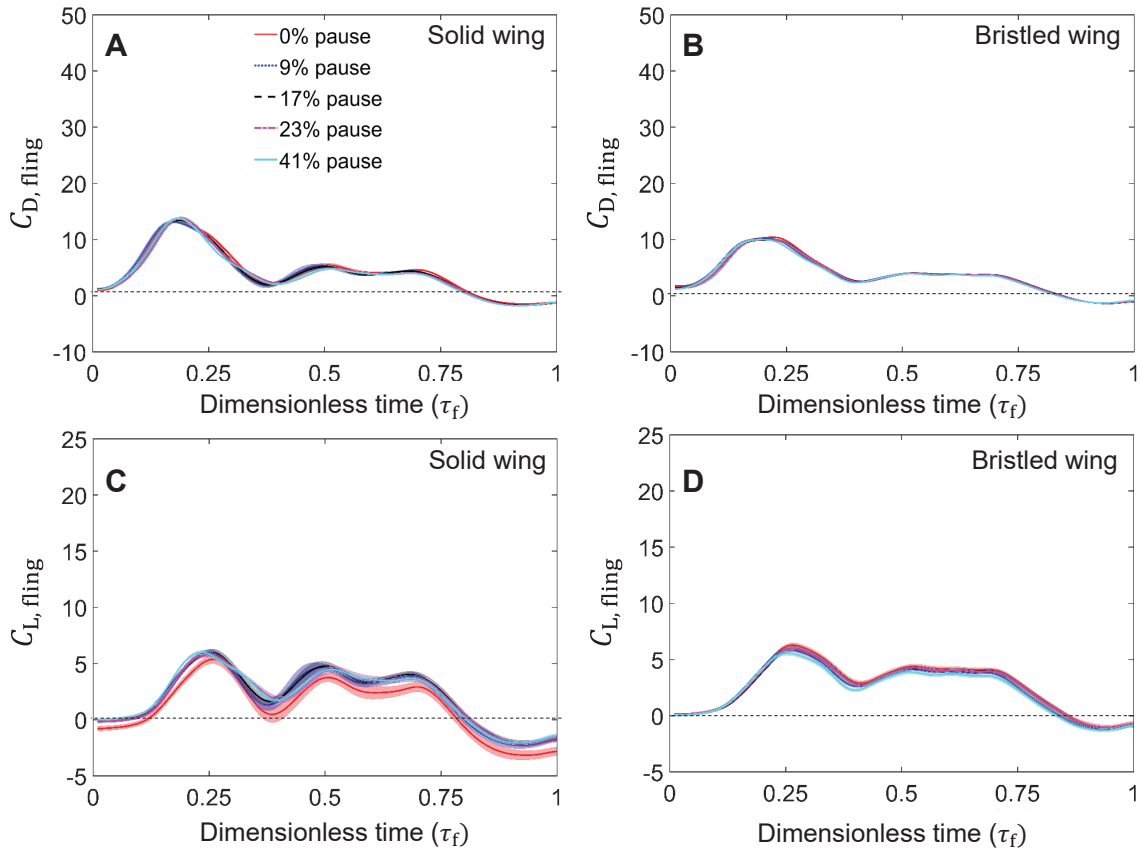

Figure 5.5: Force coefficients during downstroke (fling stroke) for a single wing at Re_c=10 with shading around each curve representing range of ± 1 standard deviation for that particular data (across 30 cycles). (A) and (C) show the drag coefficient (C_D) and lift coefficient (C_L), respectively, during downstroke (fling stroke) (τ_f) for the solid wing model at various pause times. (B) and (D) show the drag coefficient (C_D) and lift coefficient (C_L), respectively, during downstroke (fling stroke) (τ_f) for the bristled wing model at various pause times.

Single wing during downstroke (fling stroke). For a single wing (solid and bristled), C_D was found to peak during early stages of downstroke (fling stroke) (Fig. 5.5A,B), where the wings were accelerating when performing rotation and translation. For both the solid and

bristled wing, C_D mostly remained constant during constant velocity translation and decreased during deceleration. Peak drag coefficient for the solid wing was noticeably higher compared to the bristled wing. Varying pause time, which occurred before the start of fling, showed little to no variation in C_D for both the solid and bristled wings. Thus, pausing after upstroke (clap stroke) does not impact drag force generation on a single wing in downstroke (fling stroke).

In contrast to C_D, pausing the solid wing before the start of downstroke (fling stroke) resulted in noticeably changing C_L as compared to 0% pause condition (Fig. 5.5C). C_L for a single solid wing (Fig. 5.5C) was found to significantly vary during the entire downstroke (fling stroke) phase, with peak C_L occurring during early downstroke (fling stroke). Towards the end of downstroke (fling stroke) phase, we observed noticeable negative C_L owing to wing deceleration at a high angle of attack. C_L for a single bristled wing (Fig. 5.5D) was found to significantly vary during the entire downstroke (fling stroke) phase, such that peak C_L occurred during early fling, followed by nearly constant C_L during constant velocity translation and a subsequent drop in C_L towards the end of downstroke (fling stroke) when the wing starts to decelerate. In contrast to the solid wing, varying pause time for the single bristled wing resulted in no variation in C_L throughout the downstroke (fling stroke) phase.

Wing pair during downstroke (fling stroke). C_D was observed to peak during early stages of downstroke (fling stroke) for both solid and bristled wings (Fig. 5.6A,B), where the wings were accelerating when performing rotation and translation. This tremendous increase in drag coefficient during early stages of downstroke (fling stroke) was presumably due to wing-wing interaction. Interestingly, drag coefficients were found to drop for the rest of the downstroke (fling stroke) phase, when the wings moved farther apart. This clearly indicates the influence of wing-wing interaction on drag coefficient, and was also observed in several previous studies (Miller and Peskin, 2004, 2005; Arora et al., 2014; Santhanakrishnan et al., 2014; Jones et al., 2016; Kasoju et al., 2018; Ford et al., 2019). Peak C_D for

the bristled wing during downstroke (fling stroke) was significantly lower compared to the solid wing for any test condition tested in this study (Fig. 5.6A,B). Increasing the percentage of pause time before the start of downstroke (fling stroke) showed little drop in C_D. Unlike the single wing during downstroke (fling stroke) (Fig. 5.5B), increasing the pause time produced a more noticeable effect on drag force generation in two-winged downstroke (fling stroke).

Similar to C_D, C_L for both solid and bristled wings (Fig. 5.6C,D) were found to peak in the early stages of downstroke (fling stroke), showing the influence of wing-wing interaction. C_L was subsequently found to mostly remain constant and then drop during constant velocity translation and deceleration of the wing, respectively. Towards the end of downstroke (fling stroke) phase, both C_L and C_D were found to change their direction owing to wing deceleration. Similar to C_D, influence of changes in pause time were noticeable for C_L during downstroke (fling stroke). Similar to the single solid wing during downstroke (fling stroke, Fig. 5.5C), the solid wing pair showed noticeable change in C_L with varying pause time.

Single wing and wing pair during pause. Both C_D and C_L were found to remain constant throughout the pause period (see Fig. A.9. 3.1, A.9. 3.2 in supplementary material of **Appendix**). For a single wing (both solid and bristled), C_D was constant and positive-valued during the pause period. By contrast, C_D was found to be close to zero during the pause period of a wing pair (both solid and bristled wings; see Fig. A.9. 3.1 in supplementary material of **Appendix**). Irrespective of percentage of pause time, C_L was found to be close to zero during the entire pause period (see Fig. A.9. 3.2 in supplementary material of **Appendix**). In addition to non-dimensional force plots presented (see Fig. A.9. 3.1, A.9. 3.2 in supplementary material of **Appendix**), dimensional drag forces (F_D) and dimensional lift forces (F_L) for the entire cycle are provided in the supplementary material in Fig. A.9. 3.3 and A.9. 3.4, respectively. The time-varying trends in dimensional forces (F_L, F_D) for a given condition (i.e., varying pause time for solid/bristled wing; solid/bristled wing

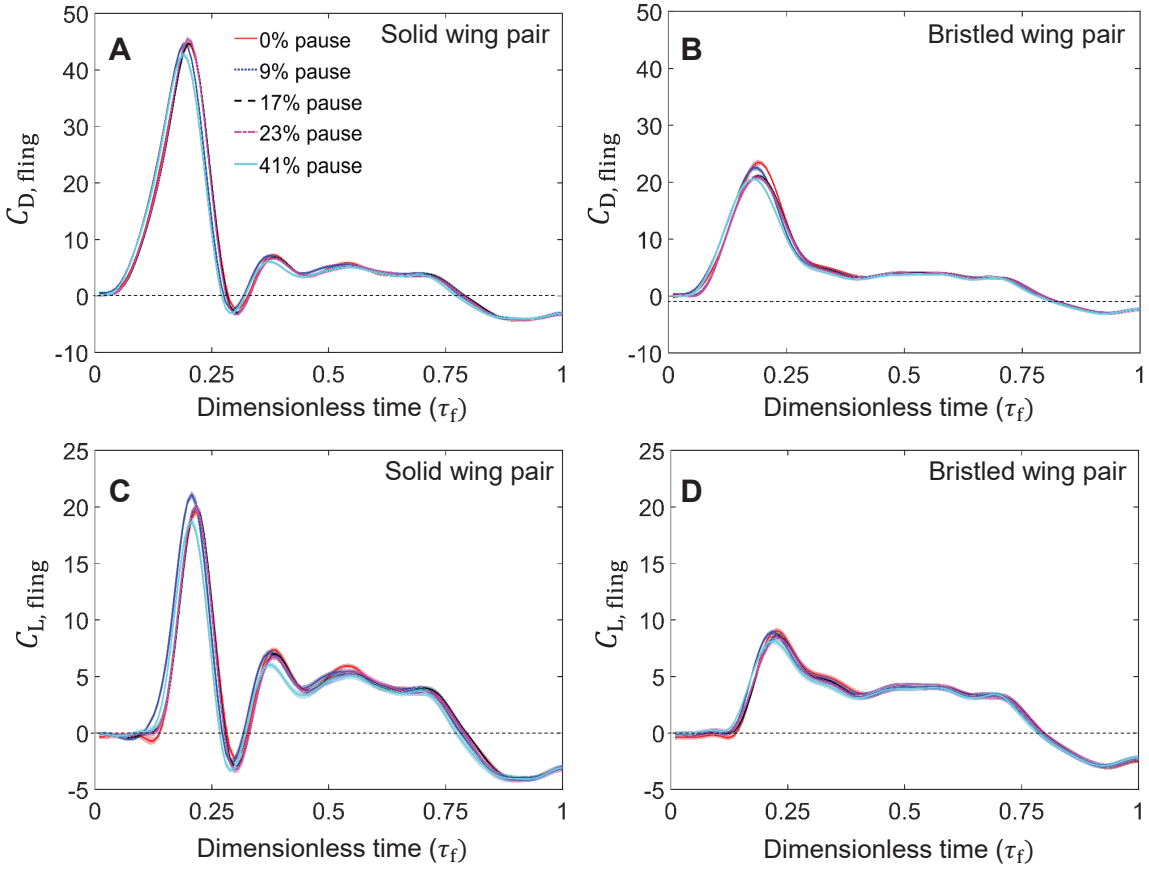

Figure 5.6: Force coefficients during downstroke (fling stroke) for a wing pair at Re_c=10 with shading around each curve representing range of ± 1 standard deviation for that particular data (across 30 cycles). (A) and (C) show the drag coefficient (C_D) and lift coefficient (C_L), respectively, during downstroke (fling stroke) (τ_f) for the solid wing pair at various pause times. (B) and (D) show the drag coefficient (C_D) and lift coefficient (C_L), respectively, during downstroke (fling stroke) (τ_f) for the bristled wing pair at various pause times.

pair) were unchanged compared to dimensionless force coefficients (C_L, C_D) for the same condition.

Phase-averaged force coefficients. To obtain an overall understanding of the changes in force coefficients with pause time in between upstroke (clap stroke) and downstroke (fling stroke) phase, we examined the magnitudes of phase-averaged force coefficients during upstroke (clap stroke, $\overline{C_{D,clap}}$ and $\overline{C_{L,clap}}$) and downstroke (fling stroke), $\overline{C_{D,fling}}$ and $\overline{C_{L,fling}}$) separately (Fig. 5.7 and 5.8).

We first discuss findings on a single wing shown in Fig. 5.7. Changes in pause time showed no influence on phase-averaged force coefficients ($\overline{C_{D,clap}}$ and $\overline{C_{L,clap}}$) for both the

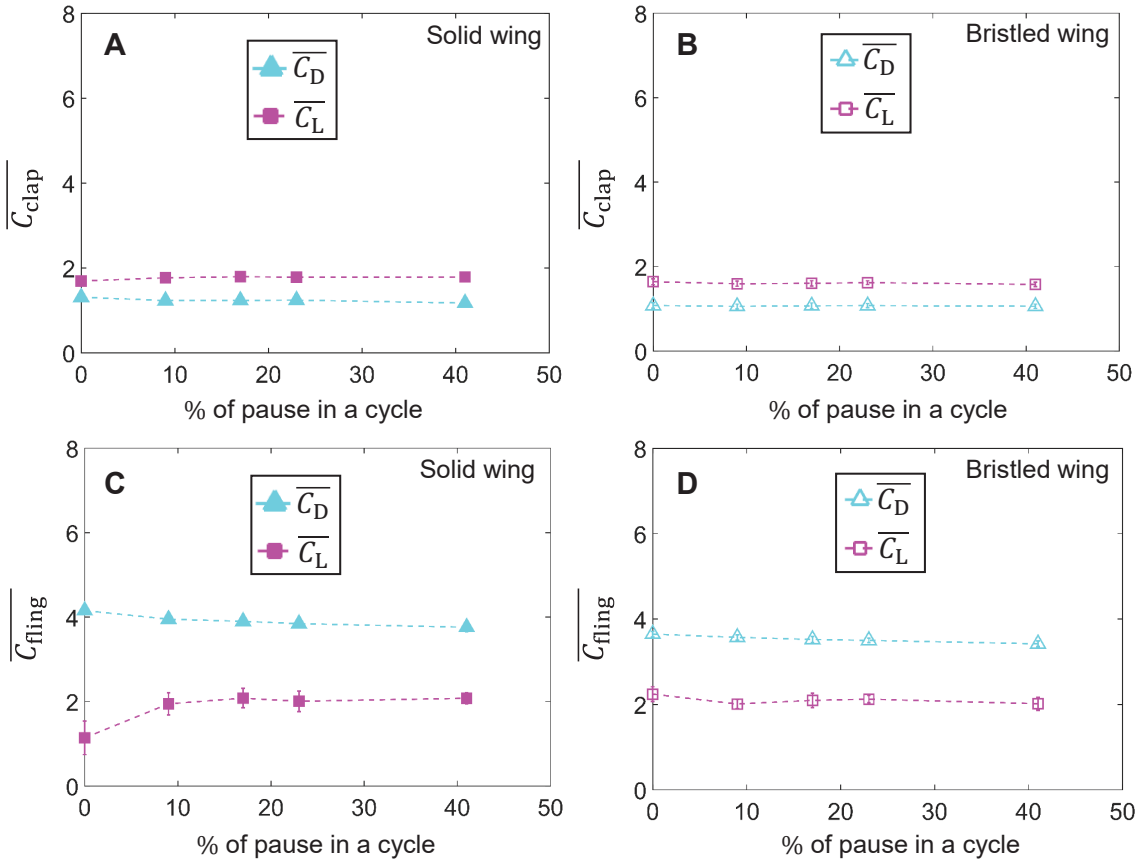

Figure 5.7: Magnitudes of phase-averaged force coefficients during upstroke (clap stroke) and downstroke (fling stroke) for a single wing at Re_c=10, presented separately for each phase with error bars representing ± 1 standard deviation for that particular data (across 30 cycles). (A) and (B) show the phase-averaged drag coefficient ($\overline{C_D}$) and phase-averaged lift coefficient ($\overline{C_L}$) for varying pause times during upstroke (clap stroke) for the solid and bristled wing models, respectively. (C) and (D) show $\overline{C_D}$ and $\overline{C_L}$ for varying pause times during downstroke (fling stroke) for the solid and bristled wing models, respectively. Solid markers represents solid wing model, hollow markers represents bristled wing model.

solid and bristled wings (Fig. 5.7A,B) during clap. Interestingly, the values of $\overline{C_{D,clap}}$ and $\overline{C_{L,clap}}$ for both solid and bristled wings were almost similar with bristled wing having lower values of $\overline{C_{D,clap}}$ and $\overline{C_{L,clap}}$ compared to solid wing. Also, due to significant negative drag (C_D) observed towards the end of upstroke (clap stroke) for a single wing configuration (solid and bristled), the phase-averaged drag coefficient ($\overline{C_{D,clap}}$) was found to be significantly decrease and $\overline{C_{D,clap}}$ was found to be noticeably lower compared to $\overline{C_{L,clap}}$ (Fig. 5.7A). During downstroke (fling stroke, Fig. 5.7C,D), changes in pause time also showed little to no influence on $\overline{C_{D,fling}}$ for both the solid and bristled wings. However, $\overline{C_{L,fling}}$ for the single

solid wing was found to increase with increasing pause time. While, $\overline{C_{\mathrm{L,fling}}}$ was found to increase from 0% pause to 9% pause and then showed no influence with increasing pause time. Similar to clap, the values of $\overline{C_{\mathrm{D,fling}}}$ for the solid and bristled wings were almost similar across all pause times. Interestingly, $\overline{C_{\mathrm{L,fling}}}$ for the bristled wing was found to be a little more or similar to that of the solid wing for all the percentages of pause time. We suspect this could be due to the added mass affect during varying wing motion (rotation and translation) affecting a solid wing (Kasoju et al., 2018; Cheng and Sun, 2016; Daniel, 1984) dominantly as compared to a bristled wing.

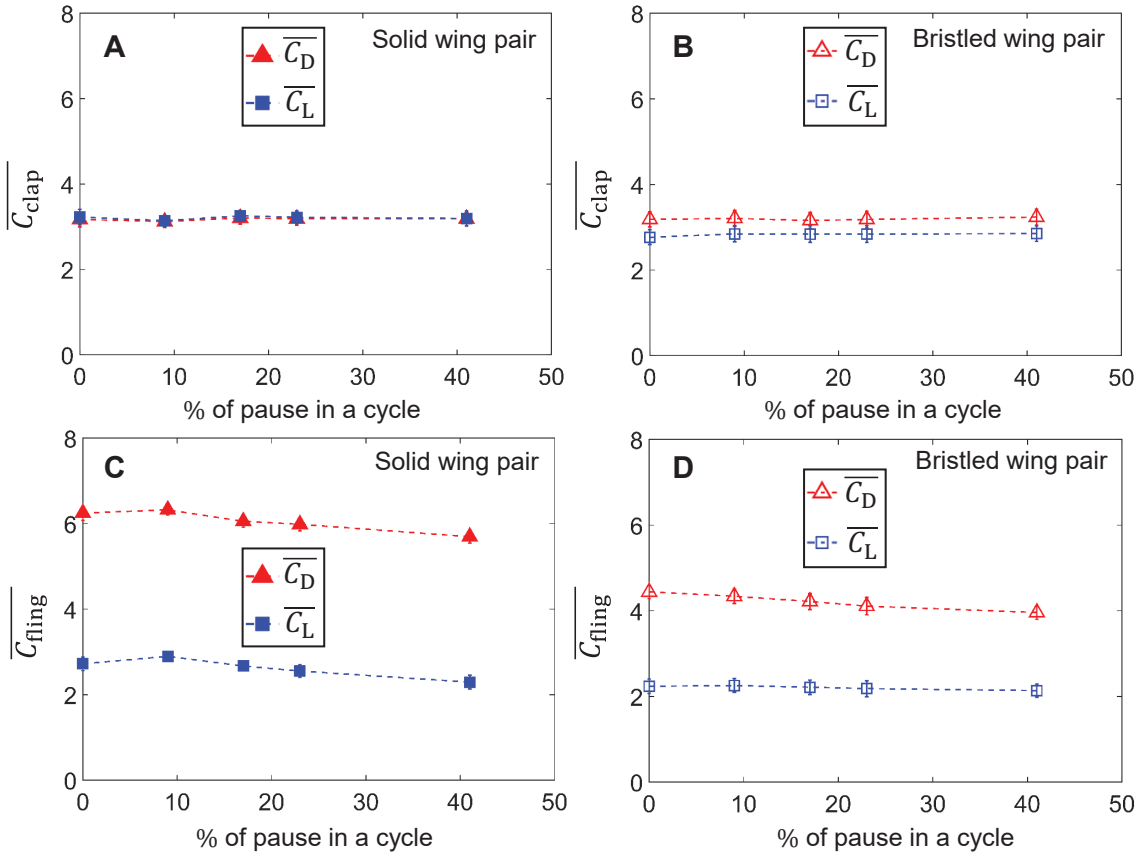

Figure 5.8: Magnitudes of phase-averaged force coefficients during upstroke (clap stroke) and downstroke (fling stroke) for wing pair at Re_c=10, presented separately for each phase with error bars representing ± 1 standard deviation for that particular data (across 30 cycles). (A) and (B) show the phase-averaged drag coefficient ($\overline{C_{\mathrm{D}}}$) and phase-averaged lift coefficient ($\overline{C_{\mathrm{L}}}$) for varying pause times during upstroke (clap stroke) for the solid and bristled wing pair, respectively. (C) and (D) show $\overline{C_{\mathrm{D}}}$ and $\overline{C_{\mathrm{L}}}$ for varying pause times during downstroke (fling stroke) for the solid and bristled wing pairs, respectively. Solid markers represents solid wing model, hollow markers represents bristled wing model.

We next discuss phase-averaged force coefficients on wing pairs as shown in Fig. 5.8. Changes in pause time showed no influence on phase-averaged force coefficients during upstroke (clap stroke, $\overline{C_{\mathrm{D,clap}}}$ and $\overline{C_{\mathrm{L,clap}}}$) for both the solid and bristled wing pairs (Fig. 5.8A,B). Similar to the single solid wing (Fig. 5.7A,B), the values of $\overline{C_{\mathrm{D,clap}}}$ and $\overline{C_{\mathrm{L,clap}}}$ for both the solid and bristled wing pairs were almost similar. For the solid wing pair during downstroke (fling stroke, Fig. 5.8C), increasing pause time decreased $\overline{C_{\mathrm{D,fling}}}$ and $\overline{C_{\mathrm{L,fling}}}$ noticeably. For the bristled wing pair during downstroke (fling stroke, Fig. 5.8D), increasing pause time showed small decrease in $\overline{C_{\mathrm{D,fling}}}$, while there was no variation in $\overline{C_{\mathrm{L,fling}}}$. $\overline{C_{\mathrm{D,fling}}}$ for the solid wing pair was greater than $\overline{C_{\mathrm{D,fling}}}$ of the bristled wing pair across all pause times. In addition, $\overline{C_{\mathrm{L,fling}}}$ showed little variation between the solid and bristled wing pairs at all pause times.

3. 2 Chordwise flow fields

Phase-averaged force coefficients ($\overline{C_{\mathrm{D}}}$ and $\overline{C_{\mathrm{L}}}$) showed little to no variation between solid and bristled wing models during upstroke (clap stroke) for both the single wing and wing pair configurations, and the flow structures were also essentially similar when comparing the solid and bristled wing models. The flow structures around solid wing pair during upstroke (clap stroke) were similar to those observed in our previous study (Kasoju et al., 2018) and are thus not shown here. Also, the flow structures for the single solid wing during upstroke (clap stroke) were similar in trend to that of the solid wing pair but with different vortex strengths.

Similar to clap, flow around a single wing (or a wing pair) during downstroke (fling stroke) showed identical trends when comparing solid and bristled wings (or wing pairs). Both the LEV and TEV were found to increase in strength during early stages of downstroke (fling stroke, Fig. 5.9-5.10) and later found to decrease in strength, with vorticity being diffused into the fluid medium surrounding the wing. The strength of the LEV and TEV of the single bristled wing in downstroke (fling stroke) was less than or similar to that of the

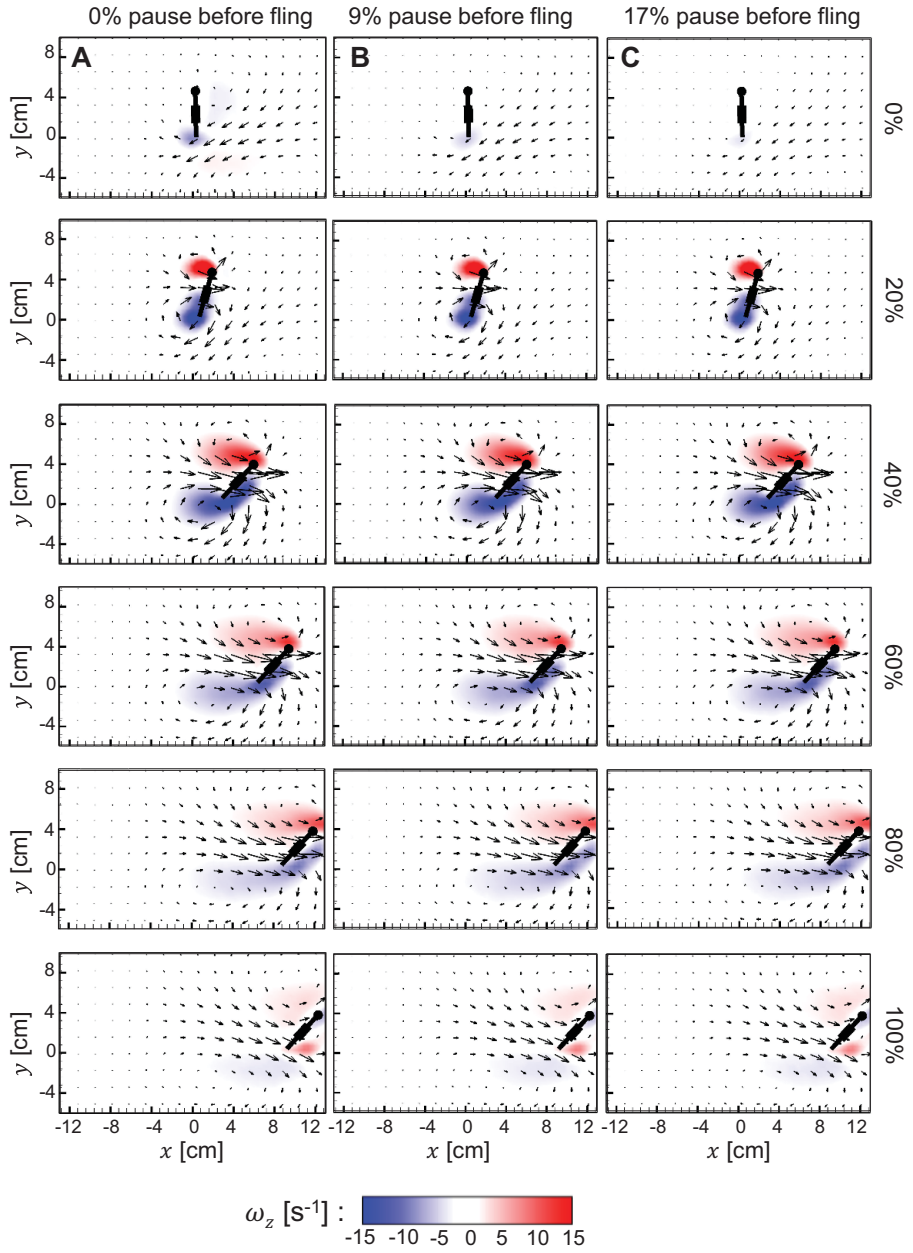

Figure 5.9: Velocity vector fields overlaid on out-of-plane z-vorticity (ω_z) contours for the single bristled wing during downstroke (fling stroke) at Re_c=10 for various pause times: (A) 0%, (B) 9%, (C) 17% of cycle time. For each pause condition, 6 timepoints (0%, 20%, 40%, 60%, 8-% and 100% of downstroke (fling stroke) time) are shown along each column (increasing time from top to bottom). Red colour represents counterclockwise vorticity, while blue represents clockwise vorticity.

bristled wing pair. Interestingly, just before the start of downstroke (fling stroke) for 0% pause case, we observed the formation of a wake with low vorticity in the fluid medium surrounding the wing (for both the single wing and wing pair configurations). This was most likely remnant of the wake generated from the upstroke (clap stroke) phase that was just completed.

3. 3 LEV and TEV circulation

Single wing during upstroke (clap stroke). We examined the strength of the flow structures by calculating LEV circulation (Γ_{LEV}) and TEV circulation (Γ_{TEV}) of the single wing models (solid and bristled) during upstroke (clap stroke, Fig. 5.11A,B) and during downstroke (fling stroke, Fig. 5.11C,D). Both Γ_{LEV} and Γ_{TEV} followed the same trend in time during upstroke (clap stroke) (except towards the end) when comparing solid (Fig. 5.11A) and bristled (Fig. 5.11B) wings. Near the end of clap, Γ_{LEV} of the single solid wing dropped close to zero unlike that of the single bristled wing. The magnitude of Γ_{LEV} during upstroke (clap stroke) for the single bristled wing model was slightly lower as compared to that of the solid wing. However, the magnitude of Γ_{TEV} during upstroke (clap stroke) for the single bristled wing was similar to that of the solid wing. Therefore, we can expect that the net circulation (i.e., $|\Gamma_{LEV}|$-$|\Gamma_{TEV}|$) for the solid wing would be a little greater than that of the bristled wing. These circulation results are in agreement with the larger lift generation during upstroke (clap stroke) for the single solid wing (Fig. 5.3C) as compared to the single bristled wing (Fig. 5.3D). Changing the pause time showed no variation in Γ_{LEV} and Γ_{TEV} during upstroke (clap stroke) for both the solid and bristled wings.

Single wing during downstroke (fling stroke). Γ_{LEV} and Γ_{TEV} for both the solid and bristled wings were found to increase during early stages of fling, remain constant during constant velocity translation and later decrease in time during wing deceleration (Fig. 5.11C,D). Compared to the solid wing, both Γ_{LEV} and Γ_{TEV} were lowered in the bristled wing. With increasing pause time, Γ_{LEV} for both the solid and bristled wings were found to

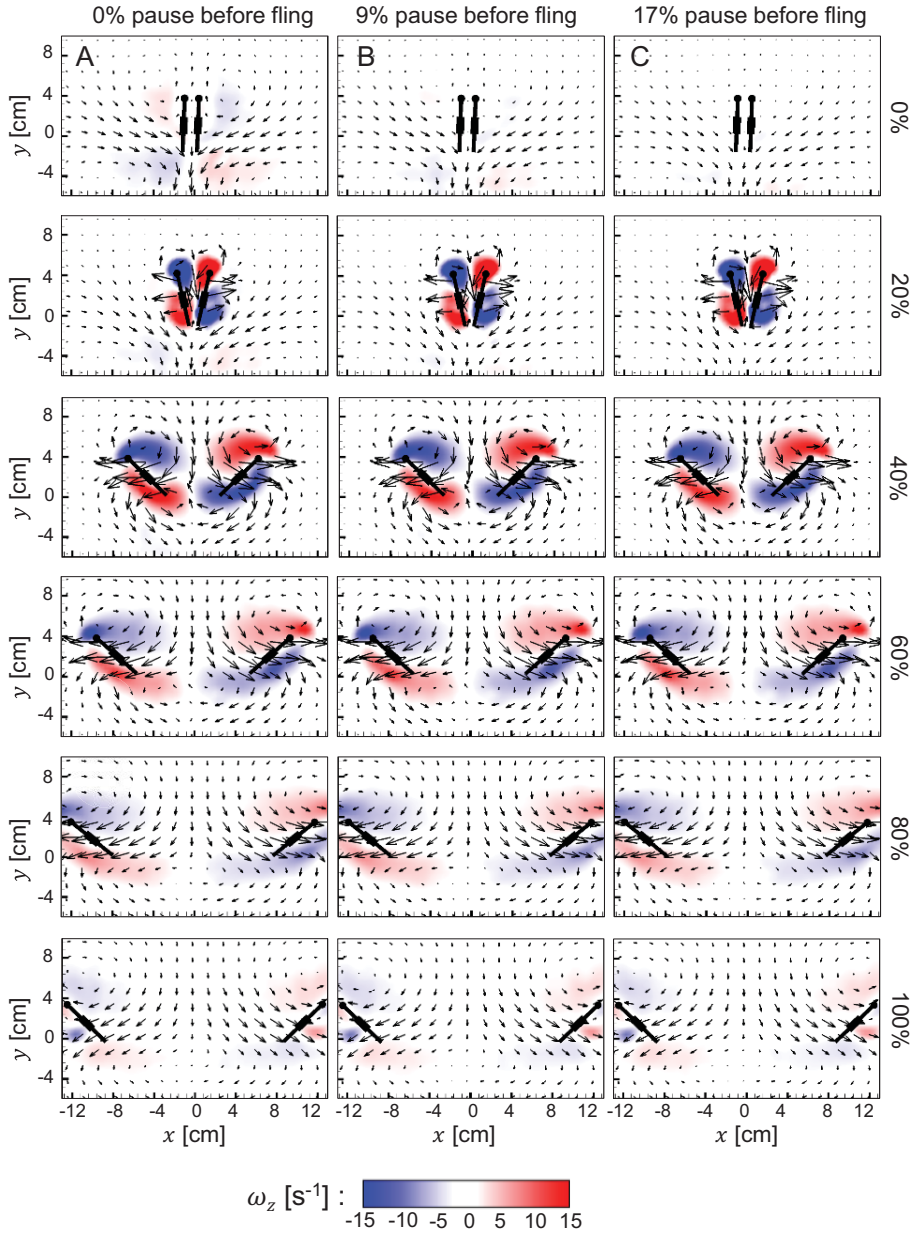

Figure 5.10: Velocity vector fields overlaid on out-of-plane z-vorticity (ω_z) contours for the bristled wing pair during downstroke (fling stroke) at Re_c=10 for various pause times: (A) 0%, (B) 9%, (C) 17% of cycle time. For each pause condition, 6 timepoints (0%, 20%, 40%, 60%, 8-% and 100% of downstroke (fling stroke) time) are shown along each column (increasing time from top to bottom). Red colour represents counterclockwise vorticity, while blue represents clockwise vorticity.

marginally decrease while Γ_{TEV} was unchanged. The net circulation over the wing (i.e., $|\Gamma_{LEV}| - |\Gamma_{TEV}|$) is thus expected to marginally decrease with increasing pause time in both the solid and bristled wing models. This is in disagreement with the observed lift generation during downstroke (fling stroke) by a single solid wing (Fig. 5.5C), where increasing pause duration beyond 0% resulted in moderately increasing C_L. Increasing pause time did not alter $C_{L,fling}$ of a single bristled wing (Fig. 5.5D), which is also in disagreement with the marginal decrease expected in net circulation of the single bristled wing with increasing pause time. These discrepancies suggest that additional lift generation mechanisms (added mass effects, delayed stall) need to be considered during downstroke (fling stroke) (as opposed to circulatory lift) in both solid and bristled wing models.

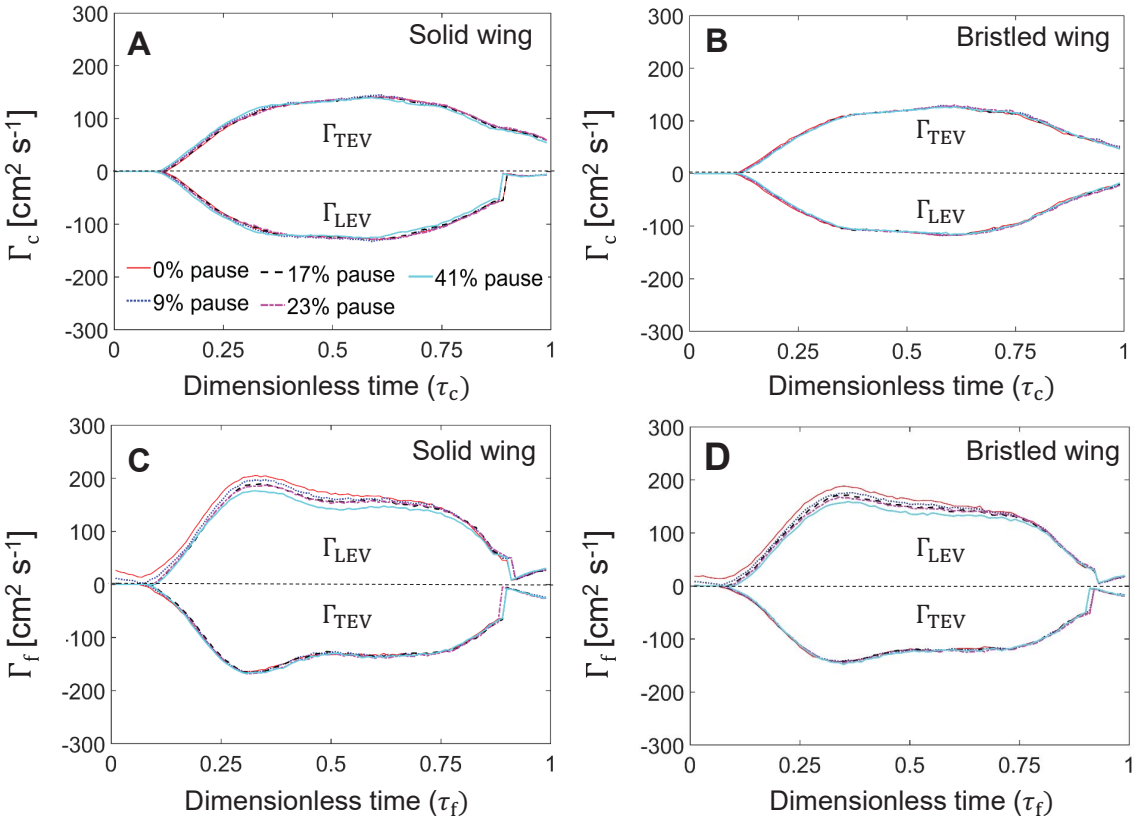

Figure 5.11: LEV AND TEV circulation of a single wing as a function of dimensionless time. (A) and (C) show circulation of the solid wing during upstroke (clap stroke) and fling, respectively. (B) and (D) show circulation of the bristled wing during upstroke (clap stroke) and fling, respectively.

Wing pair during upstroke (clap stroke). Both Γ_{LEV} and Γ_{TEV} of the solid wing pair (Fig. 5.12A)

and the bristled wing pair (Fig. 5.12B) followed the same time-varying trend during upstroke (clap stroke) as the corresponding trends of a single wing during upstroke (clap stroke, Fig. 5.11A,B). In addition, the magnitudes of Γ_{LEV} and Γ_{TEV} of the bristled wing pair during upstroke (clap stroke, Fig. 5.12B) were lower compared to those of the solid wing pair (Fig. 5.12A). This is expected to reduce the lift generated by the bristled wing pair, which is in agreement with the observed lift generation during upstroke (clap stroke, Fig. 5.4C,D). An interesting point to note is that in contrast to the single wing during upstroke (clap stroke, Fig. 5.11A,B), both Γ_{LEV} and Γ_{TEV} of wing pairs (Fig. 5.12A,B) were found to peak later in the upstroke (clap stroke) phase when the wings come in close proximity of each other (i.e., during wing-wing interaction). Overall, changing the pause time resulted in no variation in Γ_{LEV} and Γ_{TEV} during upstroke (clap stroke) of a wing pair (solid or bristled). This is in agreement with the lack of variation of $C_{L,clap}$ with pause time (Fig. 5.4C,D).

Wing pair during downstroke (fling stroke). For the solid wing pair in fling, Γ_{LEV} and Γ_{TEV} were found to steeply increase and decrease in time during early downstroke (fling stroke, Fig. 5.12C). While for the bristled wing pair, a gradual increase and decrease in both Γ_{LEV} and Γ_{TEV} was observed in early downstroke (fling stroke, Fig. 5.12D). Γ_{LEV} and Γ_{TEV} for the bristled wing pair (Fig. 5.12D) followed a similar trend to that of the single bristled wing (Fig. 5.11D). The magnitudes of Γ_{LEV} and Γ_{TEV} during downstroke (fling stroke) were lower for the bristled wing pair as compared to those of the solid wing pair, which is expected to reduce the lift generated by the bristled wing pair. This is in agreement with the observed lift generation during downstroke (fling stroke) of a wing pair (Fig. 5.6C,D). With increasing pause time, we observed little to no variation in Γ_{LEV} and Γ_{TEV} throughout downstroke (fling stroke). This 'non-effect' of pause time on circulation in downstroke (fling stroke) is not in agreement with the previously observed decrease in C_L with increasing pause time by a wing pair during downstroke (fling stroke, Fig. 5.6C,D). Similar to the discrepancies noted earlier in comparison of net circulation and lift generation of a single wing in fling, circulatory lift cannot adequately account for small changes in lift generation.

Non-circulatory lift mechanisms such as added mass effects, delayed stall and pressure distribution around the wing need to be considered to fully explain lift generation of a wing pair during fling, as has been noted in our recent study (Kasoju and Santhanakrishnan, 2021*a*).

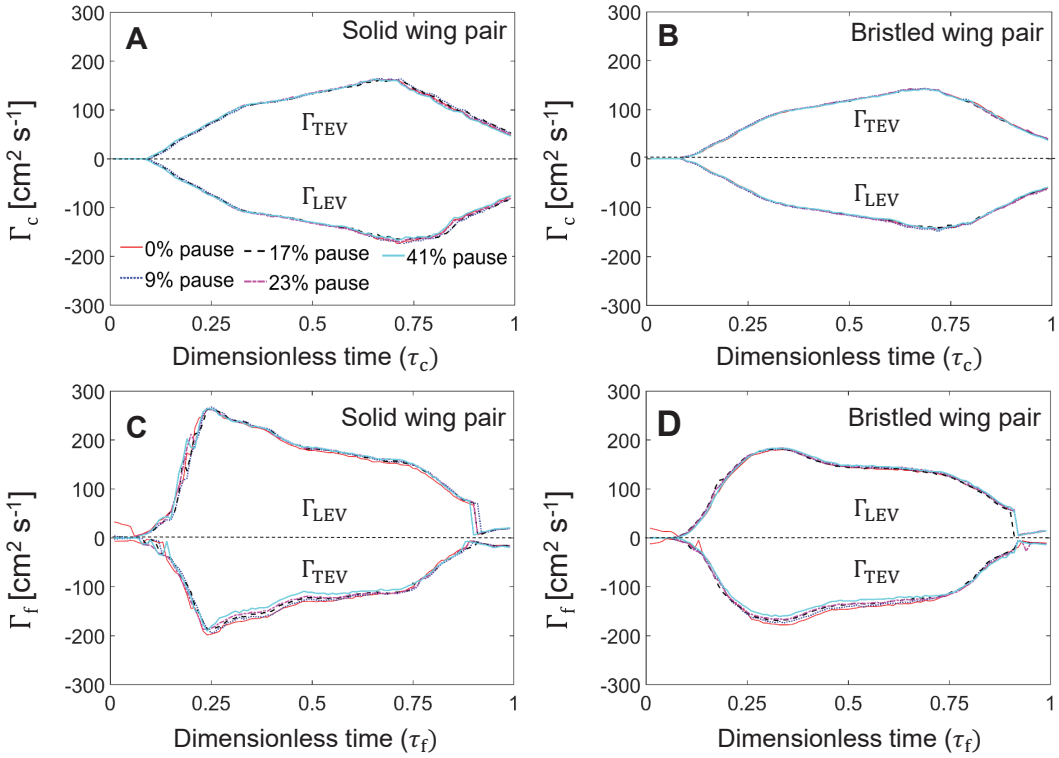

Figure 5.12: LEV AND TEV circulation of a wing pair as a function of dimensionless time. (A) and (C) show circulation of the solid wing pair during upstroke (clap stroke) and fling, respectively. (B) and (D) show circulation of the bristled wing pair during upstroke (clap stroke) and fling, respectively.

3. 4 Leakiness

Fluid leakage through the gaps between the bristles was characterized from 2D PL-PIV measurements using leakiness (*Le*) defined in equation (7.7). Since drag reduction was significantly higher for the bristled wing pair during downstroke (fling stroke) as compared to the single bristled wing during fling, we only examined *Le* of the bristled wing pair during downstroke (fling stroke, Fig. 5.13). Across all pause times, we observed *Le* to increase during early stages of fling, remain constant during constant velocity translation and then

decrease during deceleration. This trend of *Le* variation in time was similar to the time variation of C_D of the bristled wing pair in downstroke (fling stroke, Fig. 5.6B). Peak *Le* occurred in early downstroke (fling stroke) at τ_f=0.25, and decreased with increasing pause time from 0% to 23%. Interestingly, peak $C_{D,fling}$ also decreased with increasing pause time (Fig. 5.6B). Though it is intuitive to expect that C_D must decrease with increase in *Le*, this discrepancy suggests that *Le* is not the major mechanism underlying peak C_D reduction with increasing pause time in the bristled wing pair during downstroke (fling stroke). We expect that pressure distribution over each wing of the bristled wing pair Kasoju and Santhanakrishnan (2021*a*) would decrease with increasing pause time, thereby decreasing both *Le* and C_D simultaneously.

3. 5 Power requirement

To examine the amount of power required by a wing to overcome the drag generated when performing upstroke (clap stroke) and downstroke (fling stroke) motion, we calculated the power coefficient (C_P) for each pause duration from the single wing and wing pair force measurements (solid and bristled wings) using equation (5.7). The time-variation of C_P throughout a cycle, including clap, pause and downstroke (fling stroke) phases, is shown in the supplementary material (Fig. A.9. 3.5) of **Appendix**. For both solid and bristled wing models, peak C_P for the single wing was significantly lower compared to that of the wing pair, ostensibly on account of wing-wing interaction in the latter configuration. Similarly, C_P of the bristled wing was significantly lower compared to that of the solid wing in both the single wing and wing pair configurations. This was expected due to reduction in C_D during upstroke (clap stroke, Fig. 5.3B; Fig. 5.4B) and downstroke (fling stroke, Fig. 5.5B; Fig. 5.6B) by the bristled wing models as compared to solid wing models (Fig. 5.3A; Fig. 5.4A) and downstroke (fling stroke, Fig. 5.5A; Fig. 5.6A). As expected based on C_D during upstroke (clap stroke, Fig. 5.3A,B; Fig. 5.4A,B), changing pause time resulted in no impact on peak C_P during upstroke (clap stroke) phase for a given wing de-

sign (solid or bristled) and wing configuration (single wing or wing pair). For the single wing as well as the wing pair (solid or bristled), peak C_P during downstroke (fling stroke) decreased with increasing pause time (see Fig. A.9. 3.5 in supplementary material of **Appendix**). Peak C_P decrease during downstroke (fling stroke) with increasing pause time was more pronounced for wing pair configuration as compared to the single wing (solid or bristled), as expected from C_D for a wing pair in downstroke (fling stroke, see insensitivity to pause time for single wings in Fig. 5.5A,B compared to wing pairs in Fig. 5.6A,B).

4 Discussion

Using a dynamically scaled robotic platform to execute upstroke (clap stroke) and downstroke (fling stroke) kinematics in physical wing models, we measured aerodynamic forces and performed flow visualization on single wings and wing pairs (solid and bristled) with a pause duration following upstroke (clap stroke) and before the start of downstroke (fling stroke) at Re_c=10. The major results of this study are: 1) including a pause after the upstroke (clap stroke) phase does not impact magnitudes of phase-averaged force coefficients ($\overline{C_L}$, $\overline{C_D}$) and flow structures (i.e., Γ_{LEV}, Γ_{TEV}) generated during the upstroke (clap stroke) phase, irrespective of wing design (solid or bristled) and wing configuration (single wing or wing pair); 2) increasing pause time lowers peak force coefficients (C_L,C_D), phase-averaged force coefficients ($\overline{C_L}$, $\overline{C_D}$) and peak power coefficient (C_P) during fling; and 3) aerodynamic effects of including a pause after the upstroke (clap stroke) phase are minimal in a single wing (solid or bristled) as compared to a wing pair (solid or bristled). Collectively, these findings show that wing-wing interaction observed in flapping flight of tiny insects is necessary to realize any aerodynamic benefit (i.e., decreasing C_D, C_P) of pausing between upstroke (clap stroke) and downstroke (fling stroke).

Based on the high-speed video sequences of *E. Formosa* during hovering (Cheng and Sun, 2018) and forward flight (Cheng and Sun, 2021), we determined that these wasps pause for about 0.2 ms to 0.4 ms (estimated from "Top View" video sequences from 0.8

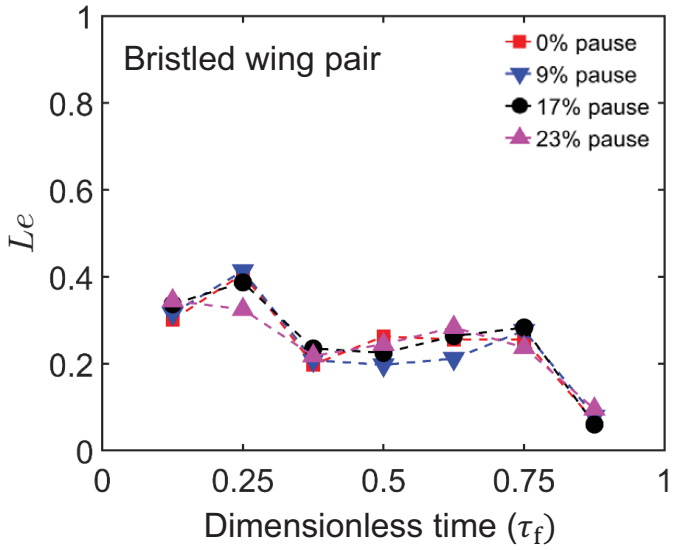

Figure 5.13: Leakiness (*Le*), representing non-dimensional flow reduction by a bristled wing during wing-wing interaction of the bristled wing pair, as a function of downstroke (fling stroke) time (τ_f).

ms to 1.2 ms in Cheng and Sun (2021)) before the start of downstroke (fling stroke). For an estimated cycle time of 2.8 ms, the pause duration of *E. formosa* is in the range of 7%-14% of their cycle. This range of pause duration is close to the range reported in our manuscript and by Ellington (1975). Further analyzing the high-speed video sequences of thrips (*Frankliniella occidentalis*) (Lyu et al., 2019*b*), we observed close to 8% pause between upstroke (clap stroke) and downstroke (fling stroke) from 3 flapping cycles. Collectively, these separate data sets show that multiple species of tiny flying insects tend to pause their wing motion before the start of downstroke (fling stroke). However, the influence of pause time on aerodynamic force generation have not been examined in previous studies of upstroke (clap stroke) and downstroke (fling stroke) at low Re_c (Miller and Peskin, 2004; Kasoju et al., 2018; Arora et al., 2014; Ford et al., 2019). In this study, a bristled wing model with total surface area equal to 33% of a geometrically similar solid wing area was tested. This drop in surface area of the wing should directly decrease the force generated by bristled wings. However, irrespective of pause time, the magnitudes of phase-averaged force coefficients during clap ($\overline{C_{\mathrm{D,clap}}}$ and $\overline{C_{\mathrm{L,clap}}}$) for a solid wing were

almost similar to that of bristled wing in both the single wing and wing pair configurations (Fig. 5.7A,B; Fig. 5.8A,B). We suspect that this close similarity in forces between the solid and bristled wings during clap is due to the blockage effect that is caused by the shear layers around the bristles at lower *G/D* ratios, as described in previous studies (Lee and Kim, 2017; Kasoju et al., 2018). This phenomenon causes the inter-bristle gap to be blocked due to shear layers formed around each bristle, thereby not allowing the fluid to pass through the gaps in between the bristles. This forces the fluid to move around the bristled wing (Davidi and Weihs, 2012), thereby generating forces that are mostly equivalent to a solid wing model. Furthermore, this similarity between the solid and bristled wing during the upstroke (clap stroke) phase (both single wing and wing pair configurations) was also evident in the circulation plots, where both $\Gamma_{c,LEV}$ and $\Gamma_{c,TEV}$ were almost similar between the solid wing and bristled wings (Fig. 5.11A,B; Fig. 5.12A,B).

In contrast to the upstroke (clap stroke) phase, phase-averaged lift coefficient during downstroke (fling stroke, $\overline{C_{L,fling}}$) at 0% pause was noticeably different between the solid and bristled wing models in both single wing (Fig. 5.7C,D) and wing pairs (Fig. 5.8C,D). With increasing pause time, $\overline{C_{L,fling}}$ of solid and bristled wings became similar in both the single wing and the wing pair configurations. In contrast to $\overline{C_{L,fling}}$, phase-averaged drag coefficient in downstroke (fling stroke, $\overline{C_{D,fling}}$) was essentially unchanged when comparing the single solid wing (Fig. 5.7C) to the single bristled wing (Fig. 5.7D) at a given pause time. However, $\overline{C_{D,fling}}$ noticeably decreased for both bristled wing pair (Fig. 5.8D) and solid wing pair (Fig. 5.8C). Further examination of the bristled wing pair during downstroke (fling stroke) showed that there was a 44% drop in peak C_D relative to that of the solid wing pair (from Fig. 5.6A,B) at 0% pause time. Interestingly, investigating the flow through the bristles using 2D PL-PIV and characterizing the leakiness (*Le*), we found that the peak leakiness was about 40% (Fig. 5.13), which is similar to drop in peak C_D of the bristled wing pair relative to the solid wing pair during downstroke (fling stroke) phase. We therefore conclude that leakiness is responsible for the observed drop in C_D during

downstroke (fling stroke) for the bristled wing pair.

From the Fig. 5.7C and Fig. 5.8C, we can see that during downstroke (fling stroke) at 0% pause time, phase-averaged drag coefficient ($\overline{C_D}$) of the solid wing pair was 50% greater than $\overline{C_D}$ of the single solid wing, while phase-averaged lift coefficient ($\overline{C_L}$) of the solid wing pair was 138% greater than $\overline{C_L}$ of the single solid wing. During downstroke (fling stroke) for non-zero pause times, $\overline{C_D}$ of the solid wing pair was 50-60% greater than $\overline{C_D}$ of the single solid wing, and $\overline{C_L}$ of the solid wing pair was 10-50% greater than $\overline{C_L}$ of the single solid wing. During upstroke (clap stroke) at 0% pause time (Fig. 5.7A, Fig. 5.8A), we observed $\overline{C_D}$ and $\overline{C_L}$ of the solid wing pair were 142% and 92% greater than those of the single solid wing, respectively. For non-zero pause times during upstroke (clap stroke), $\overline{C_D}$ of the solid wing pair was 153-172% greater than $\overline{C_D}$ of the single solid wing; and $\overline{C_L}$ of the single solid wing pair was 77-79% greater than $\overline{C_L}$ of the single solid wing.

We compared our solid wing findings to those reported by Miller and Peskin (2005) for similar wing kinematics and Reynolds number. Miller and Peskin (2005) considered 50% overlap between rotation and start of translation, which was lower than the 100% overlap considered in this study. They reported 10%-40% increase in average lift coefficient of a solid wing pair compared to that of a single solid wing during downstroke (fling stroke). Subsequent studies (Arora et al., 2014; Kasoju and Santhanakrishnan, 2021*a*) have shown that increasing the overlap between rotation and start of translation of a solid wing pair increases average force coefficients during downstroke (fling stroke). We also observed larger increase in negative lift coefficient ($C_{L,\text{fling}}$) during downstroke (fling stroke) of the single solid wing for 0% pause time as compared to other pause times (Fig. 5.5C). This large negative C_L contributed to a significant drop in $\overline{C_L}$ of the single solid wing for 0% pause time. The cause of negative lift is likely due to added mass effects experienced during wing deceleration toward the end of downstroke (fling stroke). Surprisingly, Miller and Peskin (2005) did not see any negative lift during end of downstroke (fling stroke) for both solid wing pair and single solid wing. It is important to note that whereas Miller and

Peskin (2005) performed 2D numerical simulations, the flow generated by our test facility was allowed to propagate in three-dimensions. We expect that the use of 100% overlap, negative lift generation and three-dimensionality of the flow field collectively contributed to the observed differences in $\overline{C_L}$ during downstroke (fling stroke) as compared to those reported by (Miller and Peskin, 2005).

In contrast to downstroke (fling stroke), Miller and Peskin (2005) observed negative lift coefficients ($C_{L,clap}$) being generated during upstroke (clap stroke) by both a solid wing pair and a single solid wing. However, we observed little to no negative $C_{L,clap}$ (Fig. 5.3C,Fig. 5.4C) during upstroke (clap stroke). This is likely due to Miller and Peskin (2005) prescribing wing rotation to start towards the end of upstroke (clap stroke) unlike the combined rotation and translation (i.e., 100% overlap) used in the present study.

Unlike the lift coefficient, Miller and Peskin (2005) observed drag coefficient (C_D) to remain positive during the entire upstroke (clap stroke) and downstroke (fling stroke) for both a solid wing pair and a single solid wing. However, we observed C_D to become negative during both upstroke (clap stroke) and downstroke (fling stroke) for both solid wing pair and single solid wing. As explained earlier when comparing C_L, differences in C_D between our study and those reported by Miller and Peskin (2005) can also be attributed to our use of 100% overlap in rotation and linear translation, added mass effects and three-dimensionality of the flow generated by the experimental test facility.

Similar to the single solid wing, we observed drag coefficients to become negative for the single bristled wing (Fig. 5.3B, Fig. 5.3D) towards the end of upstroke (clap stroke). However, we observed marginal to no negative lift for the single bristled wing during the end of upstroke (clap stroke). We suspect that this noticeable change in sign for drag coefficients is due to wing deceleration with varying angle of attack, which can contribute to significant added mass effect on the wings (Cheng and Sun, 2016). The contribution of added mass effects in driving lift force coefficient to negative for single bristled wing were likely minimal. Compared to the single solid wing, C_L and C_D for both the solid

wing pair and the bristled wing pair performing upstroke (clap stroke, Fig. 5.4) did not show noticeable negative values. This difference between the single wing and wing pair configurations suggests that added mass effects can be dampened by the opposing motion of the two wings of a wing pair. Similar to the upstroke (clap stroke), forces changed in sign during deceleration in the downstroke (fling stroke) of single wing models (both solid and bristled, Fig. 5.5) and wing pairs (solid wing pair and bristled wing pair, Fig. 5.6). Wing-wing interaction is negligible during deceleration of the solid wing pair or bristled wing pair, as the wings are farther apart. Across both the upstroke and downstroke, we can therefore conclude that wing-wing interaction decreases the contribution of added mass effects on both the single wing and wing pair models.

4. 1 Implications of varying pause time on cycle-averaged and peak coefficients

Fig. 5.14A,B shows cycle-averaged coefficients ($\overline{C_{\mathrm{L,net}}}$ and $\overline{C_{\mathrm{D,net}}}$) for the entire cycle (including upstroke (clap stroke) time, pause time and downstroke (fling stroke) time). Increase in pause time increases the entire cycle time. With increasing pause time, $\overline{C_{\mathrm{D,net}}}$ was found to decrease for both the solid wing pair and the bristled wing pair. By contrast, $\overline{C_{\mathrm{D,net}}}$ showed little variation with increasing pause time in both the single solid wing and the single bristled wing. With increasing pause time, $\overline{C_{\mathrm{L,net}}}$ was found to decrease for both single wing and wing pair configuration. With increasing duration of pause time, $\overline{C_{\mathrm{L,net}}}$ of the solid wing was found to reach values close to that of the bristled wing in both the single wing and wing pair configurations (Fig. 5.14A,B). Therefore, a significant reduction in cycle-averaged net force generation occurs with increasing pause time among wing pairs performing wing-wing interaction unlike a single wing (solid or bristled) where wing-wing interaction is absent. It must also be noted that while pausing for longer reduces $\overline{C_{\mathrm{D,net}}}$, there is a compromise associated with simultaneous reduction in $\overline{C_{\mathrm{L,net}}}$—i.e., a tiny insect would inevitably need to expend more energy to regain its vertical position with a longer

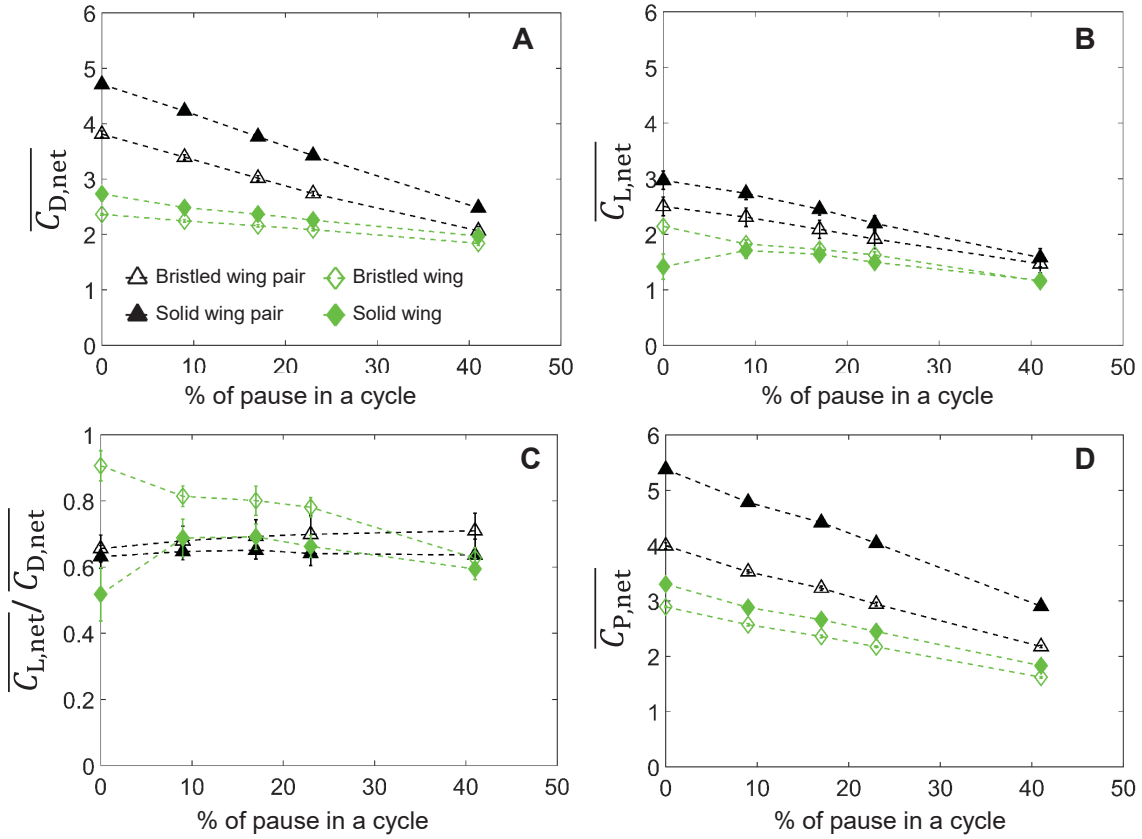

Figure 5.14: (A,B) Cycle-averaged net force coefficients ($\overline{C_{\mathrm{D,net}}}$, $\overline{C_{\mathrm{L,net}}}$), (C) ratio of cycle-averaged net lift over cycle-averaged net drag ($\overline{C_{\mathrm{L,net}}}/\overline{C_{\mathrm{D,net}}}$), and (D) Cycle-averaged net power coefficient ($\overline{C_{\mathrm{P,net}}}$) calculated over the entire cycle (upstroke (clap stroke) phase, pause time and downstroke (fling stroke) phase) across varying pause times. Legend is shown in part A. Solid markers represents solid wing model, hollow markers represents bristled wing model.

pause.

Further examining the cycle-averaged drag force coefficients ($\overline{C_{\mathrm{D,net}}}$, Fig. 5.14A), we observed $\overline{C_{\mathrm{D,net}}}$ for wing pair models (solid and bristled) to decrease at a faster rate with increasing pause time in comparison to $\overline{C_{\mathrm{D,net}}}$ variation with pause time for single wing models (solid and bristled). This reduction in the rate of decrease in $\overline{C_{\mathrm{D,net}}}$ with increasing pause time for single wing models is due to non-zero drag coefficients (C_{D}) for the single wing during the pause period (Fig. A.9. 3.1). In contrast to the single wing (both solid and bristled), we observed almost zero C_{D} for both solid and bristled wing pair during pause period. This suggests that wing-wing interaction acts like a dampener.

We examined the cycle-averaged net lift to cycle-averaged net drag ratio ($\overline{C_{\mathrm{L,net}}}/\overline{C_{\mathrm{D,net}}}$, Fig. 5.14C) as a measure of aerodynamic efficiency. We observed that the aerodynamic efficiency of solid and bristled wing pairs were essentially invariant with changing pause time (Fig. 5.14C). However, for the single bristled wing case, we observed $\overline{C_{\mathrm{L,net}}}/\overline{C_{\mathrm{D,net}}}$ to decrease with increasing pause time. For the single solid wing, $\overline{C_{\mathrm{L,net}}}/\overline{C_{\mathrm{D,net}}}$ was found to increase and then decrease with increasing pause time. These results potentially suggest that tiny insects that tend to pause their wing motion between upstroke (clap stroke) and downstroke (fling stroke) need not compromise their aerodynamic efficiency when doing so.

Ellington (1975) hypothesized that including a pause before the start of downstroke (fling stroke) could help the insects in elastic storage of high mechanical energy that would be needed to downstroke (fling stroke) the wings apart. Although elastic storage of energy in flight has not been examined for tiny insects such as thrips, a previous study by Dickinson and Lighton (1995) presented clear evidence that fruit flies need elastic mechanisms for efficient flight. Another study by Alexander (1995) suggested that wing muscles of many insects can function as springs and store energy for reuse in the next flapping stroke. Another means to achieve efficient flight is to have effective muscle efficiency, which requires larger metabolic energy consumption. It remains unknown at present as to whether thrips use elastic storage.

If we were to assume there is no elastic storage, tiny insects such as thrips require large muscle power to overcome severe viscous drag during the start of downstroke (fling stroke) or during braking. A non-dimensional estimate of the power required to overcome the drag (C_{P}) is presented in supplementary material (Fig. A.9. 3.5) of **Appendix**. While C_{P} did not vary with pause time during upstroke (clap stroke) for a given wing design and wing configuration, C_{P} decreased with increasing pause time during fling for both single wing and wing pair configurations. C_{P} was lower for the bristled wing and the bristled wing pair as compared to the equivalent configuration of the solid wings. In addition, increas-

ing the pause time resulted in a larger decrease of the cycle-averaged net power coefficient ($\overline{C_{P,net}}$, Fig. 5.14D) for the wing pair configurations as compared to the single wing configurations. Pausing effectively lowers the power required to clap wings together and fling them apart in both the solid and bristled wing pairs. A significant drop in $\overline{C_{P,net}}$ was observed for the bristled wing pair (as compared to the solid wing pair) at 0% pause time compared to 41% pause time. Therefore, bristled wing pairs benefit from larger power reduction at lower pause times.

To support the above comparisons made using statistically estimated (i.e., cycle-averaged) $\overline{C_{L,net}}$, $\overline{C_{D,net}}$ and $\overline{C_{P,net}}$, we examined peak values of force and power coefficients (Fig. 5.15) extracted from instantaneous measurements of C_L and C_D (Fig. 5.3-5.6), and direct calculations of time-varying C_P from instantaneous C_D using equation (5.7) provided in the supplementary material (Fig. A.9. 3.5) of **Appendix**. The peak values were extracted from C_L, C_D, C_P across the entire cycle consisting of upstroke (clap stroke) phase, pause and downstroke (fling stroke) phase. For a single wing (solid or bristled), we observed essentially no variation in peak drag coefficient ($C_{D,max}$, Fig. 5.15A) and peak lift coefficient ($C_{L,max}$, Fig. 5.15B) with increasing pause time. Irrespective of pause time, $C_{D,max}$ for the single solid wing was slightly greater than that of the single bristled wing. However, $C_{L,max}$ did not show variation between the single solid wing and the single bristled wing across all pause times. In contrast to the single wing configuration, we observed $C_{D,max}$ to decrease (by 4%-13%) with increasing pause time for the bristled wing pair. The largest reduction of $C_{D,max}$ for the bristled wing pair occurred at 17% pause time, and increasing the pause time further did not alter $C_{D,max}$. Compared to $C_{D,max}$, we observed smaller reduction (by 1%-10%) of $C_{L,max}$ for the bristled wing pair with increasing pause time (Fig. 5.15B). For the solid wing pair, increasing the pause time resulted in little to no variation of both $C_{D,max}$ and $C_{L,max}$. For a given pause time, $C_{D,max}$ of the solid wing pair was significantly higher than the bristled wing pair. Compared to $C_{D,max}$ reduction between the solid and bristled wing pairs, $C_{L,max}$ reduction by the bristled wing pair (as compared to the solid wing pair)

was significantly lower (Fig. 5.15B). Overall, these observations are in agreement with results of previous studies (Kasoju et al., 2018; Ford et al., 2019) that have shown wing-wing interaction using bristled wings to provide larger drag reduction and smaller lift reduction when compared to solid wings.

For a single solid wing, $C_{P,max}$ increased slightly with increasing pause time (Fig. 5.15C). $C_{P,max}$ showed little to no variation with increasing pause time for a single bristled wing. With increasing pause time, $C_{P,max}$ for the bristled wing pair was significantly lowered (by 7%-17%) as compared to the corresponding reduction of $C_{P,max}$ of the solid wing pair (by 4%-8%). When collectively comparing both the single wing and wing pair configurations, the bristled wing pair provided the largest $C_{P,max}$ reduction with increasing pause time along with a small reduction in $C_{L,max}$.

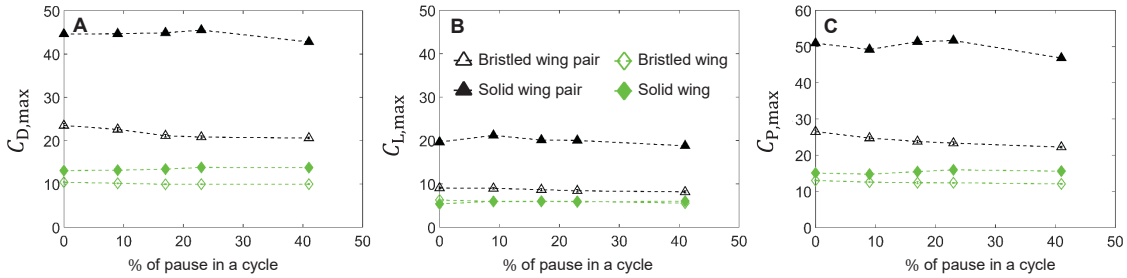

Figure 5.15: (A,B) Peak force coefficients ($C_{D,max}$, $C_{L,max}$) and (C) peak power coefficient ($C_{P,max}$) calculated over the entire cycle (upstroke (clap stroke) phase, pause time and downstroke (fling stroke) phase) across varying pause times. Legend is shown in part B. Solid markers represents solid wing model, hollow markers represents bristled wing model.

From the biological standpoint, tiny insects such as thrips show the obligatory use of wing-wing interaction during free flight (Lehmann et al., 2005). This strategy has been associated with increased lift generation in a challenging flow regime where viscous dissipation of kinetic energy is significant (Sane, 2003; Miller and Peskin, 2009; Sane, 2016). However, large drag forces are required to fling the wings apart at low Re_c Miller and Peskin (2005). Bristled wing structure characteristic of insects flying at this Re_c have been reported in several studies to offer beneficial drag reduction Santhanakrishnan et al. (2014); Jones et al. (2016); Kasoju et al. (2018); Ford et al. (2019). However, far less is known as

to how specific aspects of the wingbeat kinematics can further benefit flight at this low Re_c. Despite evidence of a pause incorporated at the end of upstroke (clap stroke) phase in *E. formosa* Ellington (1975) and in thrips (current study), the aerodynamic effects of including a pause between upstroke (clap stroke) and downstroke (fling stroke) have not been previously examined. We find that in addition to increase in lift force generation with wing-wing interaction, including a pause between the upstroke (clap stroke) and downstroke (fling stroke) phases can decrease the power required by reducing both cycle-averaged and peak drag coefficients (Fig. 5.14D, Fig. 5.15C). Arguably, using large pause times between upstroke (clap stroke) and downstroke (fling stroke) would be more beneficial by reducing the required power. However, increasing the pause time is also associated with reduction of the cycle-averaged net lift coefficient (Fig. 5.14B), and peak lift coefficient (Fig. 5.15B). Opting for a small pause period ($\sim$10% of cycle) between upstroke (clap stroke) and fling, as observed in the free take-off flight of thrips in this study, can be beneficial in reducing power consumption with a small compromise in lift force generation.

4. 2 Implications of varying pause time on flow generation

From 2D TR-PIV flow fields in the chordwise direction (Fig. 5.9, Fig. 5.10), we observed the formation of a wake with low vorticity in the fluid medium surrounding the wing (for both single bristled wing and bristled wing pair) just before the start of fling for 0% pause case. This was most likely a remnant of the wake generated from the upstroke (clap stroke) that was just completed. However, this wake was found to diminish for pause time of 9% and greater than 9%. We expect that waiting until the wake vorticity is fully diminished could decrease the drag forces acting on the wing which would further decrease the power requirement.

For bristled wing pair during downstroke (fling stroke), we observed a small decrease in phase-averaged drag coefficient ($\overline{C_{\mathrm{D,fling}}}$) with increasing pause time (Fig. 5.8D). However, $\overline{C_{\mathrm{L,fling}}}$ showed no variation with increasing pause time (Fig. 5.8D). Therefore, as

the wake diminishes with increasing pause time at the start of downstroke (fling stroke, Fig. 5.10), drag on the wing was found to decrease with no changes in lift generation. This drop in drag directly relates to drop in power required to fling the wings.

For a solid wing pair, we observed noticeable drop in both $\overline{C_{\mathrm{D,fling}}}$ and $\overline{C_{\mathrm{D,fling}}}$ with increasing pause time (Fig. 5.8C) during downstroke (fling stroke). The chordwise flow field for solid wing pair (see Fig. A.9. 3.6 in supplementary material of **Appendix**) during downstroke (fling stroke) were similar to that observed in bristled wing pair but with increased vortex strength. Therefore, the drop in phase-averaged force coefficients ($\overline{C_{\mathrm{D,fling}}}$) and ($\overline{C_{\mathrm{L,fling}}}$) is a consequence of the wake diminishing with increasing pause time, which can be directly related to drop in power required to fling the wings (equation 5.7).

Single bristled wing showed little to no variation in $\overline{C_{\mathrm{D,fling}}}$ and $\overline{C_{\mathrm{L,fling}}}$ with increasing pause time (Fig. 5.7D). The wing wake observed for a single bristled wing at start of downstroke (fling stroke) was significantly lower with a weak clockwise vortex formed at the tip of the trailing edge (Fig. 5.9). Therefore, for a single bristled wing there is no convincing evidence that introducing pause before the start of downstroke (fling stroke) would noticeably reduce the power.

Similar to single bristled wing, single solid wing showed little to no variation in $\overline{C_{\mathrm{D,fling}}}$ with increasing pause time (Fig. 5.7C) during downstroke (fling stroke). While $\overline{C_{\mathrm{L,fling}}}$ was found to increase from 0% pause to 9% pause and then showed no influence with increasing pause time. The chordwise flow field measurements for single solid wing during (see Fig. A.9. 3.6 in supplementary material of **Appendix**) downstroke (fling stroke) were similar to that observed in single bristled wing but with increased vortex strength. Formation of strong trailing edge vortex with no leading-edge vortex before the start of the downstroke (fling stroke) would significantly drop the lift force. This was also evident from phase-averaged lift coefficient $\overline{C_{\mathrm{L,fling}}}$ plot (Fig. 5.7C). Therefore, for a single solid wing introducing pause before the start of downstroke (fling stroke) showed minimal to no change in $\overline{C_{\mathrm{D,fling}}}$ with small increase in $\overline{C_{\mathrm{L,fling}}}$.

In contrast to downstroke (fling stroke), introducing pause after upstroke (clap stroke) did not show any noticeable changes in either chordwise flow fields or force measurements $\overline{C_{\mathrm{D,clap}}}$ and $\overline{C_{\mathrm{L,clap}}}$ during upstroke (clap stroke) for both single wing and wing pair configurations. Therefore, from the observed flow fields and aerodynamic force analysis measurements, we can confirm that pause after upstroke (clap stroke) can help to reduce the drag force during downstroke (fling stroke) for wing pair configuration and single solid wing, which in turn decreases the power requirement.

4. 3 Limitations

It is to be noted that the above results were based on rigid wing models. However, the wings of tiny insects are flexible (Miller and Peskin, 2009) and could have the capability to store energy from the wake in the fluid at the end of upstroke (clap stroke) and potentially use this stored energy at the start of downstroke (fling stroke) toward overcoming large drag forces. These hypotheses need to be further investigated with flexible bristled wing models in future studies. In addition, the bristled wings of tiny insects show broad variation in terms of bristle lengths on either side of the membrane. In this study, we used symmetric bristle lengths because changes to bristle length on each side of the membrane would likely impact aerodynamic force generation. Further, using asymmetric bristle lengths may also lead to three-dimensional flow fields during upstroke (clap stroke) and fling, which are not as well-resolved using planar PIV measurements as in this study. To minimize confounding effects from varying bristle lengths, we used a bristled wing design with equal bristle lengths on each side of the membrane. Further studies need to be conducted to understand the effect of including asymmetric bristle lengths on force generation and flow structures in upstroke (clap stroke) and downstroke (fling stroke).

5 Conclusions

This study showed that pause time between upstroke (clap stroke) and downstroke (fling stroke) has no significant influence on time-varying aerodynamic forces generated during the upstroke (clap stroke) phase (phase before the pause) for both the single wing and wing pair configurations (solid and bristled wing models) at a chord-based Reynolds number of 10. However, we observed variations in time-varying aerodynamic forces with increasing pause time during the downstroke (fling stroke) phase (phase after pause). Considering the force coefficients averaged across the entire cycle (upstroke (clap stroke) phase, pause time, downstroke (fling stroke) phase), both solid and bristled wing pairs were found to provide drag reduction with increasing pause time. Observations of the chordwise flow showed that introducing pause before the start of downstroke (fling stroke) led to the complete dissipation of the wake generated from upstroke (clap stroke). Diminishing the vorticity shed from the upstroke (clap stroke) helped in decreasing the drag force on the wing pair configuration (solid and bristled) during downstroke (fling stroke). With increasing pause time, the cycle-averaged net power coefficient was found to decrease significantly during wing-wing interaction of a wing pair as compared to that of a single wing. Collectively, our findings suggest that pausing before downstroke (fling stroke) can help to reduce the power consumption in clap and fling motion, with a small compromise in lift.

CHAPTER VI

SA 4: Flapping flight with bristled wings at low Reynolds numbers

1 Introduction

Tiny flying insect species of body lengths in the order of 1 mm are known to be highly populated winged insect species accounting to more than half of the entire insect population (Terry, 2001; Horridge, 1956; Dudley, 2002). However, little information is known about their flapping flight consisting of complex wing morphology and kinematics (Ellington et al., 1996; Sane, 2003; Miller and Peskin, 2004; Wang, 2005; Lentink and Dickinson, 2009; Santhanakrishnan et al., 2014; Sane, 2016; Lyu et al., 2019*b*). Apart from the biofluid mechanics standpoint, these tiny insects are known to be of agricultural, ecological and economic importance (Ullman et al., 2002; Jones, 2005; Santhanakrishnan et al., 2018). Most of the tiny flying insects such as thrips (Thysanoptera) and fairflies (Mymaridae) have shown to posses bristled or hairy wings comprising of a membrane with several hair like structures extending from the membrane (Horridge, 1956; Weis-Fogh, 1975; Ellington, 1980; Loudon and Koehl, 1994). These tiny insects fly at Reynolds number, Re in the order of 10 (Re is defined as the ratio of inertial forces to viscous forces, $Re = \rho U c/\mu$, where ρ and μ represents the density and viscosity of the fluid medium, U represents the mean wing tip velocity and c represents the chord length). Viscous forces are significant at such small scales and the hairy or bristled appendages are known to reduce the forces acting against the wing (drag) by allowing the fluid leakage through the gaps between the bristles (Santhanakrishnan et al., 2014; Jones et al., 2016; Kasoju et al., 2018; Ford et al., 2019; Kasoju and Santhanakrishnan, 2021*a*; Lee et al., 2020*b*). This flow in the gaps between the hairy appendages is Reynolds number dependent and is known to transition from rake like

behaviour to a paddle with decreasing Reynolds number (Loudon and Koehl, 1994; Cheer and Koehl, 1987; Koehl, 1995). The rake like behaviour from an array of bristles results in the decrease of drag force significantly, while paddle like behaviour allows them to behave more like a solid plate through strong viscous diffusion of shear layer around the solid surface of the bristles thereby forming a virtual fluid barrier in the gaps. This Reynolds number sensitive flow in the gaps between the bristles indicate that tiny insects such as thrips and fairyflies have the ability to vary aerodynamic force generation on the bristled wings when needed.

Many previous studies studies have investigated the aerodynamic performance of a bristled wing and reported significant aerodynamic benefits in terms of noticeable drag reduction at low Reynolds number flows during steady translation or simple rotational motions (Sunada et al., 2002; Davidi and Weihs, 2012; Barta and Weihs, 2006; Lee and Kim, 2017). However, there are significant challenges associated with generating lift at such low Reynolds number. Tiny insects are found to employ additional flight strategies to enhance lift generation, such as delayed stall mechanism, added mass, wing-wake interaction and wing-wing interaction (Sane, 2003; Dickinson et al., 1999; Wang, 2005; Usherwood and Ellington, 2002). The most well known mechanism for lift enhancement in tiny insects flying at Reynolds number in the order of 10 was the "clap and fling" mechanism proposed by Weis-Fogh (Weis-Fogh, 1973). During clap and fling, the insect bring their wings close together at the end of upstroke termed as 'clap' and then 'fling' the wings apart at the start of downstroke. While Weis-Fogh (Weis-Fogh, 1973) observed clap and fling mechanism in a tiny wasp *Encarsia Formosa*, later observation have shown that this is a very common mechanism in tiny insects such as thrips, green house white flies and parasitoid wasps (Weis-Fogh, 1975; Ellington, 1984*a*; Santhanakrishnan et al., 2014; Miller and Peskin, 2005, 2009; Jones et al., 2016). One of the early studies by Santhanakrishnan et al. (2014) in modeling bristled wing as porous wings has reported flow leakage through porous surfaces resulted in significant drag reduction during clap and fling motion. This

was again supported by Jones et al. (2016), who modelled bristles as an array of cylinders. Experimental studies by Kasoju et al. (2018) and Ford et al. (2019) reported that bristled wings increases the lift over drag ratio during clap and fling at low Reynolds numbers. Kasoju et al. (2018) experimentally visualized the inter-bristled flow and shear layer formation for varying gap width on a 3D bristled wing during both clap and fling which helped in realizing large leakiness through the gaps between the bristles for larger gap widths. While many previous studies have experimentally, numerically and theoretically investigated the importance of a full clap and fling mechanism in lift augmentation (Weis-Fogh, 1973; Lighthill, 1973; Spedding and Maxworthy, 1986; Birch et al., 2004; Miller and Peskin, 2005; Lehmann et al., 2005; Lehmann and Pick, 2007; Miller and Peskin, 2009; Arora et al., 2014; Cheng and Sun, 2019, 2021, 2018), very little information is available on partial clap and fling mechanism (Cheng and Sun, 2016, 2017; Lehmann et al., 2005). During a full clap and fling, wings on both sides of the abdomen come in close proximity along the entire wing surface. While during partial clap and fling, the wing tips come in close proximity and wings roots are farther ways from each other. Previous studies (Cheng and Sun, 2016, 2017; Lehmann et al., 2005) have reported that partial clap and fling is less effective (5%-7% increase) in lift augmentation compared to a full clap and fling (20%-70% increase). In addition to the above mentioned unsteady flapping strategies, tiny insect are found to use varying wing beat kinematics throughout their flapping cycle (Fry et al., 2005; Lyu et al., 2019*b*; Cheng and Sun, 2018, 2019, 2021, 2016).

High speed video recording of tiny insects flying have shown that these insects flap their wings back and forth in a non-horizontal stroke plane with a U-shaped upstroke at frequencies in the range of 200-1000 Hz (Lyu et al., 2019*b*; Santhanakrishnan et al., 2014; Weis-Fogh, 1973; Cheng and Sun, 2018). The mean wing tip velocity (U) is given by $U = 2\phi fR$, where ϕ represents stroke amplitude, f represents the stroke frequency, R represents the radius of wing from tip to root. For tiny insects with wing tip radius, R$\approx$0.5-4 mm, $f \approx$ 200-1000 and $\phi \approx 50^{\circ}$-180°, the corresponding Reynolds number (Re) are in the

order of 10-120 (Lyu et al., 2019*b*). As the *Re* decreases from 120 to 10, the shallower U-shaped upstroke observed in tiny insects is changed to a deep U-shape (Cheng and Sun, 2018). Therefore, within a small *Re* range of 10-120, we observed significant variation in wing beat kinematics. However, very little information is available on the aerodynamic implications of each of these wing kinematics at different Reynolds numbers.

In this study, using a dynamically scaled robotic model, we replicated the flapping wing kinematics motion relevant to tiny insects for varying pitch and revolution angle in an horizontal stroke plane. An elliptical bristled wing model was designed from within the biological relevent bristled wing design maintaining number of bristles, inter-wing gap to bristle diameter ratio (G/D) and solid membrane area to total wing area ratio ($A_\mathrm{m}/A_\mathrm{T}$). Using this developed dynamically scaled model, we examine a single and dual solid and bristled wing model performing partial clap and fling motion for three different real insect wing kinematics at *Re* = 10-120. The real wing kinematics of thrips *Frankliniella occidentalis*, leafminer *Liriomyza sativae* and fruitfly *Drosophila melanogaster* were taken from previously published studies (Lyu et al., 2019*b*; Cheng and Sun, 2016; Fry et al., 2005). For all these studies a constant initial wing tip to wing tip spacing was maintained. We examined the aerodynamic forces generated by a sing wing and wing pair (solid and bristled) at different Reynolds number (*Re* = 10-120) for varying wing kinematics. Two dimensional phase-locked particle image velocimetry (2D PL-PIV) was performed at various instances in time along the plane cutting the wing at mid span for all the *Re* and wing kinematics for a single solid and single bristled wing. This will help in examining the implications of wing circulation on force generation on a solid and bristled wing model.

2 Materials and methods

2. 1 Flapping robotic model

We developed a dynamically scaled robotic model to replicate the back and forth motion of an insect wing in three dimensions for varying pitch (ψ) and revolution angle (θ_rev) in

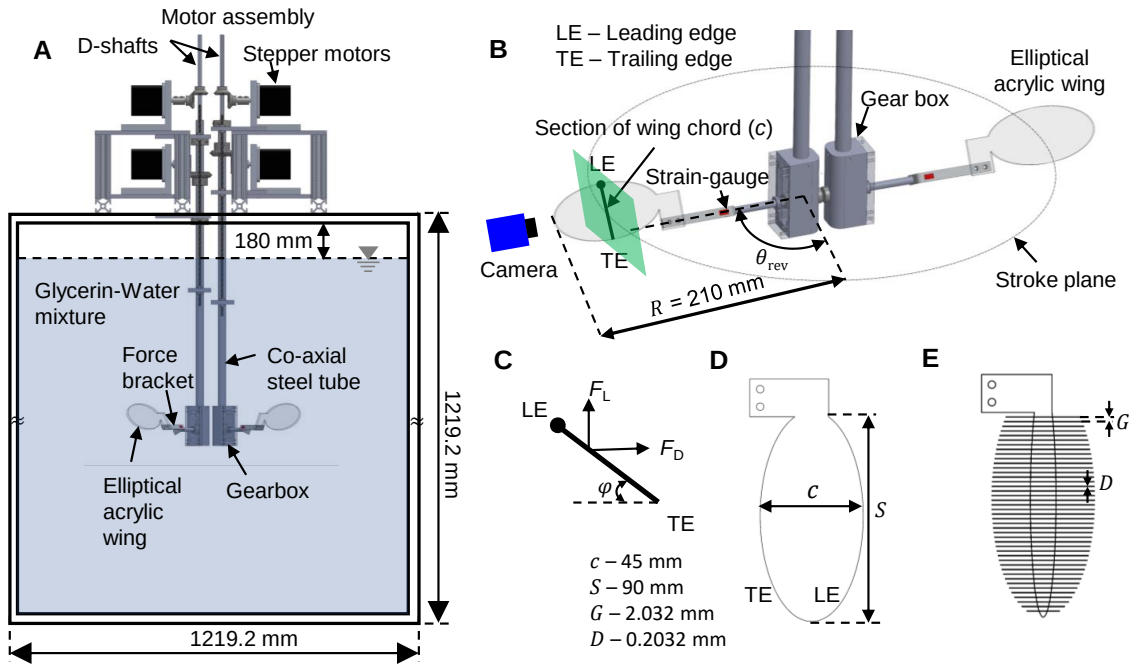

Figure 6.1: (A) Dynamically scaled flapping model and experimental set-up. (A) Front view of the 4-foot square tank with flapping robotic model mounted on the top of the tank containing Glycerin-water mixture. (B) Zoomed in view of the gearbox with solid elliptical wings mounted on an L-bracket with strain gauges at a position angle, θ_{rev} and wing tip radius, R. Also shown are the 2D phase locked Particle image velocimetry (2D PL-PIV) setup with laser sheet positioned at mid-span and camera position perpendicular to the laser plane. (C) Section of the wing chord (c) showing pitch angle (ψ), leading edge (LE) and trailing edge (TE). Lift force (F_L) was measured in the vertical direction and drag force (F_D) was measured in the direction opposite to the wing motion along the stroke plane. (D) Solid elliptical wing model with wing chord (c) = 45 mm and wing span (S) = 90 mm. (E) Elliptical bristled wing model equivalent to a solid wing model with 76 bristles placed uniformly along the wing span at both LE and TE with inter-bristle spacing (G) = 2.032 mm and bristle diameter (D) = 0.2032 mm.

an horizontal stroke plane. The robotic model consists of a scaled-up wing model (solid or bristled) immersed in a 4-foot optically clear square acrylic tank filled with glycerin (Fig. 6.1A). Each wing was attached to a stainless steel D-shaft (diameter=6.35 mm) using custom made L-brackets (Kasoju et al., 2018). Uniaxial strain gauges were mounted on the L-brackets to measure lift and drag forces. Two 2-phase hybrid stepper motors with integrated encoders (ST234E, National Instruments Corporation, Austin, TX, USA) were used to perform wing revolution and pitching motion. Wing revolution was achieved using a bevel gear coupled to a motor and a hollow stainless steel tube. Another D- shaft is inserted co-axially through the hollow stainless steel tube and was able to rotate independently with respect to stainless steel tube using ball bearings. Both the D-shaft and stainless steel tube are attached to the gear box (Fig. 6.1B) which helps in pitching the wing. All the stepper motors (4 motors needed for a wing pair, 2 motors needed for a single wing) were controlled using a multi-axis controller (PCI-7350, National Instruments Corporation, Austin, TX, USA) via a custom LabVIEW program (National Instruments Corporation, Austin, TX, USA).

2. 2 Wing models

A solid elliptical wing model was designed with a wing chord (c) of 45 mm and wing span (S) of 90 mm. An equivalent elliptical bristled wing model was designed from within the biological relevant range (Jones et al., 2016; Ford et al., 2019; Kasoju et al., 2020*b*) of number of bristles (n = 76), inter-wing gap to bristle diameter ratio (G/D = 10) and solid membrane area to total wing area ratio (A_m/A_T = 12.5%) (Fig. 6.1D,E). Both solid and bristled wings were fabricated from a 3 mm thick optically clear acrylic. The maximum width of a bristled wing acrylic membrane was 5.63 mm and bristles made of 304 stainless steel wires of diameter (D = 0.2032 mm) were attached on the wing in form of an elliptical shape (Fig. 6.1D,E). The inter-bristle gap (G) was maintained at 2.032 mm throughout the wing, to obtain G/D=10 in the range of G/D of tiny insect wings (Jones et al., 2016; Kasoju

et al., 2020*b*). These wing models were tested using dynamically scaled flapping robotic model described in the subsection 2. 1. Each of the wings were attached to the robotic model using a custom made L-bracket with wing tip radius (R) of 210 mm.

2. 3 Wing kinematics

The robotic platform enabled wing pitching and revolution in an horizontal stroke plane and therefore we didnot consider the wing elevation or changes in stroke plane angle. In this study, we used real wing kinematics of thrips *Frankliniella occidentalis*, leafminer *Liriomyza sativae* and fruitfly *Drosophila melanogaster* taken from previously published studies (Lyu et al., 2019*b*; Cheng and Sun, 2016; Fry et al., 2005). The wing kinematics for each of these insects are shown in Fig. 6.2. These three insect wing kinematics showed significant variation in pitch angle (ψ) and position angle (θ_{rev}) between each kinematics within a small Reynolds number (Re) range of 10-120. Pitch angle (ψ) represents the angle made by a section of the wing chord with the stroke plane (Fig. 6.1C), while the position angle (θ_{rev}) represents the angle made by the wing with respect to the wing position when they are parallel to each other (Fig. 6.1B). Both ψ and θ_{rev} are presented in degrees with respect to dimensionless cycle time, τ. Dimensionless cycle time (τ) is defined as ratio of instantaneous time (t) to the entire time to complete one cycle (T, see Table 1 for values of T).

Considering the position profile (θ_{rev}) in time (τ) for each of the wing kinematics, we can clearly see the leafminers profile (Fig. 6.2C) to have maximum stroke amplitude, ϕ ($\theta_{\text{rev,max}}$-$\theta_{\text{rev,min}}$, 178°) compared to thrips (ϕ = 140°, Fig. 6.2C) and fruitfly (ϕ = 143°, Fig. 6.2E) profile. The position where θ_{rev} reaches maximum ($\theta_{\text{rev,max}}$) is considered as the end of downstroke. The downstroke period is represented using shaded region in the Fig. 6.2A,C,E and the non-shaded region represents upstroke. While θ_{rev} for all the kinematics are closely resembling a sinusoidal profile, thrips profile reach the initial position very early in time (τ = 0.85) compared to leafminers or fruitfly profile.

To have a better understanding of how pitch angle changes in time, we presented match stick diagram representing a section of wing chord during both upstroke and downstroke for each of the insect wing profiles (Fig. 6.2B,D,F). In contrast to thrips and fruitfly wing kinematics, pitch profile (ψ) looked to be symmetrical in upstroke and downstroke for leafminers wing kinematics. Also, thrips profile was found to have a steeper and higher pitch angle (ψ) compared to other profiles. The motion of a single wing intuitively follows the prescribed motion profile irrespective of starting position angle (θ_{rev}). While for wing pair, we had the wings start at initial negative position angle (θ_{rev} = -10°). This allows the wings to perform a partial clap and fling towards the end of the upstroke with wings being closer at the wing tips and farther at the wing roots. The initial inter-wing spacing at the wing tips was set to 10% of chord length (c). Free flight recording of thrips (Santhanakrishnan et al., 2014) and leafminers (Cheng and Sun, 2016) have shown wings to not come in full contact but rather have roughly the same separation considered in this study. Many previous studies (Kolomenskiy et al., 2011; Santhanakrishnan et al., 2014; Arora et al., 2014; Jones et al., 2016; Cheng and Sun, 2016; Kasoju and Santhanakrishnan, 2021*a*) have looked at the variability in spacing between the wings during clap and fling and so is not considered in this study.

2. 4 Test Conditions

Solid and bristled wing (both single and wing pair configurations) were comparatively tested for varying Reynolds number (Re) from 10-120, defined as:

$$Re = \frac{2\phi f R c}{\nu} \tag{6.1}$$

where ϕ represents the stroke amplitude, f represents stroke cycle frequency given by $1/T$ where T represents cycle time, R represents wing tip radius, c represents wing chord and ν is the kinematic viscosity of the fluid. Each of the above test conditions are repeated for thrips, leafminers and fruitfly kinematics. The wing models being tested

	Re = 10		Re = 30		Re = 60		Re = 120	
	U_{st} (m/s)	T (s)	U_{st} (m/s)	T (s)	U_{st} (m/s)	T (s)	U_{st} (m/s)	T (s)
Thrips	0.102	10.1	0.305	3.37	0.099	10.33	0.199	5.17
Leafminers	0.102	12.85	0.305	4.28	0.099	13.14	0.199	6.57
Fruitfly	0.102	10.32	0.305	3.44	0.099	10.55	0.199	5.28

Table 6.1: Experimental conditions for each wing kinematics tested in this study. For each Reynolds numbers (Re) tested, their corresponding steady velocity (U_{st}) and cycle time (T) are presented.

were completely immersed in glycerine-water mixture. We used two different glycerin-water mixtures with kinematic viscosities of 457 cSt for Re = 10, 30 and 74 cSt for Re = 60,120, respectively. The kinematic viscosity of glycerin solutions in which wing models were tested was measured using a Cannon-Fenske routine viscometer (size 400, Cannon Instrument Company, State College, PA, USA). Table 7.1 shows the Reynolds numbers and their corresponding velocities and time taken to complete one complete cycle for each insect wing kinematics.

2. 5 Flow visualization

We conducted 2D phase-locked particle image velocimetry (2D PL-PIV) measurements to visualize time-varying chordwise flow generated by the motion of a single wing for varying wing kinematics in a plane located at mid-span (Fig. 6.1(B)). 2D PL-PIV based 2-component velocity vector fields were also used to determine the strength of the LEV and TEV circulation. For more details on 2D PL-PIV, and PIV processing, refer to **Appendix A.6 and A.7**, respectively.

2. 6 Definitions for calculated quantities

2. 6.1 Force measurements

Similar to our previous studies (Kasoju et al., 2018; Ford et al., 2019; Kasoju and Santhanakrishnan, 2021*a*,*b*), force data were collected using uniaxial strain gauges mounted on both sides of custom L-brackets in half-bridge configuration. A strain gauge conditioner

continuously measured the forces in the form of voltage signals based on L-bracket deflection during wing motion. Two different, custom L-brackets were used for non-simultaneous acquisition of normal and tangential forces (Fig. 6.1(C)) that were subsequently used for calculating lift and drag forces. The design of lift and drag L-brackets and validation of the methodology can be found in Kasoju et al. (2018). Normal and tangential forces (and thus lift and drag forces) were only measured on one wing in tests involving a solid/bristled wing pair, with the assumption that the forces generated by the other wing would be equal in magnitude (as the motion was symmetric for both wings of a wing pair). A pause time of 30 seconds was included between one cycle to the next cycle, in order to exclude any mechanical disturbance between cycles (e.g., sudden bending of L-bracket when the wings come to rest quickly). The raw voltage data was acquired using a data acquisition board (NI USB-6210, National Instruments Corporation, Austin, TX, USA) once the LabVIEW program (used for driving the motors) triggered to start the recording. Force data and angular position of the wings were acquired during each cycle at a sample rate of 10 kHz for all the test conditions mentioned in subsection 2. 4. The raw data was processed in the same manner as in our previous studies (Kasoju et al., 2018; Ford et al., 2019; Kasoju and Santhanakrishnan, 2021*a*) and implemented via a custom MATLAB script. A third order low-pass Butterworth filter with a cutoff frequency of 12 Hz was first applied to the raw voltage data. The baseline offset (obtained with wing at rest) was averaged in time and subtracted from the filtered voltage data. The lift and drag brackets were calibrated manually, and the calibration was applied to the filtered voltage data obtained from the previous step. The lift and drag brackets measured the tangential (F_T) and normal (F_N) forces acting on the wing. Lift force (F_L) and drag force (F_D) were defined along the vertical and horizontal directions, respectively, and calculated using non-simultaneous measurements of tangential (F_T) and normal (F_N) forces. F_T and F_N measurements were phase-averaged over 20 cycles for further analyses of F_L and F_D. We acquired 20 cycles of force data to account for variability in the mechanical operation of our robotic platform, and characterized

this variability using standard deviation across the 20 cycles. Dimensionless lift coefficient (C_L) and drag coefficient (C_D) were calculated using components of measured F_N and F_T using the following equations:

$$C_L = \frac{F_L}{0.5\rho U^2 A} = \frac{F_T \cos(90-\psi) + F_N \sin(90-\psi)}{0.5\rho U^2 A} \tag{6.2}$$

$$C_D = \frac{F_D}{0.5\rho U^2 A} = \frac{F_T \sin(90-\psi) + F_N \cos(90-\psi)}{0.5\rho U^2 A} \tag{6.3}$$

where ψ is the instantaneous angular position of the wing relative to the vertical and ρ is the density of the fluid medium (ρ of the glycerin solution used in this study was measured to be 1259 kg m^{-3} for Re = 10, 30 and 1234 kg m^{-3} for Re = 60, 120).

2. 6.2 Circulation

Circulation was calculated to quantify the strength of the leading edge vortex (LEV) and trailing edge vortex (TEV) using the out of plane vorticity (ω). ω was calculated from the exported phase-averaged PL-PIV velocity fields using the following equation implemented in a custom MATLAB script:

$$\omega = \frac{\partial v}{\partial x} - \frac{\partial u}{\partial y}. \tag{6.4}$$

Here u, v represents the horizontal and vertical components of velocity, respectively in a 2D plane where PL-PIV recordings were acquired. Horizontal direction is represented by x-axis and vertical direction is represented by y-axis.

Circulation (Γ) was calculated from ω fields at all time instants and test conditions where PL-PIV data were acquired, using the following equation in a custom MATLAB script:

$$\Gamma = \iint_S \omega \, ds \tag{6.5}$$

where S is the vorticity region for either the LEV or TEV. For more details on circulation calculations, refer to **Appendix A.8**.

3 Results

3. 1 Single wing

3. 1.1 Chordwise flow

Velocity vector fields were obtained from 2D PL-PIV data in a vertical plane located at about 50% of wing span. This allowed us in observing the chordwise flow changes for varying wing kinematics at various *Re*. Plots showing velocity vector fields overlaid on top of vorticity contours are presented here at mid-span at 5 selected timepoints (τ = 0.2, 0.4, 0.6, 0.8, 1) for *Re* = 10 and 120 for each wing kinematics (Fig. 6.3, 6.4, 6.5).

We observed the formation of two counter-rotating vorticies at the leading edge (LEV) and trailing edge (TEV) of both solid and bristled wing for any wing kinematics at all *Re* tested. The strength of LEV and TEV are significantly higher at higher Reynolds number (*Re* = 120) compared to *Re* = 10 for each wing kinematics and wing model tested (Fig. 6.3, 6.4, 6.5). While for any *Re*, the strength of LEV and TEV noticeably changes in time (τ) for each wing kinematics tested (solid and bristled wing models), we observed the peak vorticity to occur at τ = 0.8 irrespective of wing kinematics and wing model.

Once the wing reaches maximum pitch angle (ψ) in the downstroke ($\tau \approx 0.2$, Fig. 6.3A,F) of thrips kinematics at *Re* = 10, we observed little to no vorticity at leading and trailing edges for both solid and bristled wing. While later into the downstroke (with increasing τ), the strength of the vortex at both LEV and TEV were found to increase until the end of downstroke (Fig. 6.3B,C,G,H). During upstroke, both LEV and TEV were found to vary significantly in τ similar to the pitch angle (ψ) with peak vorticity of LEV and TEV occurring at τ = 0.8 (Fig. 6.3D,I). The strength of LEV and TEV for solid wing model is a little higher compared to bristled wing model during both upstroke and downstroke. At *Re* = 120, vorticity distribution followed similar trend as that of *Re* = 10 but with significantly higher strength at both LEV and TEV (Fig. 6.3K-T). Also, the LEV and TEV were found to be elongated along wing chord and noticeably advected into the wing wake at *Re* = 120.

The vorticity strength at LEV and TEV for *Re* = 30 (refer Supplementary Fig. A.9. 4.1 A-J in **Appendix**) is significantly higher compared to any *Re* and it follows the same trend in τ as other *Re* with vorticity at LEV and TEV to be concentrated closer to the wing for both solid and bristled wing. The vorticity strength at LEV and TEV for *Re* = 60 (refer Supplementary Fig. A.9. 4.1 K-T in **Appendix**) is significantly lower compared to *Re* = 30 and 120 but a little higher than *Re* = 10 but it follows the similar trend in τ as other *Re*.

For leafminers kinematics, the strength of LEV and TEV were found to increase until τ = 0.3 and then decrease with increasing τ during downstroke at *Re* = 10 and 120 for both solid and bristled wing (Fig. 6.4A-B, F-G, K-L, P-Q). However during early upstroke (τ = 0.6, Fig. 6.4C, H, M, R) we don't see any noticeable LEV or TEV until τ = 0.7 for both solid and bristled wing at *Re* = 10 and 120. For $\tau \geq 0.7$, we observed LEV and TEV to increase in strength and reach maximum at τ = 0.8 irrespective of wing model and *Re* (Fig. 6.4D, I, N, S). Similar to thrips kinematics, LEV and TEV were found to be elongated along wing chord and noticeably advected into the wing wake at *Re* = 120 (Fig. 6.4K-T). Similar to thrips kinematics, leafminers kinematics has higher strength of LEV and TEV for *Re* = 30 compared to any *Re* (refer Supplementary Fig. A.9. 4.2 A-J in **Appendix**). Variation in LEV and TEV follows the same trend in τ as other *Re* with vorticity at LEV and TEV to be concentrated closer to the wing for both solid and bristled wing. The vorticity strength at LEV and TEV for *Re* = 60 is significantly lower compared to any *Re* = 30 and 120 but a little higher than *Re* = 10 and it follows the similar trend in τ as other *Re* (refer Supplementary Fig. A.9. 4.2 K-T in Appendix).

For fruitfly kinematics, we observed the strength of LEV and TEV to increase until τ = 0.1 and then decrease with further increase in τ until the end of downstroke at *Re* = 10 and 120 for both solid and bristled wing (Fig. 6.5A-B, F-G, K-L, P-Q). During upstroke, the strength of LEV and TEV were found to increase with increasing τ until τ = 0.8 and then decrease with further increase in τ at *Re* = 10 and 120 for both solid and bristled wing (Fig. 6.5C-E, H-J, M-O, R-T). Similar to thrips and leafminers kinematics, LEV and TEV

were found to be elongated along wing chord and noticeably advected into the wing wake at *Re* = 120 (Fig. 6.5K-T). Similar to thrips and leafminers kinematics, fruitfly kinematics has higher strength of LEV and TEV for *Re* = 30 compared to any *Re* (refer Supplementary Fig. A.9. 4.3 A-J in **Appendix**). Variation in LEV and TEV follows the same trend in τ as other *Re* with vorticity at LEV and TEV to be concentrated closer to the wing for both solid and bristled wing. The vorticity strength at LEV and TEV for *Re* = 60 is significantly lower compared to any *Re* = 30 and 120 but a little higher than *Re* = 10 and it follows the similar trend in τ as other *Re* (refer Supplementary Fig. A.9. 4.3 K-T in **Appendix**).

3. 1.2 Aerodynamic force generation

Fig. 6.6, 6.7 gives the time course of drag (C_D) and lift (C_L) coefficient during all the three wing kinematics (thrips, leafminers and fruitfly) for solid and bristled wing at *Re* = 10 and 120. Irrespective of wing kinematics, both C_D and C_L were found to peak during upstroke at about $\tau = 0.8$ for both solid and bristled wing at *Re* = 10 and 120.

Both C_D and C_L for thrips kinematics were found to significantly vary in time (τ) for both solid and bristled wing at *Re* = 10 and 120 (Fig. 6.6A,D and Fig. 6.7A,D). During downstroke, we observed two positions in time where C_D and C_L reached close to zero ($\tau \approx 0.2$ and 0.5). At $\tau \approx 0.2$, we observed the wing has reached maximum pitch angle (ψ) in downstroke (Fig. 6.2A) and later found to decrease (ψ) with further increase in τ. At $\tau \approx 0.5$, the wing is closer to the end of downstroke. Apart from C_D and C_L peaking at τ = 0.8 during upstroke, we observed C_D and C_L to reach close to zero at $\tau \approx 0.7$ and 0.9. At $\tau = 0.7$. the wing has reached maximum pitch angle (ψ) in upstroke (Fig. 6.2A) and later found to decrease (ψ) with further increase in τ. At $\tau \approx 0.9$, the wing has reached to quick rest before the end of upstroke causing C_L to go negative in time. We observed similar trend in time course of C_D and C_L at *Re* = 30 (refer Supplementary Fig. A.9. 4.4 A,D in **Appendix**) and *Re* = 60 (refer Supplementary Fig. A.9. 4.5 A,D in **Appendix**). The magnitude of C_D and C_L for solid wing is noticeably higher compared to that of bristled

wing at any *Re* tested. In addition, with increasing *Re* we observed noticeably decrease in peak C_D and C_L.

Both C_D and C_L for leafminers kinematics were found to significantly vary in time (τ) for both solid and bristled wing at *Re* = 10 and 120 (Fig. 6.6B,E and Fig. 6.7B,E). During downstroke, both C_D and C_L were found to increase and then decrease with increasing τ and reach close to zero way earlier in the downstroke ($\tau \approx 0.45$) at both *Re* (10 and 120). In contrast to thrips kinematics, leafminers kinematics didnot show any significant negative C_L at the end of upstroke. We observed similar trend in time course of C_D and C_L at *Re* = 30 (refer Supplementary Fig. A.9. 4.4 B,E in **Appendix**) and *Re* = 60 (refer Supplementary Fig. A.9. 4.5 B,E in **Appendix**). The magnitude of C_D and C_L for solid wing is noticeably higher compared to that of bristled wing at any *Re* tested. In addition, with increasing *Re* we observed noticeably decrease in peak C_D and C_L.

Both C_D and C_L for fruitfly kinematics were found to significantly vary in time (τ) for both solid and bristled wing at *Re* = 10 and 120 (Fig. 6.6C,F and Fig. 6.7C,F). During downstroke, we observed two positions in time where C_D and C_L reached close to zero ($\tau \approx 0.1$ and 0.45). At $\tau \approx 0.1$, we observed the wing has reached maximum pitch angle (ψ) in downstroke (Fig. 6.2A) and later found to decrease (ψ) with further increase in τ. At $\tau \approx 0.45$, the wing is closer to the end of downstroke. Apart from C_D and C_L peaking at $\tau = 0.8$ during upstroke, we observed C_D and C_L to peak and drop at $\tau \approx 0.7$. At this time point. the wing has reached maximum pitch angle (ψ) in upstroke (Fig. 6.2A) and later found to decrease (ψ) with further increase in τ. We observed similar trend in time course of C_D and C_L at *Re* = 30 (refer Supplementary Fig. A.9. 4.4 C,F in **Appendix**) and *Re* = 60 (refer Supplementary Fig. A.9. 4.5 C,F in **Appendix**). The magnitude of C_D and C_L for solid wing is noticeably higher compared to that of bristled wing at any *Re* tested. In addition, with increasing *Re* we observed noticeably decrease in peak C_D and C_L.

Fig. 6.8 gives the cycle-averaged drag ($\overline{C_D}$) and lift ($\overline{C_L}$) coefficient for solid and bristled wing with varying *Re* and wing kinematics. Irrespective of *Re*, $\overline{C_D}$ for thrips kinematics

is significantly higher compared to fruitfly and leafminer kinematics for both solid and bristled wing. However, irrespective of *Re*, $\overline{C_L}$ for leafminers and thrips kinematics falls within the same range while taking standard deviations into consideration for both solid and bristled wing. $\overline{C_D}$, $\overline{C_L}$ for solid wing is noticeably higher compared to bristled wing irrespective of wing kinematics and *Re*. Irrespective of wing kinematics, $\overline{C_D}$, $\overline{C_L}$ decreased with increasing *Re*.

3. 2 Wing pair

3. 2.1 Aerodynamic force generation

The aerodynamic force generated (C_D, C_L) by a solid wing pair and bristled wing follows similar trend to that of single solid and single bristled wing irrespective of *Re* and wing kinematics (refer Supplementary Fig. A.9. 4.6, A.9. 4.7, A.9. 4.8, A.9. 4.9). However the magnitude of C_D and C_L is a little higher compared to that of single solid and single bristled wing during early downstroke due to wing-wing interaction. While for the rest of the flapping cycle, the magnitude of C_D and C_L for a wing pair configuration closely resembles that of a single wing configuration for every kinematics and *Re* tested

Similar to single wing configuration, the cycle-averaged drag ($\overline{C_D}$) and lift ($\overline{C_L}$) coefficient for solid wing pair is noticeably higher compared to bristled wing pair irrespective of *Re* and wing kinematics (Fig. 6.9). At each *Re* tested, $\overline{C_D}$ for thrips kinematics is significantly higher compared to fruitfly and leafminer kinematics for both solid and bristled wing pair. $\overline{C_L}$ for leafminers and thrips kinematics falls within the same range while taking standard deviations into consideration for both solid and bristled wing pair. Irrespective of wing kinematics, $\overline{C_D}$, $\overline{C_L}$ decreased with increasing *Re*.

3. 3 Aerodynamic performance

To better understand the aerodynamic performance of wing model tested for each *Re* and wing kinematics, we presented the the cycle-averaged lift over cycle-averaged drag ratio

($\overline{C_L}/\overline{C_D}$) for both single wing and wing pair configuration (Fig. 6.10). Irrespective of wing configuration (single wing or wing pair), leafminers kinematics provided better aerodynamic performance compared to thrips or fruitfly profile at each *Re* tested for both solid and bristled wings. $\overline{C_L}/\overline{C_D}$ for leafminers kinematics did not change noticeably with *Re* or wing configuration. For a single solid wing, $\overline{C_L}/\overline{C_D}$ for fruitfly kinematics was found to decrease with increasing *Re* (Fig. 6.10A). Similar trend was observed for thrips kinematics with increasing *Re*. For a single bristled wing, $\overline{C_L}/\overline{C_D}$ for fruitfly kinematics was found to show little to no variation with increasing *Re* (Fig. 6.10B). Similar trend was observed for thrips kinematics with increasing *Re*. For solid wing pair, $\overline{C_L}/\overline{C_D}$ for fruitfly kinematics was found to decrease with increasing *Re* (Fig. 6.10C). However, thrips kinematics showed little to no variation in $\overline{C_L}/\overline{C_D}$ with increasing *Re*. For a bristled wing pair, $\overline{C_L}/\overline{C_D}$ for fruitfly kinematics was found to show little to no variation with increasing *Re* (Fig. 6.10D). Similar trend was observed for thrips kinematics with increasing *Re*.

4 Discussion

Tiny insects flying within *Re* range of 10-120 have shown to have significant variation in wing beat kinematics. Although previous studies have investigated each of these wing beat kinematics individually (Fry et al., 2005; Lyu et al., 2019*b*; Cheng and Sun, 2018, 2019, 2021, 2016; Dickinson et al., 1999; Lehmann et al., 2005), a comparative study of analysing the aerodynamic performance at varying *Re* was missing. In this study, we used a dynamically scaled robotic model to mimic the flapping flight relevant to tiny insects (thrips, leafminers and fruitfly) with varying pitch angle and position angle in an horizontal stroke plane using solid and bristled wings (single and wing pair configurations) for varying *Re* in range of 10-120. We found that (1) Irrespective of wing kinematics, vorticity at LEV and TEV was found to peak at $\tau \approx 0.8$ in the upstroke, (2) peak C_D and C_L occurred at $\tau \approx 0.8$ in the upstroke, (3) While thrips kinematics generated higher $\overline{C_D}$ and $\overline{C_L}$, the aerodynamic performance ($\overline{C_L}/\overline{C_D}$) was noticeably higher for leafminer kinematics for both

solid and bristled wing models (single and wing pair configuration) for all *Re* tested.

4. 1 Effect of varying *Re*

With varying *Re*, we have observed significant changes in the strength of leading edge (LEV) and trailing edge (TEV) of both solid and bristled wing irrespective of wing kinematics (Fig. 6.3, 6.4, 6.5). For higher *Re* (= 120), we observed the traces of shed TEV in the wake with stronger LEV and TEV vortices still attached to the wing for both solid or bristled wing for all wing kinematics tested (refer Supplementary Movies A.9. 4.11, A.9. 4.12 and A.9. 4.13 in **Appendix**) at about midway during both upstroke and downstroke (τ = 0.2-0.3 and τ = 0.7-0.8). Elongated vorticies at leading edge (LE) and trailing edge (TE) of a wing at higher *Re* (= 120) represents flow advection into the wake with increased kinetic energy in the flow. These elongated vortices could also be result of spanwise flow (Santhanakrishnan et al., 2018; Kolomenskiy et al., 2011). Previous studies have shown that shedding of TEV with only LEV being attached to the wing would result in significant increase in lift force (Ellington, 1999; Miller and Peskin, 2009; Santhanakrishnan et al., 2018). In the present study, we observed the C_{L} to increase within τ = 0.2-0.3 and τ = 0.7-0.8, where vortex shedding was observed thereby supporting the results from previous studies. Increasing *Re* showed decreased $\overline{C_{\mathrm{D}}}$ and $\overline{C_{\mathrm{L}}}$ for all wing kinematics and wing models (single wing and wing pair configuration) tested (Fig. 6.8, 6.9). While significant drop in cycle-averaged coefficients ($\overline{C_{\mathrm{D}}}$ and $\overline{C_{\mathrm{L}}}$) were observed from *Re* = 10 to 30, minimal drop were observed from *Re* = 60 to 120. Although the strength of LEV and TEV were higher for higher *Re* (= 120), we observed the lift force generation to be lower due to formation flow advection into the wake causing the drop in net circulation on the wing.

For lower *Re* (= 10, 30, 60), we didnot see any shedding of TEV during both upstroke and downstroke for any wing kinematics for both solid and bristled wing. While at *Re* = 10, both LEV and TEV were found to be diffused but still attached to the wing due to relative effect of viscosity being significantly higher at low *Re* flows helping in stabilizing

the vortex (Santhanakrishnan et al., 2018). While the formation of stable LEV and TEV increases the lift force generation at low *Re*, the amount of drag force was also significantly higher. Surprisingly, we observed the strength of vorticity of LEV and TEV to be significantly higher at *Re* = 30 compared to *Re* = 60 for both solid and bristled wing for any wing kinematics (refer to Supplementary Fig. A.9. 4.1, A.9. 4.2, A.9. 4.3). This is due to the kinetic energy of the flow to be significantly higher at *Re* = 30 compared to *Re* = 60 (refer Table 7.1)

4. 2 Effect of stroke amplitude and pitch rate

From Fig. 6.2, we observed the leafminers kinematics to have significantly higher stroke amplitude, ϕ ($\theta_{\text{rev,max}}$-$\theta_{\text{rev,min}}$, 178°) compared to thrips (ϕ = 140°, Fig. 6.2C) and fruitfly (ϕ = 143°, Fig. 6.2E) profile. This would intuitively result in increased force generation (C_{D} and C_{L}) for leafminers kinematics. However, we didnot see any such improvement in force generation for leafminers kinematics compared to other kinematics. However. the aerodynamic efficiency ($\overline{C_{\text{L}}}/\overline{C_{\text{D}}}$) for leafminers kinematics was higher compared to thrips or fruitfly kinematics having lower stroke amplitude. Also, previous study by Wang et al. (2004) have showed that force coefficients have shown weak dependence on stroke amplitude in range of 60° to 120°. This uncertainity in force generation for varying stroke amplitude (ϕ) needs to be further investigated in future studies. For a wing pair configuration, increasing the stroke amplitude to the maximum ($\approx$ 180) would result in wing-wing interaction which would increase the net force generation on the wing (Weis-Fogh, 1973; Ellington, 1984*a*; Miller and Peskin, 2005). In the present study, due to mechanical limitation of the flapping model, we were unable to perform a full clap and fling at the end of upstroke. Unlike full clap and fling motions observed in thrips (Santhanakrishnan et al., 2014; Lyu et al., 2019*b*), partial clap and fling have been observed in leafminers (Cheng and Sun, 2016). Using partial clap and fling in the present study, we have observed about 7% - 9% increase in $\overline{C_{\text{L}}}$ and $\overline{C_{\text{D}}}$ at low *Re* (= 10,30) for solid wing pair compared to single

solid wing. This is in agreement with the results from Cheng and Sun (2017). However for a bristled wing pair, we observed $< 5\%$ increase in $\overline{C_{\mathrm{L}}}$ and $\overline{C_{\mathrm{D}}}$ at low *Re* (= 10,30). At higher *Re* (> 30), we didnot see any significant variation in $\overline{C_{\mathrm{L}}}$ and $\overline{C_{\mathrm{D}}}$ between wing pair and single wing configuration. We expect the augmentation in forces to be remarkable for a full clap and fling motion.

To understand how the pitch rate is changing in time for different kinematics used in this study, we plotted non-dimensional pitch rate ($\dot{\psi}/\dot{\psi}_{\mathrm{max}}$) with non-dimensional time (τ) for all the wing kinematics (Fig. 6.11). Negative value of $\dot{\psi}/\dot{\psi}_{\mathrm{max}}$ represents wing pitching/rotating in counter-clockwise direction (left wing in a single wing or wing pair configuration) called as negative pitching. This generally mean decreasing angle of attack in downstroke and increasing angle of attack in upstroke. Positive value of $\dot{\psi}/\dot{\psi}_{\mathrm{max}}$ represents wing pitching/rotating in clockwise direction (left wing in a single wing or wing pair configuration) called as positive pitching or increasing angle of attack. This generally mean increasing angle of attack in downstroke and decreasing angle of attack in upstroke. During downstroke (τ = 0-0.5), the wings were in acceleration with negative pitching for longer duration (until $\tau \approx 0.1$) for thrips kinematics. Whereas for leafminers and fruitfly kinematics, we observed an early acceleration followed with a quick deceleration. This early acceleration resulted in formation of quicker LEV and TEV with higher strengths for leafminers and fruitfly kinematics for single solid and bristled wing at *Re* = 10 and 120 (Fig. 6.4, 6.5). Leafminers kinematics was found to have negative pitching for longer duration of downstroke compared to other kinematics. This resulted in stable lift force generation for most duration of downstroke for both single wing and wing pair configurations (solid and bristled) at all *Re* (Fig. 6.6E, 6.7E, Supplementary Fig. A.9. 4.4E-A.9. 4.9E). During the later half of the downstroke, we observed positive pitching for all the wing kinematics (Fig. 6.11). While leafminers kinematic showed close to steady increase in positive pitch rate, thrips and fruitfly kinematics were observed to follow a wavy pattern in increasing the pitch rate. This could possible be the reason for a wavy pattern in their lift force generation

(Fig. 6.6D,E, 6.7D,E, Supplementary Fig. A.9. 4.4D,E-A.9. 4.9D,E) during later half of downstroke.

For most part of early upstroke, the wings were in deceleration with positive pitch rate, with thrips kinematics showing steeper change compared to other kinematics. At around τ = 0.65-0.7, we observed change in pitching direction i.e, wings start rotating in opposite direction (positive to negative pitching). Around this time, we observed lift coefficient to drop for all the wing kinematics for both single and wing pair configuration (solid and bristled) at all *Re*. At around τ = 0.8, we observed peak lift and drag coefficient for all the wing kinematics and for all the test conditions. At this τ, the wings were either in acceleration or deceleration increasing the angle of attack thereby increasing the force generation. Towards the end of upstroke, thrips kinematics showed no changes in pitch rate in contrast to other kinematic profile. During similar time period, position profile for thrips was also unchanged. This suggests that wings are almost at pause during end of upstroke. Varying this pause period has been investigated in our recent study (Kasoju and Santhanakrishnan, 2021*b*) and we found that increasing the pause time resulted in larger decrease in power coefficient required to fling the wings in comparison to lift coefficient.

4. 3 Effect of perturbed pitch profiles

As the kinematics profiles used in the present study were redrawn from the mean profile data shown in the previous studies (Lyu et al., 2019*b*; Cheng and Sun, 2016; Fry et al., 2005) without considering the standard deviation in the profiles, we performed a perturbation test for pitch profile of leafminers kinematics. We varied the maximum pitch angle (ψ) in a complete flapping cycle by 10% in both positive and negative direction as shown in the Fig. 6.2C. We measured the aerodynamic force generated for the perturbed pitch profiles (ψ^+, ψ^-) of leafminers kinematics at *Re* = 30 (Fig. 6.12). We didnot see any noticeable variation in C_D or C_D in time for both single wing and wing pair configuration (solid and bristled). This suggests that our results holds good within the standard deviation of 10% on

the pitch profiles that were tested.

4. 4 Implication of flow generation on lift force

To estimate the strength of the flow in the flow field around the wing, we measured circulation of the vorticies at the leading edge (LEV) and trailing edge (TEV) using the equation 6.5 and are presented in Fig. 6.13 and Supplementary Fig. A.9. 4.10. Irrespective of *Re* and wing kinematics, LEV circulation (Γ_{LEV}) and TEV circulation (Γ_{TEV}) were found to peak at around $\tau = 0.8$. This was the same timepoint where peak lift coefficient was observed. Looking at the thrips kinematics at *Re* = 10 (Fig. 6.13A), 30 (Supplementary Fig. A.9. 4.10A), 60 (Supplementary Fig. A.9. 4.10D) and 120 (Fig. 6.13D), we observed circulation to drop close to zero around mid downstroke and around the end of downstroke. This was in agreement with lift force generation in time for their respective *Re*. Similarly, the time course point of circulation (Γ) were in agreement with lift coefficient (C_{L}) for other kinematics tested . Therefore, circulation around the wing could help in explaining the lift force generation in time in a flapping flight. However, the magnitude of circulation (Γ) was significanty varyimg with *Re* and looks to be dependent of wing velocity and also on the viscosity of the fluid. Therefore, a non-dimensional circulation (Γ^{*}) given by Γ/cU_{st} where c represents the wing chord and U_{st} represents steady velocity of the wing, could help in understanding Γ variation with respect to *Re*.

4. 5 Limitations on wing kinematics

Within a small variation in *Re* (10-120), we have observed significant variation of wing beat kinematics in tiny insects (comparing the kinematics of thrips, leafminers and fruitfly). As the size of the insect increases, the deviation in stroke plane angle in one complete cycle is minimized. i.e., larger insects tend to use narrow stroke plane compared to a deeper stroke plane used by tiny insects such as thrips. Use of deeper non-horizontal stroke plane in tiny insects led them to use drag to produce the weight supporting vertical force (Cheng and

Sun, 2018). However, in this study we used horizontal stroke plane irrespective of wing kinematics (thrips or leafminers or fruitfly). This is one of the major limitations of the current study and need to be investigated in future studies. Previous studies have shown that use of horizontal stroke plane instead decreased the net vertical or lift force generation by 2/3 rd of total lift generated using actual wing kinematics with non-horizontal stroke plane (Cheng and Sun, 2018). However, the trend of drag or lift force generation in time was not altered between an horizontal or non-horizontal stroke plane. This suggests that the results from the current study regarding the trend in variation of force generation in time for each wing kinematics for each test conditions holds good irrespective of horizontal or non-horizontal stroke plane.

5 Conclusion

Using a dynamically scaled robotic model that mimics the flapping flight relevant to tiny insects in an horizontal stroke plane, we investigated the aerodynamic force generation and flow characteristics of a solid and bristled wings (single and wing pair configurations) for varying *Re* in range of 10-120 for thrips, leafminers and fruitfly wing kinematics. We found the circulation at LEV and TEV to peak at $\tau \approx 0.8$, which was similar to where peak lift force generation was observed for single wing configuration (solid and bristled) for all wing kinematics tested. Wing pitch rate was found to significantly influence the aerodynamic force generation on the wings. While thrips kinematics generated higher $\overline{C_{\mathrm{D}}}$ and $\overline{C_{\mathrm{L}}}$, the aerodynamic performance ($\overline{C_{\mathrm{L}}}/\overline{C_{\mathrm{D}}}$) was noticeably higher for leafminer kinematics for both solid and bristled wing models (single and wing pair configuration) and at all *Re* tested. Solid wing pair configuration with partial clap-and-fling was found to show 7%-9% increase in lift force compared to single solid wing at *Re* = 10 for all wing kinematics tested.

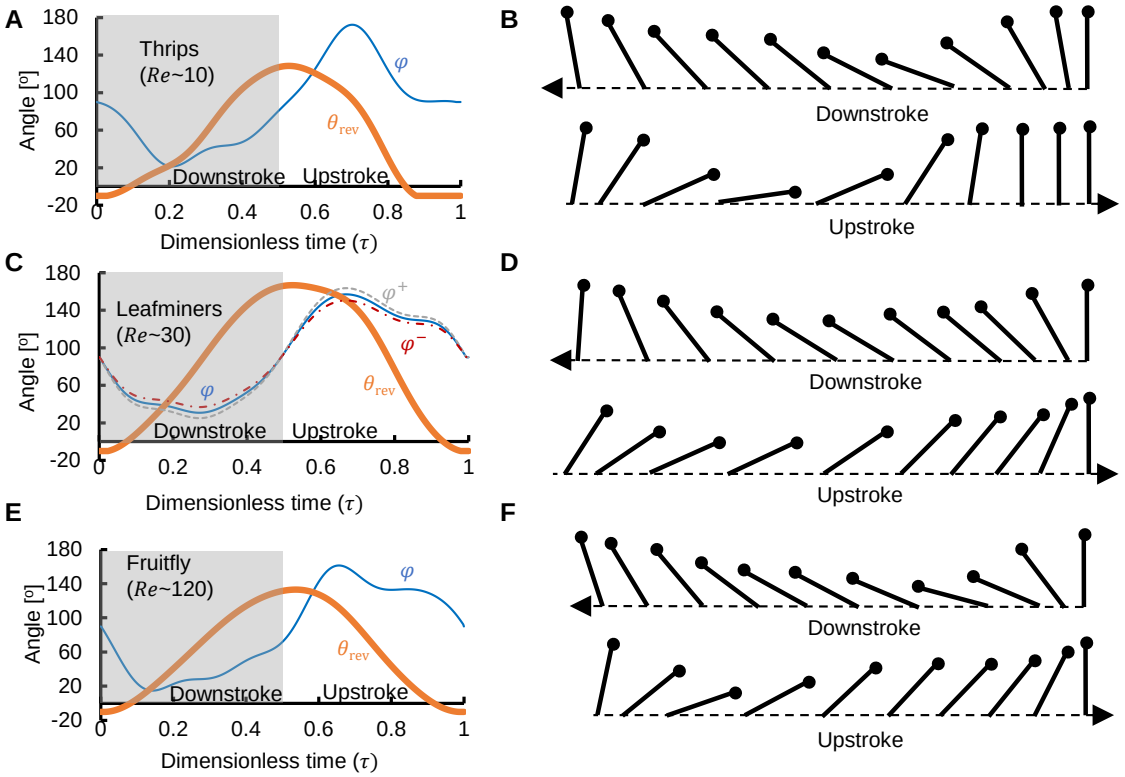

Figure 6.2: Real wing kinematics of insects modified and replotted from previously published studies (Fry et al., 2005; Cheng and Sun, 2016; Lyu et al., 2019*b*). Pitch angle (ψ) and position angle (θ_{rev}) in degrees during one cycle defined using dimensionless time (τ) for (A) thrips kinematics replotted from Lyu et al.Lyu et al. 2019*b*, (C) Leafminers kinematics replotted from Cheng and Sun (2016). Also shown are the positive and negative perturbated pitch profiles (ψ^+, ψ^-) with 10% of maximum ψ during upstroke and downstroke and (E) Fruitfly kinematics replotted from Fry et al. (2005). The corresponding wing positions are shown using a match stick diagram in (B), (D) and (E), respectively. Downstroke represents from right to left while upstroke goes from left to right. Shaded region in (A), (C) and (E) represents downstroke of a cycle and therefore non-shaded region represents the upstroke. Approximate Reynolds numbers (Re) at which thrips, leafminers and fruitfly fly are 10, 30 and 120, respectively. Thick lines represents position angle (θ_{rev}), thin lines represents Pitch angle (ψ). Dashed lines in (C) represents the perturbation pitch angles (ψ^+, ψ^-).

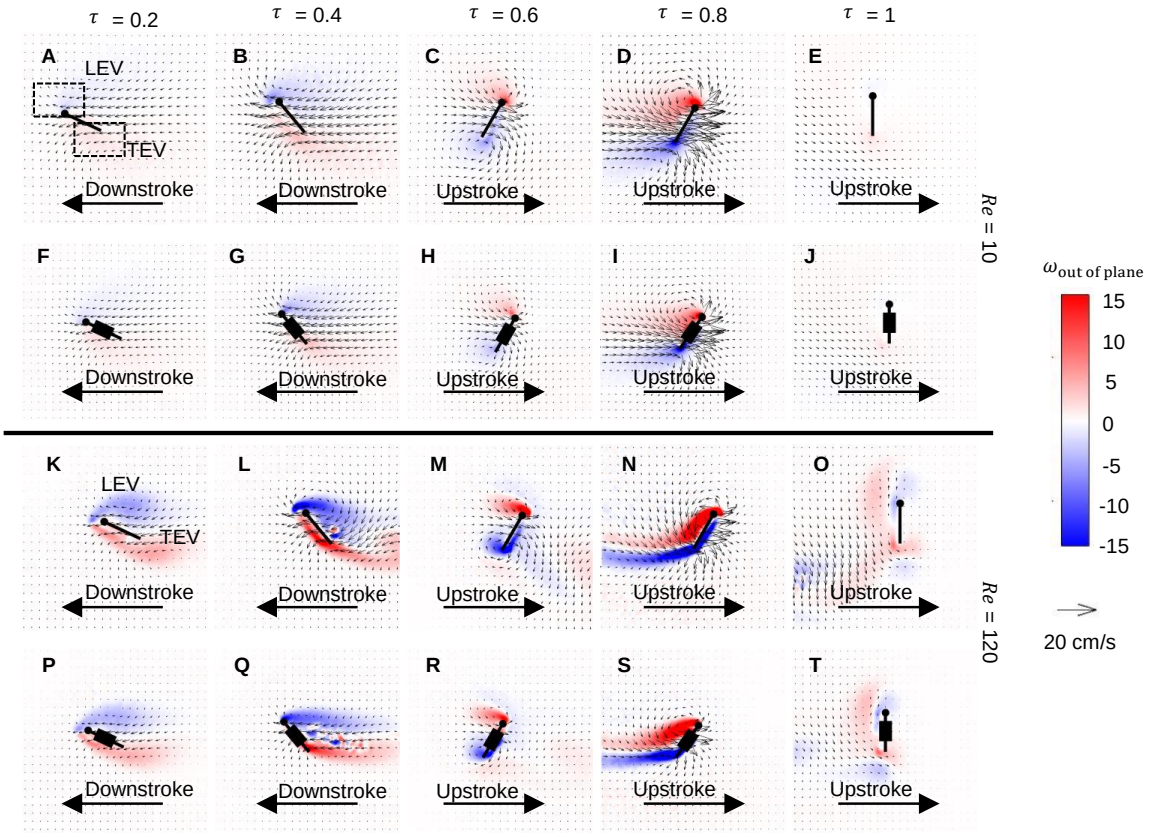

Figure 6.3: 2D phase-locked PIV (PL-PIV) showing vorticity contours overlaid on top of velocity vectors performing thrips kinematics at 5 dimensionless times (τ= 0.2, 0.4, 0.6, 0.8, 1) for (A-E) single solid wing at Re = 10, (F-J) single bristle wing at Re = 10, (K-O) single solid wing at Re = 120, (P-T) single bristled wing at Re = 120. The dashed boxes around the leading edge vortex (LEV) and trailing edge vortex (TEV) represents the region of interest for calculating circulation (Γ).

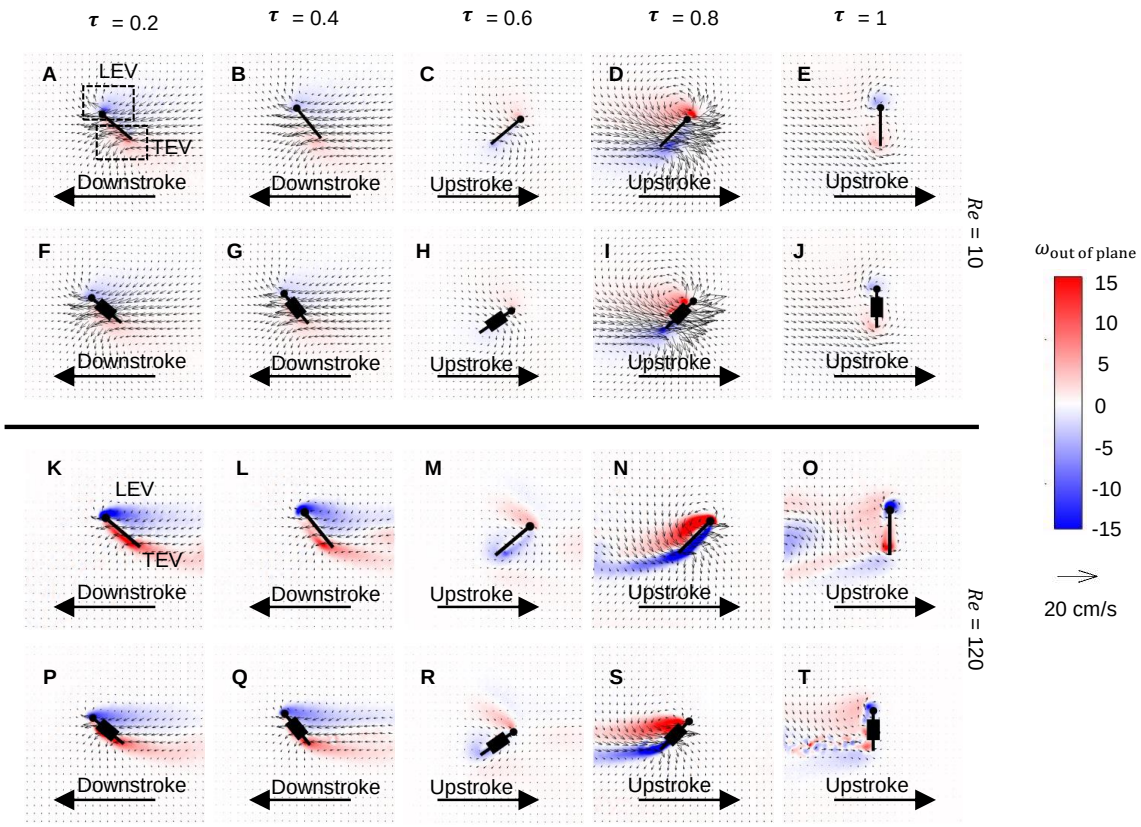

Figure 6.4: 2D phase-locked PIV (PL-PIV) showing vorticity contours overlaid on top of velocity vectors performing leafminer kinematics at 5 dimensionless times (τ= 0.2, 0.4, 0.6, 0.8, 1) for (A-E) single solid wing at Re = 10, (F-J) single bristle wing at Re = 10, (K-O) single solid wing at Re = 120, (P-T) single bristled wing at Re = 120. The dashed boxes around the leading edge vortex (LEV) and trailing edge vortex (TEV) represents the region of interest for calculating circulation (Γ).

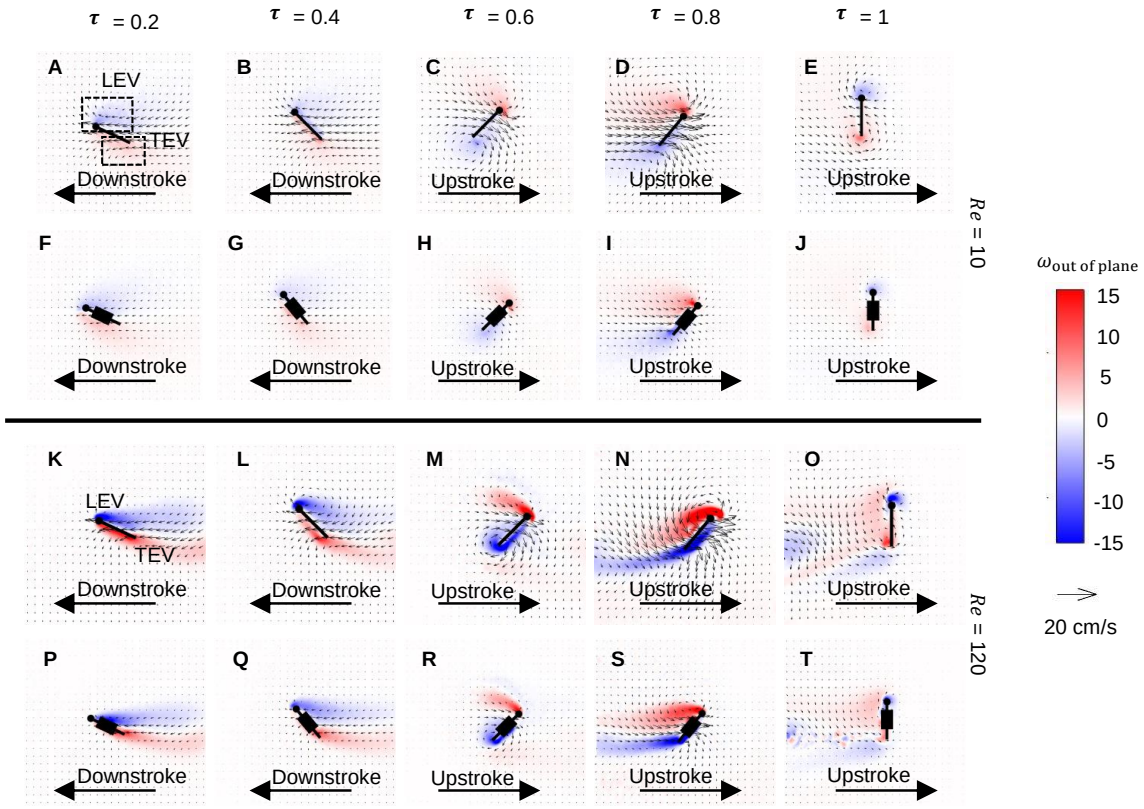

Figure 6.5: 2D phase-locked PIV (PL-PIV) showing vorticity contours overlaid on top of velocity vectors performing fruitfly kinematics at 5 dimensionless times (τ= 0.2, 0.4, 0.6, 0.8, 1) for (A-E) single solid wing at Re = 10, (F-J) single bristle wing at Re = 10, (K-O) single solid wing at Re = 120, (P-T) single bristled wing at Re = 120. The dashed boxes around the leading edge vortex (LEV) and trailing edge vortex (TEV) represents the region of interest for calculating circulation (Γ).

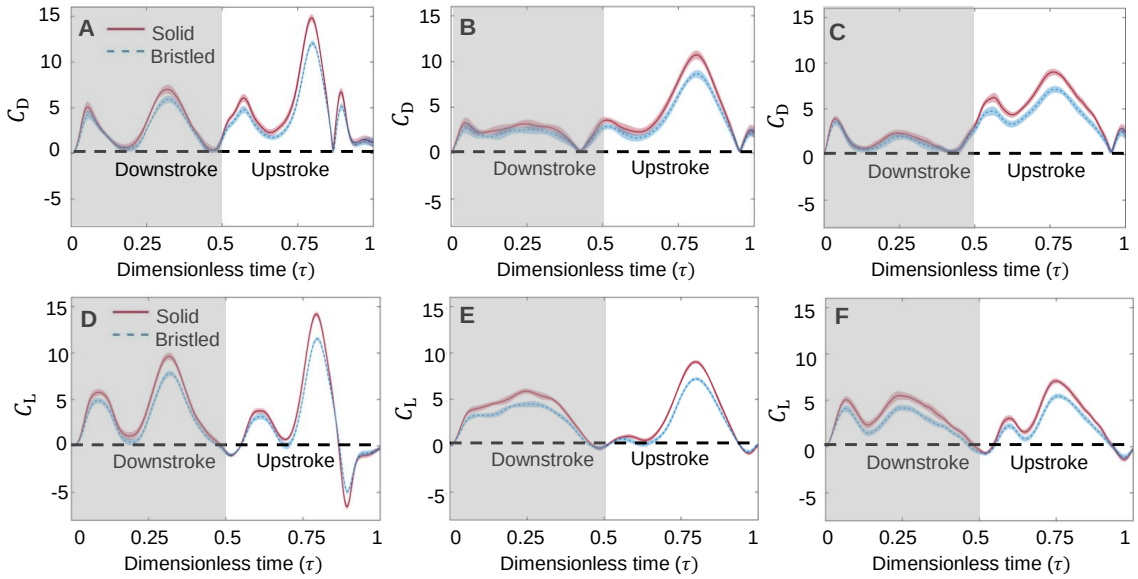

Figure 6.6: Time variation of drag coefficient (C_D) and lift coefficient (C_L) for a single solid and single bristled wing performing (A,D) Thrips kinematics, (B, E) Leafminers kinematics, (C, F) Fruitfly kinematics at Re = 10, respectively. Shaded region represents downstroke and non-shaded region represents upstroke.

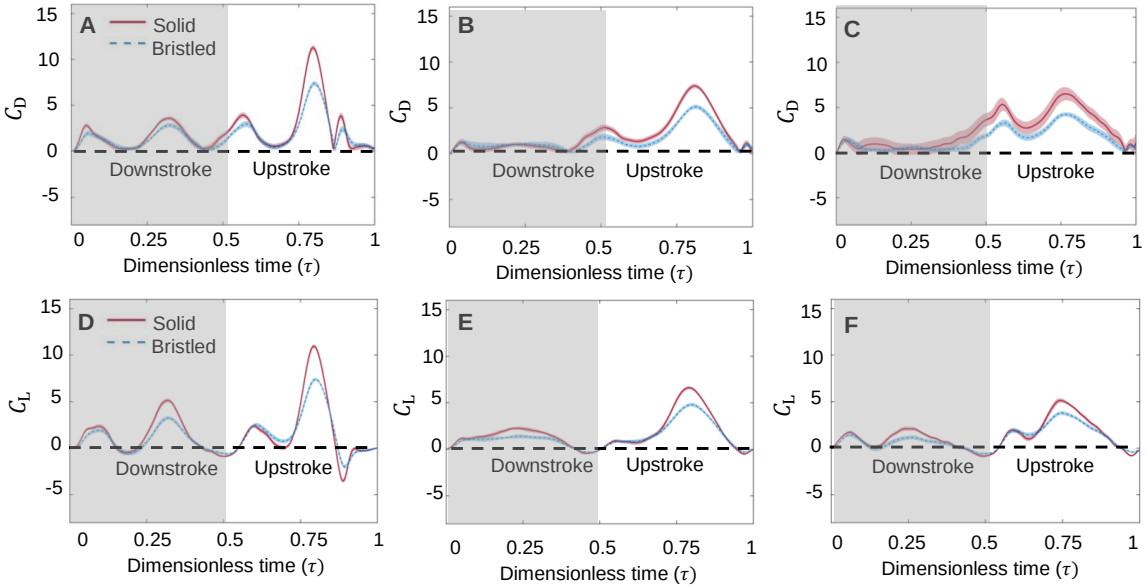

Figure 6.7: Time variation of drag coefficient (C_D) and lift coefficient (C_L) for a single solid and single bristled wing performing (A,D) Thrips kinematics, (B, E) Leafminers kinematics, (C, F) Fruitfly kinematics at Re = 120, respectively. Shaded region represents downstroke and non-shaded region represents upstroke.

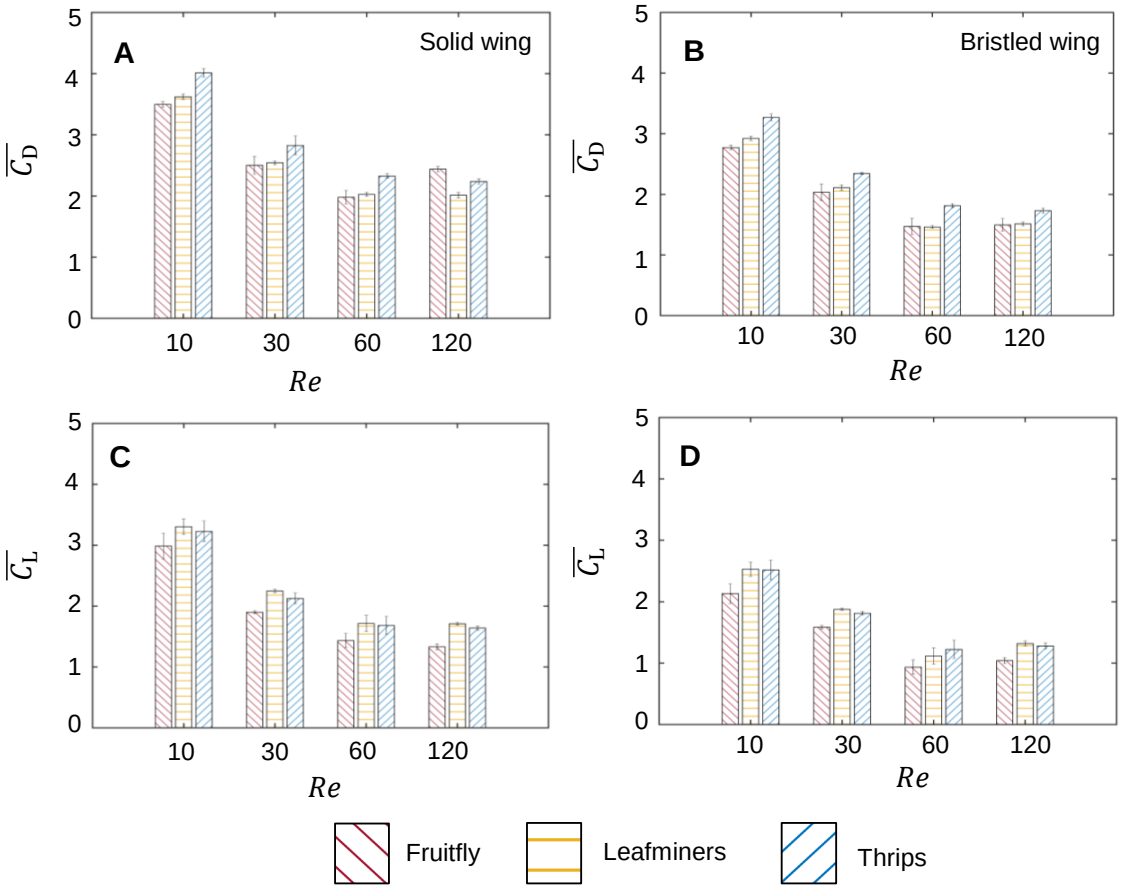

Figure 6.8: Cycle-averaged drag coefficient ($\overline{C_D}$) and lift coefficient ($\overline{C_L}$) for all the three wing kinematics (Fruitfly, Leafminers and Thrips) with varying *Re* for (A, C) single solid wing, (B, D) single bristled wing, respectively.

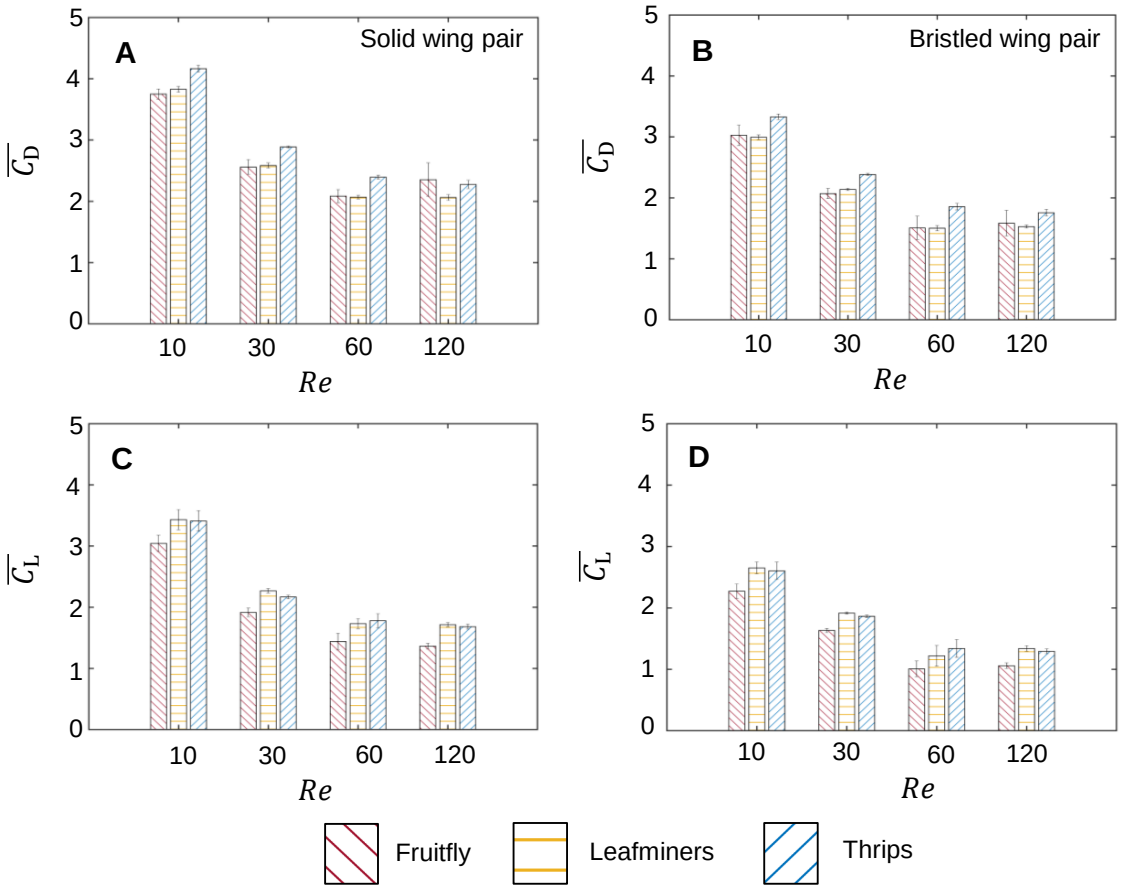

Figure 6.9: Cycle-averaged drag coefficient ($\overline{C_D}$) and lift coefficient ($\overline{C_L}$) for all the three wing kinematics (Fruitfly, Leafminers and Thrips) with varying *Re* for (A, C) solid wing pair, (B, D) bristled wing pair, respectively.

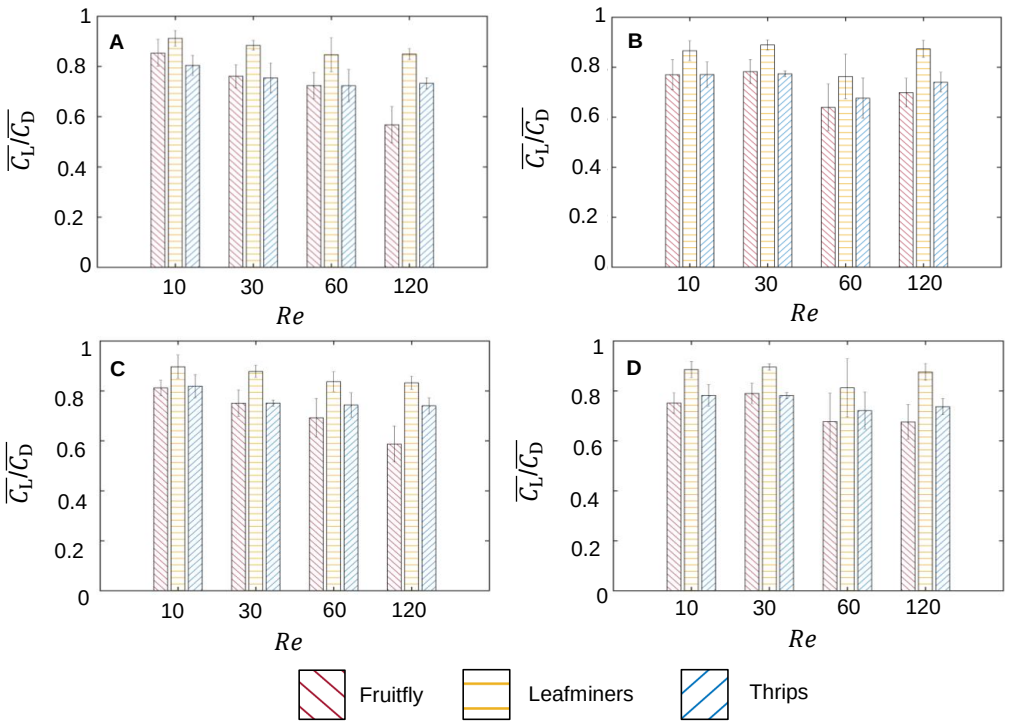

Figure 6.10: Ratio of cycle-averaged lift to drag coefficient ($\overline{C_L}/\overline{C_D}$) for all the three wing kinematics (Fruitfly, Leafminers and Thrips) with varying *Re* for (A) single solid wing, (B) single bristled wing, (C) solid wing pair, (D) bristled wing pair

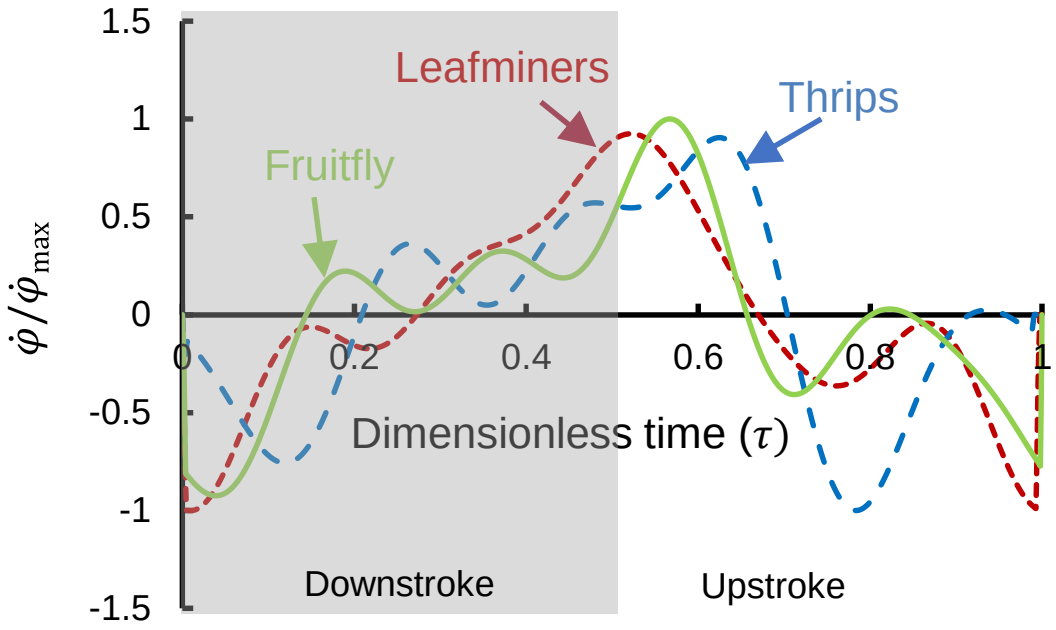

Figure 6.11: Non-dimensional pitch rate (ψ/ψ_{max}) of real wing kinematics of fruitly, leafminers and thrips measured from previously published studies (Fry et al., 2005; Cheng and Sun, 2016; Lyu et al., 2019*b*).

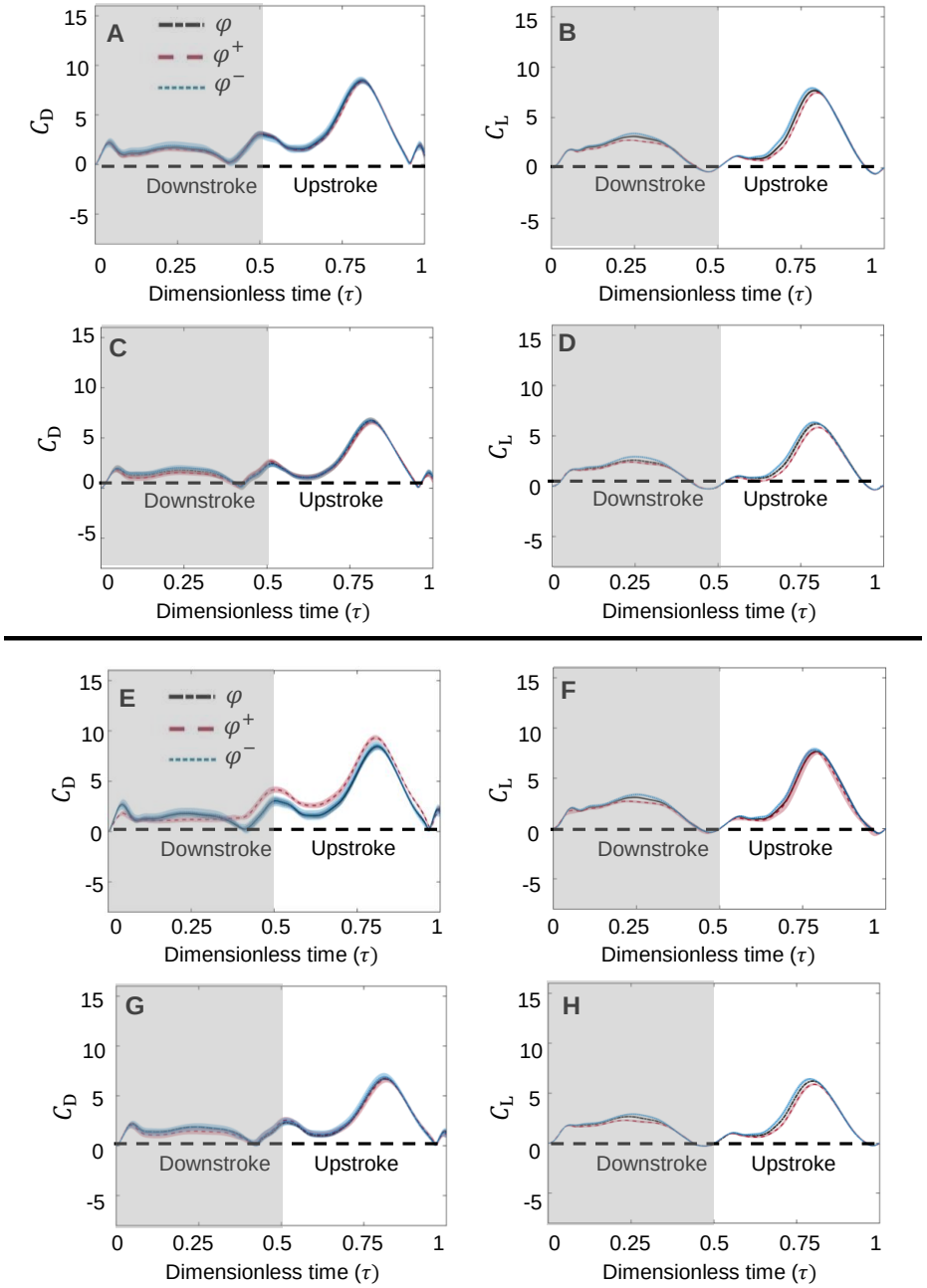

Figure 6.12: Time variation of drag coefficient (C_D) and lift coefficient (C_L) at Re = 30 for perturbated leafminer kinematics for (A,B) single solid wing, (C,D) single bristled wing, (E,F) solid wing pair, (G,H) bristled wing pair, respectively. Shaded region represents downstroke and non-shaded region represents upstroke. Positive perturbation is represented by ψ^+, Negative perturbation is represented by ψ^- and No perturbation is represented by ψ.

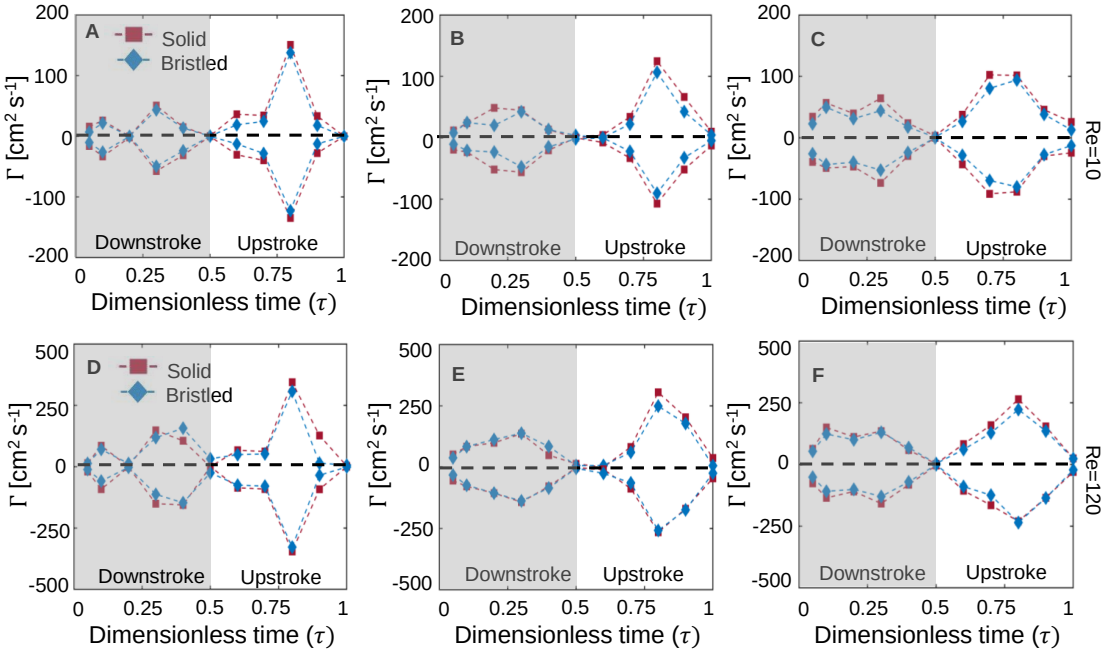

Figure 6.13: Time variation of LEV and TEV circulation (Γ) for single solid wing and single bristled wing performing (A,D) Thrips kinematics, (B, E) Leafminers kinematics, (C, F) Fruitfly kinematics at Re = 10 and 120, respectively. Top row: Re = 10, Bottom row: Re = 120. Shaded region represents downstroke and non-shaded region represents upstroke. Positive values of Γ in downstroke represents TEV circulation, negative values of Γ in downstroke represents LEV circulation. Positive values of Γ in upstroke represents LEV circulation, negative values of Γ in upstroke represents TEV circulation.

CHAPTER VII

SA 5: Parachuting with bristled wings

1 Introduction

Flying insects have fascinated fluid dynamicists for decades due to the complex fluid-structure interactions arising from the interplay of wing morphology and kinematics. Numerous studies have investigated the flapping flight of large-scale insects such as hawk moths, fruit flies and dragonflies using solid wing geometries (Ellington et al., 1996; Dickinson et al., 1999; Bomphrey et al., 2002; Sane, 2003; Wang, 2005; Lentink and Dickinson, 2009; Sane, 2016). In contrast, miniature flying insects ($<$ 2 mm in body length) such as thrips are capable of short-distance flapping flight using wings comprising of a solid membrane with long bristles at the fringes (Horridge, 1956; Weis-Fogh, 1975; Ellington, 1980; Loudon and Koehl, 1994). These tiny insects fly at Reynolds number (*Re*) on the orders of 1–10, where $Re=\rho U l/\mu$ (ρ=fluid density, μ=fluid viscosity (dynamic), U= wing tip velocity, l=characteristic length scale—wing chord being used to obtain the above *Re* range). At such small scales, viscous forces are significant and bristled wings help in drag reduction through viscous diffusion, limiting flow to leak through inter-bristle gaps (Santhanakrishnan et al., 2014; Jones et al., 2016; Kasoju et al., 2018; Ford et al., 2019; Lee et al., 2020*b*; Kasoju and Santhanakrishnan, 2021*a*).

Bristled/hairy appendages are common in animals and facilitate functions such as feeding, locomotion, gas exchange (Loudon and Koehl, 1994). As *Re* decreases, flow through an array of bristled appendages can transition from a leaky rake to a solid paddle (Lee and Leal, 1986; Cheer and Koehl, 1987; Koehl, 1995). A rake-like behavior can occur in sparsely bristled appendages with large inter-bristle gaps at higher *Re* (where *Re* is based

on bristle diameter and flow speed relative to the appendage), as flow leaks through the bristles due to the limited extent of shear layers formed around individual bristles that in turn minimizes aerodynamic interaction between neighboring bristles. An array of densely bristled appendages with narrow gaps behaves like a solid paddle at lower *Re*, where strong viscous diffusion of shear layers formed around the bristles result in a virtual fluid barrier, hindering flow from leaking through the array and influencing the aerodynamic loading on the array as a whole. This transition from solid paddle to leaky rake, based on the bristle diameter based *Re*, can help tiny insects to vary the aerodynamic loading on their wings by combing their bristles (Ellington, 1980), varying flapping frequency and modulating inter-wing angles.

Sunada et al. (2002) comparatively examined the aerodynamic performance of dynamically scaled bristled and solid (i.e., non-bristled) wing models under rotation and translation at chord-based Re=10, and reported minimal force reduction for the bristled wing relative to the solid wing. Subsequently, numerical (Davidi and Weihs, 2012) and analytical (Barta and Weihs, 2006) studies found that wings with closely-spaced bristles could generate approximately 90% of the force produced by solid wings with solid wing surface area to total wing area of 1:10. A recent study by Lee and Kim (2017) reported that the comb-like plate can achieve better aerodynamic performance per unit mass at low Reynolds number ($Re\approx10$) than at higher Reynolds number ($Re\approx100$). Another recent study by Kolomenskiy et al. (2020*b*) reported that a single scaled-up bristled wing modeled after tiniest beetles produced 10% less drag force with very small change in lift force in comparison to an equivalent solid wing model at $Re\approx10$. A central limitation of all these studies is in considering only a single wing in linear translation and/or rotation. During active flapping flight, tiny insects have been reported to employ complex stroke kinematics (Cheng and Sun, 2016) that involve wing-wing interaction (clap-and-fling Weis-Fogh 1973).

Studies of wing-wing interaction using solid wings have shown that clap-and-fling can augment lift by generating attached leading edge vortices on the wings (Weis-Fogh, 1973;

Lighthill, 1973; Spedding and Maxworthy, 1986; Birch et al., 2004; Miller and Peskin, 2005; Lehmann et al., 2005; Lehmann and Pick, 2007; Miller and Peskin, 2009; Arora et al., 2014; Cheng and Sun, 2019, 2021, 2018). By modeling bristled wings as porous surfaces, Santhanakrishnan et al. (2014) reported that flow leakage through the wings reduced drag during wing-wing interaction. Subsequently, Jones et al. (2016) reported that wing bristles reduce the drag force needed to fling wings apart. Kasoju et al. (2018) experimentally visualized inter-bristle flow and shear layer formation for varying gap width on a bristled wing and reported that bristled wings increases the lift over drag ratio during clap-and-fling at low Reynolds numbers. Ford et al. (2019) reported largest values of peak lift over peak drag ratios for bristled wing models with solid membrane area (A_{M}) to total wing area (A_{T}) ratio similar to thrips forewings (15% to 30%) at *Re* in the order of 10. Although previous studies have reported that bristled wings are beneficial during active flight, very little is known how a bristled wing perform aerodynamically during a passive flight.

During a passive flight, tiny insects do not use any wing stroke motion and fall slowly and stably. This mechanism is referred to as "Parachuting" (Alexander, 2013). Unlike gliding, parachuting relies on drag generation and not lift generation (Santhanakrishnan et al., 2014). Many previous studies (Willmarth et al., 1964; Field et al., 1997; Ern et al., 2012; Zhong and Lee, 2012) have investigated free fall of thin flat disc and found that at *Re* in the order of 1 to 10, they exhibit straight vertical motion in a steady state. In addition, including a hole in a disk enabled it to reach a stable motion in shorter distance compared to full solid disk (Vincent et al., 2016). Inspired from parachuting motion in tiny insects with bristled wings, Lee et al. (2020*a*) modelled bristled disks and experimentally investigate freely falling bristled disks over a wide range of Reynolds numbers by changing the number of bristles. They found that formation of fully formed virtual fluid barrier in the gaps between the bristles at low-Reynolds numbers would make it behave like a full circular disk and reduce their falling speeds and also aiding in stable free fall. Recent study by Cummins et al. (2018) reported that the porosity of the dandelion bristles were tuned precisely to stabilize

a unique form of a separated vortex ring which was responsible for the steady flight of a dandelion seed. This also resulted in maximizing the aerodynamic drag and also suppressing wake oscillation behind the body at $Re \sim \mathcal{O}(10^2)$. These studies suggest that bristled wings modelled as bristled disks have a more stable free fall compared to a full circular disk or a solid wing. High-speed video recordings of free-falling thrips (Santhanakrishnan et al., 2014) showed that thrips positioned their wings at a particular inter-wing angle ('V'-shaped) and parachuted downward. Smaller the inter-wing angle between the wings, larger will be the wing-wing interaction. (Loudon and Koehl, 1994) have reported that the presence of a nearby surface can alter leakiness through the gaps between bristled appendages. Therefore, varying inter-wing angles during parachuting significantly alters the fluid flow in the gaps between the bristle and needs to be further investigated. Also, none of the previous studies have looked at the aerodynamic performance of a bristled wing pair during steady fall with varying spacing between the bristles and varying inter-wing angle at *Re* on the orders of 10 to 100. In the present study, we comparatively examined aerodynamic characteristics of bristled and solid wing pairs during steady free-fall using numerical simulations and experiments. A wide range of inter-wing angles were examined across Reynolds numbers based on wing span (Re_s) ranging from 20–400.

2 Materials and methods

2. 1 Thrips measurements

We measured the inter-wing angle (θ) between the forewings and speed of the free fall (U) from a published parachuting video of thrips Santhanakrishnan et al. (2014) using ImageJ software (Schindelin et al., 2012). We extracted 15 consecutive snapshots from this video during the steady portion of free fall and found the average inter-wing angle was 97.4° with a standard deviation between the 15 frames to be 4° (see Fig. A.9. 5.1 in Supplementary Material of Appendices section). The speed of the free fall (U) was measured to be 0.6 m s^{-1}. Using a published image of thrips (*Frankliniella occidentalis* from Riley et al.

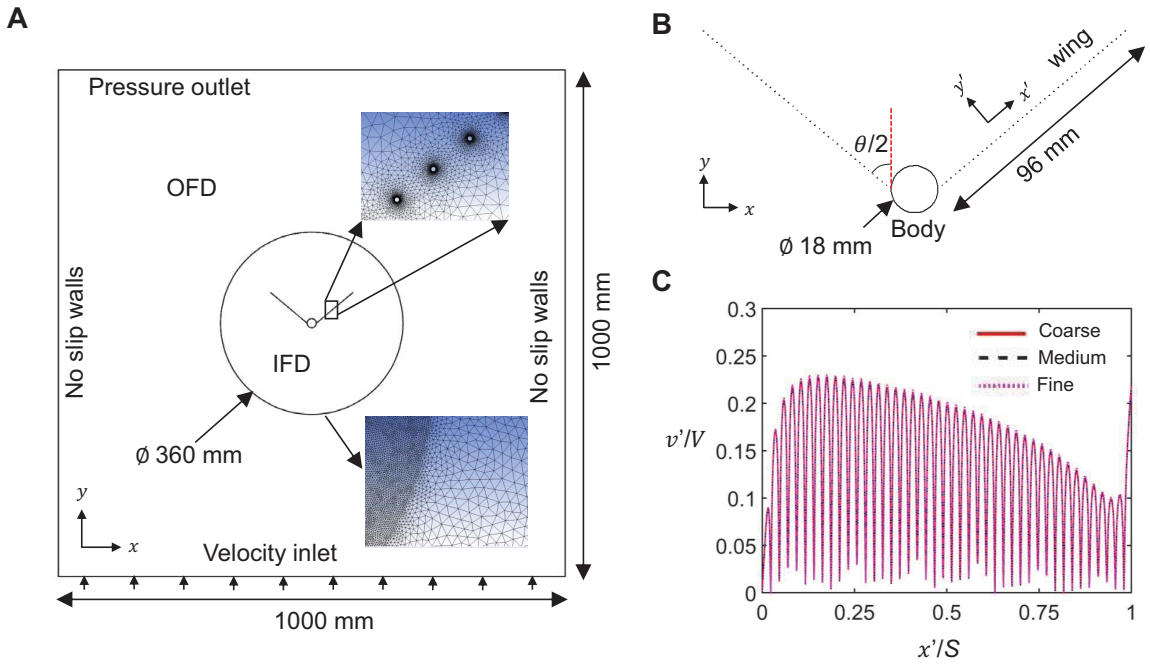

Figure 7.1: (A) Schematic of the numerical model used in this study. An inner fluid domain (IFD) of 360 mm diameter enclosed the scaled-up insect model, with greater mesh density as compared to the outer fluid domain (OFD). (B) Geometry representing scaled-up two-dimensional bristled wings attached to a circular body. θ=inter-wing angle. (x,y) represents global coordinates. (x',y') represents a local coordinate system, where x' was defined along the wing span and y' was defined perpendicular to the wing. v' and V' denote local vertical velocity component and local free stream velocity (both along y'), respectively. (C) Outcome of mesh independence tests showing non-dimensional velocity profile (v'/V') between coarse grid (2.85×10^5 cells), medium grid (6.67×10^5 cells) and fine grid (1.30×10^6 cells).

2011), we traced the outer edges of the body, measured the ratio of body length to forewing length, and forewing membrane width to forewing length. We measured body length as the vertical distance from where the antennae contact their head to the farthest tip of the abdomen. Similarly, wing length was measured as the distance from the wing root to the wing tip. The ratio of body length to wing length for *F. occidentalis* Riley et al. (2011) was calculated to be 1.63. Membrane width was determined by calculating the membrane area of the forewing and dividing this area by the forewing length. The ratio of forewing membrane width to forewing length was calculated to be 0.068. For an approximated wing span of 1 mm (Jones et al., 2016; Santhanakrishnan et al., 2014; Kasoju et al., 2020*b*),

Reynolds number based on wing span (Re_s) was measured to be around 40. Similarly, for an approximated bristle diameter of 1 μm (Jones et al., 2016), Reynolds number based on bristle diameter (Re_b) was measured to be around 0.04.

2. 2 Numerical model

We conducted two-dimensional (2D) numerical simulations using a commercial computational fluid dynamics (CFD) software ANSYS Fluent 2019 R3 (ANSYS, Inc., Canonsburg, PA, USA) to examine drag force generation and inter-bristle flow during steady flow for varying θ and Re_s. Previous studies (Jones et al., 2016; Ford et al., 2019; Kasoju and Santhanakrishnan, 2021*a*) have used 2D flow simplification to examine flow through bristled wings for $Re \sim \mathcal{O}(10) - \mathcal{O}(100)$.

The scaled-up insect body was modeled as a circular cylinder of 18 mm diameter and wing span (S) of 96 mm. Wing bristles were modeled as smaller circular cylinders spread across the wing span along a single line on both sides of the insect body (Fig. 7.1A,B). Two bristled wing geometries with densely and sparsely spaced bristles were considered for CFD simulations. For the densely-bristled wing model, the bristles were tightly packed along the wing span with 42 bristles in contrast to the sparsely-bristled wing model with 8 bristles on each side of wing membrane. For a rectangular bristled wing, the number of bristles (n) on both sides of a rectangular membrane can be calculated using the following equation (Kasoju et al., 2018):

$$n = \frac{2S}{D\left(\frac{G}{D}+1\right)} \tag{7.1}$$

where G represents the uniform spacing between adjacent bristles, D represents bristle diameter, and S represents the wing span. In a 2D bristled wing that is symmetric about the wing span (as modeled here, see Fig. 7.1B), each side of the wing membrane will thus include $n/2$ bristles. In our 2D CFD simulations, we modeled bristles only on one side of the membrane assuming the flow is symmetric about the wing span. The densely-

bristled wing model consisted of bristles of 0.2032 mm in diameter (D), while the sparsely-bristled wing model consisted of D=1 mm bristles. For both bristled wing models, we maintained S = 96 mm to be constant, along with identical inter-bristle spacing to diameter ratio (i.e., G/D) of 10. This is in the range of biologically relevant G/D observed in thrips species (Jones et al., 2016).

We divided the entire fluid domain into two regions for mesh generation: 1) an inner fluid domain (IFD) consisting of a circular region of 360 mm diameter (= 3.75S) that enclosed the body and the bristles; and 2) an outer fluid domain (OFD) consisting of a rectangular domain (1 m x 1 m) that enclosed the IFD (Fig. 7.1A). The enclosing walls of the OFD and the solid surfaces of insect model (within the IFD) were prescribed as no-slip surfaces. The triangular element size in the OFD was 5×10^{-3} m. To improve mesh quality, we increased the IFD mesh density by decreasing element size to 1×10^{-3} m. We further refined the mesh near the body and the bristles by using 5 layers of inflation to improve solution quality near the walls.

A semi-implicit method, pressure-linked equations-consistent (SIMPLEC), was used to solve pressure and velocity fields. The Green-Gauss node-based method was applied for spatial discretization. Second order and second order upwind spatial discretization were used for pressure and momentum, respectively. We assumed flow to be incompressible and laminar, which was appropriate for the Reynolds number (Re_s) range of 20-400 tested in this study. We used glycerin as the fluid medium with density (ρ) of 1259 kg m^{-3} and dynamic viscosity (μ) of 0.68 Pa s.The governing equations consisted of the 2D continuity equation and the Navier–Stokes equations,

$$\nabla.\vec{u} = 0 \tag{7.2}$$

$$\frac{\partial \vec{u}}{\partial t} + \vec{u}\cdot\nabla\vec{u} = -\nabla p + \mu\nabla^2\vec{u} + \rho\vec{g} \tag{7.3}$$

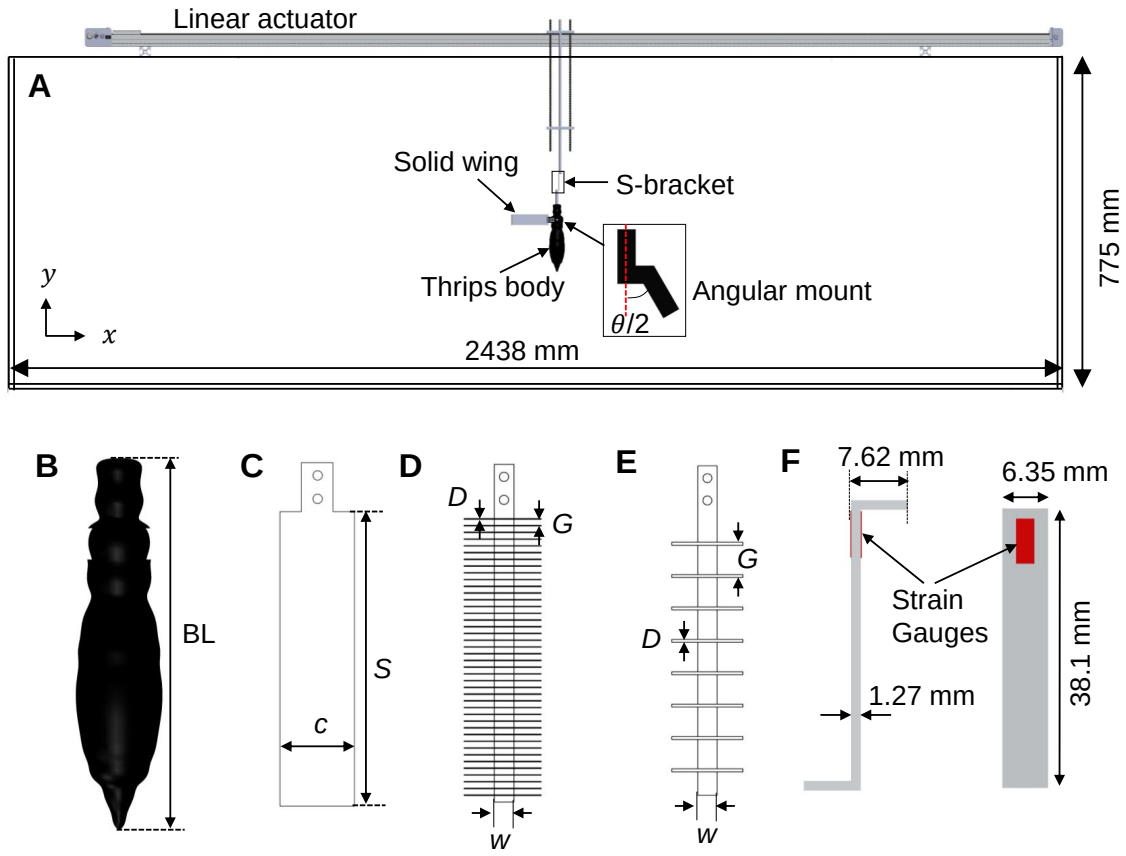

Figure 7.2: Dynamically scaled model and experimental setup. (A) Front view of the 2.44 m (8 ft) long glass tank with parachuting model mounted on top of a linear actuator. Parachuting model consisted of a scaled-up body of thrips with angular mounts to position the wings at different inter-wing angles defined using θ. (B) Body of thrips *Franklinella occidentalis*, traced from Riley et al. (2011) and scaled-up by 108 times of the true BL. BL=body length=156 mm. (C) Solid wing model. S=wing span=96 mm; c=chord=24 mm. (D) Densely-bristled wing with identical S and c as the solid wing. Bristles were fabricated using stainless steel wires (0.2032 mm diameter) and attached on top of a solid membrane of width w=6.5 mm. (E) Sparsely-bristled wing with identical S and c as the solid wing. Stainless steel wires of 1 mm diameter were used to fabricate the bristles. The ratio of inter-bristle spacing (G) to bristle diameter (D) was identical between sparsely-bristled and densely-bristled wing pairs (G/D=10). (F) A custom S-bracket with strain gauges was used to measure drag force generated when the entire model (body and wing pair) was in steady linear translation in water-glycerin mixtures at Reynolds number based on span (Re_s) of 20, 40 and 400.

where t, $\vec{u}$, $\vec{g}$, p denote time, 2D flow velocity, gravitational acceleration and pressure field, respectively. The convergence residuals for x-velocity (u), y-velocity (v) and continuity were set to 1×10^{-6} with maximum number of iterations of 15,000. Drag force (in N) acting on the body and the bristles were calculated separately.

A relative coordinate system was defined with respect to the bristled wing (i.e., 2D array of bristles) such that x' was defined along the wing span and y' was defined perpendicular to the bristle array (Fig. 7.1B). For mesh independence studies, three meshes were tested (Fig. 7.1C). Velocity profiles were extracted along the wing span along the line connecting the centers of the bristles in the (x',y') coordinate system. The non-dimensional velocity profile along y' (v'/V') was defined using local velocity (v') and maximum flow velocity (V') in (x',y') coordinate system. The velocity profile converged as the number of elements were increased. The difference in non-dimensional velocity profiles between the fine grid and medium meshes was less than 1%. We used the medium grid for all our computational simulations.

2. 3 Experimental arrangements

We used a motorized, belt-driven linear actuator capable of 2 m maximum travel (model X-BLQ-2095, Zaber Technologies Inc., Vancouver, British Columbia, Canada) to translate a wing pair attached to the body (Fig. 7.2A). The actuator was mounted on top of a 2.44 m long (96 in.) x 0.77 m tall (30.5 in.) x 0.65 m wide (25.5 in.) glass tank filled with water-glycerin mixture (Fig. 7.2A). The model (wing pair + body) was coupled to a custom 'S'-bracket that in turn was suspended from the stage of the linear actuator using screw rods and D-shafts. The model was submerged mid-depth inside the tank, such that the bottom face of the wing closer to the tank floor were approximately 0.38 m (15 in.) away from the tank floor. To vary inter-wing angle (θ), 3D printed angular mounts were used to connect the wings to the body. These angular mounts were attached to the body via a slot built in on the sides of the body (Fig. 7.2A). The wings started and ended their translation at a distance

of 0.64 m (25 in.) from either side wall to minimize the influence of confining boundaries.

Scaled-up physical models of solid and bristled wing pairs were designed with a wing span (S) of 96 mm, identical to S used in the numerical model. Based on measurements of body length (BL) and membrane width (w) in terms of wing length (latter being the same as S) obtained from published thrips images (as described in 2A), and to obtain aspect ratio (S over chord, c) of 4 relevant to thrips, we calculated BL=156 mm, w=6.5 mm and c=24 mm for the physical models. Using the calculated model BL, we scaled-up the 2D sketch of the outer edge of the thrips body by 108 times and designed a 3D body by revolving the scaled up 2D sketch (Fig. 7.2B). The body was then 3D printed on a CraftBot 3D printer (Craft Unique, Stillwater, OK, USA) using polylactic acid (PLA) filament.

We fabricated a rectangular solid wing pair (S=96 mm; c=24 mm; w=6.5 mm) from laser cutting a clear acrylic sheet measuring 3.175 mm in thickness (Fig. 7.2C). A densely-bristled wing pair (Fig. 7.2D) and a sparsely-bristled wing pair (Fig. 7.2E), each varying in the number of bristles, were fabricated with the same S, c and w as the solid wing pair. For densely-bristled wings, we used stainless steel wires measuring 0.2 mm in diameter (D) as bristles. For sparsely-bristled wings, we used D=1 mm glass rods. For both bristled wing models, we maintained the same ratio of inter-bristle spacing (G) to bristle diameter (i.e., G/D) ratio of 10. The wing models tested in this study were simplified to rectangular shape to minimize the variability of flow along the wing span. 2D simplification that was used in the numerical model. In addition, bristle length on either side of the membrane of 8.75 mm was maintained constant for both the bristled wing pairs.

A trapezoidal profile was prescribed to the linear actuator for towing the parachuting model. Total travel distance was fixed to 1 m. Acceleration (start of model motion) and deceleration (end of model motion) were identically set to 12.25% of the total towing distance (1000 mm). The model was translated at a constant (i.e., steady-state) velocity (V) in between the acceleration and deceleration phases. V was varied to modify Re_{s}, defined via the relation,

$$Re_s = \frac{\rho V S}{\mu} \tag{7.4}$$

where μ was maintained constant across all the experiments.

Using the same trapezoidal profile the model was allowed to return back (backward translation) to its home position after one cycle of forward translation. This allowed us to tow the model for multiple forward translations. The steady translational velocity (V) and cycle duration to complete one forward translation (T) for each $Re_s$are provided in Table 7.1. Once the model reaches the home position after a cycle of forward translation, we paused for about 30 sec before the start of next forward translation. This allowed us to ensure initial conditions were identical between different cycles. For data analysis, we defined dimensionless time (τ) as the ratio of instantaneous time (t) to time taken for forward translation (T).

2. 4 Test conditions

For both experimental and computational studies, each wing pair (i.e., solid, densely-bristled, sparsely-bristled) was tested at Re_s of 20, 40, and 400. Also, θ was varied for each Re_s from 20° to 180°, in steps of 40°.

For the numerical study, we used water-glycerin mixture as the fluid medium (μ=0.68 Pa s; ρ=1259 kg m^{-3}). The corresponding inlet velocities for Re_s of 20, 40 and 400 were 0.1125 m s^{-1}, 0.225 m s^{-1} and 2.25 m s^{-1}, respectively.

For the experiments, we used two different water-glycerin mixtures: μ=0.68 Pa s for Re_s=20 and 40; and μ=0.092 Pa s for Re_s=400. The kinematic viscosity ($\nu = \mu/\rho$) of the fluid media were measured using a Cannon-Fenske routine viscometer (size 400, Cannon Instrument Company, State College, PA, USA). We calculated the steady translational velocity (V) from equation 7.4, using desired $Re_s$and measured ν of the fluid medium.

Re_s	V (m s^{-1})	T (s)	T_s (s)
20	0.1125	11.07	6.70
40	0.225	5.54	3.35
400	0.3106	4.01	2.43

Table 7.1: Test conditions showing Reynolds numbers (Re) and their corresponding steady translational velocity (V), cycle time (T) and steady translational time period (T_s).

2. 5 Definitions of calculated quantities

2. 5.1 Force measurements

For the experimental study, force data was acquired during steady translation (forward motion) using custom 'S'-shaped brackets with two uniaxial strain gauges bonded on either side of the bracket in half-bridge configuration (Fig. 7.2F). A LabVIEW program (National Instruments Corporation, Austin, TX, USA) was used to trigger data acquisition at the start of model motion. A signal conditioning unit connected to the strain gauges provided analog voltage signal as the output, and a data acquisition board (model NI USB-6210, National Instruments Corporation, Austin, TX, USA) was used to acquire the raw voltage data. Force data was acquired for complete forward translation (i.e., τ=0–1) at a sampling rate of 10 kHz for each Re_s (20, 40, 400) and for each θ (20°, 60°, 100°, 140°, 180°). We used the same post-processing procedure as described in Kasoju et al. (2018) and is described briefly here. Voltage signal was recorded prior to the start of model motion to obtain the baseline offset. Raw voltage data acquired during model motion were next processed using a custom MATLAB script (The Mathworks Inc., Natick, MA, USA), using a third order low-pass Butterworth filter with a cutoff frequency of 24 Hz. Separately, we also acquired voltage data using the same S-bracket and strain gauges assembly when towing just the body (without a wing pair) for all Re_s and subtracted the filtered body-only voltage data from the filtered voltage data (generated by wing pair + body) to isolate the filtered voltage data generated by a wing pair. The baseline offset was then time-averaged and subtracted from the filtered voltage data corresponding to just the wing pair (after body-only filtered voltage data were subtracted). The S-brackets were calibrated manually using a separate

setup described in Kasoju et al. (2018)), and the calibration was applied to the filtered voltage data obtained from the previous step to calculate drag force (F_{D}) generated by a wing pair during steady linear translation.

For both the experimental and computational studies, the dimensionless drag coefficient (C_{D}) generated by a wing pair during steady linear translation was calculated using the relation:

$$C_{\mathrm{D}} = \frac{F_{\mathrm{D}}}{\frac{1}{2}\rho V^2 A} \tag{7.5}$$

where F_{D} denotes measured drag force (in N) and A denotes the frontal surface area of both the wings. For the experimental study, standard deviations were calculated for C_{D} across 15 non-consecutive cycles of steady forward translation. C_{D} was initially time-averaged during steady translational time period (T_{s} in Table 7.1) and finally cycle-averaged across the 15 non-consecutive cycles.

2. 5.2 Non-dimensional vorticity

The primary reason for performing numerical simulations in conjunction with experiments was to characterize flow through inter-bristle gaps, in order to understand the relation between inter-bristle flow (not resolved in experiments) and drag generated by wing pairs as a function of varying θ and Re_{s}. Out-of-plane component of vorticity (ω_z) was calculated in ANSYS Fluent 2019 R3 (ANSYS, Inc., Canonsburg, PA, USA) from 2D velocity fields obtained via numerical simulations, using the relation:

$$\omega_z = \frac{\partial v}{\partial x} - \frac{\partial u}{\partial y} \tag{7.6}$$

where u and v are the velocity components along the x and y coordinates of the fluid domain, respectively. ω_z obtained from numerical simulations was non-dimensionalized by dividing ω_z by V^2/ν. The rationale for using this scaling was to examine how viscous dis-

sipation (proportional to ν) impacted kinetic energy of the inter-bristle flow (proportional to V^2), where V is the steady velocity prescribed at the inlet of the 2D numerical model. Alternatively, if we assume ω_z scales as V/L (L being a characteristic length scale, say S), then the proposed dimensionless vorticity ($\omega_z \nu/V^2$) would scale as ν/VL, which corresponds to $1/Re_L$. A large value of the proposed dimensionless vorticity can thus be interpreted as viscous dissipation being significant as compared to the kinetic energy (and vice versa).

2. 5.3 Leakiness

The inter-bristle flow along the wing span can experience a 'leaky rake to solid paddle' transition (Loudon and Koehl, 1994) depending on θ and Re_s. A bristled wing can thus potentially function as a solid/non-porous plate with no (or minimal) flow through the inter-bristle gaps, or as a sieve that permits fluid to leak through the inter-bristle gaps. The converged velocity fields from the simulations were used to characterize fluid volume leaked through the bristles along the wing span. Cheer and Koehl (1987) proposed a non-dimensional parameter called leakiness (Le) to characterize the extent of flow leakage through bristled appendages. We calculated Le using the volumetric flow rate per unit depth (Q) of inter-bristle flow in the direction opposite to the inlet flow using the relation:

$$Le = \frac{Q_{\text{viscous}}}{Q_{\text{inviscid}}} \tag{7.7}$$

where Q_{viscous} represents flow rate leaked through the inter-bristle gaps under viscous conditions (calculated from the velocity field along y'-axis in Fig. 7.1B), and Q_{inviscid} represents ideal flow rate that would be leaked through the inter-bristle gaps under no viscous resistance (Kasoju et al., 2018).

3 Results

3. 1 Numerical model: aerodynamic force generation

To understand how the aerodynamics changes with varying the inter-wing angle (θ), we investigated the drag force acting on the bristles alone during steady flow at Re_s = 20, 40 and 400. We further calculated the drag coefficient (C_D) during steady translation using equation 7.5. We observed a non-linear increment in C_D with increasing inter-wing angle (θ) for both dense and sparse wing models at all Re_s tested (Fig. 7.3A-C). Although the drag coefficient (C_D) for θ = 20° to 60° were almost similar between dense and sparse wing model for all Re_s, further increasing θ showed significant changes in C_D between dense and sparse wing model. At Re_s = 400, we observed C_D to plateau for both dense and sparse wing models for $\theta \geq 100°$ (Fig. 7.3C). From these results, we observed that at low Re_s, drag force generated by a bristled wing (both dense and sparse wing model) increases with increasing θ. However at high Re_s in the order of 100, we observed the drag forces to plateau for $\theta \geq 100°$ irrespective of bristled wing model.

3. 2 Experimental study: aerodynamic force verification

As a part of verification and validation, we performed steady translation of solid and bristled wing models for varying θ (20° - 180°) at Re_s = 20, 40 and 400 (Fig. 7.3D-F). Drag coefficients were measured in the horizontal x-direction (Fig. 7.3D) during entire translation. Here, we presented the drag coefficients averaged across the steady state (C_D) with varying θ for all Re_s (Fig. 7.3D-F). We observed a non-linear increment in average drag coefficient (C_D) with increasing inter-wing angle for all wing models at Re_s = 20, 40 (Fig. 7.3D,E). Dense bristled wing model was found to match with solid wing model until θ = 100° and then showed to decrease at both Reynolds numbers (Re_s= 20 and 40). However, at Re_s = 400 (Fig. 7.3F), we found C_D for a solid and dense bristled wing model to plateau for $\theta > 60°$. Also, the difference in C_D between a solid and a dense bristled wing model

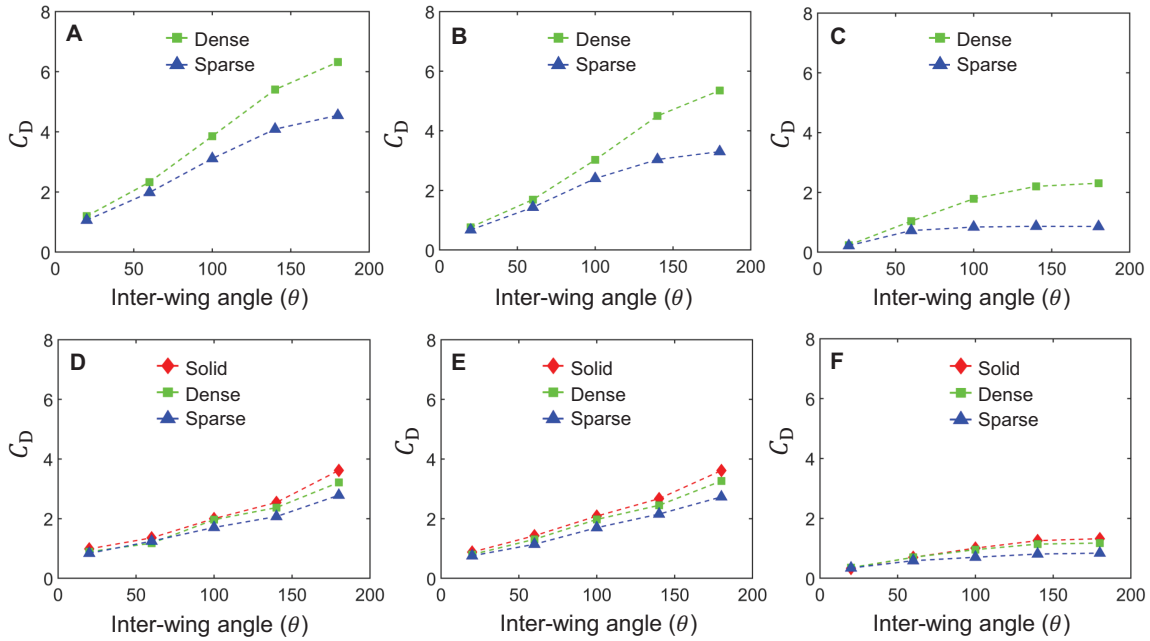

Figure 7.3: Drag coefficients (C_D) measured on the bristles for all the wing models (Dense and Sparse) for varying inter wing angles (θ) numerically (A-C) and experimentally (D-F) at Re_s= 20 (A,D), Re_s = 40 (B, E), Re_s = 400 (C,F).

are lower suggesting that a dense bristled wing model behaves similar to that of a solid wing. Similar to dense bristled wing model, C_D for sparse wing model was found to keep up with solid wing at low inter-wing angles (θ) of $\theta = 20^\circ$ and 60° at all Reynolds numbers. At Re_s = 400, C_D for sparse wing model was found to plateau for $\theta > 60^\circ$. Independent of solid wing, C_D for both the bristled wings were found to follow close to similar trend to that of the computational results with noticeable differences in magnitudes. These changes between numerical and experimental study are owed to- 1) use of three-dimensional wings affecting the flow in the chord-wise plane and 2) Inertial forces acting on the wings during translation while towing the experimental model could also effect the drag acting on the wings. Considering the above reasoning, we can confirms that the results obtained from the numerical solution are acceptable.

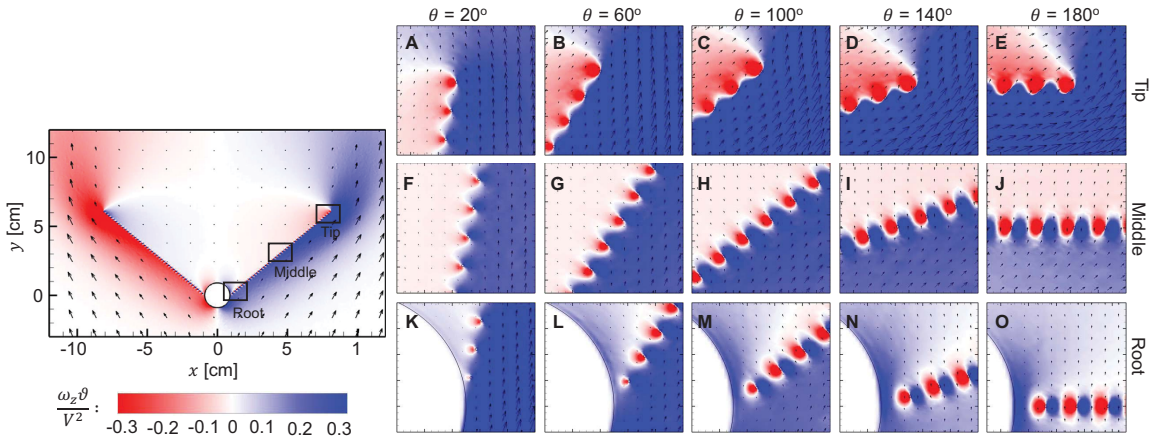

Figure 7.4: Velocity vector fields overlaid on non-dimensional vorticity contours for a dense bristled wing at Re_s =20 for various inter-wing angles (θ). The zoomed-out image on the left gives an overall understanding of non-dimensional vorticity distribution on the wing for $\theta = 100^\circ$. Inter-bristle flow with non-dimensional vorticity contours for varying θ are presented at the wing tip (A)-(E), middle of the wing (F)-(J) and wing root (K)-(O).

3. 3 Non-dimensional vorticity distribution

In this study, we looked at the flow characteristics while varying the θ for two bristled wing designs under steady flow at $Re_s = 20$, 40 and 400. The non-dimensional vorticity ($\omega_z v/V^2$) was calculated from the numerical solution for the entire fluid domain. For a dense bristled wing model with $\theta = 100^\circ$ at $Re_s = 20$, we observed strong non-dimensional vorticity to spread across the wing span (zoomed out image in Fig. 7.4). The non-dimensional vorticity distribution on the bristled wings were symmetric with respect to y-axis. As the Reynolds number increased (Re_s= 400), the strength of non-dimensional vorticity significantly decreased along the wing span while still maintaining the symmetricity about y-axis (Fig. 7.5).

Similar to dense bristled wing model, we observed strong non-dimensional vorticity along the wing span for a sparse bristled wing model at $Re_s = 20$ (Fig. 7.6). As the Reynolds number increased to $Re_s = 400$, the strength of the non-dimensional vorticity decreased along the wing span (Fig. 7.7). Interestingly, due to sparsely spaced bristled arrangement, we can clearly observe the formation of non-dimensional vorticity pair (positive and negative vorticity) on each bristle for a sparse bristled wing. This formation of vorticity pair

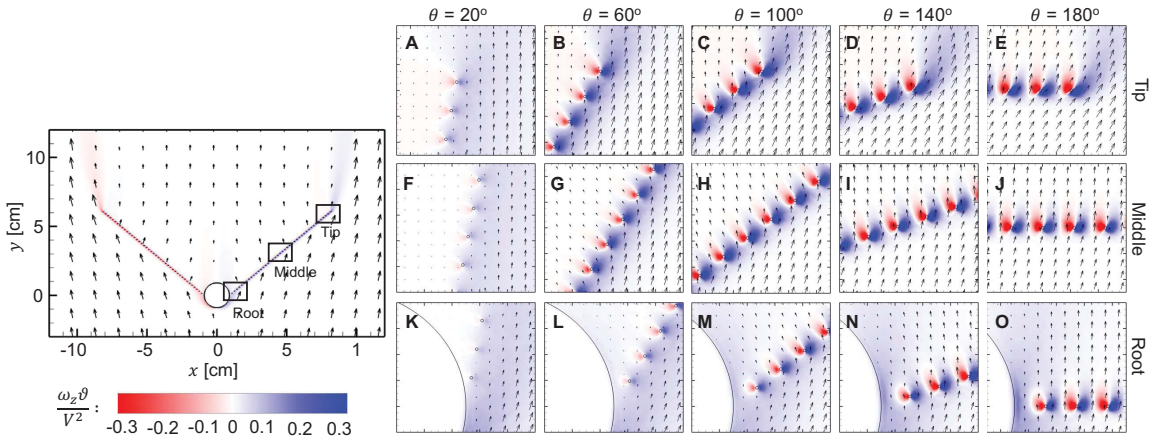

Figure 7.5: Velocity vector fields overlaid on non-dimensional vorticity contours for a dense bristled wing at $Re_s = 400$ for various inter-wing angles (θ). The zoomed-out image on the left gives an overall understanding of non-dimensional vorticity distribution on the wing for $\theta = 100^\circ$. Inter-bristle flow with non-dimensional vorticity contours for varying θ are presented at the wing tip (A)-(E), middle of the wing (F)-(J) and wing root (K)-(O).

holds true for a dense bristled wing model also, but due to densely packed bristles it was not clearly visible from zoomed out images in Fig. 7.4,7.5. Between a dense bristled wing model and a sparse bristled wing model at $Re_s = 20$, we observed the non-dimensional vorticity to seep in through the inter-bristle spacing for a sparsely spaced bristled wing. Therefore for sparsely spaced bristled wing model, the non-dimensional vorticity magnitude in the inter-wing spacing was higher compared to that of a densely packed bristled wing model. Although as Re_s increased to 400, we still don't see a significant diffusion of non-dimensional vorticity through the bristled spacings into the inter-wing spacing for dense bristled wing model (Fig. 7.5). However, for the sparsely spaced bristled wing model at $Re_s = 400$, we observed the non-dimensional vorticity to ooze through the spacing's via formations of elongated vorticies on each bristles in the direction of the flow (Fig. 7.7).

The non-dimensional vorticity distribution will give a better understanding of strength of viscous energy to kinetic energy in the flow. Higher the magnitude of non-dimensional vorticity, viscous energy would be higher compared to kinetic energy and vice-versa. At low Re_s, we observed higher magnitudes of non-dimensional vorticity around the bristled wings suggesting viscous energy in dominant in the flow. At high Re_s, we observed lower

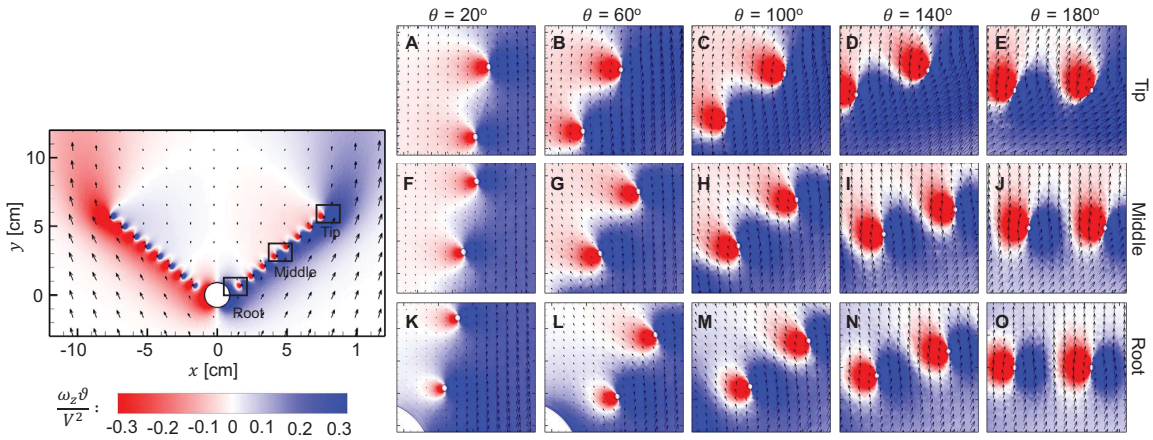

Figure 7.6: Velocity vector fields overlaid on non-dimensional vorticity contours for a sparse bristled wing at $Re_s = 20$ for various inter-wing angles (θ). The zoomed-out image on the left gives an overall understanding of non-dimensional vorticity distribution on the wing for $\theta = 100^\circ$. Inter-bristle flow with non-dimensional vorticity contours for varying θ are presented at the wing tip (A)-(E), middle of the wing (F)-(J) and wing root (K)-(O).

magnitudes of non-dimensional vorticity around the bristled wings suggesting kinetic energy in dominant in the flow.

To understand the flow characteristics in the gap between the bristles, we presented zoom in sequences of non-dimensional vorticity distribution at three locations along the wing span: 1) wing tip, 2) middle and 3) wing root (Fig. 7.4, 7.5, 7.6, 7.7; A-O). For a dense bristled wing model at $Re_s = 20$, as we move from wing tip to wing root, the strength of both positive and negative non-dimensional vorticity on the bristles decreases for any θ (Fig. 7.4). The magnitude of non-dimensional vorticity on each bristle was found to increase with increasing θ at all three locations on the wing (Fig. 7.4). Also at lower θ, the non-dimensional positive vorticity around each bristle was found to be highly diffused throughout the entire wing span thereby blocking the gaps between the bristles (Cheer and Koehl, 1987; Loudon and Koehl, 1994; Lee and Kim, 2017; Lee et al., 2020*b*; Kasoju et al., 2018; Ford et al., 2019). In contrast to a dense bristled wing model, there was little to no variation in the non-dimensional vorticity distribution on each bristle at wing root and middle of the wing for a sparsely spaced bristled wing model (Fig. 7.6) for any θ. At the wing root, the bristle was sufficiently far enough from the body and therefore have no

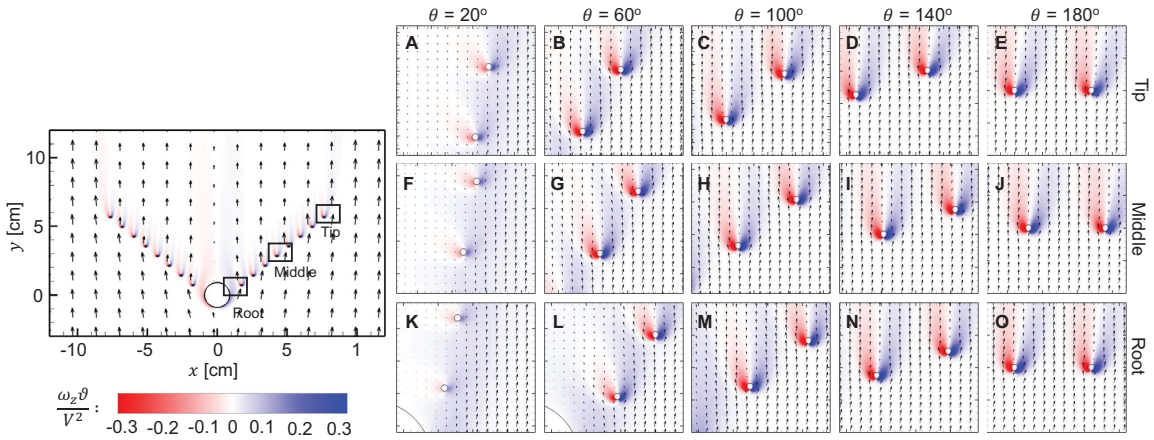

Figure 7.7: Velocity vector fields overlaid on non-dimensional vorticity contours for a sparse bristled wing at $Re_s = 400$ for various inter-wing angles (θ). The zoomed-out image on the left gives an overall understanding of non-dimensional vorticity distribution on the wing for $\theta = 100^\circ$. Inter-bristle flow with non-dimensional vorticity contours for varying θ are presented at the wing tip (A)-(E), middle of the wing (F)-(J) and wing root (K)-(O).

significant interaction with vorticity generated around the body. However at the wing tips for any θ, the non-dimensional positive vorticity around each bristle were found to diffuse into each other behaving like a single wavy vortex similar to that observed in dense bristled wing.

From a dense bristled wing model to a sparse bristled wing model, we have the spacing between the bristles and the diameter of the bristles to increase. This led to increase in the size of the non-dimensional vorticity (both positive and negative) on a bristle for a sparsely spaced bristled wing model. Also, as the inter-wing angle (θ) increased from 20° to 180°, we observed the positive and negative non-dimensional vorticity around each bristle to become symmetric at the wing root and the middle of the wings for both dense and sparse bristled wings. Since the strength of non-dimensional vorticity around each bristle for a sparse bristle wing model is little lower than a densely packed bristled wing model. Based on the positive and negative non-dimensional vorticity distribution around each bristles and the vorticity seep inside the inter-wing spacing, we expect that the non-dimensional vorticity formed around each bristle for a dense packed bristles acts like barrier to allow the flow to leak through compared to sparse bristled wing model at $Re_s = 20$.

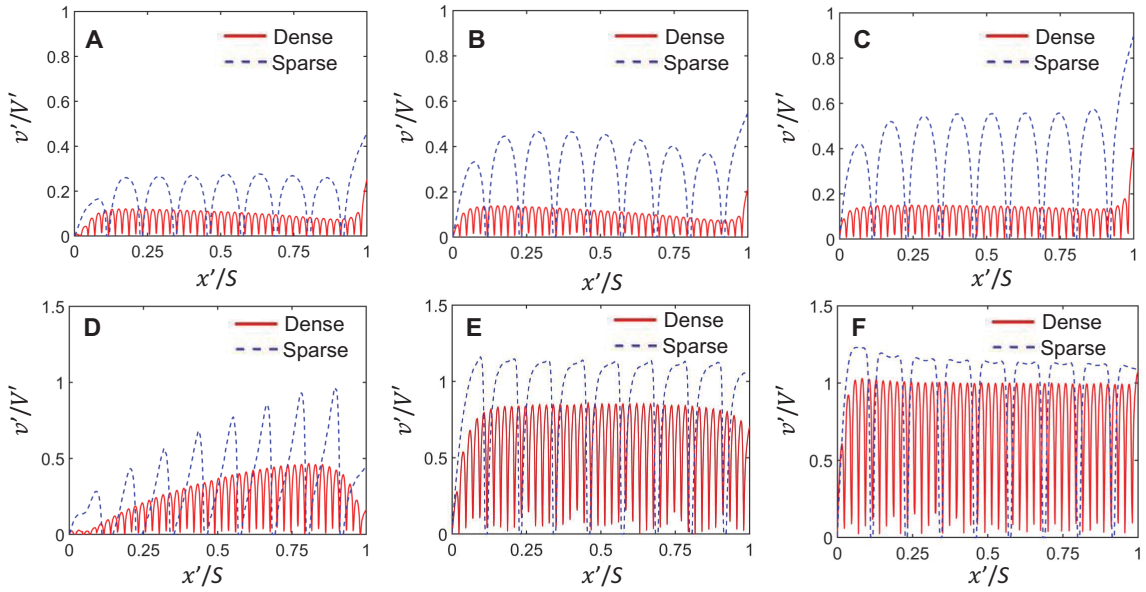

Figure 7.8: Non-dimensional velocity profile (v'/V') along the wing-span (represented using non-dimensional term x'/S) for varying inter-wing angle, θ (A, D) 20°, (B, E) 100° and (C, F) 180°, at Re_s = 20 (A-C) and 400 (D-F) for dense and sparse wing models.

As the Re_s increased to 400, irrespective of θ, we observed symmetric positive and negative non-dimensional vorticity around each bristle for both densely spaced and sparsely spaced bristled wings. For a dense bristled wing model, we observed the non-dimensional vorticity strength to decrease from wing tip to the root of the wing for $\theta < 100°$. In contrast to dense bristled wing model, we didnot observe such trend in sparse bristled wing model. In addition, the non-dimensional vorticity around each bristle for sparsely spaced wing model were elongated in the direction of the flow suggesting the diffusion of vorticity through the bristle spacing. From these results, we expect that a sparsely spaced bristled wing model would allow more fluid to leak through the bristle spacing compared to densely packed bristled wing model at Re_s = 400.

3. 4 Non-dimensional velocity profiles

Based on section 3C, non-dimensional vorticity distribution provided an understanding of viscous energy to kinetic energy in the flow. At high Re_s and for sparsely spaced bristled wing model, we observed more kinetic energy in the flow fields in the gaps between the

bristles. This can further be validated by verifying the velocity profile in the flow field. The velocity profiles were extracted along the wing span on a line connecting the centers of the bristles to the wing root. The extracted velocities (v) were transformed into $x'y'$ reference frame (v', Fig. 7.1B) and were made dimensionless using free stream velocity along y' given by V'. The non-dimensional velocity profile (v'/V') will give us better understanding of the flow velocity distribution along the wing span. v'/V' value of 1 indicates that velocity in inter-bristle gap is equivalent to free stream velocity and the surrounding bristles have no influence on the flow.

At $Re_s = 20$ for both dense and sparse wing models, the non-dimensional velocity distribution was observed to remain almost constant through the wing span except at the wing root and the wing tip at all θ (Fig. 7.8A-C). The variation in velocity profile at the wing root was due to the flow interaction between body and the bristles are different compared to flow interaction between bristle-bristle. Similarly at the wing tips, there is sudden transition in the flow due to absence of bristles in the fluid medium after the wing tip. At low Re_s due to significant viscous diffusion in the flow leading to asymmetric flow interactions at the wing root and tips in comparison with the middle of the wing, the velocity profile at the wing root and the tips are different from the middle of the wing. In addition, we observed little increase in non-dimensional velocity with increasing θ from 20° to 180° for dense wing model at $Re_s = 20$ (Fig. 7.8A-C). However for sparse wing model, non-dimensional velocity increased noticeably with increasing θ from 20° to 180°. The non-dimensional velocity for sparse wing is significantly higher compared to dense wing model suggesting leaky flow.

At $Re_s = 400$ for both dense and sparse wing models, the non-dimensional velocity distribution was observed to vary significantly along the wing span at low inter-wing angles ($\theta = 20°$) with least velocities near the wing root (Fig. 7.8D-F). For inter-wing angles, $\theta \geq 100°$, the non-dimensional velocity distribution was observed to remain almost constant through the wing span except at the wing root and the wing tip for a dense bristled wing

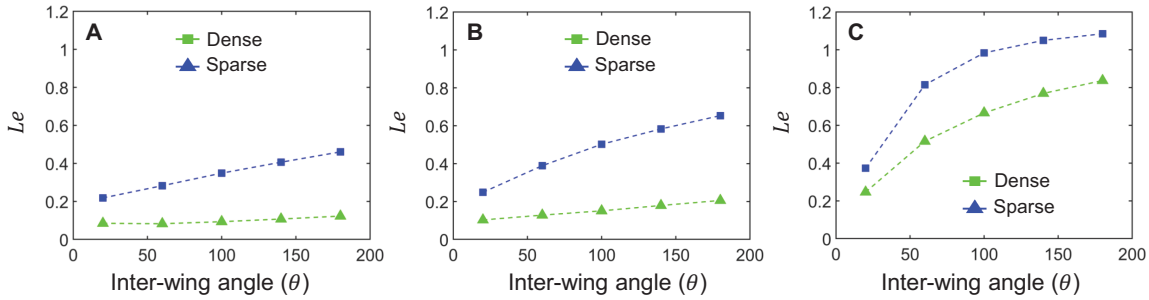

Figure 7.9: Leakiness (*Le*) measured along wing span on a line connecting centers of the bristles for all the wing models (Dense and Sparse) for varying inter-wing angles (θ) at (A) $Re_s = 20$, (B) $Re_s = 40$, (C) $Re_s = 400$.

model. In contrast, for a sparse bristled wing model, for $\theta \geq 100°$, the non-dimensional velocity distribution was observed to remain almost alike through the wing span. This suggests that at high Re_s and $\theta \geq 100$, the flow through the bristles has reached an optimum condition for a sparse bristled wing model. Similar to $Re_s = 20$, the non-dimensional velocity was higher for sparse wing model compared to dense wing model. With increasing θ, we observed the non-dimensional velocity to reach 1 and above for both dense and sparse wing models. This suggests that at higher Re_s and higher θ, bristles help in accelerating the fluid in the gaps with respect to free stream velocity which is in agreement with non-dimensional vorticity plots presented in Section 3C.

In process of quantifying the amount of fluid leaked through the bristles gaps, we calculated leakiness (*Le*) using equation 7.7 on the same line where non-dimensional velocity profiles were presented. At $Re_s = 20$, *Le* was found to increase linearly with increasing θ for sparse wing model. In contrast, we observed little to no variation in *Le* with increasing θ for dense bristled wing model. These results are in agreement with non-dimensional vorticity distribution (Fig. 7.4,7.6), where small counter rotating vorticies with high viscous energy around the bristles blocks the fluid to flow through the gaps between the bristles. This was also further evident in non-dimensional velocity profiles (Fig. 7.8), where the profile looked alike for all inter-wing angles (θ). At $Re_s = 40$, *Le* was found to increase with increasing θ for both sparse and dense wing models. The increase in *Le* was non-linear for

sparse wing model and linear for dense wing model. As the Re_s increased to 400, *Le* was found to increase non-linearly with increasing θ for both sparse and dense wing models and showed smaller variation at higher θ. In addition, *Le* for sparse wing model was found to be greater than 1 for $\theta > 100^\circ$. Surprisingly, non-dimensional velocity profile was also found to be greater than 1 for sparse wing model at $Re_s = 400$. This confirms that presence of bristles was actually helping in accelerating the flow between the bristles at high Re_s and thereby increasing the leakiness through the bristles.

4 Discussion

Based on high speed video sequences of thrips parachuting from Santhanakrishnan et al. (2014), we measured the inter-wing angle (θ) between the fore-wings during a steady free fall and found θ to be around 97° with standard deviation of 4°. Although many previous studies have looked at steady/unsteady flow through bristled wings (Santhanakrishnan et al., 2014; Jones et al., 2016; Lee and Kim, 2017; Kasoju et al., 2018; Lee et al., 2018; Ford et al., 2019; Lee et al., 2020*b*,*a*; Kasoju and Santhanakrishnan, 2021*a*), the influence of inter-wing angle (θ) between a pair of bristled wings have not been examined. In this study, we varied the θ for two bristled wing designs under steady flow at Re_s= 20, 40 and 400. We found that 1) At high Re_s(= 400), the steady drag coefficient (C_D) was found to plateau for $\theta > 100^\circ$ for both bristled wing models, 2) At low Re_s(= 20, 40), the steady drag coefficient (C_D) increased with increasing θ for both bristled wing models, 3) The non-dimensional vorticity distribution around each bristle for a dense packed bristles acts like barrier to not allow fluid to leak through compared to sparse bristled wing model at Re_s = 20 and 4) At higher Re_s, bristles helps in accelerating the flow in the gaps between the bristles and thereby increasing the leakiness (*Le*) through the bristles for $\theta > 100^\circ$.

4. 1 Varying Reynolds number (Re_s)

With increasing Re_s , we observed C_D to decrease monotonically for both the bristled wing models (Dense and Sparse) at all the inter-wing angles (θ) tested in this study (Fig. 7.3A-C). In contrast, the non-dimensional vorticity ($\omega_z \nu/V^2$) decreased with increasing Re_s(Fig. 7.4,7.6). This suggesting that at low Re_s significant viscous forces acting on the bristles leads to formation of shear layers(Lee and Kim, 2017; Kasoju et al., 2018) around the bristles which further leads to blockage of gap between the bristles. This was also evident from the non-dimensional velocity profiles (v'/V') for both the bristled wing models (Fig. 7.8A-C) where v'/V' was significantly lower at low Re_sat all θ. Further, calculating the leakiness (Le) through the bristles at low Re_s confirmed that viscous blockage between the bristles led to overall decrease in Le along the wing span. This explains the significantly higher C_D at low Re_s.

While at higher Re_s, kinetic energy in the flow supported in leaking the flow through the gaps between the bristles which was also evident in increased non-dimensional velocity (v'/V') for both the bristled wing models tested in the study (Fig. 7.8D-F). With increasing θ, we observed the v'/V' to reach 1 and above for both dense and sparse wing models. This suggests that at higher Re_s and higher θ, bristles help in accelerating the fluid in the gaps with respect to free stream velocity. While leakiness (Le) was found to be significantly higher for both the bristled wing models at higher Re_s compared to lower Re_s, the increase in Le was non-linear with increasing θ. The increase in Le with increase in $\theta > 100^\circ$ is noticeably lower compared to $\theta < 100^\circ$. In addition, Le for both the bristled wing was found to be significantly higher for $\theta > 100^\circ$. This is in agreement with the force data (Fig. 7.3C), as C_D was found to plateau for higher θ ($> 100^\circ$). These results clearly suggest that leaky flow through the bristles (Le) and force generation (C_D) are coupled and are inversely related(Santhanakrishnan et al., 2014; Jones et al., 2016; Lee and Kim, 2017; Kasoju et al., 2018; Kasoju and Santhanakrishnan, 2021*a*).

4. 2 Varying wing design

The non-dimensional vorticity around each bristle for sparsely spaced wing model were either bigger in size or elongated in the direction of the flow depending on the Re_s(Fig. 7.4,7.5,7.6,7.7). In contrast for a dense bristled wing model, the non-dimensional vorticity around each bristle was coherent and smaller in size due to smaller spacing between the bristles. This explains the the larger spacing between the bristles, the larger is the scope for the flow to get diffused either in terms of viscous diffusion or kinematic diffusion based on the Re_s. This was also evident from the non-dimensional velocity profiles (v'/V'), where v'/V' for sparse wing was significantly higher compared to dense wing model suggesting leaky flow (Fig. 7.8A-F). Further calculating the *Le* along the wing span showed that *Le* for sparse wing model was found to be significantly higher than dense bristled wing model at any $Re_s$and θ tested (Fig. 7.8A-C). Also, *Le* for a sparse bristled wing model was found to be greater than 1 for $\theta > 100^\circ$ at higher Re_s(Fig. 7.8C). These results confirms that presence of sparsely spaced bristles actually helping in accelerating the flow between the bristles at high Re_s and thereby increasing the leakiness through the bristles. Comparing drag coefficient (C_D) with leakiness (*Le*), we observed *Le* to be higher for sparse bristled wing model in comparison with dense bristled wing model, while C_D was lower (Fig. 7.3A-C). At any Re_s tested, both *Le* and C_D showed significant variation between the bristled wing models at higher θ ($> 100^\circ$). For a sparse wing model at low Re_s(= 20 and 40), linear increase in *Le* with varying θ resulted in smaller increase in C_D. Similarly for a sparse wing model at high Re_s(= 400), *Le* and C_D were found to plateau at higher θ. This collectively suggests that irrespective of Re_s, wing design is important while working at higher inter-wing angles (θ).

4. 3 Implications of inter-bristle flow on aerodynamic loading

In the process of estimating the effective loading on the wings, we calculated a non-dimensional parameter defined as aerodynamic loading per leakiness (C_D/*Le*). As the Re_s in-

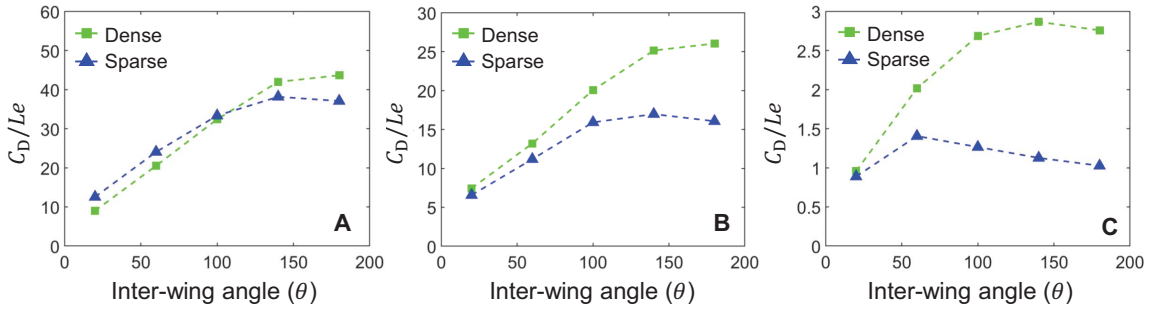

Figure 7.10: Aerodynamic loading per leakiness represented using non-dimensional term (C_D/Le) calculated for all the wing models (Dense and Sparse) for varying inter-wing angles (θ) at (A) Re_s = 20, (B) Re_s = 40, (C) Re_s = 400.

creased, C_D/Le value decreased significantly at all θ and for all wing models tested (Fig. 7.10). At low Reynolds number(Re_s = 20), C_D/Le was significantly higher for both the wing models and showed little variation between dense and sparse wing model at any θ tested in this study (Fig. 7.10A). Interestingly at $\theta = 100^\circ$, we observed effective loading on the wing to be same for both the wing models tested. This inter-wing angle ($\theta = 100^\circ$) is close to our observations from high-speed video recordings of thrips during parachuting ($\theta = 97.5^\circ$). From biological point of view, irrespective of the wing design, the effective loading on the insects wings would not change significantly for $\theta = 100^\circ$ at Re_s = 20. This removes the pressure on the insects for maintaining an optimum wing design for maintaining the aerodynamic loading on the wings. As the Re_s increased, we observed noticeable variation in C_D/Le between dense and sparse wing model (Fig. 7.10B,C) especially at higher inter-wing angles ($\theta \geq 100^\circ$). At Re_s = 20 and 40, the aerodynamic loading per leakiness on the wings was found to increase with θ and plateau for $\theta > 100^\circ$ for both wing models tested. Similar trend for C_D/Le was observed for dense bristled wing model at Re_s = 400. For sparse bristled wing model, C_D/Le increased until $\theta = 60^\circ$ and decreased with further increase in θ.

For tiny insects to travel longer distances during passive flight (parachuting), the wings of the insect should maximize the aerodynamic loading with less amount of fluid leaking through the bristles i.e., insects needs to maximize the effective loading on the wings. Al-

though many previous studies(Lee et al., 2020*b*; Kasoju et al., 2020*b*) have investigated the bristle wing design for maximizing the lift over drag ratio of the wing during active flight. However far less is known about wing design during passive flight. From the results of the present study, it can be inferred that tiny insects with densely packed bristles would have same aerodynamic loading per leakiness on the wings for inter-wing angles, $\theta > 100^{\circ}$. At $Re_{\mathrm{s}} = 20$, the effective loading on the wing is independent of wing design at $\theta = 100^{\circ}$. This allows the insects to have less pressure in having a particular bristled wing design. Therefore insects parachuting at low Re_{s} could use $\theta = 100^{\circ}$ irrespective of their wing design for aerodynamic loading per leakiness. This agrees well with high speed video recording published by Santhanakrishnan et al. (2014), where the insect was found to parachute at $\theta = 97.5^{\circ}$ under standard air flow conditions (low wind speeds). At higher Re_{s} (40 and 400), wing design plays a crucial role in defining the aerodynamic loading per leakiness on the wings. Therefore, insects parachuting in high speed winds would probably end of using $\theta > 100^{\circ}$ for maximizing the aerodynamic loading per leakiness on the wings.

4. 4 Biological implications

Bristle appendages are known to aid in locomotion, weight reduction and food capture (Loudon and Koehl, 1994; Cheer and Koehl, 1987; Santhanakrishnan et al., 2014; Jones et al., 2016; Cummins et al., 2018; Lee et al., 2020*b*). Recent study by Cummins et al. (2018) have shown that formation of a separated ring vortex helps in stabilizing the free fall of dandelion seeds using a bunch of bristles (pappus). The formation of this separated ring vortex was dependent on the geometry of the bristles and also on the porosity or leakiness through the bristles. Surprisingly in the present study of passive dispersal in tiny insects (thrips) with bristled wings, we did not see the formation of any such separated ring vortex in the inter-wing spacing's for any inter-wing angles (θ) or Reynolds number (Re_{s}) tested in this study. However, we observed the formation of small wing-tip vorticies (Fig. 7.4,7.5,7.6,7.7) closer

to the wing with counter rotating vortices on each bristle at all Re_s and θ tested. This suggests an unknown fluid behaviour in the biological world of bristle appendages leading to a steady passive dispersal. One interesting difference between a thrips wing and dandelion seed is the arrangement of the bristles. While the dandelion seeds can be approximated to a porous circular disk (Cummins et al., 2017, 2018; Lee et al., 2020*b*), thrips wings cannot due to higher aspect ratio of the wing.

From the high speed video recording of thrips parachuting (Santhanakrishnan et al., 2014) (assuming a fore-wing span of 1 mm (Sunada et al., 2002)), these insects were found to free fall at Reynolds number (Re_s) of approximately 40 at inter-wing angle (θ) of 97°. Assuming the insect mass of 10μg (Ellington, 1999), the drag required for a stable free fall of the insect should be around the mass of the insect. Considering the above published measurements, the drag force on the wings at Re_s =40 was measured to be 12μg and 9.7μg (Fig. 7.3B) for dense and sparse wing model, respectively at θ = 100°. For any $\theta > 100°$ or $< 100°$, the drag force acting on the wings would allow a faster fall or a slower fall than that observed from high speed video recording. Due to the availability of a single video of thrips parachuting in a controlled environment, it is hard to interpret if these insects would use the same inter-wing angles during parachuting in a windy flows. However, based on the observations of matched drag force generation at Re_s =40 between a real insect parachuting and a numerical model, we can claim that- 1) at low Re_s flow compared to the free-fall recording, insects could increase the θ beyond 100° to match the aerodynamic loading on the wings close to that of the body weight, 2) at high Re_s, using θ beyond 100° would show negligible influence on aerodynamic loading on the wings. Therefore, the maximum energy demand for an insect in free fall (parachuting) would be to overcome the weight of the insect. Comparing it with active flight, the insect would require to overcome the weight and also the drag generated during the flight which would be significantly higher than a free fall.

5 Conclusions

Using numerical and experimental models of steady free fall of densely and sparsely bristled wing pairs, we investigated the effects of varying inter-wing angle (θ) on aerodynamic performance and flow characteristics at Re_s=20, 40 and 400. The non-dimensional vorticity distribution around each bristle for a densely-bristled wing pair acts like a virtual fluid barrier, not permitting fluid to leak through as compared to a sparsely-bristled wing pair at Re_s=20. With increasing Re_s>20 and for θ>100°, bristles help in accelerating the flow in the gaps between the bristles and thereby increasing the leakiness of flow through the bristles. The aerodynamic loading per leakiness on the wing showed little variation in wing design for $\theta \leq 100°$. At high Re_s (=400), wing design was crucial for maintaining aerodynamic loading per leakiness on the wings. Collectively, at low Re_s irrespective of wing design, formation of fluid barrier in the gaps between the bristles was found to maintain the aerodynamic loading per leakiness on the wings for $\theta \geq 100°$ by maximizing drag force and minimizing the leakiness. Similarly at higher Re_s for a dense bristled wing model, accelerating the flow in the gaps between the bristles increased the leakiness and therefore the maximum aerodynamic loading per leakiness was obtained for $\theta > 100°$.

Our intention in this study was to understand the influence of inter-wing angles on bristled wing design and therefore we limited our model to a simple 2D bristled wing with equal inter-bristle and symmetric inter-wing spacing. Based on the results from this study, in future we aim to examine roles of asymmetric inter-wing spacing, unequally spaced bristles and realistic (i.e., three-dimensional) bristled wing geometries.

CHAPTER VIII

Summary

A methodology was developed to understand the aerodynamic force generation and flow physics of bristled wings in active and passive flight of tiny insects. The approach utilized scaled-up robotic models that were designed and developed to mimic the flapping flight observed in tiny insects. Simplified bristled wing models inspired from fore-wings of tiny insects were developed to undergo the prescribed motion using robotic models. Aerodynamic forces were measured using strain gauges attached on a L-bracket where the wing models were mounted. Flow around the bristled wings was quantified using Particle Image Velocimetry (PIV) technique. These experimental setups were used to study 5 topics which considers several aspects of active and passive flight observed in tiny insects. Detail summaries for each of these studies were presented in final sections of the chapters 3, 4, 5, 6 and 7. This section is essentially a condensed version featuring the significant contributions of each of these studies.

1 Interspecific variation in bristle number on forewings of tiny insects does not influence clap-and-fling aerodynamics

One of the significant accomplishments of this phase of was analysing the aerodynamic characteristics of bristle wing pair during clap and fling with varying wing morphology (gap between the bristles, G; bristle diameter, D; number of bristles, n; inter-bristle gap to diameter ratio, G/D; and wing span, S) based on morphological analysis of fore-wings images of 59 species of thrips and fairyflies. Our analysis of forewing morphology in thrips and fairyflies showed similar scaling relationships between the two groups in the variables

tested (n, G/D and $S_{\max}$). Within the biologically relevant range of Re_{b} (0.01–0.1) for tiny insects, we observed that increasing the inter-bristle spacing (G) for fixed bristle Re_{b} diameter (D) decreased drag forces significantly. This was supported by a significant increase in leakiness observed during early fling. However, changes in average lift forces were minimal, suggesting that having the capability of increasing the inter-bristle spacing during free flight could help these insects to overcome large drag forces with minimal changes in lift force. We also found that varying bristle diameter (D) had no effect on aerodynamic force generation, and varying the non-dimensional inter-bristle gap to diameter ratio (G/D) showed no significant influence on aerodynamic force generation. Finally, although we found that drag forces significantly decreased with decreasing number of bristles (n), lift force only minimally changed for $n < 100$. At $n > 100$, we observed a significant jump in lift forces. Considering the broad variation of n (32–161) observed across species, the lack of change in lift forces for $n < 100$ suggests that tiny insects may experience less biological pressure to optimize n for a given wingspan. Alternatively, stabilizing selection may maintain species within a range of values that does not affect flight performance.

2 Aerodynamic interaction of bristled wing pairs in fling

We examine wing-wing interaction of bristled wings in fling at $Re_{\mathrm{c}} = 10$, as a function of initial inter-wing spacing (δ) and degree of overlap between rotation and linear translation. Using dynamically scaled robotic platform, aerodynamic forces and flow structures generated by a single bristled wing and a bristled wing pair undergoing rotation about the TE(s), linear translation at a fixed angle and their combination were investigated for varying initial inter-wing spacing at $Re_{\mathrm{c}} = 10$. Irrespective of θ_{r}, θ_{t} and ζ, increasing δ in a bristled wing pair decreased drag by a larger extent as compared to lift reduction due to weakening wing-wing interaction, resulting in the wing pair behaving as two single wings. During wing rotation (θ_{r}) at smaller δ, positive pressure on the leading surface of each interacting wing (ventral surface) diffused through the inter-bristle gaps due to large viscous forces. This re-

sulted in the formation of a strong +ve pressure region in between the wings, necessitating large drag force to move the wings apart. The positive pressure region diminished with increasing θ_r, which in turn reduced drag forces. This finding suggests that a likely reason for tiny insects to employ large rotational angles (relative to vertical) in fling (Cheng and Sun, 2017) is to reduce drag. Finally, we find that rotational acceleration of a bristled wing aids in early development of LEV and TEV. Previous studies (Santhanakrishnan et al., 2014; Jones et al., 2016) have reported δ ranges from 10% to 25% in thrips based on free-flight recordings. Lift was largest for δ=10% across all wing kinematics that were tested in this study, which also falls within the above observed range of δ in thrips.

3 Pausing after clap reduces power required to fling wings apart at low Reynolds number

From high-speed videos of free take-off flight of thrips, we observed that their forewings remain clapped for approximately 10% of the wingbeat cycle before start of downstroke (fling stroke). We sought to examine if there are aerodynamic advantages associated with pausing wing motion after upstroke (clap stroke) and before downstroke (fling stroke) at Re_c=10. We found that pause time between upstroke (clap stroke) and downstroke (fling stroke) has no significant influence on time-varying aerodynamic forces generated during the upstroke (clap stroke) phase (phase before the pause) for both the single wing and wing pair configurations (solid and bristled wing models) at a chord-based Reynolds number of 10. However, we observed variations in time-varying aerodynamic forces with increasing pause time during the downstroke (fling stroke) phase (phase after pause). Considering the force coefficients averaged across the entire cycle (upstroke (clap stroke) phase, pause time, downstroke (fling stroke) phase), both solid and bristled wing pairs were found to provide drag reduction with increasing pause time. Observations of the chordwise flow showed that introducing pause before the start of downstroke (fling stroke) led to the complete dissipation of the wake generated from upstroke (clap stroke). Diminishing the vorticity

shed from the upstroke (clap stroke) helped in decreasing the drag force on the wing pair configuration (solid and bristled) during downstroke (fling stroke). With increasing pause time, the cycle-averaged net power coefficient was found to decrease significantly during wing-wing interaction of a wing pair as compared to that of a single wing. Collectively, our findings suggest that pausing before downstroke (fling stroke) can help to reduce the power consumption in clap and fling motion, with a small compromise in lift.

4 Flapping flight with bristled wings at low Reynolds numbers

Our previous 2D clap-and-fling studies have shown that bristled wings augment lift-over-drag ratio at $Re_c = 10$ relevant to tiny insect flight. This study aims to evaluate if the aerodynamic benefits of bristled wings are also observed when using 3D wingbeat kinematics. Using a dynamically scaled robotic model that mimics the 3D flapping flight relevant to tiny insects in an horizontal stroke plane, we investigated the aerodynamic force generation and flow characteristics of a solid and bristled wings (single and wing pair configurations) for varying Re_c in range of 10-120 for thrips, leafminers and fruitfly wing kinematics. We found the circulation at LEV and TEV to peak at $\tau \approx 0.8$ which was similar to where peak lift force generation was observed for single wing configuration (solid and bristled) for all wing kinematics tested. Wing pitch rate was found to significantly influence the aerodynamic force generation on the wings. While thrips kinematics generated higher $\overline{C_D}$ and $\overline{C_L}$, the aerodynamic performance ($\overline{C_L}/\overline{C_D}$) was noticeably higher for leafminer kinematics for both solid and bristled wing models (single and wing pair configuration) and at all Re tested. Solid wing pair configuration with partial clap-and-fling was found to show 7%-9% increase in lift force compared to single solid wing at $Re_c = 10$ for all wing kinematics tested.

5 Parachuting in steady flow using bristled wings

Free takeoff flight recordings of thrips show that they can intermittently cease flapping and float passively downwards by spreading their bristled wings. This type of drag-based parachuting can be advantageous in lowering the falling speed, and could potentially aid in long-distance dispersal by minimizing energetic demands needed for active flight. It is unclear whether bristled wings such as those observed in thrips can reduce drag generated in parachuting. Forewing inter-wing angles measured during free fall obtained from free takeoff flight videos show that thrips parachute with inter-wing angle of about 97°. Using numerical and experimental models, we investigated the aerodynamic performance and flow characteristics of varying inter-wing angle (θ) under a steady flow for a dense and sparse bristled wing model at Re_s = 20, 40 and 400. The non-dimensional vorticity distribution around each bristle for a dense packed bristles acts like barrier to not allow fluid to leak through compared to sparse bristled wing model at Re_s = 20. While for higher Re_s, bristles helps in accelerating the flow in the gaps between the bristles and thereby increasing the leakiness (Le) through the bristles for $\theta > 100°$. The aerodynamic loading per leakiness on the wing showed little variation in wing design for $\theta \leq 100°$. At high Re_s(= 400), wing design is crucial for maintaining aerodynamic loading per leakiness on the wings. Collectively, at low Re_s irrespective of wing design, formation of fluid barrier in the gaps between the bristles was found to maintain the aerodynamic loading per leakiness on the wings for $\theta \leq 100°$ by maximizing drag force and minimizing the leakiness. Similarly at higher Re_s for a dense bristled wing model, accelerating the flow in the gaps between the bristles increased the leakiness and therefore the maximum aerodynamic loading per leakiness was obtained for $\theta > 100°$.

CHAPTER IX

Conclusions and recommendations for future work

1 Conclusions

Through a series of studies, we presented detailed understandings of bristled wings and their aerodynamic implications during active and passive flight in tiny insects. For the very first time, we recorded the biological variation and phylogenetic analysis of bristled wing morphology across 59 species of miniature insects. Despite broad biological variation, we observed minimal influence of number of bristles, n and inter-bristle gap to bristle diameter ratio, G/D on clap-and-fling aerodynamics. This suggests that tiny insects may experience lower biological pressure to functionally optimize n and G/D for a given wingspan. While the pressure distribution on a wing gives an accurate representation of aerodynamic forces generated by that wing, the pressure distribution in the inter-wing spacing (δ) was also found to significantly alters the drag force generation. Smaller δ resulted in large positive pressure distribution between the wings which was directly proportional to drag force generation. However, tiny insects were found to use large rotational angles to overcome these drag penalties. Active flapping at tiny scales such as thrips and fairyflies looks very exhausting due to large power requirements. Therefore, these insects were found to employ two new strategies: 1) pausing the wing motion before the start of downstroke, and 2) intermittently parachute with their bristled wings wide open at inter-wing angle ($\theta \approx 100$). Pausing helps in reducing the power consumption in clap and fling motion with small compromise in lift generation. During parachuting at low Reynolds number, insects could increase the θ beyond 100° to match the aerodynamic loading on the wings close to that of the body weight aiding in longer dispersal compared to active flight. While the

above studies investigated a portion of a flapping flight (clap and fling), we developed a 3D flapping robotic model to mimic entire flapping flight of any insect in an horizontal stroke plane. Investigating the flapping kinematics of three insects in Re_c range of 10-120 using bristled wing revealed that circulation of LEV and TEV wing was significant higher closer towards the end of upstroke where also peak lift force was generated. Overall, from engineering point of view, these finding on bristled wing for varying wing kinematics and wing morphology would act as a stepping stone for development of miniature aerial vehicles.

2 Recommendations for future work

Through the course of these studies many interesting question have arisen. First, many bristle-winged insects show asymmetry in wing shape Jones et al. (2016). We did not consider the effects of the asymmetric bristle lengths on either side of the forewing (i.e., leading edge and trailing edge) and of bristle angle relative to the horizontal. Asymmetry in bristle lengths within the biological Re_b range may not noticeably impact clap-and-fling aerodynamics, because damage may occur to the wing bristles during an insect's life and biological systems are often robust to such perturbations. Nonetheless, this may be a worthwhile direction for future work. Similarly, our physical models did not account for variation in wing shape and were simplified to a rectangular planform. There is much additional diversity in wing shape, especially when comparing fairyflies (teardrop-shaped) to thrips (smaller chord relative to span) (Ford et al., 2019). At Re_c = 10, changes in wing shape did not significantly affect the trend of aerodynamic force generation in time during clap-and-fling (comparing lift and drag force generation of rectangular bristled wing pairs used in Kasoju et al. (2018) to approximated elliptical bristled wing pairs used in Ford et al. (2019)). However, the possible effects of wing shape on flying in bristle-winged insects – particularly across body sizes – would be valuable to study. The bristles on the wings of these insects are considerably flexible, yet we suspect them to behave stiffer in motion due to high viscous forces. This was also evident with the stainless-steel wires that we used as

bristles. Although these wires looked very flexible in air, the wires did not flex when tested in glycerin. We chose bristles that did not flex during motion because no quantitative data are available on flexibility of bristles in tiny insects. Based on published high-speed video of thrips (Santhanakrishnan et al., 2014; Cheng and Sun, 2018; Lyu et al., 2019*b*), it is evident they flex their wings along the spanwise direction when flinging their wings apart at the start of downstroke. Since the variability in the wing flexibility along the wingspan has not yet been characterized in any published study, we used rigid wing models. Future studies are needed to document interspecific diversity in wing shape and flexibility to examine how they might affect aerodynamic forces.

In addition, the aerodynamic mechanics used by these tiny insects under windy flow using bristled wings would pave a way in developing wind resistant micro aerial vehicles. It is possible that the tiny insects such as thrips and fairyflies use different wing kinematics during hovering/free flight similar to fruitflies (Dickinson et al., 1999) and needs to be investigated in future studies. Jones et al. (2016) suggested that bristles would enhance electrostatic charge, which was shown to aid in dispersal of spiders and needs to be investigated. High-speed video recordings of thrips have shown that these insects use 2 wing pairs (fore-wing pair and hind-wing pair) with variable angle between hind-wing and fore-wing during active flight. In addition, investigating the variation in phase-lag between fore-wing and hind-wing kinematics would help in better understanding significant aerodynamic lift force generation at such tiny scales.

These insects were found to unfold the wings and sense the air flow before taking off. Previous studies (Ai et al., 2010; Ai, 2013) have shown the bristles on a fruitfly wing to sense airflow and wing vibrations, and it is possible that bristles on the wings of tiny insects would serve the same purpose. These tiny insects were found to use unusual wing kinematics such as rowing, clap and fling motion and parachuting. While rowing was found to generate 70% of vertical force required for the flight, other 30% was generated by clap and fling motion (Cheng and Sun, 2018). However, it is unclear if tiny insects use the same

rowing kinematics during swimming compared to free flight and the consequences of using bristled wing in swimming vs flying needs to be investigated. In addition, parachuting using bristled wings in a background flow (windy flow) would help us in understandings how thrips were able to migrate to such large distances. While the bristled wings are crucial in aerodynamic performance during the flight of tiny insects, it is unknown if the insect body play a role in their altered wing kinematics compared to large scale insect. Since the wings are attached closer to the head of the insect, we suspect high moment on the body altering the stability of their flight due to significant drag force generation at such tiny scales. Future studies needs to be carried out to investigate the stability of the flight with varied body shapes.

References

Ai, H. (2013), 'Sensors and sensory processing for airborne vibrations in silk moths and honeybees', *Sensors* **13**(7), 9344–9363.

Ai, H., Yoshida, A. and Yokohari, F. (2010), 'Vibration receptive sensilla on the wing margins of the silkworm moth *bombyx mori*', *J. Insect Physiol.* **56**(3), 236–246.

Alexander, R. M. (1985), 'The ideal and the feasible: physical constraints on evolution', *Biological Journal of the Linnean Society* **26**(4), 345–358.

Alexander, R. M. (1995), 'Springs for wings', *Science* **268**, 50–51.

Alexander, R. M. (2013), *Principles of animal locomotion*, Princeton University Press.

Arora, N., Gupta, A., Sanghi, S., Aono, H. and Shyy, W. (2014), 'Lift-drag and flow structures associated with the "clap and fling" motion', *Physics of fluids* **26**(071906).

Barta, E. and Weihs, D. (2006), 'Creeping flow around a finite row of slender bodies in close proximity', *J. Fluid Mech.* **551**, 1.

Bhat, S. S., Zhao, J., Sheridan, J., Hourigan, K. and Thompson, M. C. (2019), 'Uncoupling the effects of aspect ratio, reynolds number and rossby number on a rotating insect-wing planform', *Journal of Fluid Mechanics* **859**, 921–948.

Birch, J. M., Dickson, W. B. and Dickinson, M. H. (2004), 'Force production and flow structure of the leading edge vortex on flapping wings at high and low reynolds numbers', *J. Exp. Biol.* **207**(7), 1063–1072.

Blount, Z. D., Lenski, R. E. and Losos, J. B. (2018), 'Contingency and determinism in evolution: Replaying life's tape', *Science* **362**(6415).

Bomphrey, R. J., Srygley, R. B., Taylor, G. K. and Thomas, A. L. (2002), 'Visualizing the flow around insect wings', *Physics of Fluids* **14**(9), S4–S4.

Buckman, R. S., Mound, L. A. and Whiting, M. F. (2013), 'Phylogeny of thrips (insecta: Thysanoptera) based on five molecular loci', *Systematic Entomology* **38**(1), 123–133.

Burnham, K. and Anderson, D. (2002), 'Model selection and multimodel inference: a practical information-theoretic approach. nd. edition springer', *New York, USA* .

Butler, M. A. and King, A. A. (2004), 'Phylogenetic comparative analysis: a modeling approach for adaptive evolution', *The American Naturalist* **164**(6), 683–695.

Cavalleri, A., Lindner, M. F. and Mendonça, M. d. S. (2016), 'New neotropical haplothripini (thysanoptera: Phlaeothripidae) with a key to central and south american genera.', *J. Nat. Hist.* **50**.

Cavalleri, A. and Mound, L. A. (2012), 'Toward the identification of *Frankliniella* species in brazil (thysanoptera, thripidae).', *Zootaxa* **3270**.

Cavalleri, A. and Mound, L. A. (2014), 'The neotropical flower-living genus *Lenkothrips* (thysanoptera, heterothripidae): three new species and an identification key.', *Zootaxa* **3814**.

Cheer, A. and Koehl, M. (1987), 'Paddles and rakes: fluid flow through bristled appendages of small organisms', *Journal of Theoretical Biology* **129**(1), 17–39.

Cheng, X. and Sun, M. (2016), 'Wing-kinematics measurement and aerodynamics in a small insect in hovering flight', *Scientific reports* **6**, 25706.

Cheng, X. and Sun, M. (2017), 'Aerodynamic forces and flows of the full and partial clap-fling motions in insects', *PeerJ* **3002**.

Cheng, X. and Sun, M. (2018), 'Very small insects use novel wing flapping and drag principle to generate the weight-supporting vertical force', *J. Fluid Mech.* **855**, 646–670.

Cheng, X. and Sun, M. (2019), 'Revisiting the clap-and-fling mechanism in small wasp encarsia formosa using quantitative measurements of the wing motion', *Physics of Fluids* **31**(10), 101903.

Cheng, X. and Sun, M. (2021), 'Wing kinematics and aerodynamic forces in miniature insect encarsia formosa in forward flight', *Physics of Fluids* **33**(2), 021905.

Crespi, B. J., Carmean, D. A. and Chapman, T. W. (1997), 'Ecology and evolution of galling thrips and their allies', *Annu. Rev. Entomol.* **42**.

Cummins, C., Seale, M., Macente, A., Certini, D., Mastropaolo, E., Viola, I. M. and Nakayama, N. (2018), 'A separated vortex ring underlies the flight of the dandelion', *Nature* **562**(7727), 414–418.

Cummins, C., Viola, I. M., Mastropaolo, E. and Nakayama, N. (2017), 'The effect of permeability on the flow past permeable disks at low reynolds numbers', *Physics of Fluids* **29**(9), 097103.

Dabiri, J. O., Bose, S., Gemmell, B. J., Colin, S. P. and Costello, J. H. (2014), 'An algorithm to estimate unsteady and quasi-steady pressure fields from velocity field measurements', *Journal of Experimental Biology* **217**(3), 331–336.

Dang, L.-H., Mound, L. A. and Qiao, G.-X. (2014), 'Conspectus of the phlaeothripinae genera from china and southeast asia (thysanoptera, phlaeothripidae)', *Zootaxa* **3807**(1), 1–82.

Daniel, T. L. (1984), 'Unsteady aspects of aquatic locomotion', *American Zoologist* **24**(1), 121–134.

Davidi, G. and Weihs, D. (2012), 'Flow around a comb wing in low-reynolds-number flow', *AIAA Journal* **50**(1).

Davis, R. B., Baldauf, S. L. and Mayhew, P. J. (2010), 'The origins of species richness in the hymenoptera: insights from a family-level supertree', *BMC evolutionary biology* **10**(1), 1–16.

Dickinson, M. H. and Gotz, K. G. (1993), 'Unsteady aerodynamic performance of model wings at low reynolds numbers', *J. Exp. Biol.* **174**(1), 45–64.

Dickinson, M. H., Lehmann, F.-O. and Sane, S. P. (1999), 'Wing rotation and the aerodynamic basis of insect flight', *Science* **284**(5422), 1954–1960.

Dickinson, M. H. and Lighton, J. (1995), 'Muscle efficiency and elastic storage in the flight motor of Drosophila', *Science* **268**, 87–90.

Dudley, R. (2002), *The biomechanics of insect flight: form, function, evolution*, Princeton University Press.

Ellington, C. (1980), 'Wing mechanics and take-off preparation of Thrips *Thysanoptera*', *J. Exp. Biol.* **85**(1), 129–136.

Ellington, C. P. (1975), Non-steady-state aerodynamics of the flight of encarsia formosa, *in* 'Swimming and flying in nature', Springer, pp. 783–796.

Ellington, C. P. (1984*a*), 'The aerodynamics of hovering insect flight. iv. Aerodynamic mechanisms', *Phil. Trans. R. Soc. Lond. B* **305**, 79–113.

Ellington, C. P. (1984*b*), 'The aerodynamics of insect flight. iii. Kinematics', *Phil. Trans. R. Soc. Lond. B* **305**, 41–78.

Ellington, C. P. (1999), 'The novel aerodynamics of insect flight: applications to micro-air vehicles', *J. Exp. Biol.* **202**(23), 3439–3448.

Ellington, C. P., Van Den Berg, C., Willmott, A. P. and Thomas, A. L. (1996), 'Leading-edge vortices in insect flight', *Nature* **384**(6610), 626–630.

Ern, P., Risso, F., Fabre, D. and Magnaudet, J. (2012), 'Wake-induced oscillatory paths of bodies freely rising or falling in fluids', *Annual Review of Fluid Mechanics* **44**, 97–121.

Field, S. B., Klaus, M., Moore, M. and Nori, F. (1997), 'Chaotic dynamics of falling disks', *Nature* **388**(6639), 252–254.

Ford, M. P., Kasoju, V. T., Gaddam, M. G. and Santhanakrishnan, A. (2019), 'Aerodynamic effects of varying solid surface area of bristled wings performing clap and fling', *Bioinspir. Biomim* **14**(4).

Freckleton, R. P., Harvey, P. H. and Pagel, M. (2015), 'Phylogenetic analysis and comparative data: a test and review of evidence', *The American Naturalist* .

Fry, S. N., Sayaman, R. and Dickinson, M. H. (2005), 'The aerodynamics of hovering flight in drosophila', *J. Exp. Biol.* **208**(12), 2303–2318.

Futuyma, D. and Kirkpatrick, M. (2017), 'Evolution, 4th edn sunderland', *MA: Sinauer.[Google Scholar]* .

Garmann, D. and Visbal, M. (2012), 'Three-dimensional flow structure and aerodynamic loading on a low aspect ratio, revolving wing.', *42nd AIAA Fluid Dyn. Conf. Exhib.* **2012-3277**.

Gartner, G. E., Hicks, J. W., Manzani, P. R., Andrade, D. V., Abe, A. S., Wang, T., Secor, S. M. and Garland Jr, T. (2010), 'Phylogeny, ecology, and heart position in snakes', *Physiological and biochemical zoology* **83**(1), 43–54.

Gibson, G. A., Read, J., Huber, J. T. et al. (2007), 'Diversity, classification and higher relationships of mymarommatoidea (hymenoptera)', *Journal of Hymenoptera Research* **16**(1), 51–146.

Glazier, D. S. (2021), 'Biological scaling analyses are more than statistical line fitting', *Journal of Experimental Biology* **224**(11), jeb241059.

Goldaracena, A. and Hance, T. (2017), 'A new species of *Frankliniella* with 7-segmented antennae from mexico (thysanoptera, thripinae).', *Zootaxa* **4231**.

Gould, S. J. (2002), *The structure of evolutionary theory*, Harvard University Press.

Gould, S. J. and Lewontin, R. C. (1979), '5 the spandrels of san marco and the panglossian paradigm: A critique of the adaptationist programme', *Conceptual Issues in Evolutionary Biology* **205**, 79.

Han, J. S., Chang, J. W. and Cho, H. K. (2015), 'Vortices behavior depending on the aspect ratio of an insect-like flapping wing in hover.', *Exp. Fluids* **56**.

Hansen, B. and Tiselius, P. (1992), 'Flow through the feeding structures of suspension feeding zooplankton: a physical model approach', *Journal of Plankton Research* **14**.

Hansen, T. F. and Martins, E. P. (1996), 'Translating between microevolutionary process and macroevolutionary patterns: the correlation structure of interspecific data', *Evolution* **50**(4), 1404–1417.

Hansen, T. F. and Orzack, S. H. (2005), 'Assessing current adaptation and phylogenetic inertia as explanations of trait evolution: the need for controlled comparisons', *Evolution* **59**(10), 2063–2072.

Harbig, R. R., Sheridan, J. and Thompson, M. C. (2013), 'Reynolds number and aspect ratio effects on the leading-edge vortex for rotating insect wing planforms.', *J. Fluid Mech.* **717**.

Hedrick, T. L., Cheng, B. and Deng, X. (2009), 'Wingbeat time and the scaling of passive rotational damping in flapping flight', *Science* **324**(5924), 252–255.

Heraty, J. M., Burks, R. A., Cruaud, A., Gibson, G. A., Liljeblad, J., Munro, J., Rasplus, J.-Y., Delvare, G., Janšta, P., Gumovsky, A. et al. (2013), 'A phylogenetic analysis of the megadiverse c halcidoidea (h ymenoptera)', *Cladistics* **29**(5), 466–542.

Horridge, G. A. (1956), 'The flight of very small insects', *Nature* **178**, 1334–1335.

Housworth, E. A. and Martins, E. P. (2001), 'Random sampling of constrained phylogenies: conducting phylogenetic analyses when the phylogeny is partially known', *Systematic Biology* **50**(5), 628–639.

Huber, J. and Baquero, E. (2007), 'Review of *Eustochus*, a rarely collected genus of mymaridae (hymenoptera).', *J. Entomol. Soc. Ontario* **138**.

Huber, J. and Noyes, J. (2013*a*), 'A new genus and species of fairyfly, tinkerbella nana (hymenoptera, mymaridae), with comments on its sister genus kikiki, and discussion on small size limits in arthropods', *Journal of Hymenoptera Research* **32**, 17.

Huber, J. T. (2005), 'The gender and derivation of genus-group names in mymaridae and mymarommatidae (hymenoptera)', *Acta Societatis Zoologicae Bohemicae* **69**, 167–183.

Huber, J. T. (2017), '*Eustochomorpha Girault*, *Neotriadomerus* gen. n., and *Proarescon* gen. n.(hymenoptera, mymaridae), early extant lineages in evolution of the family', *Journal of Hymenoptera Research* **57**, 1.

Huber, J. T., Gibson, G. A., Bauer, L. S., Liu, H. and Gates, M. (2008), 'The genus *Mymaromella* (hymenoptera: Mymarommatidae) in north america, with a key to described extant species.', *J. Hymenopt. Res.* **17**.

Huber, J. T., Mendel, Z., Protasov, A. and La Salle, J. (2006), 'Two new australian species of *Stethynium* (hymenoptera: Mymaridae), larval parasitoids of *Ophelimus maskelli* (ashmead) (hymenoptera: Eulophidae) on eucalyptus.', *J. Nat. Hist.* **40**.

Huber, J. T. and Noyes, J. S. (2013*b*), 'A new genus and species of fairyfly, *Tinkerbella nana* (hymenoptera, mymaridae), with comments on its sister genus *Kikiki*, and discussion on small size limits in arthropods.', *J. Hymenopt. Res.* **17**.

Huber, J. T. et al. (1986), 'Systematics, biology, and hosts of the mymaridae and mymarommatidae (insecta: Hymenoptera): 1758–1984', *Entomography* **4**(0), 185.

Jalali, S. K., Mohanraj, P. and Lakshmi, B. L. (2016), Trichogrammatids, *in* Omkar, ed., 'Ecofriendly Pest Management for Food Security', Academic Press, San Diego, CA, USA, chapter 5, pp. 139–181.

Johnson, K. P., Dietrich, C. H., Friedrich, F., Beutel, R. G., Wipfler, B., Peters, R. S., Allen, J. M., Petersen, M., Donath, A., Walden, K. K. et al. (2018), 'Phylogenomics and the evolution of hemipteroid insects', *Proceedings of the National Academy of Sciences* **115**(50), 12775–12780.

Jones, D. R. (2005), 'Plant viruses transmitted by thrips', *Eur. J. Plant Pathol.* **113**(2).

Jones, S. K., Yun, Y. J., Hedrick, T. L., Griffith, B. E. and Miller, L. A. (2016), 'Bristles reduce the force required to 'fling' wings apart in the smallest insects', *J. Exp. Biol.* **219**(23), 3759–3772.

Jones, S., Laurenza, R., Hedrick, T. L., Griffith, B. E. and Miller, L. A. (2015), 'Lift vs. drag based mechanisms for vertical force production in the smallest flying insects', *Journal of theoretical biology* **384**, 105–120.

Kasoju, V. T., Ford, M. P., Ngo, T. T. and Santhanakrishnan, A. (2020*a*), 'Inter-species variation in number of bristles on forewings of tiny insects does not impact clap-and-fling aerodynamics', *bioRxiv Preprint* .
URL: *https://www.biorxiv.org/content/early/2020/10/27/2020.10.27.356337*

Kasoju, V. T., Ford, M. P., Ngo, T. T. and Santhanakrishnan, A. (2020*b*), 'Inter-species variation in number of bristles on forewings of tiny insects does not impact clap-and-fling aerodynamics', *bioRxiv Preprint* .
URL: *https://www.biorxiv.org/content/early/2020/10/27/2020.10.27.356337*

Kasoju, V. T. and Santhanakrishnan, A. (2021*a*), 'Aerodynamic interaction of bristled wing pairs in fling', *Physics of Fluids* **33**(3), 031901.

Kasoju, V. T. and Santhanakrishnan, A. (2021*b*), 'Pausing after clap reduces power required to fling wings apart at low reynolds number', *Bioinspiration & Biomimetics* .

Kasoju, V. T., Terrill, C. L., Ford, M. P. and Santhanakrishnan, A. (2018), 'Leaky flow through simplified physical models of bristled wings of tiny insects during clap and fling', *Fluids* **3**(44).

Koehl, M. A. (1995), 'Fluid flow through hair-bearing appendages: feeding, smelling and swimming at low and intermediate reynolds numbers', *Symp Soc Exp Biol* **49**.

Kolomenskiy, D., Farisenkov, S., Engels, T., Lapina, N., Petrov, P., Lehmann, F.-O., Onishi, R., Liu, H. and Polilov, A. (2020*a*), 'Aerodynamic performance of a bristled wing of a very small insect', *Experiments in Fluids* **61**(9), 1–13.

Kolomenskiy, D., Farisenkov, S., Engels, T., Lapina, N., Petrov, P., Lehmann, F.-O., Onishi, R., Liu, H. and Polilov, A. (2020*b*), 'Aerodynamic performance of a bristled wing of a very small insect', *Experiments in Fluids* **61**(9), 1–13.

Kolomenskiy, D., Moffatt, H. K., Farge, M. and Schneider, K. (2010), 'Vorticity generation during the clap–fling–sweep of some hovering insects', *Theoretical and Computational Fluid Dynamics* **24**(1-4), 209–215.

Kolomenskiy, D., Moffatt, H. K., Farge, M. and Schneider, K. (2011), 'The Lighthill–Weis-Fogh clap–fling–sweep mechanism revisited', *J. Fluid Mech.* **676**, 572–606.

Kuethe, A. M. (1975), On the mechanics of flight of small insects, *in* 'Swimming and flying in nature', Springer, pp. 803–813.

Lee, M., Lee, S. H. and Kim, D. (2020*a*), 'Stabilized motion of a freely falling bristled disk', *Physics of Fluids* **32**(11), 113604.

Lee, S. H. and Kim, D. (2017), 'Aerodynamics of a translating comb-like plate inspired by a fairyfly wing', *Physics of fluids* **29**(081902).

Lee, S. H., Lahooti, M. and Kim, D. (2018), 'Aerodynamic characteristics of unsteady gap flow in a bristled wing.', *Phys. Fluids* **30**.

Lee, S.-H. and Leal, L. G. (1986), 'Low-reynolds-number flow past cylindrical bodies of arbitrary cross-sectional shape', *J. Fluid Mech.* **164**, 401–427.

Lee, S. H., Lee, M. and Kim, D. (2020*b*), 'Optimal configuration of a two-dimensional bristled wing', *J. Fluid Mech.* **888**, A23.

Lehmann, F.-O. and Dickinson, M. H. (1998), 'The control of wing kinematics and flight forces in fruit flies (drosophila spp.).', *J. Exp. Biol.* **201**(3), 385–401.

Lehmann, F.-O. and Pick, S. (2007), 'The aerodynamic benefit of wing-wing interaction depends on stroke trajectory in flapping insect wings.', *J. Exp. Biol.* **210**.

Lehmann, F.-O., Sane, S. P. and Dickinson, M. H. (2005), 'The aerodynamic effects of wing-wing interaction in flapping insect wings', *J. Exp. Biol.* **208**, 3075–3092.

Lentink, D. and Dickinson, M. H. (2009), 'Rotational accelerations stabilize leading edge vortices on revolving fly wings', *J. Exp. Biol.* **212**(16), 2705–2719.

Leonard, A. B. P. (1993), 'The biomechanics, autecology and behavior of suspension-feeding in crinoid echinoderms.'.

Lighthill, M. (1973), 'On the Weis-Fogh mechanism of lift generation', *J. Fluid Mech.* **60**(1), 1–17.

Lima, F. B. and Mound, L. A. (2016), 'Species-richness in neotropical sericothripinae (thysanoptera: Thripidae).', *Zootaxa* **4162**.

Liu, H. and Aono, H. (2009), 'Size effects on insect hovering aerodynamics: an integrated computational study', *Bioinspiration & Biomimetics* **4**(1), 015002.

Liu, H., Ravi, S., Kolomenskiy, D. and Tanaka, H. (2016), 'Biomechanics and biomimetics in insect-inspired flight systems', *Phil. Trans. R. Soc. B* **371**, 20150390.

Losos, J. B. (1994), 'An approach to the analysis of comparative data when a phylogeny is unavailable or incomplete', *Systematic Biology* **43**(1), 117–123.

Loudon, B. and Koehl (1994), 'When does motion relative to neighboring surfaces alter the flow through arrays of hairs?', *J. Exp. Biol.* **193**.

Luo, G. and Sun, M. (2005), 'Effects of corrugation and wing planform on the aerodynamic force production of sweeping model insect wings', *Acta Mech. Sin. Xuebao* **21**.

Lyu, Y. Z., Zhu, H. J. and Sun, M. (2019*a*), 'Aerodynamic forces and vortical structures of a flapping wing at very low reynolds numbers', *Physics of Fluids* **31**(4), 041901.

Lyu, Y. Z., Zhu, H. J. and Sun, M. (2019*b*), 'Flapping-mode changes and aerodynamic mechanisms in miniature insects', *PHYSICAL REVIEW E* **99**(012419).

MAF Plant Health & Environment Laboratory (2011).
URL: *http://www.padil.gov.au.*

Mao, S. and Xin, Y. (2003), 'Flows around two airfoils performing fling and subsequent translation and translation and subsequent clap', *Acta Mechanica Sinica* **19**(2), 103–117.

Martins, E. P. (1996), 'Conducting phylogenetic comparative studies when the phylogeny is not known', *Evolution* **50**(1), 12–22.

Martins, E. P. and Hansen, T. F. (1997), 'Phylogenies and the comparative method: a general approach to incorporating phylogenetic information into the analysis of interspecific data', *The American Naturalist* **149**(4), 646–667.

Martins, E. P. and Housworth, E. A. (2002), 'Phylogeny shape and the phylogenetic comparative method', *Systematic biology* **51**(6), 873–880.

Masumoto, M., Ng, Y. F. and Okajima, S. (2013), 'A new genus of Thripinae (Thysanoptera, Thripidae) collected from *Pandanus* in Japan, Malaysia and Australia, with three new species', *Zootaxa* **3709**(6), 543–554.

Maxworthy, T. (1979), 'Experiments on the Weis-Fogh mechanism of lift generation by insects in hovering flight. Part I. Dynamics of the 'fling'', *J. Fluid Mech.* **93**(1), 47–63.

Miller, L. A. and Peskin, C. S. (2004), 'When vortices stick: an aerodynamic transition in tiny insect flight', *J. Exp. Biol.* **207**(17), 3073–3088.

Miller, L. A. and Peskin, C. S. (2005), 'A computational fluid dynamics ofclap and fling'in the smallest insects', *J. Exp. Biol.* **208**(2), 195–212.

Miller, L. A. and Peskin, C. S. (2009), 'Flexible clap and fling in tiny insect flight', *J. Exp. Biol.* **212**(19), 3076–3090.

Minaei, K. and Aleosfoor, M. (2013), 'A new species of *Haplothrips* from southern iran (thysanoptera, phlaeothripidae).', *Zookeys* **275**.

Misof, B., Liu, S., Meusemann, K., Peters, R. S., Donath, A., Mayer, C., Frandsen, P. B., Ware, J., Flouri, T., Beutel, R. G. et al. (2014), 'Phylogenomics resolves the timing and pattern of insect evolution', *Science* **346**(6210), 763–767.

Moen, D. S., Irschick, D. J. and Wiens, J. J. (2013), 'Evolutionary conservatism and convergence both lead to striking similarity in ecology, morphology and performance across continents in frogs', *Proceedings of the Royal Society B: Biological Sciences* **280**(1773), 20132156.

Moen, D. S., Morlon, H. and Wiens, J. J. (2016), 'Testing convergence versus history: convergence dominates phenotypic evolution for over 150 million years in frogs', *Systematic Biology* **65**(1), 146–160.

Morse, J. G. and Hoddle, M. S. (2006), 'Invasion biology of thrips', *Annu. Rev. Entomol.* **51**, 67–89.

Mound, L. A. (2009), 'New taxa and new records of australian panchaetothripinae (thysanoptera, thripidae).', *Zootaxa* **33**.

Mound, L. A. and Reynaud, P. (2005), '*Franklinothrips*; a pantropical thysanoptera genus of ant-mimicking obligate predators (aeolothripidae)', *Zootaxa* **16**.

Mound, L. A. and Tree, D. J. (2016), 'Genera of the leaf-feeding dendrothripinae of the world (thysanoptera, thripidae), with new species from australia and sulawesi, indonesia.', *Zootaxa* **4109**.

Munro, J. B., Heraty, J. M., Burks, R. A., Hawks, D., Mottern, J., Cruaud, A., Rasplus, J.-Y. and Jansta, P. (2011), 'A molecular phylogeny of the chalcidoidea (hymenoptera)', *Plos one* **6**(11), e27023.

Ng, Y. F. and Mound, L. A. (2015), 'Species of thripinae (thysanoptera) from bamboo in malaysia, with one new species and six new records.', *Zootaxa* **3918**.

O'Meara, B. C. (2012), 'Evolutionary inferences from phylogenies: a review of methods', *Annual Review of Ecology, Evolution, and Systematics* **43**, 267–285.

Pagel, M. (1993), 'Seeking the evolutionary regression coefficient: an analysis of what comparative methods measure', *Journal of theoretical Biology* **164**(2), 191–205.

Pagel, M. (1999), 'Inferring the historical patterns of biological evolution', *Nature* **401**(6756), 877–884.

Pélabon, C., Firmat, C. J. P., Bolstad, G. H., Voje, K. L., Houle, D., Cassara, J., Le Rouzic, A. and Hansen, T. F. (2014), 'Evolution of morphological allometry'.

Percin, M., Hu, Y., van Oudheusden, B. W., Remes, B. and Scarano, F. (2012), 'Wing flexibility effects in clap-and-fling', *Int. J. Micro Air Veh* **3**(4).

Pereyra, V., Cavalleri, A., Szumik, C. and Weirauch, C. (2019), 'Phylogenetic analysis of the new world family heterothripidae (thysanoptera, terebrantia) based on morphological and molecular evidence', *Insect Systematics & Evolution* **50**(5), 702–716.

Poinar Jr, G. and Huber, J. T. (2011), 'A new genus of fossil mymaridae (hymenoptera) from cretaceous amber and key to cretaceous mymarid genera', *ZooKeys* (130), 461.

Polilov, A. A. (2015), 'Small is beautiful: features of the smallest insects and limits to miniaturization', *Annual review of entomology* **60**.

Posada, D. and Buckley, T. R. (2004), 'Model selection and model averaging in phylogenetics: advantages of akaike information criterion and bayesian approaches over likelihood ratio tests', *Systematic biology* **53**(5), 793–808.

Revell, L. J. (2010), 'Phylogenetic signal and linear regression on species data', *Methods in Ecology and Evolution* **1**(4), 319–329.

Revell, L. J. (2012), 'phytools: an r package for phylogenetic comparative biology (and other things)', *Methods in ecology and evolution* **3**(2), 217–223.

Riley, D. G., Joseph, S. V., Srinivasan, R. and Diffie, S. (2011), 'Thrips vectors of tospoviruses.', *J. Integr. Pest Manag.* **1**.

Rodriguez-Saona, C. R., Polavarapu, S., Barry, J. D., Polk, D., Jörnsten, R., Oudemans, P. V. and Liburd, O. E. (2010), 'Color preference, seasonality, spatial distribution and species composition of thrips (thysanoptera: Thripidae) in northern highbush blueberries', *Crop Protection* **29**(11), 1331–1340.

Rohle, F. J. (2006), 'A comment on phylogenetic correction', *Evolution* **60**(7), 1509–1515.

Samaee, M., Nelsen, N. H., Gaddam, M. G. and Santhanakrishnan, A. (2020), 'Diastolic vortex alterations with reducing left ventricular volume: an in vitro study', *J. Biomech. Eng.* **142**(12), 121006.

Sane, S. P. (2003), 'The aerodynamics of insect flight', *J. Exp. Biol.* **206**(23), 4191–4208.

Sane, S. P. (2016), 'Neurobiology and biomechanics of flight in miniature insects', *Curr. Opin. Neurobiol.* **41**, 158–166.

Sane, S. P. (2017), 'Eppur si vola (and yet it flies)', *J. Exp. Biol.* **220**(4), 514–516.

Sane, S. P. and Dickinson, M. H. (2002), 'The aerodynamic effects of wing rotation and a revised quasi-steady model of flapping flight', *J. Exp. Biol.* **205**, 1087–1096.

Santhanakrishnan, A., Jones, S. K., Dickson, W. B., Peek, M., Kasoju, V. T., Dickinson, M. H. and Miller, L. A. (2018), 'Flow structure and force generation on flapping wings at low reynolds numbers relevant to the flight of tiny insects', *fluids* **3**.

Santhanakrishnan, A., Robinson, A. K., Jones, S., Low, A. A., Gadi, S., Hedrick, T. L. and Miller, L. A. (2014), 'Clap and fling mechanism with interacting porous wings in tiny insect flight', *J. Exp. Biol.* **217**(21), 3898–3909.

Schindelin, J., Arganda-Carreras, I., Frise, E., Kaynig, V., Longair, M., Pietzsch, T., Preibisch, S., Rueden, C., Saalfeld, S., Schmid, B. et al. (2012), 'Fiji: an open-source platform for biological-image analysis', *Nature methods* **9**(7), 676–682.

Shyy, W. and Liu, H. (2007), 'Flapping wings and aerodynamic lift: the role of leading-edge vortices', *AIAA journal* **45**(12), 2817–2819.

Smith, B. L. and Neal, D. R. (2016), Particle image velocimetry, Crc Press, pp. 1–27.

Sokal, R. R. and Rohlf, F. J. (1995), 'biometry'.

Spedding, G. and Maxworthy, T. (1986), 'The generation of circulation and lift in a rigid two-dimensional fling', *J. Fluid Mech.* **165**, 247–272.

Srygley, R. and Thomas, A. (2002), 'Unconventional lift-generating mechanisms in free-flying butterflies', *Nature* **420**(6916), 660–664.

Stadler, T. (2011), 'Simulating trees with a fixed number of extant species', *Systematic biology* **60**(5), 676–684.

Sun, M. and Yu, X. (2006), 'Aerodynamic force generation in hovering flight in a tiny insect', *AIAA Journal* **44**(7).

Sunada, S., Takashima, H., Hattori, T., Yasuda, K. and Kawachi, K. (2002), 'Fluid-dynamic characteristics of a bristled wing', *J. Exp. Biol.* **205**(17), 2737–2744.

Symonds, M. R. (2002), 'The effects of topological inaccuracy in evolutionary trees on the phylogenetic comparative method of independent contrasts', *Systematic Biology* **51**(4), 541–553.

Taylor, G. and Thomas, A. (2014), *Evolutionary biomechanics: selection, phylogeny, and constraint*, OUP Oxford.

Team, R. C. et al. (2013), 'R: A language and environment for statistical computing'.

Terry, I. (2001), 'Thrips and weevils as dual, specialist pollinators of the australian cycad macrozamia communis (zamiaceae)', *Int. J. Plant Sci* **162**(6).

Trizila, P., Kang, C.-K., Aono, H. and Shyy, W. (2011), 'Low-reynolds-number aerodynamics of a flapping rigid flat plate', *AIAA Journal* **49**(4).

Tung Ho, L. s. and Ané, C. (2014), 'A linear-time algorithm for gaussian and non-gaussian trait evolution models', *Systematic biology* **63**(3), 397–408.

Ullman, D. E., Meideros, R., Campbell, L. R., Whitfield, A. E., Sherwood, J. L. and German, T. L. (2002), 'Thrips as vectors of tospoviruses.', *Adv. Bot. Res* **36**.

Usherwood, J. and Ellington, C. (2002), 'The aerodynamics of revolving wings. ii. propeller force coefficients from mayfly to quail', *J. Exp. Biol.* **205**.

Vincent, L., Shambaugh, W. S. and Kanso, E. (2016), 'Holes stabilize freely falling coins', *Journal of Fluid Mechanics* **801**, 250–259.

Voje, K. L. and Hansen, T. F. (2013), 'Evolution of static allometries: adaptive change in allometric slopes of eye span in stalk-eyed flies', *Evolution: International Journal of Organic Evolution* **67**(2), 453–467.

Wang, Z. J. (2000), 'Two dimensional mechanism for insect hovering', *Physical review letters* **85**(10), 2216.

Wang, Z. J. (2005), 'Dissecting insect flight', *Annu. Rev. Fluid Mech.* **37**, 183–210.

Wang, Z. J., Birch, J. M. and Dickinson, M. H. (2004), 'Unsteady forces and flows in low reynolds number hovering flight: two-dimensional computations vs robotic wing experiments', *Journal of Experimental Biology* **207**(3), 449–460.

Wang, Z. and Tong, X. (2016), '*Siamothrips balteus*, a new species of *Scirtothrips* genus-group from china (thysanoptera, thripidae).', *Zookeys* **2016**.

Weihs, D. and Barta, E. (2008), 'Comb wings for flapping flight at extremely low Reynolds numbers', *AIAA J.* **46**, 285–288.

Weis-Fogh, T. (1973), 'Quick estimates of flight fitness in hovering animals, including novel mechanisms for lift production', *J. Exp. Biol.* **59**(1), 169–230.

Weis-Fogh, T. (1975), 'Unusual mechanisms for the generation of lift in flying animals', *Scientific American* **233**(5), 80–87.

Whitfield, A. E., Ullman, D. E. and German, T. L. (2005), 'Tospovirus-thrips interactions', *Annu. Rev. Phytopathol.* **43**, 459–489.

Willmarth, W. W., Hawk, N. E. and Harvey, R. L. (1964), 'Steady and unsteady motions and wakes of freely falling disks', *The physics of Fluids* **7**(2), 197–208.

Willmott, A. P., Ellington, C. P. and Thomas, A. L. (1997), 'Flow visualization and unsteady aerodynamics in the flight of the hawkmoth, *Manduca sexta*', *Philosophical Transactions of the Royal Society of London. Series B: Biological Sciences* **352**(1351), 303–316.

Wu, J. C. (1981), 'Theory for aerodynamic force and moment in viscous flows', *AIAA Journal* **19**(4), 432–441.

Zamar, M. I., Hernández, M. C., Soto-Rodríguez, G. A. and Retana-Salazar, A. P. (2013), 'A new neotropical species of *Liothrips* (thysanoptera: Phlaeothripidae) associated with *Ludwigia* (myrtales: Onagraceae)', *Revista de la Sociedad Entomológica Argentina* **72**(1-2), 83–89.

Zhang, H., Mound, L. A. and Xie, Y. (2010), 'A new genus and species from southwestern china in the *Frankliniella* genus-group (thysanoptera: Thripidae).', *Zootaxa* **68**.

Zhong, H.-J. and Lee, C.-B. (2012), 'The wake of falling disks at low reynolds numbers', *Acta Mechanica Sinica* **28**(2), 367–371.

APPENDICES

A.1 Forewing morphological data of thrips and fairyflies

Species	Group	Family	BL [μm]	Wing area [μm²]	Chord [μm]	Span [μm]	*n*	*GM*	Image source
Allanagrus_magniclava	Fairyflies	Mymaridae	653	137873	173.87	793	96	3.68	Lin et al. 2007
Cleruchoides_noackae	Fairyflies	Mymaridae	470.5	105608	129.59	815	81	4.9	Lin et al. 2007
Dicopomorpha_schleideni	Fairyflies	Mymaridae	326.5	57316	104.6	548	43	8.14	Lin et al. 2007
Eubroncus_dubius	Fairyflies	Mymaridae	861	100113	130.02	770	83	4.46	Lin et al. 2007
Eustochus_besucheti	Fairyflies	Mymaridae	742	193588	218.75	885	71	3.85	Huber & Baquero 2007
Eustochus_nearticus	Fairyflies	Mymaridae	703.5	301731	264.68	1140	88	8.09	Huber & Baquero 2007
Eustochus_nipponicus	Fairyflies	Mymaridae	1023.5	237216	225.92	1050	78	8.95	Huber & Baquero 2007
Eustochus_pengellyi	Fairyflies	Mymaridae	781	187288	203.8	919	81	9.66	Huber & Baquero 2007
Eustochus_yoshimotoi	Fairyflies	Mymaridae	845	226367	235.2	965	92	8.98	Huber & Baquero 2007
Kikiki_huna	Fairyflies	Mymaridae	180	20101	75.57	266	32	9.59	Huber & Noyes 2013
Mimalaptus_victoria	Fairyflies	Mymaridae	346.5	237236	275.22	862	69	5.43	Lin et al. 2007
Mymaromella_chaoi	Fairyflies	Mymaridae	378	11406	63.37	180	44	5.56	Huber et al. 2008
Mymaromella_cyclopterus	Fairyflies	Mymaridae	409	27941	96.35	290	64	8.21	Huber et al. 2008
Mymaromella_mira	Fairyflies	Mymaridae	376	23297	91.01	256	74	7.56	Huber et al. 2008
Mymaromella_pala	Fairyflies	Mymaridae	321.5	22306	85.8	260	66	6.92	Huber et al. 2008
Prionaphes_depressus	Fairyflies	Mymaridae	553.5	166574	208.22	800	71	4.02	Lin et al. 2007
Richteria_lamennaisi	Fairyflies	Mymaridae	813	158410	180.83	876	41	4.67	Lin et al. 2007
Schizophragma_basalis	Fairyflies	Mymaridae	614	84870	142.88	594	78	6.79	Lin et al. 2007
Stethynium_brevioviposito r	Fairyflies	Mymaridae	585	86512	155.32	557	87	4.16	Huber et al. 2006
Stethynium_ophelimi	Fairyflies	Mymaridae	590	178413	211.65	843	104	3.56	Huber et al. 2006
Tinkerbella_nana	Fairyflies	Mymaridae	237.5	26113	94.62	276	36	10.63	Huber & Noyes 2013
Akarethrips_iotus	Thrips	Phlaeothripidae	1525	NA	NA	NA	NA	4.11	Dang et al. 2014
Bhattithrips_borealis	Thrips	Thripidae	1370	NA	NA	NA	NA	4.05	Mound 2009
Ceratothripoides_claratris	Thrips	Thripidae	1235	84398	143.78	587	64	NA	Riley et al. 2011
Clypeothrips_idrisi	Thrips	Thripidae	1350	NA	NA	NA	NA	4.65	Ng & Mound 2015
Frankliniella_brunneicornis	Thrips	Thripidae	2460	NA	NA	NA	NA	2.37	Mound & Reynaud 2005
Frankliniella_gemina	Thrips	Thripidae	1500	130100	176.53	737	64	NA	Riley et al. 2011
Frankliniella_intonsa	Thrips	Thripidae	1740	141059	163.46	863	76	NA	Riley et al. 2011
Frankliniella_occidentalis	Thrips	Thripidae	1685	178471	199.19	896	70	NA	Riley et al. 2011
Frankliniella_schultzei	Thrips	Thripidae	1670	119750	179.81	666	71	NA	Riley et al. 2011
Frankliniella_strasseni	Thrips	Thripidae	3010	NA	NA	NA	NA	2.05	Mound & Reynaud 2005
Frankliniella_veracrucensis	Thrips	Thripidae	1295	NA	NA	NA	NA	4.27	Goldarazena & Hance 2017
Gynaikothrips_ficorum	Thrips	Phlaeothripidae	1800	51271	123.25	416	161	NA	*MAF lab. (2011)
Haplothrips_dissociatus	Thrips	Phlaeothripidae	1700	NA	NA	NA	NA	3.87	Cavalleri et al. 2016
Haplothrips_herajius	Thrips	Phlaeothripidae	1845	NA	NA	NA	NA	1.88	Minaei & Aleosfoor 2013
Hoplandrothrips_sp	Thrips	Phlaeothripidae	1870	179289	238.1	753	136	NA	*MAF lab. (2011)
Hydatothrips_aliceae	Thrips	Thripidae	1370	NA	NA	NA	NA	3.69	Mound & Tree 2009
Karnyothrips_sp	Thrips	Phlaeothripidae	1340	72010	155.87	462	69	NA	*MAF lab. (2011)
Kenyattathrips_katarinae	Thrips	Thripidae	1400	NA	NA	NA	NA	3.45	Mound 2009
Lenkothrips_guaranitic us	Thrips	Heterothripidae	1200	NA	NA	NA	NA	7.31	Cavalleri & Mound 2014
Lenkothrips_kaminskii	Thrips	Heterothripidae	1300	NA	NA	NA	NA	4.52	Cavalleri & Mound 2016
Leucothrips_piercei	Thrips	Thripidae	550	31950	101.43	315	54	NA	*MAF lab. (2011)
Limothrips_cerealium	Thrips	Thripidae	1220	131038	199.76	656	104	NA	*MAF lab. (2011)
Liothrips_ludwigi	Thrips	Phlaeothripidae	2940	457976	352.02	1301	161	NA	Zamar et al. 2013
Neohydatothrips_clavisetis	Thrips	Thripidae	980	NA	NA	NA	NA	6.23	Lima & Mound 2016
Neohydatothrips_notialis	Thrips	Thripidae	995	NA	NA	NA	NA	6.01	Lima & Mound 2016
Neohydatothrips_renatae	Thrips	Thripidae	940	NA	NA	NA	NA	4.51	Lima & Mound 2016
Neohydatothrips_samayunkur	Thrips	Thripidae	720	64836	129.68	500	101	NA	*MAF lab. (2011)
Pandanothrips_ryukyuensis	Thrips	Thripidae	1530	NA	NA	NA	NA	4.57	Masumoto & Okajima 2013
Pandanothrips_wangi	Thrips	Thripidae	1120	NA	NA	NA	NA	6.05	Masumoto & Okajima 2013
Pseudodendrothrips_marissae	Thrips	Thripidae	900	NA	NA	NA	NA	5.06	Mound & Tree 2016
Scirtothrips_dorsalis	Thrips	Thripidae	935	71988	138.98	518	44	NA	Riley et al. 2011
Scirtothrips_sp	Thrips	Thripidae	470	26623	87.29	305	53	NA	*MAF lab. (2011)
Siamothrips_balteus	Thrips	Thripidae	940	NA	NA	NA	NA	4.53	Wang & Tang 2016
Stenchaetothrips_langkawiensis	Thrips	Thripidae	1150	NA	NA	NA	NA	8.75	Ng & Mound 2012
Thrips_tazanii	Thrips	Thripidae	1430	NA	NA	NA	NA	6.75	Masumoto & Okajima 2013
Thrips_setosus	Thrips	Thripidae	1400	135609	174.09	779	62	NA	Riley et al. 2011
Thrips_tabaci	Thrips	Thripidae	1500	143076	182.27	785	68	NA	Riley et al. 2011
Yaobinthrips_yangtzei	Thrips	Thripidae	1500	NA	NA	NA	NA	4.19	Zhang et al. 2010

Figure A.1. 0.1: All phenotypic data used in the analyses of thrips and fairyfly wings.

A.2 Phylogeny simulation details

We simulated phylogenies for our study taxa because very few of our study species have been sampled in published phylogenies. Of our 38 species of thrips with phenotypic data, only eight were in any one of the most comprehensive phylogenies published to date (Buckman et al., 2013; Lima and Mound, 2016; Pereyra et al., 2019). For fairyflies, the most comprehensive species-level phylogeny included only one of our 21 species (Munro et al. 2011). Moreover, no tree was ultrametric (i.e. all branches of extant species contempora-

neous), which is optimal for phylogenetic comparative analyses (Butler and King, 2004; O'Meara, 2012). Thus, because most of our species could not be placed in phylogenies, we simulated many possible phylogenies for our study species and conducted regressions across these trees. This procedure allowed for both integration over phylogenetic uncertainty (Martins 1996) and for assessment of the sensitivity of our results to any specific potential phylogeny (Losos 1994). Moreover, we note that our regression analyses are likely to be robust to phylogenetic variation or inaccuracy for many reasons. First, the phylogenetic regression is generally robust to tree misspecification (Stone, 2011). Second, our use of lambda should mitigate problems associated with contrasting phylogenetic and phenotypic structure in our data (e.g. phenotypically very different but closely related species, as in the same genus; Martins and Housworth 2002). Finally, ordinary least-squares regression (i.e. without phylogeny) and phylogenetic regression both give unbiased estimates of the interspecific regression slope (Pagel, 1993; Rohle, 2006), our focus here.

Adding some phylogenetic structure to simulated trees, rather than using completely random approaches, increases accuracy in downstream comparative analyses (Housworth and Martins, 2001; Martins, 1996; Martins and Housworth, 2002; Symonds, 2002). Thus, we ensured the simulated trees fit best estimates of taxonomy, given that taxonomy in principle reflect estimates of evolutionary relationships. At the lowest taxonomic level, all species of given genus were each other's closest relatives in every simulated tree. By adding additional taxonomic structure (i.e. subfamilies, families, suborders), our simulated trees were similarly constrained to best represent estimated relationships among higher taxa (Buckman et al., 2013).

For thrips, we first extracted taxonomic information from the Thrips Wiki. This source is updated regularly by researchers studying thrips systematics and is consistent with the current best estimate of higher-level thrips phylogeny (Buckman et al., 2013). Data were extracted on genera within families and families within the two major sub-orders of thrips (Terebrantia and Tubulifera). In some cases genera were placed into subfamilies, which were placed in families. All genera were included, including extinct genera and those unrepresented in our phenotypic data, to best simulate the branch-length structure among groups (e.g. mean genus age in a family of 100 genera will be lower than mean genus age in an equally old family of two genera). Current estimates of wasp systematics suggest that fairyflies are a polyphyletic group of two families in two superfamilies of wasps (Mymarommatoidea: Mymarommatidae and Chalcidoidea: Myrmaridae; Huber et al. 1986; Davis et al. 2010; Munro et al. 2011). However, the two superfamilies may be sister clades, and Mymaridae is the sister family to all other clades within Chalcidoidea (Heraty et al., 2013; Munro et al., 2011). Thus, additional taxonomic structure would not have greatly improved our simulated trees. So for analysis purposes, we assumed these two families to be each other's sister taxon. We compiled genera for these two families from taxonomic accounts (Gibson et al., 2007; Huber, 2005, 2017; Huber and Noyes, 2013*a*; Poinar Jr and Huber, 2011).

We simulated phylogenies in the package phytools v.0.7-70 (Revell, 2012) in R v.4.0.2 (R Core Team 2020). Because thrips and fairyflies are so distantly related phylogenetically (separated for more than 350 million years; Johnson et al. 2018; Misof et al. 2014), we started each simulated tree with these two groups as sister clades using the function "pbsim". We then simulated structure at sequentially lower taxonomic levels using the func-

tion "genus.to.species". Both of these functions simulated both tree topology and branch lengths. For both fairyflies and thrips, multiple levels of taxonomic ranks were imposed in simulations. In thrips, this meant randomly placing the branching time of the two suborders within Thysanoptera, then families within those suborders, subfamilies within some families, genera within (sub)families, and species within genera. For fairyflies, families were placed within superfamilies, genera within families, and species within genera.

We simulated 10,000 trees for our analyses. To remove variation in tree length due to stochastic simulation variation (Stadler, 2011), each simulated tree was rescaled to a total length of 1.0. Note that the relative (not absolute) amount of shared history between any two species determines the effect of phylogeny in PGLS (Hansen and Martins, 1996; Martins and Hansen, 1997). Thus our choice of 1.0 for tree length was arbitrary and did not affect our results. After simulation, each tree was pruned to only include the species for which we had phenotypic data, which varied based on the response variable (see above).

A.3 Dynamically scaled robotic platform

The experimental setup consists of a scaled-up bristled wing pair (or a single bristled wing) immersed in a 510 mm (length)×510 mm (width)×410 mm (height) optically clear acrylic tank filled with glycerin. Each wing was attached to a stainless steel D-shaft (diameter=6.35 mm) using custom made L-brackets Kasoju et al. (2018). Uniaxial strain gauges were mounted on the L-brackets to measure lift and drag forces. Two 2-phase hybrid stepper motors with integrated encoders (ST234E, National Instruments Corporation, Austin, TX, USA) were used to drive the D-shaft to perform rotational and translational motion. Rotational motion was achieved using a bevel gear coupled to a motor and a D-shaft, while translational motion was achieved using a rack-and-pinion mechanism driven by a second motor. All the stepper motors (4 motors needed for a bristled wing pair, 2 motors needed for a single wing) were controlled using a multi-axis controller (PCI-7350, National Instruments Corporation, Austin, TX, USA) via a custom LabVIEW program (National Instruments Corporation, Austin, TX, USA).

A.4 2D flow validation

Our assumption of 2D flow simplification is valid for two key reasons. First, in our previous study (Kasoju et al., 2018), we observed no flow along the z-direction of a rectangular bristled wing model. Second, in our more recent study (Kasoju and Santhanakrishnan, 2021*a*), we found a very small region of non-zero 2D divergence in the flow field, suggesting that 2D flow simplification is a reasonable approximation. Our 2D flow simplification is also in agreement with a recent study (Santhanakrishnan et al., 2018) of a revolving elliptical wing of similar aspect ratio (≈2) as this study, where spanwise flow was reduced for $Re_c < 10$.

A.5 2D TR-PIV

The glycerine solution was seeded with 55 μm diameter titanium dioxide filled polyamide particles (density=1.2 g cm^{-3}, LaVision GmbH, Göttingen, Germany). Seeding particles

were mixed in the glycerin solution at least one day before TR-PIV data acquisition to allow adequate time to realize homogenous initial distribution. The flow field was illuminated using a 527 nm wavelength single cavity Nd:YLF high-speed laser with a maximum repetition rate of 10 kHz and pulse energy of 30 mJ (Photonics Industries International, Ronkonkoma, NY, USA). This laser provided a 0.5 mm diameter beam that was passed through a -20 mm focal length plano-concave cylindrical lens to generate a 3 mm thick laser sheet, which was then oriented horizontally along the mid-span (HP). Raw TR-PIV images for each of the test conditions were acquired using a high-speed complementary metal-oxide-semiconductor (CMOS) camera (Phantom Miro 110, Vision Research Inc., Wayne, NJ, USA) with a spatial resolution of 1280×800 pixels, maximum frame rate of 1630 frames s^{-1}, and pixel size of 20×20 microns. A 50 mm constant focal length lens (Nikon Micro Nikkor, Nikon Corporation, Tokyo, Japan) was attached to the TR-PIV camera with the aperture set to 1.4 for all the measurements. A digital pulse was generated with a LabVIEW program to use as a trigger to begin recording TR-PIV images synchronized to the start of wing motion. For each of the test conditions, 100 images were acquired per cycle for 5 consecutive cycles.

A.6 2D PL-PIV

2D PL-PIV measurements were performed to examine inter-bristle flow characteristics along the wing span at a plane located at $0.5L_b$ measured from the LE (VP). The reason for conducting 2D PL-PIV measurements for calculating RFC, as opposed to TR-PIV, was to avoid PIV particle distortion due to astigmatism when viewing through a non-planar surface (Smith and Neal, 2016). We needed the camera to image the laser plane through a planar surface (front face of the acrylic tank) to avoid particle distortion. For a fixed laser plane (VP, *x*-*z* plane) and camera position, the bristles will not always be perpendicular to the laser plane during wing motion. We rotated the experimental setup for each instant where PL-PIV data was acquired so as to always have the wing bristles to be perpendicular to laser plane (VP). This allowed us to visualize inter-bristle flow along a plane perpendicular to the bristles. The same seeding particles as those used in TR-PIV were used for PL-PIV measurements. Illumination for PL-PIV measurements was provided using the same laser used for TR-PIV measurements, but in double-pulse mode where two short laser pulses were emitted at a specified pulse separation interval (dt). The laser beam was converted into a planar sheet using the same optics as in TR-PIV. dt ranged between 1,500-19,845 μs across all the test conditions. Raw PL-PIV image pairs separated by dt (frame-straddling mode, 1 image/pulse) were acquired for each of the test conditions using a scientific CMOS (sCMOS) camera (LaVision GmbH, Göttingen, Germany) with a spatial resolution of 2560×2160 pixels and a pixel size of 6.5×6.5 μm. A 60 mm constant focal length lens (same as the lens used in TR-PIV) was attached to the sCMOS camera with the aperture set to 2.8 for all PL-PIV measurements. The seeding particles illuminated by the laser sheet were focused using this lens. Similar to TR-PIV, a digital trigger signal was generated for PL-PIV using a custom LabVIEW program. This trigger signal was used as a reference to offset PL-PIV image pair acquisition to occur at specific phase-locked time points along the wing motion cycle.

A.7 PIV processing

Raw TR-PIV image sequences and PL-PIV image pairs were processed in DaVis 8.3.0 software (LaVision GmbH, Göttingen, Germany). Multi-pass cross-correlation was performed on the raw PIV images with two passes each on an initial window size of 64×64 pixels and a final window size of 32×32 pixels, each with 50% overlap. Post-processing was performed by rejecting velocity vectors with peak ratio Q less than 1.2. The post-processed 2D velocity vector fields were phase-averaged across 5 consecutive cycles at every time instant where TR-PIV and PL-PIV data were acquired. The phase-averaged 2D velocity vector fields were exported as .DAT files containing: (x,y,u,v) from TR-PIV measurements along the x-y plane; and (x,z,u,w) from PL-PIV measurements along the x-z plane. Note that u,v,w are velocity components along x,y,z coordinates, respectively. The exported TR-PIV velocity vector fields were further processed to calculate z-component of vorticity (ω_z) and pressure distribution. Similarly, the exported PL-PIV velocity vector fields were used to estimate the reverse flow capacity of the bristled wing. Visualization of exported velocity vector fields was performed using Tecplot 360 software (Tecplot, Inc., Bellevue, WA, USA).

A.8 Circulation calculation

For a particular test condition, the maximum absolute values of ω_z (i.e., $|\omega_z|$) at both LEV and TEV of a bristled wing were identified. Similar to Ford et al. (2019) and Kasoju and Santhanakrishnan (2021*a*), a 10%$|\omega_z|$ high-pass cut-off was next applied to isolate the vortex cores on a bristled wing model for that test condition. Γ of LEV or TEV was then calculated by selecting a region of interest (ROI) by drawing a box around a vortex core. A custom MATLAB script was used to automate the process of determining the ROI Samaee et al. (2020). Essentially, we iterated the selection of ROI by starting with a small square box of 2 mm edge length and compared the Γ value with that of a bigger square box of 5 mm edge length. If the circulation values matched between the 2 boxes, then we stopped further iteration. If the circulation values did not match between the 2 boxes, we increased the size of the smaller box by 3 mm and repeated the process. In order to work with single vortex (LEV or TEV) at a time and to remove any bias of Γ estimation, we ensured that ω_z of the oppositely signed vortex was zeroed out. Γ was determined for the right-hand side wing only, with the assumption that circulation for the left wing was equivalent in magnitude but oppositely signed. Note that the left-wing motion is symmetric to the right wing about the y-z plane, making our assumption justifiable.

A.9 Supplementary Material

A.9. 1 SA 1: Aerodynamic performance of simplified bristled wing models based on morphological estimates

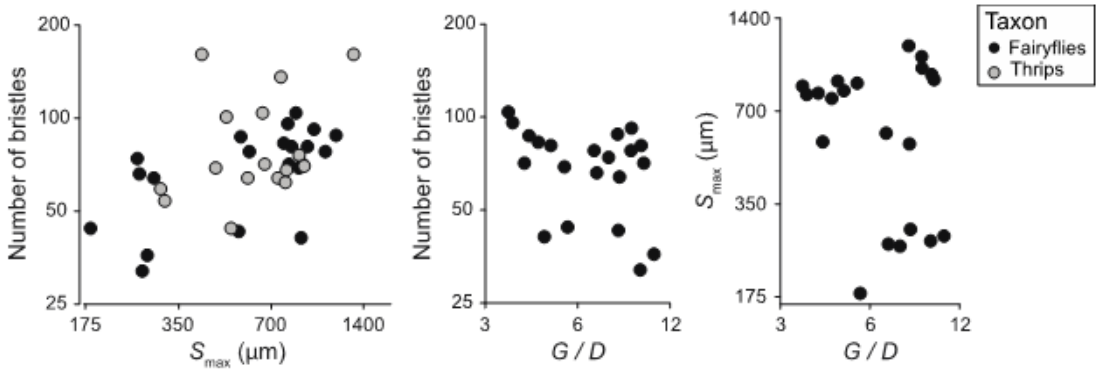

Figure A.9. 1.1: Scatter plots of wing variables measured across thrips and fairyflies. All variables are plotted in raw units on a logged scale. Fairyfly data across all plots are from the same species. Thrips species measured for $S_{\max}$ and n were different species than those for which we measured G/D, preventing plotting and correlation among those variables. All correlations among wing variables were low and statistically insignificant (Table 3.3)

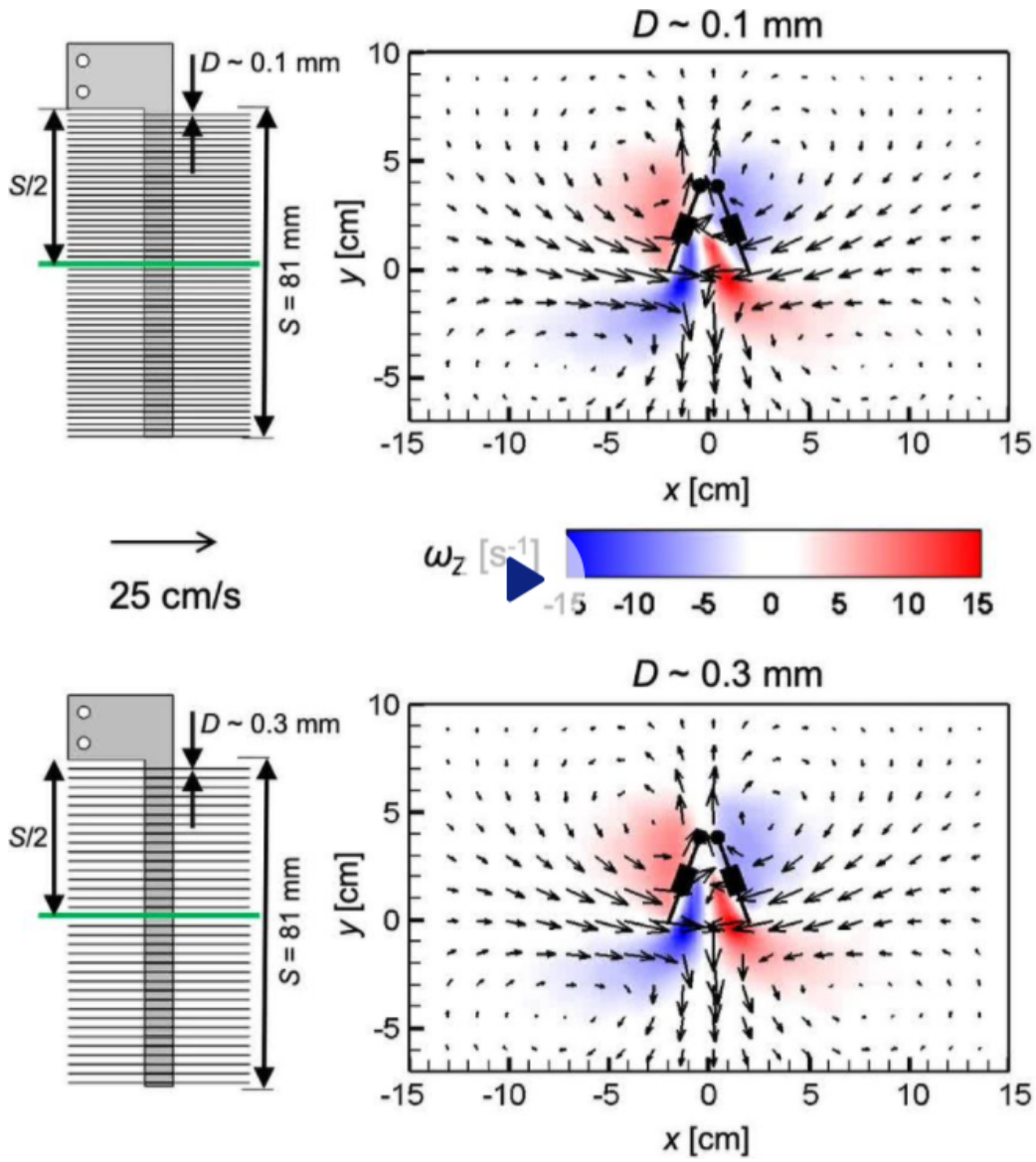

Movie A.9. 1.2: Velocity vectors overlaid on out-of-plane vorticity (ω_z) contours of bristled wing pairs during clap and fling, comparing the effect of increasing bristle diameter (D) from 0.1 mm to 0.3 mm. 10 equally spaced time instances are shown from start to end of clap, followed by 8 equally spaced time instances during fling.

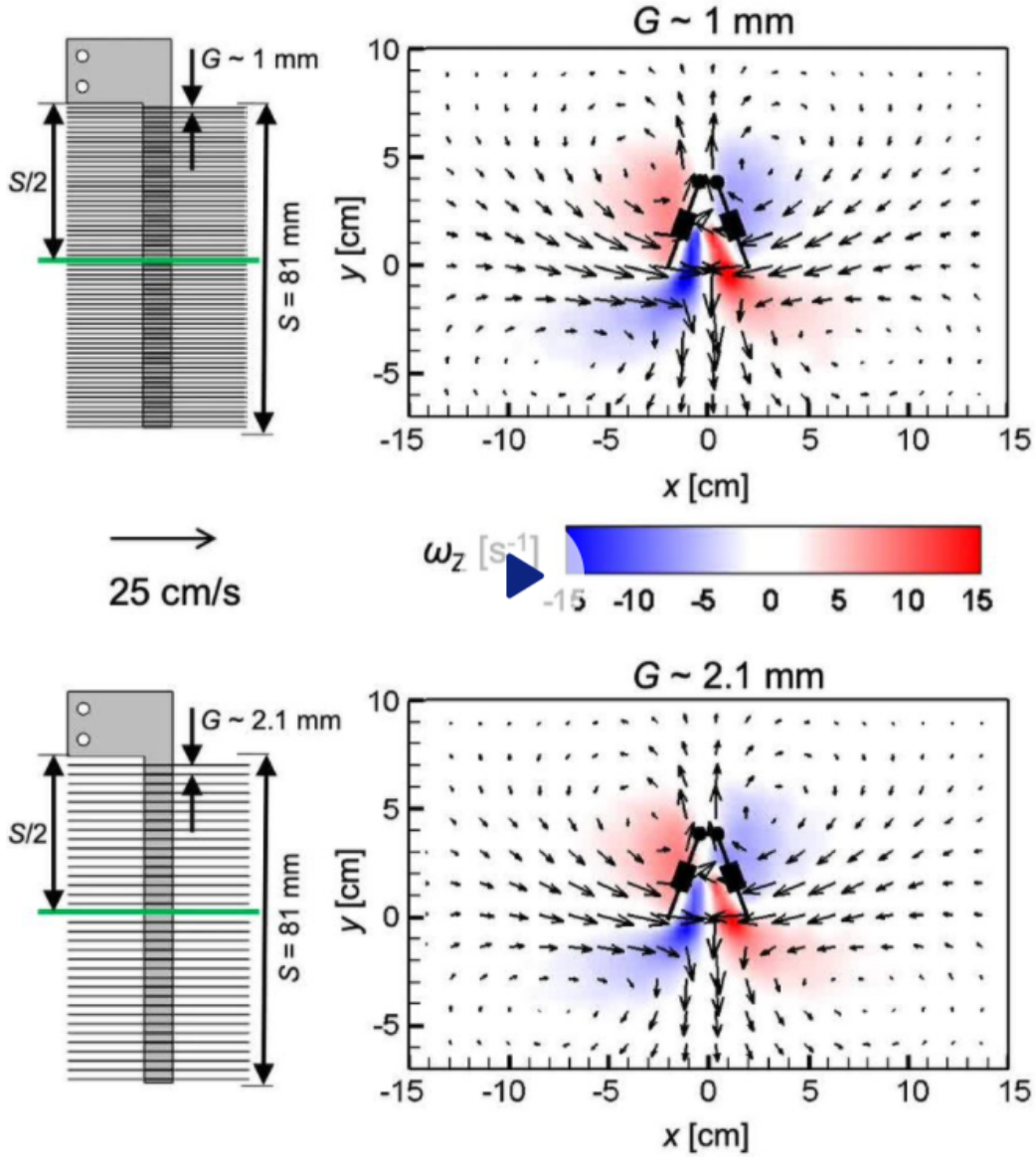

Movie A.9. 1.3: Velocity vectors overlaid on out-of-plane vorticity (ω_z) contours of bristled wing pairs during clap and fling, comparing the effect of increasing inter-bristle gap (G) from 1 mm to 2.1 mm. 10 equally spaced time instances are shown from start to end of clap, followed by 8 equally spaced time instances during fling.

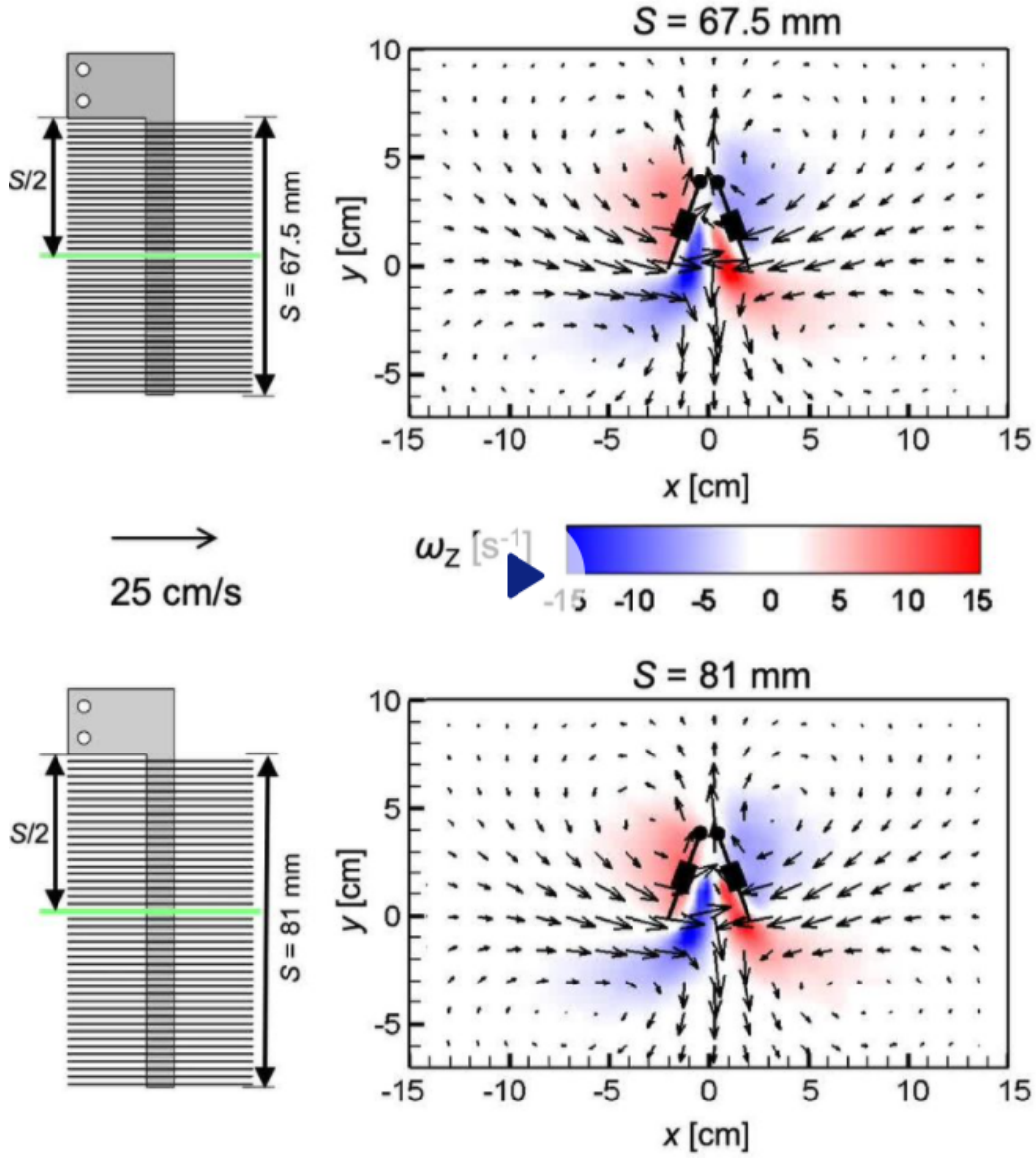

Movie A.9. 1.4: Velocity vectors overlaid on out-of-plane vorticity (ω_z) contours of bristled wing pairs during clap and fling, comparing the effect of increasing wingspan (S) from 67.5 mm to 81 mm. 10 equally spaced time instances are shown from start to end of clap, followed by 8 equally spaced time instances during fling.

A.9. 2 SA 2: Flow characterization on aerodynamic force generation during wing-wing interaction for varying wing kinematics

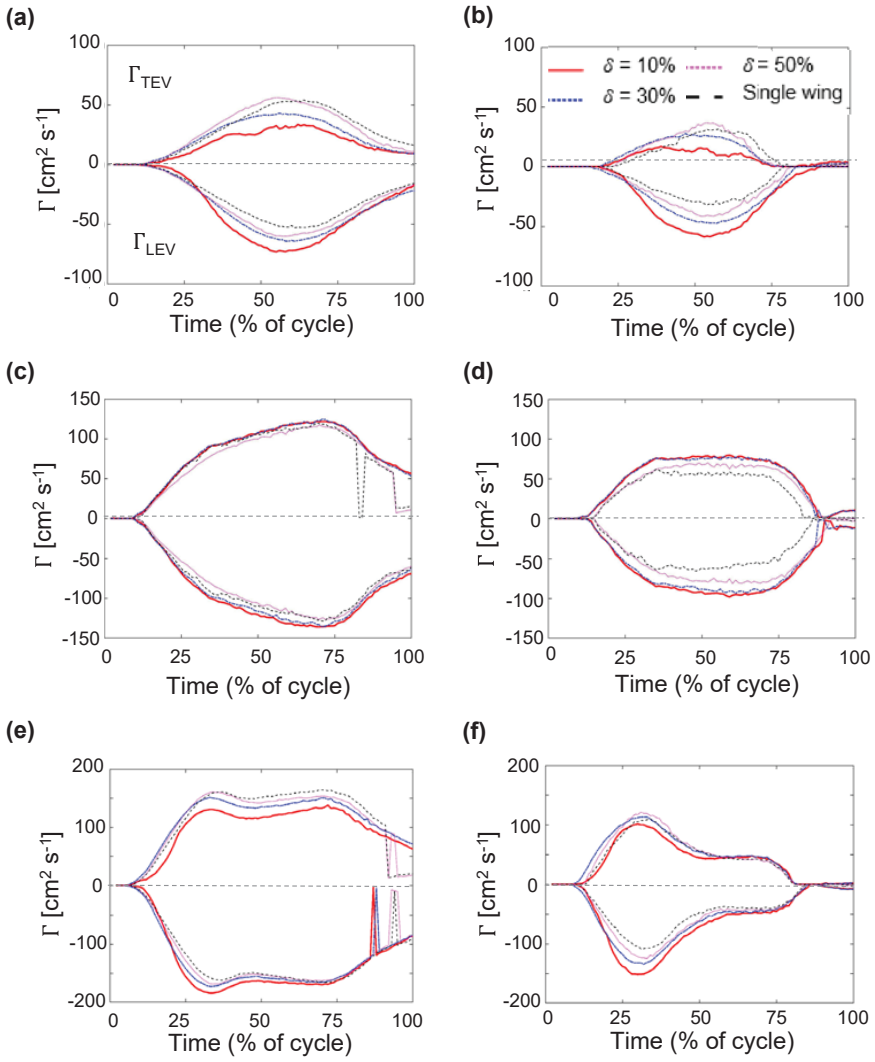

Figure A.9. 2.1: Circulation (Γ) of the leading edge vortex (LEV) and the trailing edge vortex (TEV) as a function of δ and wing kinematics. (a) and (b) show Γ during rotation for θ_r =22.5° at 5% and 25% cut-off, respectively. (c) and (d) show Γ during linear translation for θ_t =22.5° at 5% and 25% cut-off, respectively. (e) and (f) show Γ during combined rotation and linear translation for ζ = 25% at 5% and 25% cut-off, respectively. Positiv Γ corresponds to TEV and negative Γ corresponds to LEV. Legend is shown in (b). The *y*-axis range for (a) and (b) is -100 to 100, (c) and (d) is -150 to 150, (e) and (f) is -200 to 200.

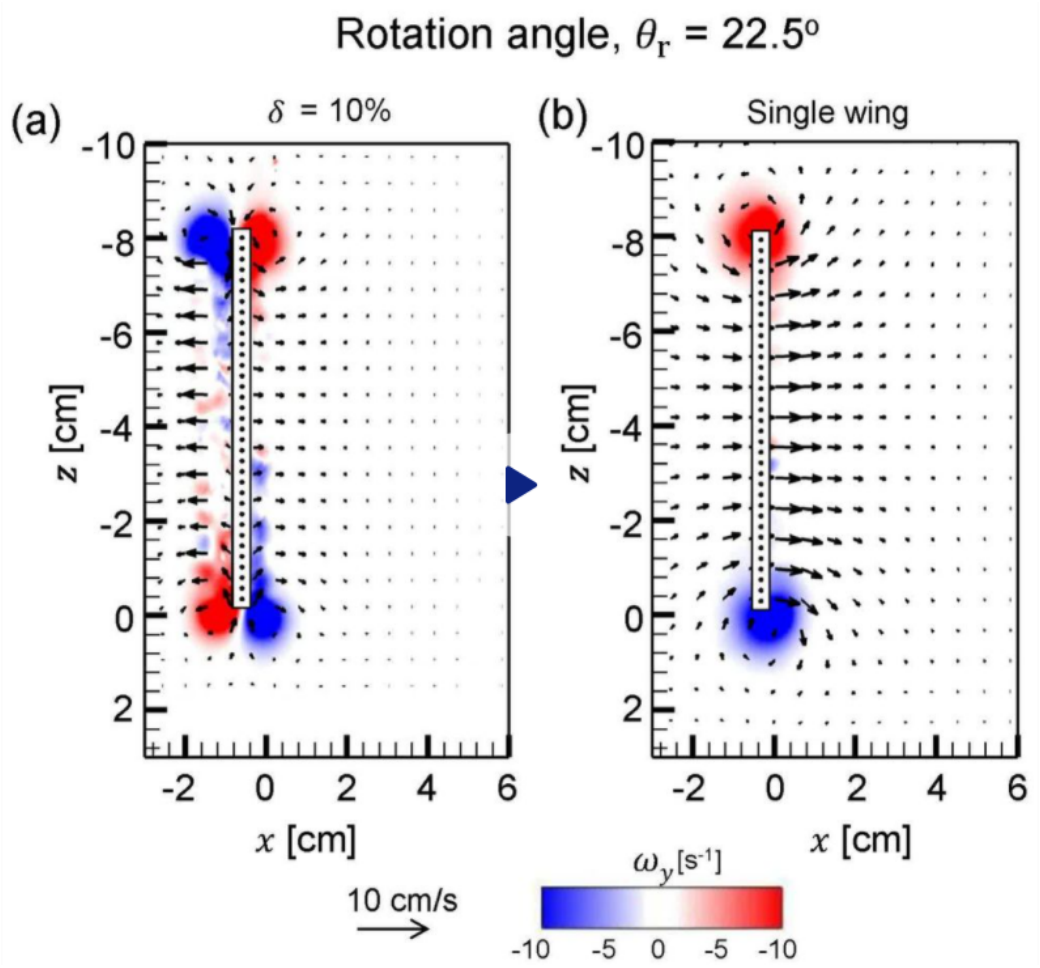

Movie A.9. 2.2: Velocity vector fields overlaid on top of vorticity contours during wing rotation at $\theta_r = 22.5^\circ$ for (a) δ=10% and (b) Single wing.

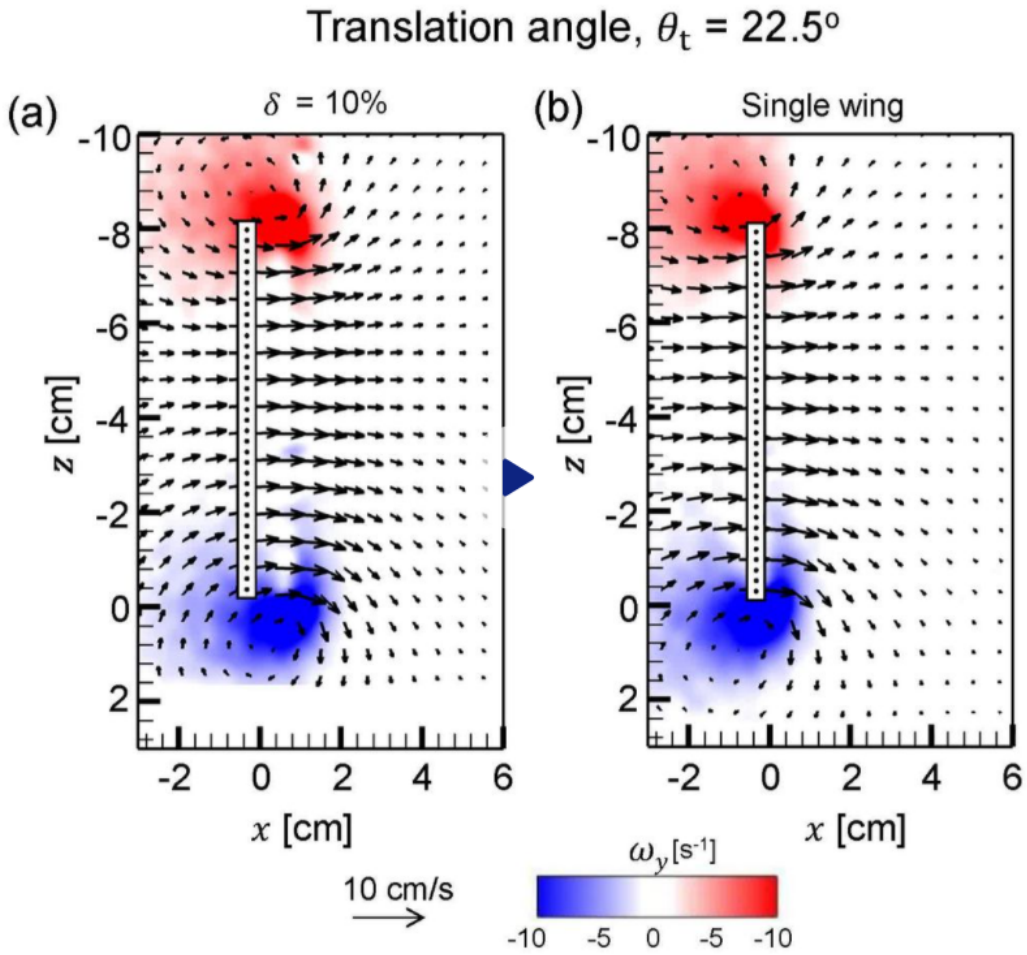

Movie A.9. 2.3: Velocity vector fields overlaid on top of vorticity contours during wing translation at $\theta_t = 22.5^\circ$ for (a) δ=10% and (b) Single wing.

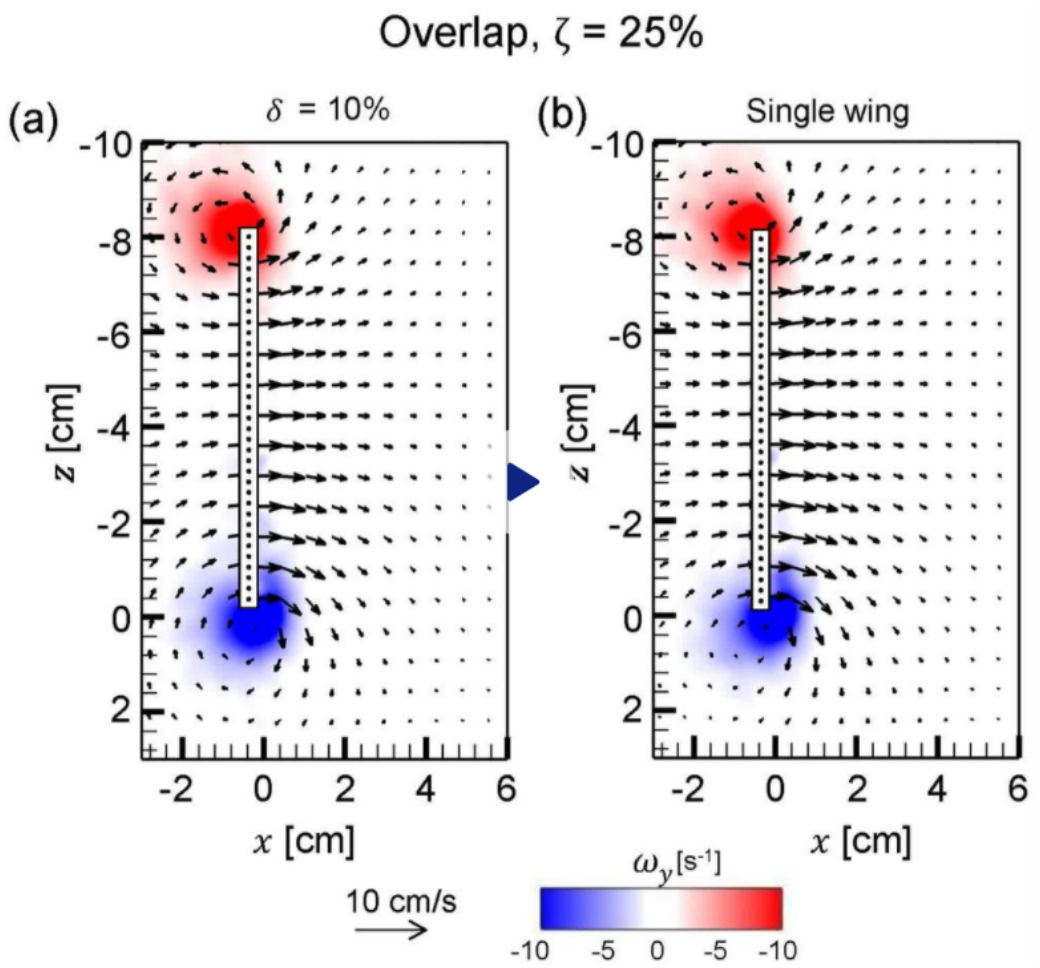

Movie A.9. 2.4: Velocity vector fields overlaid on top of vorticity contours during overlap at ζ = 25% for (a) δ=10% and (b) Single wing.

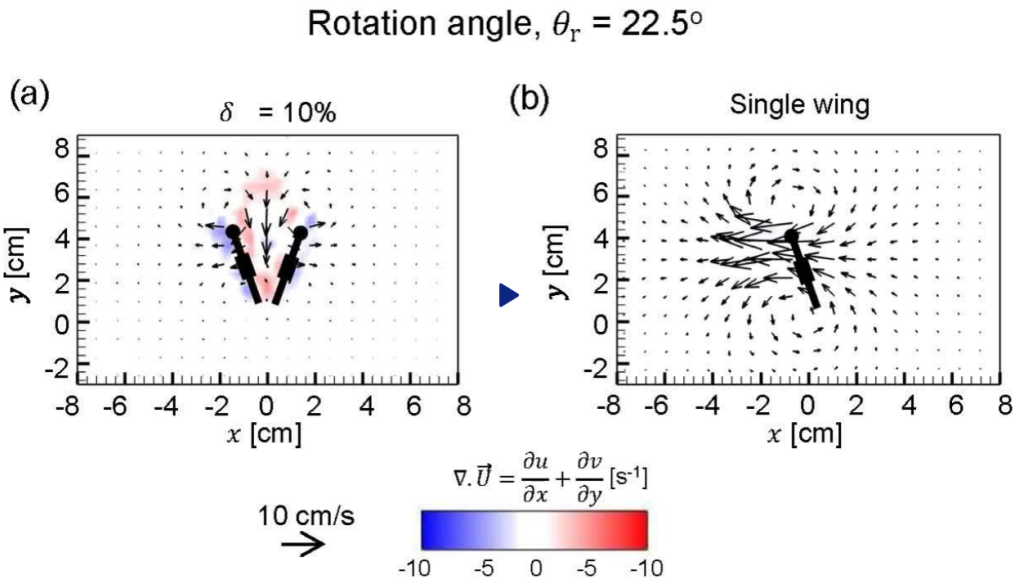

Movie A.9. 2.5: Velocity vector fields overlaid on top of divergence contours during wing rotation at $\theta_r = 22.5°$ for (a) δ=10% and (b) Single wing.

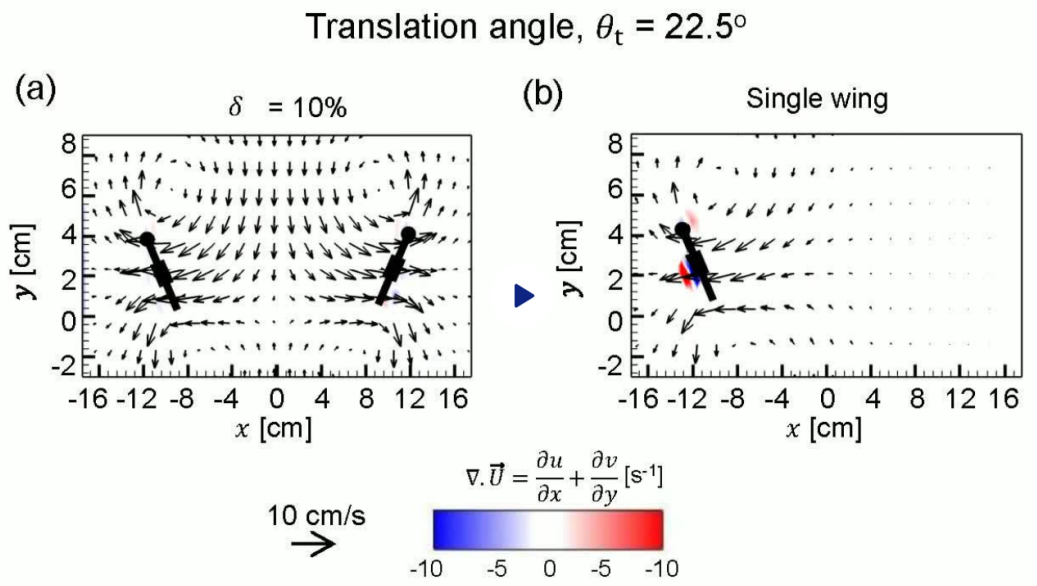

Movie A.9. 2.6: Velocity vector fields overlaid on top of divergence contours during wing translation at $\theta_t = 22.5°$ for (a) δ=10% and (b) Single wing.

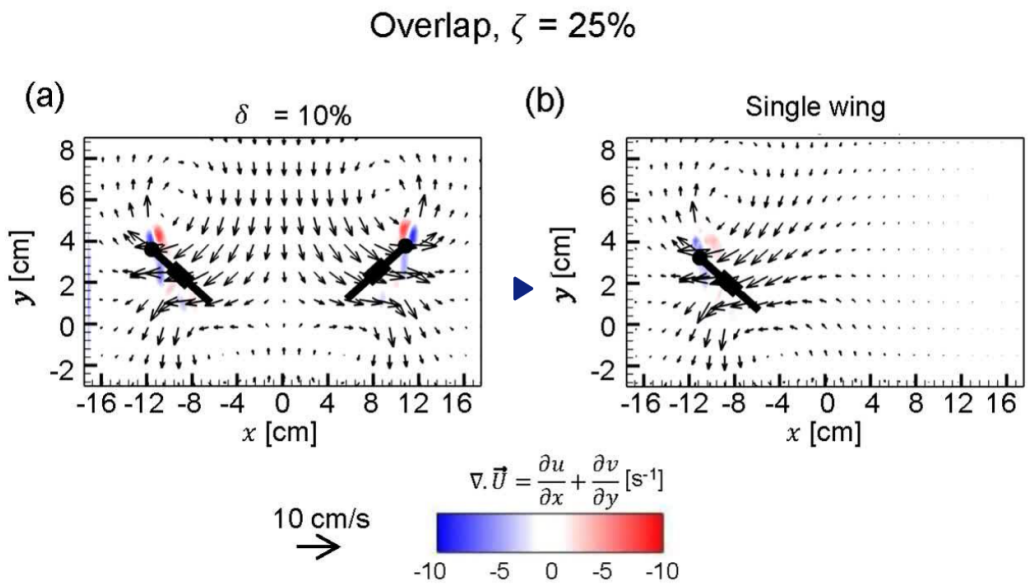

Movie A.9. 2.7: Velocity vector fields overlaid on top of divergence contours during overlap at ζ = 25% for (a) δ=10% and (b) Single wing.

A.9. 3 SA 3: Pause duration analyzed between end of upstroke and start of downstroke for several high speed video recordings

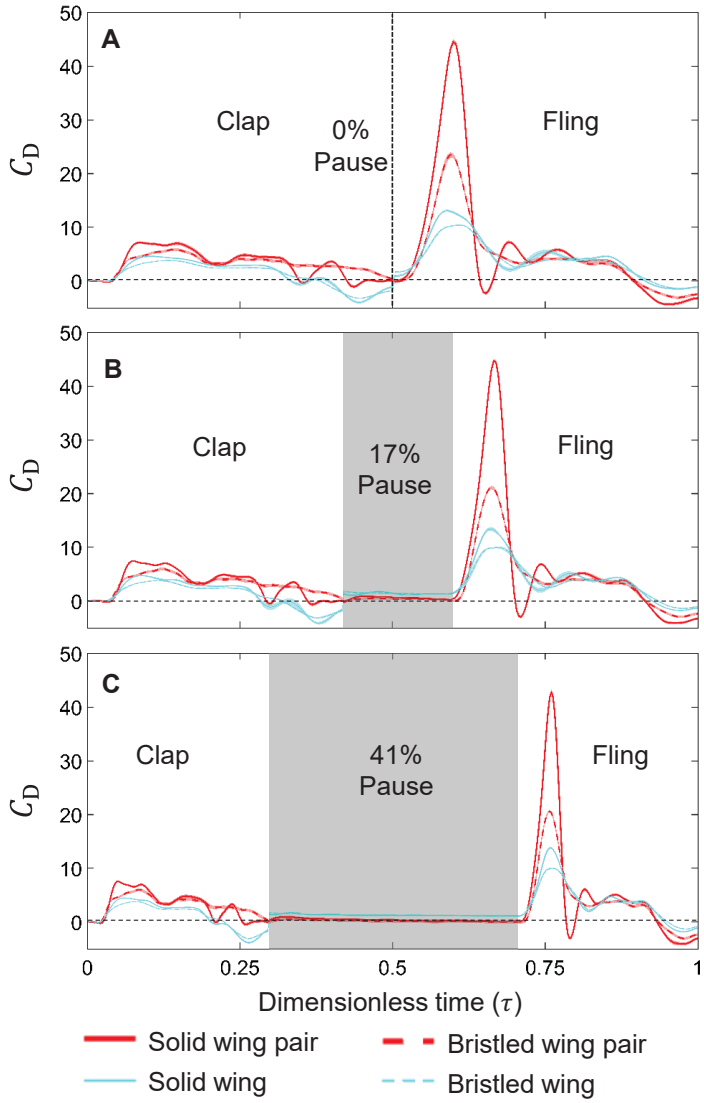

Figure A.9. 3.1: Drag coefficients (C_D) for a single wing and a wing pair at Re_c=10 during an entire cycle (including the pause time). Shading around each curve represents range of ± 1 standard deviation for that particular data (across 30 cycles). (A) 0% pause, (B) 17% pause, (C) 41% pause. Grey shaded regions in the figure represents the pause period. Legend is shown at the bottom of the figure.

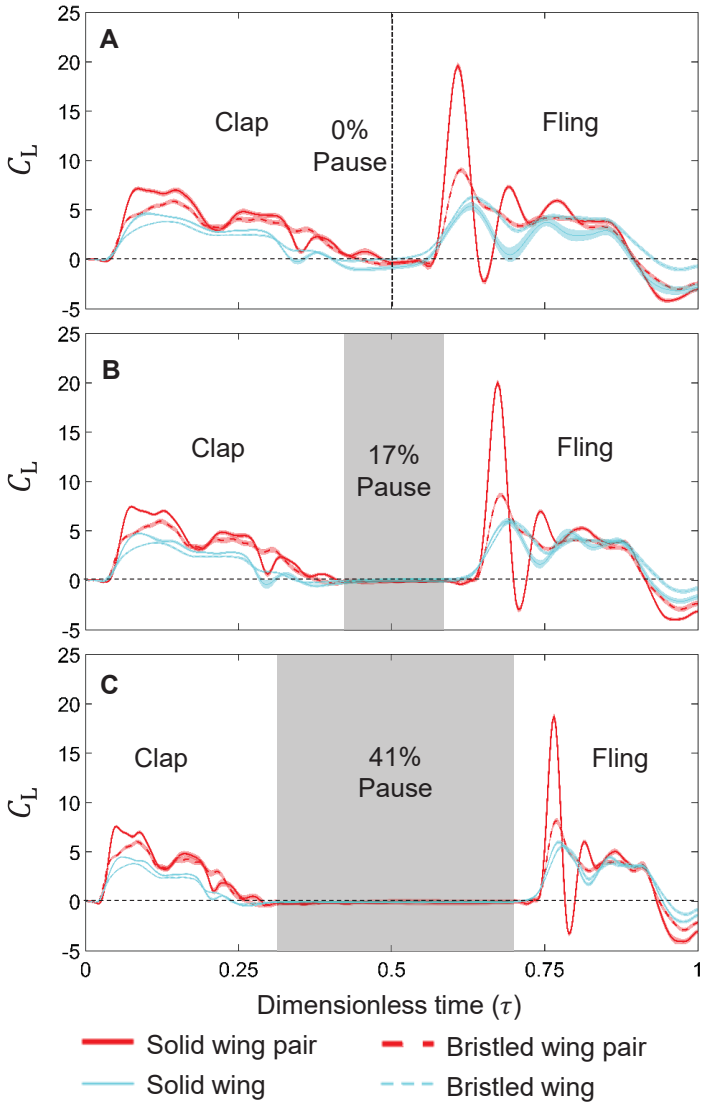

Figure A.9. 3.2: Lift coefficients (C_L) for a single wing and a wing pair at Re_c=10 during an entire cycle (including the pause time). Shading around each curve represents range of ± 1 standard deviation for that particular data (across 30 cycles). (A) 0% pause, (B) 17% pause, (C) 41% pause. Grey shaded regions in the figure represents the pause period. Legend is shown at the bottom of the figure.

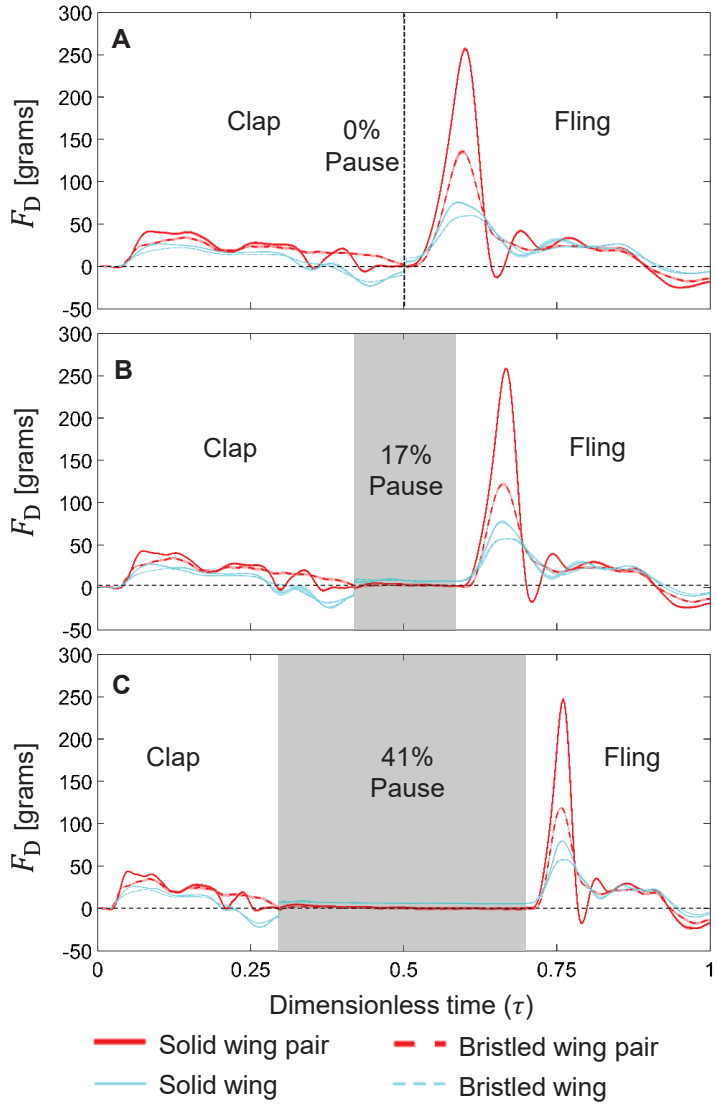

Figure A.9. 3.3: Drag force (F_D) in grams for a single wing and a wing pair at Re_c=10 during an entire cycle (including the pause time). Shading around each curve represents range of ± 1 standard deviation for that particular data (across 30 cycles). (A) 0% pause, (B) 17% pause, (C) 41% pause. Grey shaded regions in the figure represents the pause period. Legend is shown at the bottom of the figure.

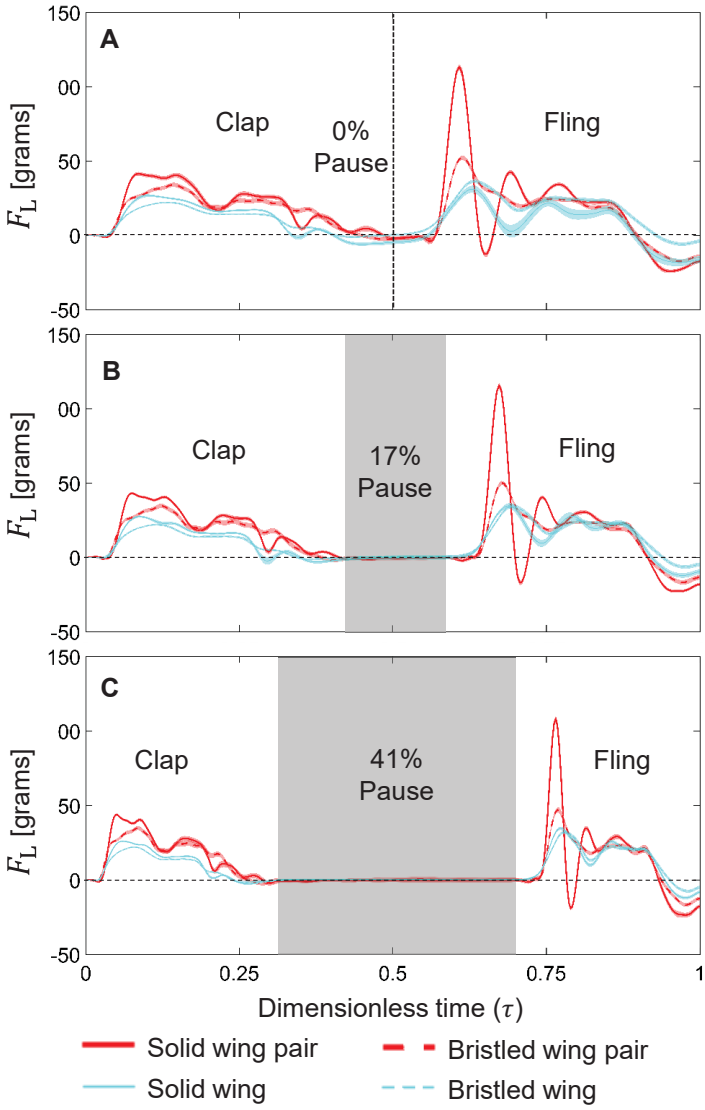

Figure A.9. 3.4: Lift force (F_L) in grams for a single wing and a wing pair at Re_c=10 during an entire cycle (including the pause time). Shading around each curve represents range of ± 1 standard deviation for that particular data (across 30 cycles). (A) 0% pause, (B) 17% pause, (C) 41% pause. Grey shaded regions in the figure represents the pause period. Legend is shown at the bottom of the figure.

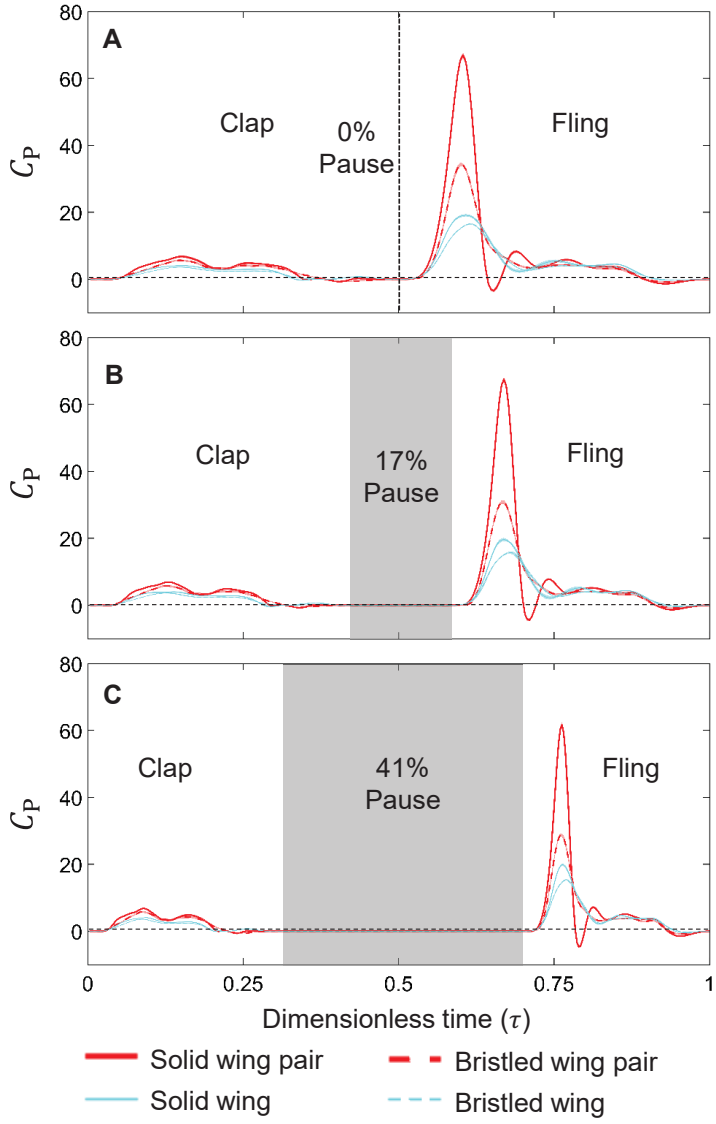

Figure A.9. 3.5: Power coefficients (C_P) for a single wing and a wing pair at Re_c=10 during an entire cycle (including the pause time). Shading around each curve represents range of ± 1 standard deviation for that particular data (across 30 cycles). (A) 0% pause, (B) 17% pause, (C) 41% pause. Grey shaded regions in the figure represents the pause period. Legend is shown at the bottom of the figure.

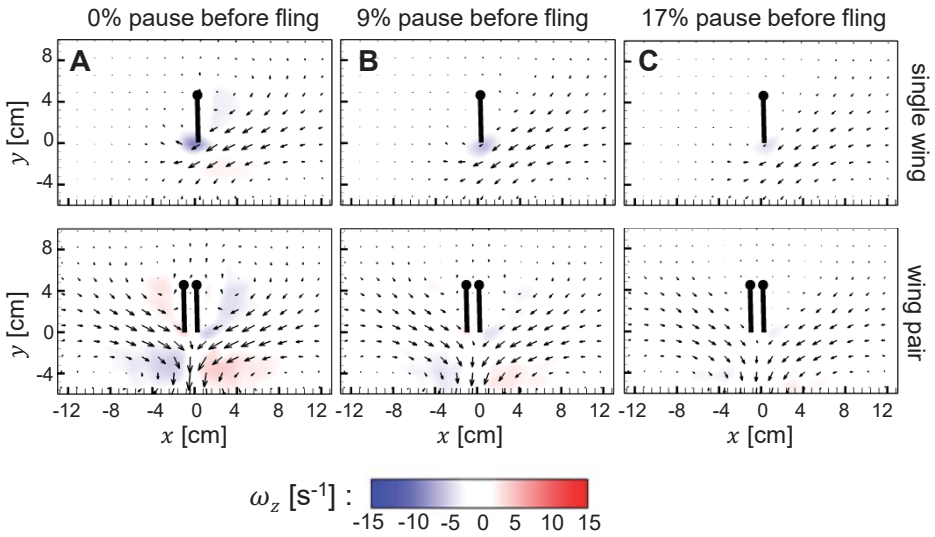

Figure A.9. 3.6: Velocity vector fields overlaid on out-of-plane z-vorticity (ω_z) contours for single solid wing and solid wing pair at Re_c = 10 for various pause times just before start of fling (0% of fling time): (A) 0%, (B) 9%, (C) 17% were displayed along each column. Red colour represents counterclockwise vorticity, while blue represents clockwise vorticity. z-vorticity (ω_z) was calculated using equations.

A.9. 4 SA 4: Flapping flight with bristled wings at low Reynolds numbers

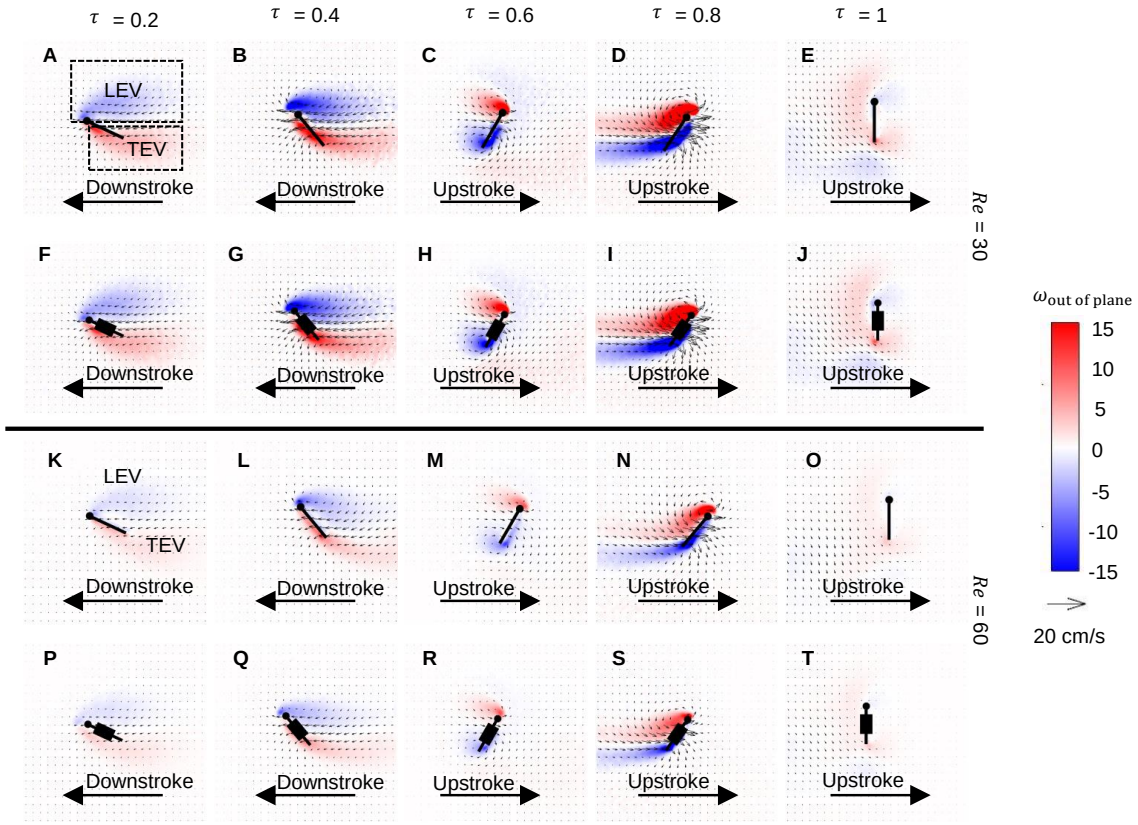

Figure A.9. 4.1: 2D phase-locked PIV (PL-PIV) showing vorticity contours overlaid on top of velocity vectors performing thrips kinematics at 5 dimensionless times (τ= 0.2, 0.4, 0.6, 0.8, 1) for (A-E) single solid wing at *Re* = 30, (F-J) single bristle wing at *Re* = 30, (K-O) single solid wing at *Re* = 60, (P-T) single bristled wing at *Re* = 60. The dashed boxes around the leading edge vortex (LEV) and trailing edge vortex (TEV) represents the region of interest for calculating circulation (Γ).

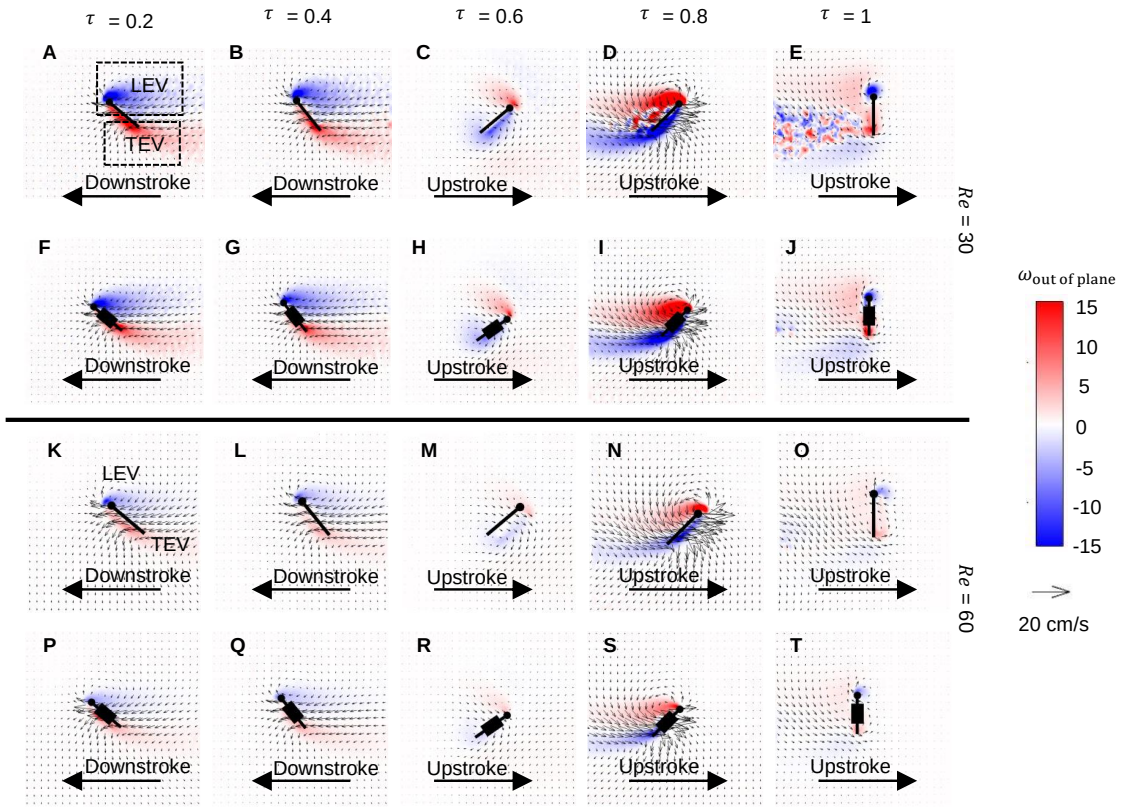

Figure A.9. 4.2: 2D phase-locked PIV (PL-PIV) showing vorticity contours overlaid on top of velocity vectors performing leafminers kinematics at 5 dimensionless times (τ= 0.2, 0.4, 0.6, 0.8, 1) for (A-E) single solid wing at *Re* = 30, (F-J) single bristle wing at *Re* = 30, (K-O) single solid wing at *Re* = 60, (P-T) single bristled wing at *Re* = 60. The dashed boxes around the leading edge vortex (LEV) and trailing edge vortex (TEV) represents the region of interest for calculating circulation (Γ).

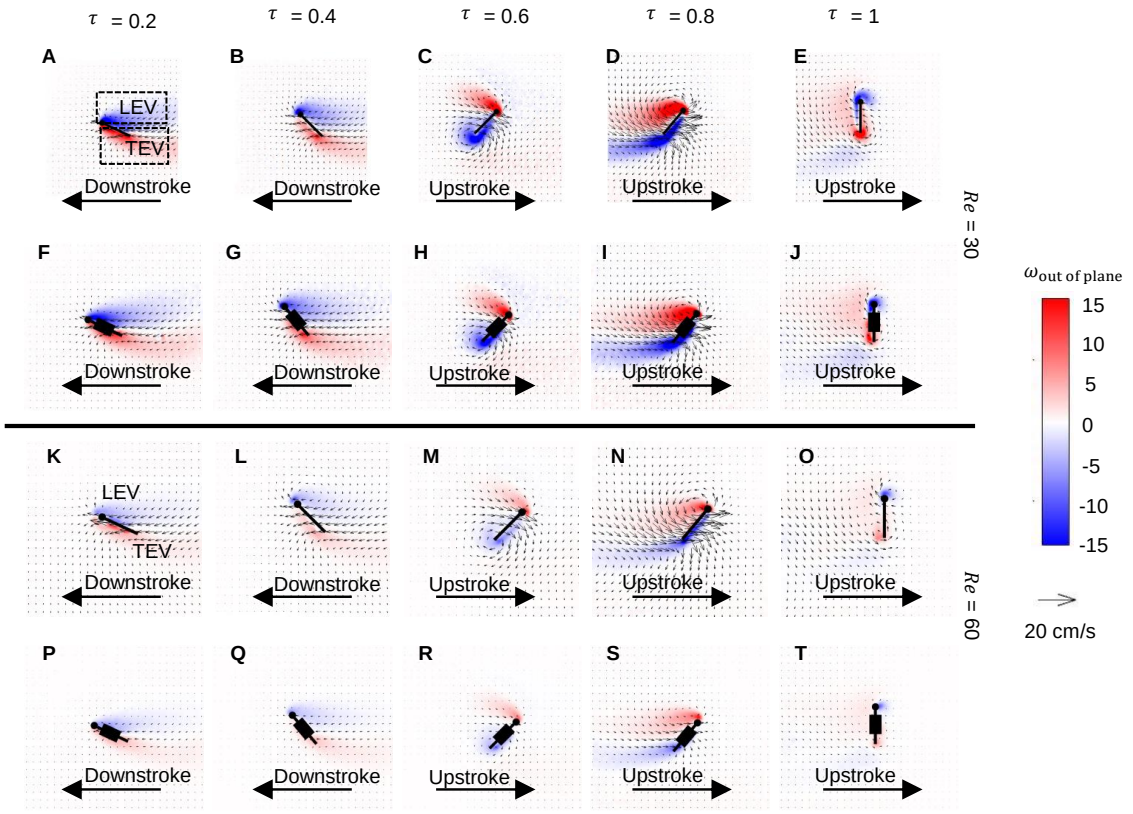

Figure A.9. 4.3: 2D phase-locked PIV (PL-PIV) showing vorticity contours overlaid on top of velocity vectors performing fruitfly kinematics at 5 dimensionless times (τ= 0.2, 0.4, 0.6, 0.8, 1) for (A-E) single solid wing at *Re* = 30, (F-J) single bristle wing at *Re* = 30, (K-O) single solid wing at *Re* = 60, (P-T) single bristled wing at *Re* = 60. The dashed boxes around the leading edge vortex (LEV) and trailing edge vortex (TEV) represents the region of interest for calculating circulation (Γ).

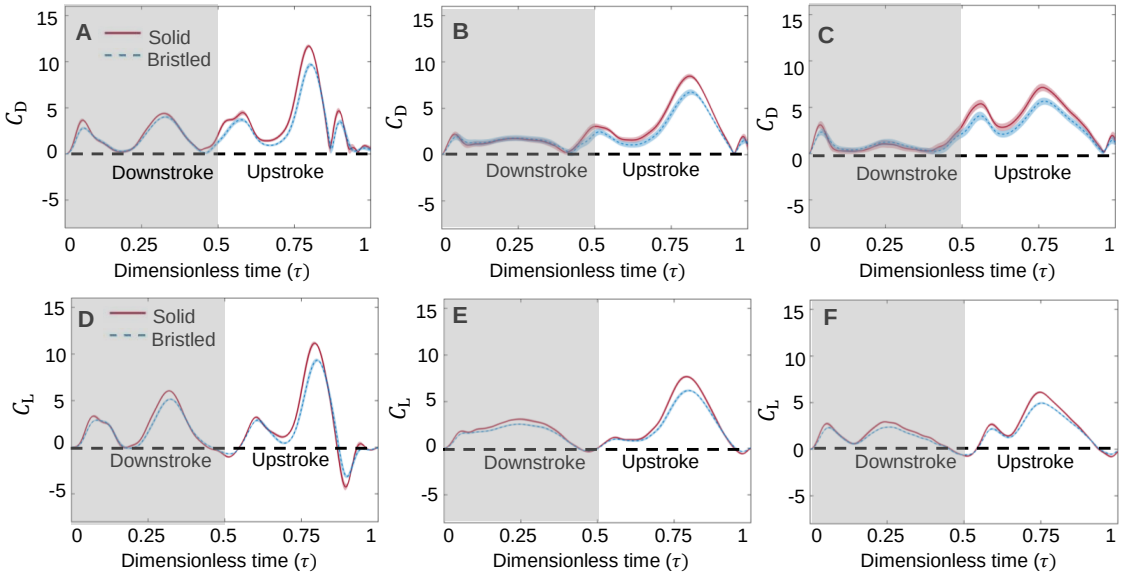

Figure A.9. 4.4: Time variation of drag coefficient (C_D) and lift coefficient (C_L) for a single solid and single bristled wing performing (A,D) Thrips kinematics, (B, E) Leafminers kinematics, (C, F) Fruitfly kinematics at Re = 30, respectively. Shaded region represents downstroke and non-shaded region represents upstroke.

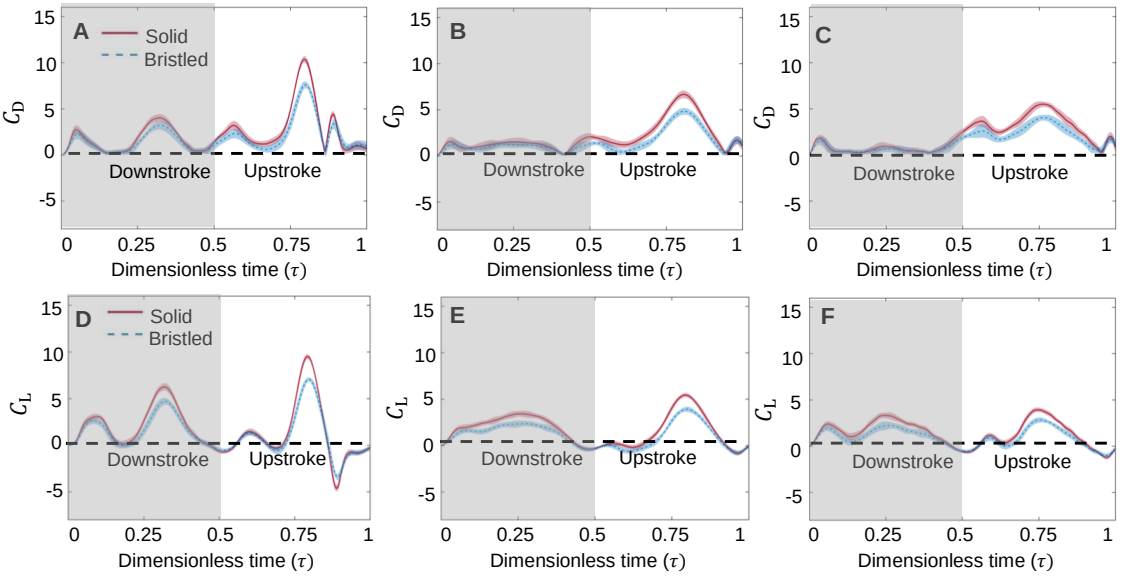

Figure A.9. 4.5: Time variation of drag coefficient (C_D) and lift coefficient (C_L) for a single solid and single bristled wing performing (A,D) Thrips kinematics, (B, E) Leafminers kinematics, (C, F) Fruitfly kinematics at Re = 60, respectively. Shaded region represents downstroke and non-shaded region represents upstroke.

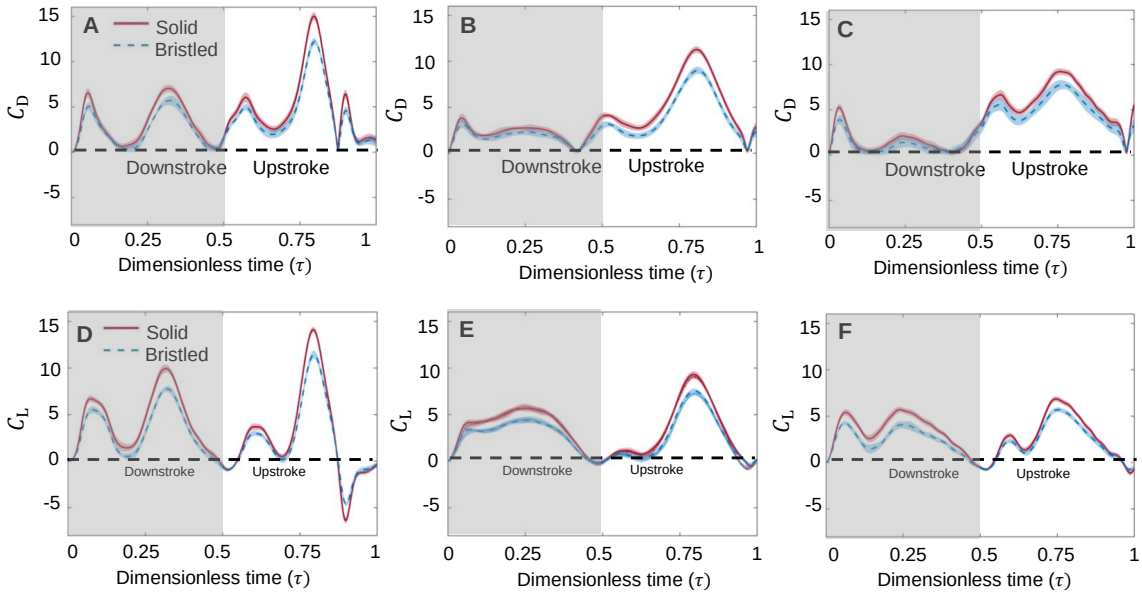

Figure A.9. 4.6: Time variation of drag coefficient (C_D) and lift coefficient (C_L) for solid wing pair and bristled wing pair performing (A,D) Thrips kinematics, (B, E) Leafminers kinematics, (C, F) Fruitfly kinematics at Re = 10, respectively. Shaded region represents downstroke and non-shaded region represents upstroke.

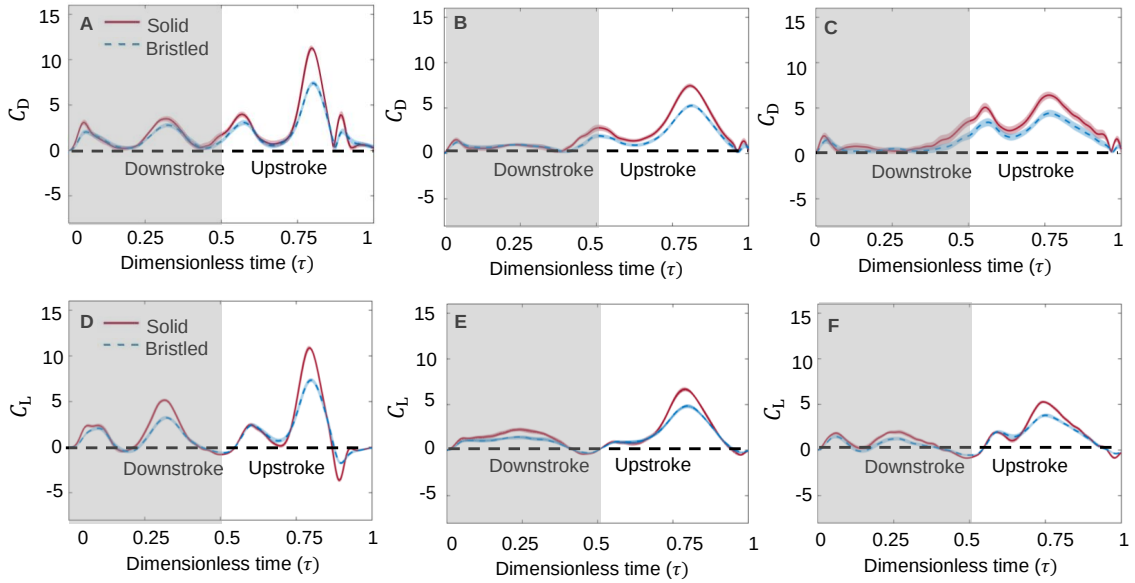

Figure A.9. 4.7: Time variation of drag coefficient (C_D) and lift coefficient (C_L) for solid wing pair and bristled wing pair performing (A,D) Thrips kinematics, (B, E) Leafminers kinematics, (C, F) Fruitfly kinematics at Re = 120, respectively. Shaded region represents downstroke and non-shaded region represents upstroke.

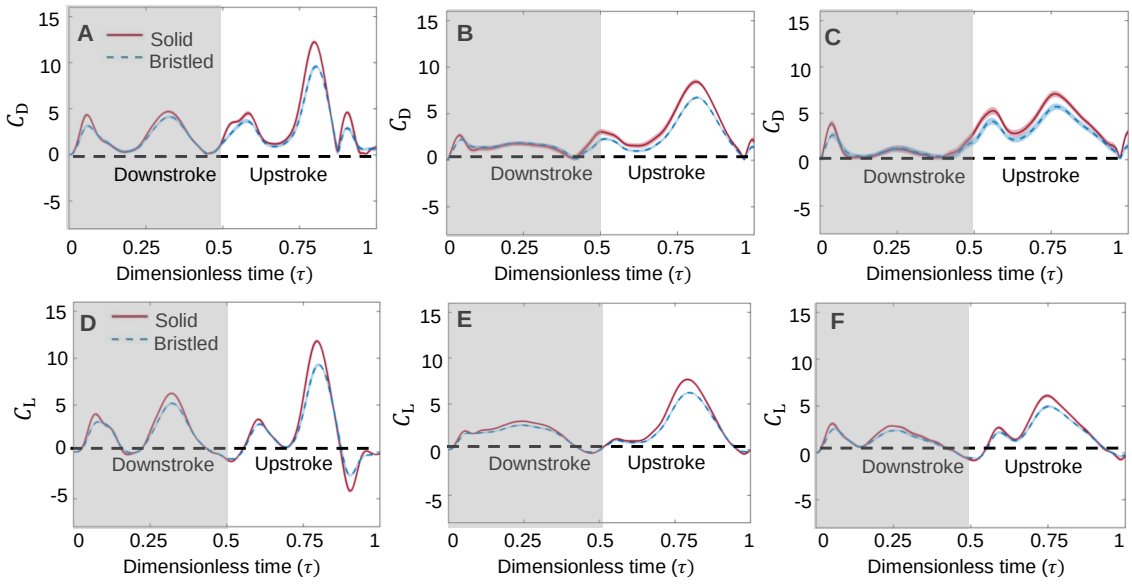

Figure A.9. 4.8: Time variation of drag coefficient (C_D) and lift coefficient (C_L) for solid wing pair and bristled wing pair performing (A,D) Thrips kinematics, (B, E) Leafminers kinematics, (C, F) Fruitfly kinematics at Re = 30, respectively. Shaded region represents downstroke and non-shaded region represents upstroke.

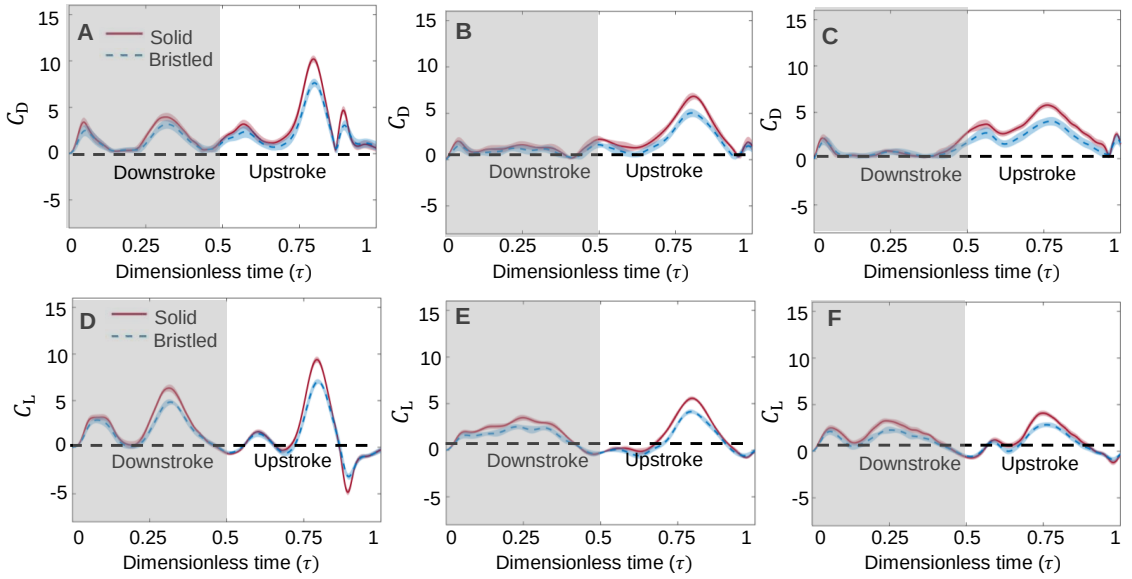

Figure A.9. 4.9: Time variation of drag coefficient (C_D) and lift coefficient (C_L) for solid wing pair and bristled wing pair performing (A,D) Thrips kinematics, (B, E) Leafminers kinematics, (C, F) Fruitfly kinematics at Re = 60, respectively. Shaded region represents downstroke and non-shaded region represents upstroke.

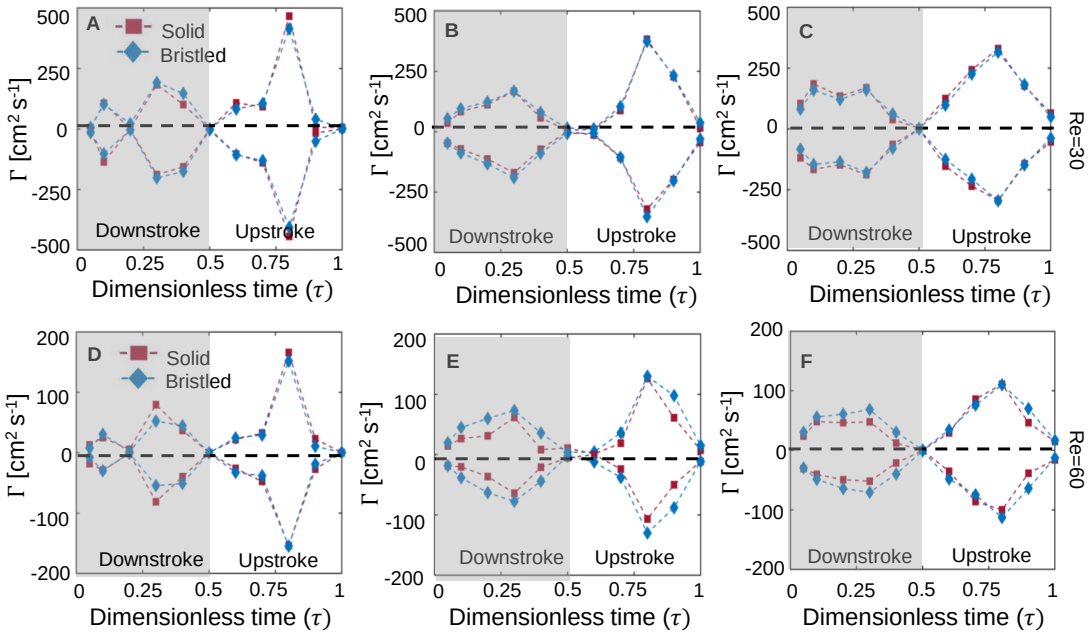

Figure A.9. 4.10: Time variation of LEV and TEV circulation (Γ) for single solid wing and single bristled wing performing (A,D) Thrips kinematics, (B, E) Leafminers kinematics, (C, F) Fruitfly kinematics at *Re* = 30 and 60, respectively. Top row: *Re* = 30, Bottom row: *Re* = 60. Shaded region represents downstroke and non-shaded region represents upstroke. Positive values of Γ in downstroke represents TEV circulation, negative values of Γ in downstroke represents LEV circulation. Positive values of Γ in upstroke represents LEV circulation, negative values of Γ in upstroke represents TEV circulation.

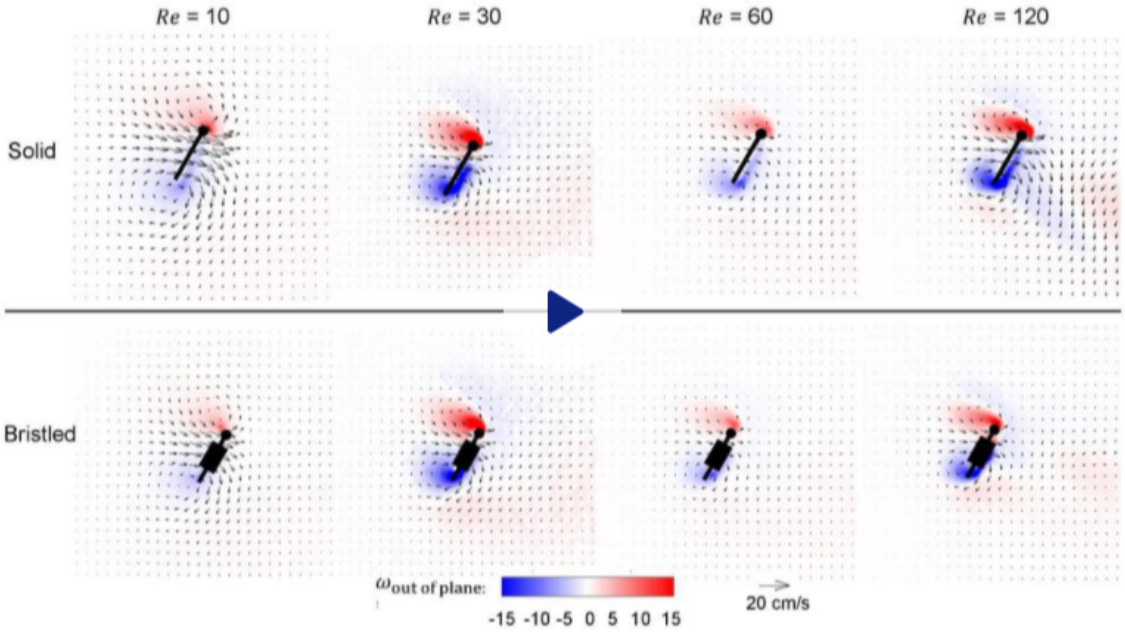

Movie A.9. 4.11: 2D phase-locked PIV (PL-PIV) showing vorticity contours overlaid on top of velocity vectors performing thrips kinematics for single solid and bristled wing.

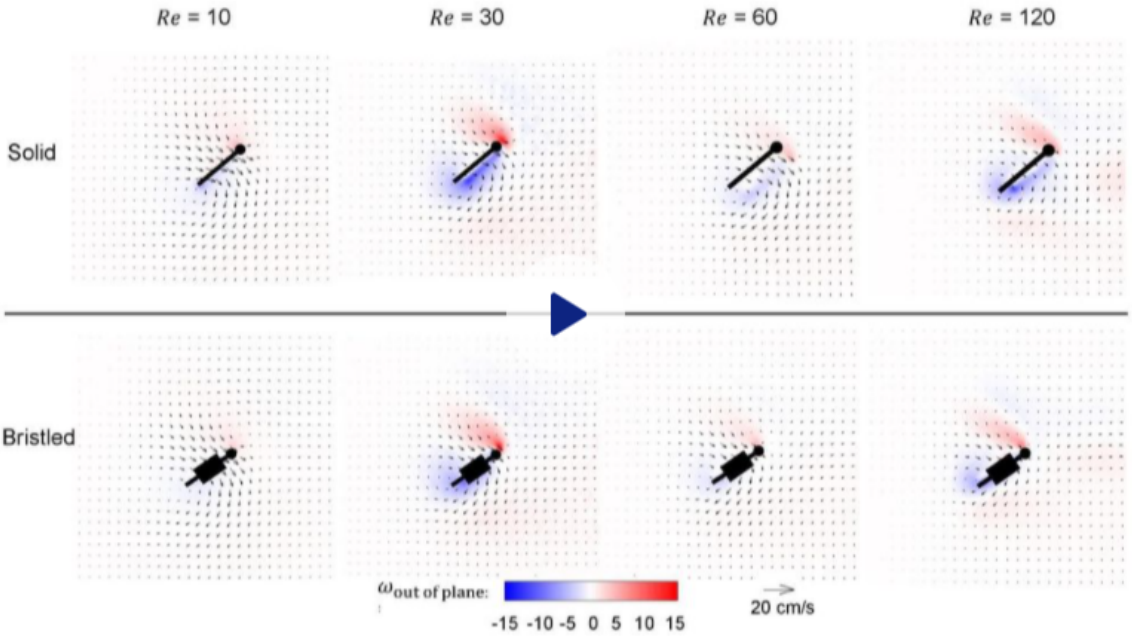

Movie A.9. 4.12: 2D phase-locked PIV (PL-PIV) showing vorticity contours overlaid on top of velocity vectors performing leafminers kinematics for single solid and bristled wing.

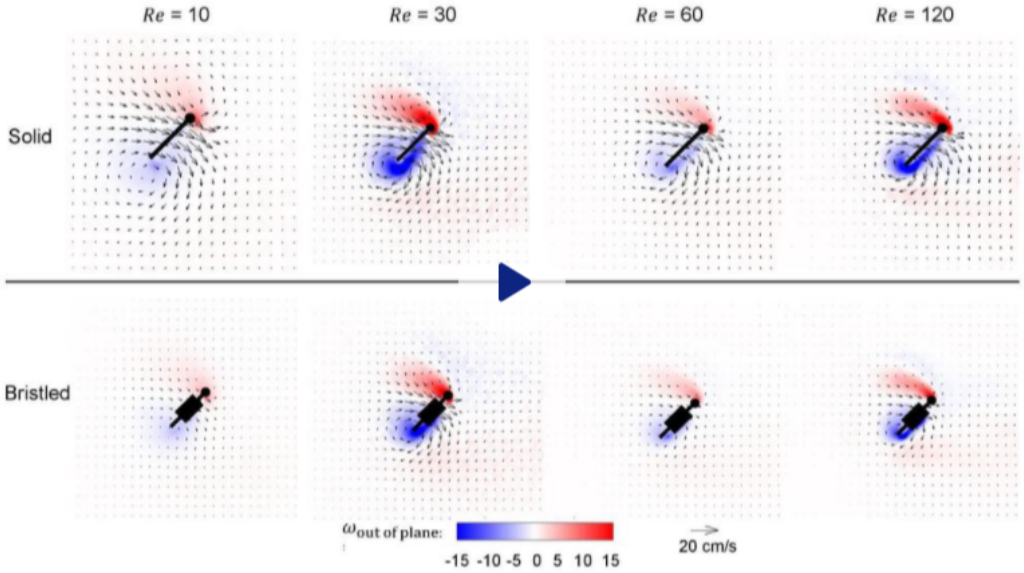

Movie A.9. 4.13: 2D phase-locked PIV (PL-PIV) showing vorticity contours overlaid on top of velocity vectors performing fruitfly kinematics for single solid and bristled wing.

A.9. 5 SA 5: Parachuting with bristled wings

T (ms)	Inter-wing angle (θ)
0	98.82
1.5	104.53
3	99.78
4.5	97.85
6	93.76
7.5	95.43
9	93.37
10.5	93.47
12	97.35
13.5	97.13
15	93.47
16.5	93.53
18	105.20
19.5	102.06
21	95.91

Figure A.9. 5.1: Reference time (T) and inter-wing angle (θ) of 15 consecutive snapshots from thrips parachuting video (Santhanakrishnan et al., 2014) during the steady portion of free fall.

A.10 Circulation code

MATLAB CODE:

```
%%%%%%%%%%%%%%%%%%%%%%%%%%%%%%%%%%%%%%%%%%%%%%%%%%%%%%%%%%%%%%%%%%%%%%%%
% Code for reading *.DAT files containing ensemble averaged PIV data &
    ↪  derived characteristics for further data analysis
% This m-file looks at CIRCULATION CALCULATION

% **IMPORTANT: Copy function "minrowvecs.m" onto the same folder as
    ↪ this m-file**
% **IMPORTANT: Copy function "FindMaxVorticity_LeftWing.m" onto the
    ↪ same folder as this m-file**

% Use "CreateDATFilewithVorticity_MultipleFolders.m" code prior to
    ↪ this to calculate ALL velocity gradients, velocity fluctuations
    ↪ , RSS, VSS, TKE

% Contact: Arvind Santhanakrishnan, E-mail: askrish@okstate.edu
% Last modified: 7/15/2021 V.Kasoju
%%%%%%%%%%%%%%%%%%%%%%%%%%%%%%%%%%%%%%%%%%%%%%%%%%%%%%%%%%%%%%%%%%%%%%%%
clear all, close all; clc;

%%%%%%%%%%%%%%%%%%%%%%%%%%%%%%%%%%%%%%%%%%%%%%%%%%%%%%%%%%%%%%%%%%%%%%%%
DEFINE USER INPUTS BELOW
%%%%%%%%%%%%%%%%%%%%%%%%%%%%%%%%%%%%%%%%%%%%%%%%%%%%%%%%%%%%%%%%%%%%%%%%

filepath = 'C:\Users\vishu\Desktop\Spring 2019\KinematicsStudy\
    ↪ Circulation'; %%Input path to read from. Assumes path\ReXXX_YYY
    ↪  (XXX is Re #, YYY is image #)
rotation = 'ccw'; %Direction of vortex rotation -- See contour color
    ↪ bar if needed Remember, CCW [-] and CW [+]
flag = 0; % Initialization for while loop below
filename = 'PureRotation_675_10_Gap'; %string -- for naming export
    ↪ file
filename_cutoffref = 'PureRotation_675_SingleWing_01'; %cutoff based
    ↪ on file defined here
Condition = 'Fling'; %Clap or fling -- for naming export file
cutoff = 0.15; %Cuttoff value for vorticity for using Vorticity method
Re =10; %Reynolds Number
n = 24; %number of contour levels in plot
NumberofDatFiles = 99;
Increments = 1;
       if Increments == 1
           I = Increments+1;
       else
```

```
            I = Increments;
        end

AP = 1:1:NumberofDatFiles;
method='vorticity'; % type either 'lambdaci' or 'vorticity'
%% Translate the x & y coordinates; this will change from 1 data set
   ↪ to another!
xoff = 0; %% X-axis offset in mm
yoff = 0; %% Y-axis offset in mm

rot_direction ={'ccw';'cw'};
ncycles = 1; %% #cardiac cycles for averaging
 %% Find maximum vorticity
T1 = length(AP); % Length of timepoint
Startpoint = 1;

[wzmin,maxvorticity_ccw,maxvorticity_cw_,maxwzpos,x_VorCen,y_VorCen,
   ↪ x_centerline,y_centerline] = FindMaxVorticity_LeftWing(filepath
   ↪ ,rot_direction,filename,Condition,Re,n,AP,xoff,yoff,cutoff);

%% Loop the calculation for timepoint and for each direction
for rot_dir = 1:1:2
    if rot_dir == 1
        rotation = 'ccw';
    else
        rotation = 'cw';
    end

for T=1:1:T1

if AP(T)<10
        bat = '0000';
elseif AP(T)>=10 && AP(T)<100
        bat = '000';
elseif AP(T)>=100
        bat = '00';
end
file = strcat(filepath,'\','AverageDatFiles','\',filename,'\','Avg_',
   ↪ num2str(filename),'_',num2str(AP(T)),'.dat'); %check the name
   ↪ formating
startRow = 4; %ignores the dat file header info, check the .dat file

%% Format for reading files
formatSpec = '%f%f%f%f%f%f%f%f%f%f%f%f%f%f%f%f%f%f%f%[^\n\r]';
```

```
%% Open the DAT file w/ ensemble averaged PIV data & velocity
   ↪ gradients
fileID = fopen(file,'r');

%% Read data according to format string above
data = textscan(fileID, formatSpec, 'Delimiter', '', 'WhiteSpace', '',
   ↪  'EmptyValue' ,NaN,'HeaderLines' ,startRow-1, 'ReturnOnError',
   ↪ false);
fclose(fileID);

        fileID = fopen(file,'r');
        Line1 = fgetl(fileID);
        Line2 = fgets(fileID);
        Line3 = fgets(fileID);
        %data = textscan(test2,'%s%[^]i=]%[^]j=]','Delimiter',',');
        Grids = textscan(Line3,'%s%s%s','Delimiter',',');
        XGrid = char(Grids {1,2});
        YGrid = char(Grids {1,3});
        lenx = length(XGrid);
        leny = length(YGrid);
        xgrid = str2num(XGrid(3:lenx));
        ygrid = str2num(YGrid(3:leny));
        %data = textscan(fileID, formatSpec,1,'Delimiter', delimiter, '
           ↪ EmptyValue' ,NaN,'HeaderLines' ,startRow-2, '
           ↪ ReturnOnError', false);
        fclose(fileID);

%% Allocate data array to variables
X = data{1,1}; %% X-coordinates
Y = data{1,2}; %% Y-coordinates
%Z = data{1,3}; %% Z-coordinates
U = data{1,3}; %% X=component of velocity
V = data{1,4}; %% Y-component of velocity
V_norm = data{1,5}; %% norm of velocity
dudx = data{1,6}; %% gradient: du/dx
dudy = data{1,7}; %% gradient: du/dy
dvdx = data{1,8}; %% gradient: dv/dx
dvdy = data{1,9}; %% gradient: dv/dy
wz = data{1,10}; %% Z-Vorticity (dv/dx-du/dy)

% %% Quiver plot of velocity vector field, NO OFFSETTING
% figure(1), hold on, box on
% quiver(X,Y,U,V,'k','LineWidth',1,'AutoScaleFactor',7);
% xlabel('x [mm]','fontsize',42,'fontweight','bold')
% ylabel('r [mm]','fontsize',42,'fontweight','bold')
```

```
% set(gca, 'FontSize', 36, 'FontWeight', 'bold');
% axis tight

%% Re-arrange all variables so that they are in X x Y format, Y not
   ↪ equal to 1!
X_new(1:xgrid,1) = X(1:xgrid,1);
for i=1:ygrid
    Y_new(i,1) = Y((i*xgrid),1);
end
U_new(1:xgrid,1) = U(1:xgrid,1);
V_new(1:xgrid,1) = V(1:xgrid,1);
dudx_new(1:xgrid,1) = dudx(1:xgrid,1);
dudy_new(1:xgrid,1) = dudy(1:xgrid,1);
dvdx_new(1:xgrid,1) = dvdx(1:xgrid,1);
dvdy_new(1:xgrid,1) = dvdy(1:xgrid,1);
wz_new(1:xgrid,1) = wz(1:xgrid,1);

for j=2:ygrid
    U_new(1:xgrid,j) = U(((j-1)*xgrid)+1:j*xgrid,1);
    V_new(1:xgrid,j) = V(((j-1)*xgrid)+1:j*xgrid,1);
    dudx_new(1:xgrid,j) = dudx(((j-1)*xgrid)+1:j*xgrid,1);
    dudy_new(1:xgrid,j) = dudy(((j-1)*xgrid)+1:j*xgrid,1);
    dvdx_new(1:xgrid,j) = dvdx(((j-1)*xgrid)+1:j*xgrid,1);
    dvdy_new(1:xgrid,j) = dvdy(((j-1)*xgrid)+1:j*xgrid,1);
    wz_new(1:xgrid,j) = wz(((j-1)*xgrid)+1:j*xgrid,1);

end

%% Quiver plot of velocity vector field, WITH OFFSET
% figure(2), hold on, box on
% quiver(X_new+xoff,Y_new+yoff,U_new',V_new','k','LineWidth',1,'
   ↪ AutoScaleFactor',5);
% xlabel('x [mm]','fontsize',42,'fontweight','bold')
% ylabel('r [mm]','fontsize',42,'fontweight','bold')
% set(gca, 'FontSize', 36, 'FontWeight', 'bold');
% axis tight
%

%% Circulation Calculation
wz_new1 = wz_new;
if strcmp(rotation,'ccw')== true
    wz_new1(wz_new<wzmin)=0;
    maxwzpos_ccw = maxwzpos(:,1);
    x_c_Vor = x_VorCen(:,1);
    y_c_Vor = y_VorCen(:,1);
```

```
    %disp('ccw')
elseif strcmp(rotation, 'cw')==true
    wz_new1(wz_new>-wzmin)=0;
    maxwzpos_cw = maxwzpos(:,2);
    x_c_Vor = x_VorCen(:,2);
    y_c_Vor = y_VorCen(:,2);
    %disp('cw')
end
% figure(3),hold on
% contourf(X_new,Y_new,wz_new1',10);
% colormap(redblue); % select region where local MAXIMA of normalized
    ↪ Im[\lambda_{ci}] occurs
xcen = x_c_Vor(T,1);
ycen = y_c_Vor(T,1);
xboxwidth = 2; %No zero input
yboxwidth = 2; %No zero input

while flag == 0

    xboxwidth_1=round(xboxwidth);
    yboxwidth_1=round(yboxwidth);

    xboxwidth_2=xboxwidth+6;
    yboxwidth_2=yboxwidth+6;

   xbox1_1 = xcen-xboxwidth_1;
   xbox1_2 = xcen+xboxwidth_1;
   ybox1_1 = ycen-yboxwidth_1;
   ybox1_2 = ycen+yboxwidth_1;

   xbox2_1 = xcen-xboxwidth_2;
   xbox2_2 = xcen+xboxwidth_2;
   ybox2_1 = ycen-yboxwidth_2;
   ybox2_2 = ycen+yboxwidth_2;

    I_xc_fov_1=find(X_new>x_centerline,1)-1;
    I_xc_fov_2=1;
    I_yc_fov_1=ygrid;
    I_yc_fov_2=1;

    I_xbox1_1=find(X_new>xbox1_1,1)-1;
    I_xbox1_2=find(X_new>xbox1_2,1)-1;
    I_ybox1_1=find(Y_new<ybox1_1,1)-1;
    I_ybox1_2=find(Y_new<ybox1_2,1)-1;
```

```
    I_xbox2_1=find(X_new>xbox2_1,1)-1;
    I_xbox2_2=find(X_new>xbox2_2,1)-1;
    I_ybox2_1=find(Y_new<ybox2_1,1)-1;
    I_ybox2_2=find(Y_new<ybox2_2,1)-1;

    if I_xbox1_2 > I_xc_fov_1
        I_xbox1_2 = I_xc_fov_1;
        xbox1_2 = X_new(I_xbox1_2,1);
    end
    if isempty(I_xbox1_1) == 1 || I_xbox1_1 == 0
        I_xbox1_1 = 1;
        xbox1_1 = X_new(I_xbox1_1,1);
    end
    if I_xbox2_2 > I_xc_fov_1
        I_xbox2_2 = I_xc_fov_1;
        xbox2_2 = X_new(I_xbox2_2,1);
    end
    if isempty(I_xbox2_1) == 1 || I_xbox2_1 == 0
        I_xbox2_1 = 1;
        xbox2_1 = X_new(I_xbox2_1,1);
    end

    if isempty(I_ybox1_1) == 1 || I_ybox1_1 == 0
        I_ybox1_1 = ygrid;
        ybox1_1 = Y_new(I_ybox1_1,1);
    end
        if isempty(I_ybox1_2) == 1 || I_ybox1_2 == 0
        I_ybox1_2 = 1;
        ybox1_2 = Y_new(I_ybox1_2,1);
        end
    if isempty(I_ybox2_1) == 1 || I_ybox2_1 == 0
        I_ybox2_1 = ygrid;
         ybox2_1 = Y_new(I_ybox2_1,1);
    end
    if isempty(I_ybox2_2) == 1 || I_ybox2_2 == 0
        I_ybox2_2 = 1;
        ybox2_2 = Y_new(I_ybox2_2,1);
    end

% %% Draw the box defining the APPROX. SIZE OF THE VORTEX CORE
% figure(4), hold on
% plot([xbox1_1,xbox1_1],[ybox1_1,ybox1_2],'k-')
% plot([xbox1_2,xbox1_2],[ybox1_1,ybox1_2],'k-')
% plot([xbox1_1,xbox1_2],[ybox1_1,ybox1_1],'k-')
% plot([xbox1_1,xbox1_2],[ybox1_2,ybox1_2],'k-')
```

```
%
% plot([xbox2_1,xbox2_1],[ybox2_1,ybox2_2],'r-')
% plot([xbox2_2,xbox2_2],[ybox2_1,ybox2_2],'r-')
% plot([xbox2_1,xbox2_2],[ybox2_1,ybox2_1],'r-')
% plot([xbox2_1,xbox2_2],[ybox2_2,ybox2_2],'r-')
%
% plot([xcen],[ycen],'c.','markersize',30)
%
% hold off;
% %

    Yes = strcmp(rotation,'ccw');
    if Yes == 1
        wz_new_pos1_box1 = wz_new1(I_xbox1_1:I_xbox1_2,I_ybox1_2:
            ↪ I_ybox1_1);
        max_wz_new_box1 = max(max(wz_new_pos1_box1,[],2));
        %wz_new_pos_normal_box1 = wz_new_pos1_box1/max_wz_new_box1;
        wz_new_pos1_box2 = wz_new1(I_xbox2_1:I_xbox2_2,I_ybox2_2:
            ↪ I_ybox2_1);
        max_wz_new_box2 = max(max(wz_new_pos1_box2,[],2));
        %wz_new_pos_normal_box2 = wz_new_pos1_box2/max_wz_new_box2;
        %[max_Xindex,max_Yindex] = find(wz_new == max_wz_new);
        %Vor_Xcen = X_new(max_Xindex);
        %Vor_Ycen = Y_new(max_Yindex);
% wz_new_pos1 = wz_new_pos;
% wz_new_pos1 (threshold_norm_im_lambda_ci = 0) = 0;

    else
        wz_new_pos1_box1 = wz_new1(I_xbox1_1:I_xbox1_2,I_ybox1_2:
            ↪ I_ybox1_1);
        max_wz_new_box1 = max(max(-1.*(wz_new_pos1_box1),[],2));
        %wz_new_pos_normal_box1 = wz_new_pos1_box1/max_wz_new_box1;

        wz_new_pos1_box2 = wz_new1(I_xbox2_1:I_xbox2_2,I_ybox2_2:
            ↪ I_ybox2_1);
        max_wz_new_box2 = max(max(-1.*(wz_new_pos1_box2),[],2));
        %wz_new_pos_normal_box2 = wz_new_pos1_box2/max_wz_new_box2;

    end


%% Initialize vorticity integral sum, vor_gamma, to be zero

    vor_gamma=0.0;
```

```
    [tempx_box1,tempy_box1]=find(wz_new_pos1_box1~=0);
    [tempx_box2,tempy_box2]=find(wz_new_pos1_box2~=0);

    xindex_box1=X_new(tempx_box1,1);
    yindex_box1=Y_new(tempy_box1,1);

    xindex_box2=X_new(tempx_box2,1);
    yindex_box2=Y_new(tempy_box2,1);


    wz3_box1=wz_new_pos1_box1(wz_new_pos1_box1~=0);
    wz3_box2=wz_new_pos1_box2(wz_new_pos1_box2~=0);

    [xx_box1,yy_box1]=find(wz_new_pos1_box1~=0);
    [xx_box2,yy_box2]=find(wz_new_pos1_box2~=0);

% figure(5)
% scatter(xindex_box1,yindex_box1, 72,'MarkerEdgeColor',[0 0 1],'
    ↪ MarkerFaceColor',[0 0 1]); hold on
% scatter(xindex_box1,yindex_box1, 30,'MarkerEdgeColor',[1 0 0],'
    ↪ MarkerFaceColor',[1 0 0]);hold off
% grid on;
% ax.GridColor = 'k';
% ax.GridLineWidth = 2;
% % pause
% figure(6)
% scatter(xx_box1,yy_box1,72,'MarkerEdgeColor',[0 0 1],'
    ↪ MarkerFaceColor',[0 0 1]); hold on
% scatter(xx_box2,yy_box2, 30,'MarkerEdgeColor',[1 0 0],'
    ↪ MarkerFaceColor',[1 0 0]);hold off
% grid on;
% ax.GridColor = 'k';
% ax.GridLineWidth = 2;
% %pause
%
    %gamma_vor=sum(wz3)*dx*dy*length(wz3);
%% Circulation calculation

dx1 = diff(X_new)*1e-3;
dx = abs(dx1(1)); % x-spacing in meters
dy1 = diff(Y_new)*1e-3;
dy = abs(dy1(1)); % y-spacing in meters
[xlength_box1, ylength_box1] = size(wz_new_pos1_box1);
[xlength_box2, ylength_box2] = size(wz_new_pos1_box2);
%gamma_vor=sum(wz3)*dx*dy*length(wz3);
```

```
for_area_box1 = wz_new_pos1_box1;
for_area_box2 = wz_new_pos1_box2;
for_area_box1(for_area_box1~=0) = 1;
for_area_box2(for_area_box2~=0) = 1;
Totallen_box1 = sum(sum(for_area_box1));
Totallen_box2 = sum(sum(for_area_box2));

gamma_vor_box1 =(sum(sum(wz_new_pos1_box1(:,:))))*dx*dy;
gamma_vor_box2 =(sum(sum(wz_new_pos1_box2(:,:))))*dx*dy;

    if gamma_vor_box1 == gamma_vor_box2
        gamma_vor = gamma_vor_box1;
        flag = 1;
    else
    xboxwidth = xboxwidth+2;
    yboxwidth = yboxwidth+2;
    flag = 0;
    end
end
flag =0;


%% Write circulation calculations to a .mat file

Gamma_final(T,1) = gamma_vor;

end

Gamma_final
matfilepath = strcat(filepath,'\AverageDatFiles\',filename, '_',
   ↪ rotation,'.mat');%output .mat file contains circulation values
   ↪ and image number
matfilepath = string(matfilepath);
save(matfilepath,'x_c_Vor', 'y_c_Vor', 'Gamma_final', 'AP');

end
clear var

%%%%%%%%%%%%%%%%%%%%%%%%%%%%%%%%%%%%%%%%%%%%%%%%%%%%%%%%%%%%%%%%%%%%%%%%%%%
% Function for calculating the maximum value of vorticity in both
   ↪ clockwise (cw) and counter clockwise (ccw) directions
% Use this maximum value for cutoff
%%%%%%%%%%%%%%%%%%%%%%%%%%%%%%%%%%%%%%%%%%%%%%%%%%%%%%%%%%%%%%%%%%%%%%%%%%%
```

```
function [wzmin,maxvorticity_ccw,maxvorticity_cw,maxwzpos,x_VorCen,
   ↪ y_VorCen,xc,yc] = FindMaxVorticity_LeftWing(filepath,
   ↪ rot_direction,filename,present,Re,n,AP,xoff,yoff,cutoff)
temp_vorticity = 0;
for T=36 % select a dat file to locate the center between the two
   ↪ wings for wing pair configuration
if AP(T)<10
       bat = '0000';
elseif AP(T)>=10 && AP(T)<100
       bat = '000';
elseif AP(T)>=100
       bat = '00';
end
file = strcat(filepath,'\','AverageDatFiles','\',filename,'\','Avg_',
   ↪ num2str(filename),'_',num2str(AP(T)),'.dat'); % check the
   ↪ filepath and filename of the dat files
startRow = 4; %ignores the headers, check the data files
%% Format for reading files dat file header info

formatSpec = '%f%f%f%f%f%f%f%f%f%f%f%f%f%f%f%f%f%f%f%[^\n\r]';
%% Open the DAT file w/ ensemble averaged PIV data & velocity
   ↪ gradients

fileID = fopen(file,'r');

%% Read data according to format string above

data = textscan(fileID, formatSpec, 'Delimiter', '', 'WhiteSpace', '',
   ↪  'EmptyValue' ,NaN,'HeaderLines' ,startRow-1, 'ReturnOnError',
   ↪ false);
fclose(fileID);

fileID = fopen(file,'r');
       Line1 = fgetl(fileID);
       Line2 = fgets(fileID);
       Line3 = fgets(fileID);
       %data = textscan(test2,'%s%[^]i=]%[^]j=]','Delimiter',',');
       Grids = textscan(Line3,'%s%s%s','Delimiter',',');
       XGrid = char(Grids {1,2});
       YGrid = char(Grids {1,3});
       lenx = length(XGrid);
       leny = length(YGrid);
       xgrid = str2num(XGrid(3:lenx));
       ygrid = str2num(YGrid(3:leny));
```

```
        %data = textscan(fileID, formatSpec,1,'Delimiter', delimiter, '
            ↪ EmptyValue' ,NaN,'HeaderLines' ,startRow-2, '
            ↪ ReturnOnError', false);
        fclose(fileID);

%% Allocate data array to variables

X = data{1,1}; %% X-coordinates
Y = data{1,2}; %% Y-coordinates
%Z = data{1,3}; %% Z-coordinates
U = data{1,3}; %% X=component of velocity
V = data{1,4}; %% Y-component of velocity
V_norm = data{1,5}; %% norm of velocity
dudx = data{1,6}; %% gradient: du/dx
dudy = data{1,7}; %% gradient: du/dy
dvdx = data{1,8}; %% gradient: dv/dx
dvdy = data{1,9}; %% gradient: dv/dy
wz = data{1,10}; %% Z-Vorticity (dv/dx-du/dy)

%% Quiver plot of velocity vector field, NO OFFSETTING
% figure(1), hold on, box on
% quiver(X,Y,U,V,'k','LineWidth',1,'AutoScaleFactor',7);
% xlabel('x [mm]','fontsize',42,'fontweight','bold')
% ylabel('r [mm]','fontsize',42,'fontweight','bold')
% set(gca, 'FontSize', 36, 'FontWeight', 'bold');
% axis tight

%% Re-arrange all variables so that they are in X x Y format, Y not
    ↪ equal to 1!
X_new(1:xgrid,1) = X(1:xgrid,1);
for i=1:ygrid
    Y_new(i,1) = Y((i*xgrid),1);
end
U_new(1:xgrid,1) = U(1:xgrid,1);
V_new(1:xgrid,1) = V(1:xgrid,1);
dudx_new(1:xgrid,1) = dudx(1:xgrid,1);
dudy_new(1:xgrid,1) = dudy(1:xgrid,1);
dvdx_new(1:xgrid,1) = dvdx(1:xgrid,1);
dvdy_new(1:xgrid,1) = dvdy(1:xgrid,1);
wz_new(1:xgrid,1) = wz(1:xgrid,1);


for j=2:ygrid
    U_new(1:xgrid,j) = U(((j-1)*xgrid)+1:j*xgrid,1);
    V_new(1:xgrid,j) = V(((j-1)*xgrid)+1:j*xgrid,1);
```

```
    dudx_new(1:xgrid,j) = dudx(((j-1)*xgrid)+1:j*xgrid,1);
    dudy_new(1:xgrid,j) = dudy(((j-1)*xgrid)+1:j*xgrid,1);
    dvdx_new(1:xgrid,j) = dvdx(((j-1)*xgrid)+1:j*xgrid,1);
    dvdy_new(1:xgrid,j) = dvdy(((j-1)*xgrid)+1:j*xgrid,1);
    wz_new(1:xgrid,j) = wz(((j-1)*xgrid)+1:j*xgrid,1);

end

%% Find the center line between the wings to consider the vorticity of
   ↪ the left wing only for calculating maximum vorticity

% figure(2), hold on, box on
% quiver(X_new+xoff,Y_new+yoff,U_new',V_new','k','LineWidth',1,'
   ↪ AutoScaleFactor',5);
% xlabel('x [mm]','fontsize',42,'fontweight','bold')
% ylabel('r [mm]','fontsize',42,'fontweight','bold')
% set(gca, 'FontSize', 36, 'FontWeight', 'bold');
% axis tight

        figure(3),hold on
        contourf(X_new,Y_new,wz_new'), colorbar % select region where
           ↪ local MAXIMA of normalized Im[\lambda_{ci}] occurs
        xlabel('x [mm]','fontsize',42,'fontweight','bold')
        ylabel('r [mm]','fontsize',42,'fontweight','bold')
        set(gca, 'FontSize', 36, 'FontWeight', 'bold');
        [xc,yc] = ginput(1); % specifies the center line between the
           ↪ wings
        temp_xcenterline = xc;
        temp_ycenterline= yc;

end

%% Loop through all the dat files in sequence to calculate the maximum
   ↪ vorticity in time for left wing alone

for T=1:1:length(AP)

if AP(T)<10
        bat = '0000';
elseif AP(T)>=10 && AP(T)<100
        bat = '000';
elseif AP(T)>=100
        bat = '00';
end
```

```
file = strcat(filepath,'\','AverageDatFiles','\',filename,'\','Avg_',
    ↪ num2str(filename),'_',num2str(AP(T)),'.dat');
startRow = 4; %ignores the dat file header info

%% Format for reading files
%formatSpec = '%8f%9f%9f%9f%9f%9f%9f%9f%9f%9f%9f%9f%9f%9f%9f%9f%f%[^\n
    ↪ \r]';
formatSpec = '%f%f%f%f%f%f%f%f%f%f%f%f%f%f%f%f%f%[^\n\r]';
%% Open the DAT file w/ ensemble averaged PIV data & velocity
    ↪ gradients
fileID = fopen(file,'r');

%% Read data according to format string above
data = textscan(fileID, formatSpec, 'Delimiter', '', 'WhiteSpace', '',
    ↪  'EmptyValue' ,NaN,'HeaderLines' ,startRow-1, 'ReturnOnError',
    ↪ false);
fclose(fileID);

fileID = fopen(file,'r');
        Line1 = fgetl(fileID);
        Line2 = fgets(fileID);
        Line3 = fgets(fileID);
        %data = textscan(test2,'%s%[^]i=]%[^]j=]','Delimiter',',');
        Grids = textscan(Line3,'%s%s%s','Delimiter',',');
        XGrid = char(Grids {1,2});
        YGrid = char(Grids {1,3});
        lenx = length(XGrid);
        leny = length(YGrid);
        xgrid = str2num(XGrid(3:lenx));
        ygrid = str2num(YGrid(3:leny));
        %data = textscan(fileID, formatSpec,1,'Delimiter', delimiter, '
            ↪ EmptyValue' ,NaN,'HeaderLines' ,startRow-2, '
            ↪ ReturnOnError', false);
        fclose(fileID);

%% Allocate data array to variables
X = data{1,1}; %% X-coordinates
Y = data{1,2}; %% Y-coordinates
%Z = data{1,3}; %% Z-coordinates
U = data{1,3}; %% X=component of velocity
V = data{1,4}; %% Y-component of velocity
V_norm = data{1,5}; %% norm of velocity
dudx = data{1,6}; %% gradient: du/dx
dudy = data{1,7}; %% gradient: du/dy
dvdx = data{1,8}; %% gradient: dv/dx
```

```
dvdy = data{1,9}; %% gradient: dv/dy
wz = data{1,10}; %% Z-Vorticity (dv/dx-du/dy)

 %% Quiver plot of velocity vector field, NO OFFSETTING
% figure(1), hold on, box on
% quiver(X,Y,U,V,'k','LineWidth',1,'AutoScaleFactor',7);
% xlabel('x [mm]','fontsize',42,'fontweight','bold')
% ylabel('r [mm]','fontsize',42,'fontweight','bold')
% set(gca, 'FontSize', 36, 'FontWeight', 'bold');
% axis tight

%% Re-arrange all variables so that they are in X x Y format, Y not
   ↪ equal to 1!
X_new(1:xgrid,1) = X(1:xgrid,1);
for i=1:ygrid
    Y_new(i,1) = Y((i*xgrid),1);
end
U_new(1:xgrid,1) = U(1:xgrid,1);
V_new(1:xgrid,1) = V(1:xgrid,1);
dudx_new(1:xgrid,1) = dudx(1:xgrid,1);
dudy_new(1:xgrid,1) = dudy(1:xgrid,1);
dvdx_new(1:xgrid,1) = dvdx(1:xgrid,1);
dvdy_new(1:xgrid,1) = dvdy(1:xgrid,1);
wz_new(1:xgrid,1) = wz(1:xgrid,1);


for j=2:ygrid
    U_new(1:xgrid,j) = U(((j-1)*xgrid)+1:j*xgrid,1);
    V_new(1:xgrid,j) = V(((j-1)*xgrid)+1:j*xgrid,1);
    dudx_new(1:xgrid,j) = dudx(((j-1)*xgrid)+1:j*xgrid,1);
    dudy_new(1:xgrid,j) = dudy(((j-1)*xgrid)+1:j*xgrid,1);
    dvdx_new(1:xgrid,j) = dvdx(((j-1)*xgrid)+1:j*xgrid,1);
    dvdy_new(1:xgrid,j) = dvdy(((j-1)*xgrid)+1:j*xgrid,1);
    wz_new(1:xgrid,j) = wz(((j-1)*xgrid)+1:j*xgrid,1);

end

% Defining a big box enclosing just the left wing based on center line
   ↪  defined above

    xcbox_1=find(X_new>xc,1)-1;
    xcbox_2=1;
    ycbox_1=ygrid;
    ycbox_2=1;
```

```
%% Determine centroid of the vortex-bounding rectangle, correct w/
   ↪ offsets

yboxwidth=Y_new(ygrid,1)-yc(1);
xboxwidth= xc(1)-X_new(1,1);% adjust this manually, in vector
   ↪ integral increments, to match the size of vortex core

%xcbox=round(0.5.*xboxwidth);
%ycbox=round(0.5.*yboxwidth);

for R = 1:length(rot_direction)
    Direction = rot_direction(R);
Yes = strcmp(Direction,'ccw');
if Yes == 1
    wz_new1 = wz_new;
    wz_new_pos = wz_new1(xcbox_2:xcbox_1,ycbox_2:ycbox_1);
    max_wz_new = max(max(wz_new_pos,[],2));
    wz_new_pos_normal = wz_new_pos/max_wz_new;
    [max_Xindex_A,max_Yindex_A] = find(wz_new == max_wz_new);
    for m_i = 1:1:length(max_Xindex_A)
        if max_Xindex_A(m_i)>= xcbox_2 && max_Xindex_A(m_i)<=
           ↪ xcbox_1
            max_Xindex = max_Xindex_A(m_i);
        end
        if max_Yindex_A(m_i)>= ycbox_2 && max_Yindex_A(m_i)<=
           ↪ ycbox_1
            max_Yindex = max_Yindex_A(m_i);
        end
    end
    Vor_Xcen = X_new(max_Xindex);
    Vor_Ycen = Y_new(max_Yindex);
    wz_new_pos1 = wz_new_pos;
    wz_new_pos1 (wz_new_pos < 0) = 0;

else
    wz_new1 = -1.* wz_new;
    wz_new_pos = wz_new1(xcbox_2:xcbox_1,ycbox_2:ycbox_1);
    max_wz_new = max(max(wz_new_pos,[],2));
    wz_new_pos_normal = wz_new_pos/max_wz_new;
    [max_Xindex_A,max_Yindex_A] = find(wz_new == (-1*max_wz_new));
    for m_i = 1:1:length(max_Xindex_A)
        if max_Xindex_A(m_i)> xcbox_2 && max_Xindex_A(m_i)< xcbox_1
            max_Xindex = max_Xindex_A(m_i);
        end
        if max_Yindex_A(m_i)> ycbox_2 && max_Yindex_A(m_i)< ycbox_1
```

```
                max_Yindex = max_Yindex_A(m_i);
            end
        end
        Vor_Xcen = X_new(max_Xindex);
        Vor_Ycen = Y_new(max_Yindex);
        wz_new_pos1 = wz_new_pos.*(-1);
        wz_new_pos1 (wz_new_pos1 > 0) = 0;

    end

    if max(temp_vorticity) < max_wz_new
        temp_vorticity = wz_new;
    end
    maxwzpos(T,R) = max_wz_new; %write the absolute value of peak
       ↪ vorticity to a new variable


%% Determine vector coords of vortex center

    x_VorCen(T,R) = Vor_Xcen;
    y_VorCen(T,R) = Vor_Ycen;

    end
end
maxvorticity_ccw=max(maxwzpos(:,1));
maxvorticity_cw=max(maxwzpos(:,2));
wzmin_ccw=cutoff*maxvorticity_ccw;
wzmin_cw=cutoff*maxvorticity_cw;
wzmin = max(wzmin_ccw,wzmin_cw);

%%%%%%%%%%%%%%%%%%%%%%%%%%%%%%%%%%%%%%%%%%%%%%%%%%%%%%%%%%%%%%%%%%%%%%%%%%%
% 2D TR-PIV DATA ANALYSIS
% THIS PROGRAM CREATES MEAN FILES TG_DOUGH CYCLE AVERAGING &
   ↪ CALCULATES
% DERIVED CHARACTERISTICS: 2D VELOCITY GRADIENTS & Z-VORTICITY

% INPUT FILES FOR CODE ARE DaVIS *.DAT FILES CONTAINING (X,Y,U,V)
% THIS PROGRAM ASSUMES THAT THE DAT FILES ARE STORED AS B*****.DAT

% Contact: Arvind Santhanakrishnan, E-mail: askrish@okstate.edu
% Last modified: 7/18/21
%%%%%%%%%%%%%%%%%%%%%%%%%%%%%%%%%%%%%%%%%%%%%%%%%%%%%%%%%%%%%%%%%%%%%%%%%%%
clear all; close all; clc;

%%%%%%%%%%%%%%%%%%%%%%%%%%%%%%%%%%%%%%%%%%%%%%%%%%%%%%%%%%%%%%%%%%%%%%%%%%%
```

```
%% DEFINE USER INPUTS BELOW
%%%%%%%%%%%%%%%%%%%%%%%%%%%%%%%%%%%%%%%%%%%%%%%%%%%%%%%%%%%%%%%%%%%%%%%%%%%%

Directory = 'C:\Users\vishu\OneDrive - Oklahoma A and M System\
    ↪ Spring2021\3DModel_Paper\CirculationCalculation\
    ↪ DatFiles_3DModel_NewProcessed';
Increments = 1;
FolderNames = ListFolderNamesinDirectory(Directory);
ncycles = 1; % number of cycles
for pj = 1:length(FolderNames)
    Folder = strcat(Directory,'\',FolderNames(pj,1));
    files_DAT = dir(Folder);
    DATCheck = ~strcmp({files_DAT.name},'*.dat') & ~strcmp({files_DAT.
        ↪ name},'.') & ~strcmp({files_DAT.name},'..');
    DATFiles = files_DAT(DATCheck);
        %Image = strcat('B000',num2str(AP(pj)));

        if Increments == 1
            I = Increments+1;
        else
            I = Increments;
        end
for AP = I-1:1:length(DATFiles)
    %for AP = 200:I:length(DATFiles)
%%%%%%%%%%%%%%%%%%%%%%%%%%%%%%%%%%%%%%%%%%%%%%%%%%%%%%%%%%%%%%%%%%%%%%%%%%%%
%% ITERATE TG_DOUGH # CYCLES
%%%%%%%%%%%%%%%%%%%%%%%%%%%%%%%%%%%%%%%%%%%%%%%%%%%%%%%%%%%%%%%%%%%%%%%%%%%%

str = DATFiles(AP).name;

        %% Initialize filepath for reading DAT file, **CHANGE '/' to
            ↪ '\' FOR PCs!!**
        path = strcat(Directory,'\',FolderNames(pj));
        file = strcat(path,'\',str);
        %file = fullfile(path,subpath1,subpath2,str);
        delimiter = {'\t',',',' '};
        startRow = 4;
%%%%%%%%%%%%%%%%%%%%%%%%%%%%%%%%%%%%%%%%%%%%%%%%%%%%%%%%%%%%%%%%%%%%%%%%%%%%
%% READING DATA FILE & ASSIGNING VARIABLES
%%%%%%%%%%%%%%%%%%%%%%%%%%%%%%%%%%%%%%%%%%%%%%%%%%%%%%%%%%%%%%%%%%%%%%%%%%%%
        %% Format for reading files
        formatSpec = '%f%f%f%f%*s%*s%*s%*s%*s%[^\n\r]';

        %% Open the DAT file w/ ensemble averaged PIV data & velocity
            ↪ gradients
```

```
    fileID = fopen(file{1},'r');

    %% Read data according to format string above
    data = textscan(fileID, formatSpec, 'Delimiter', delimiter, '
       ↪ EmptyValue' ,NaN,'HeaderLines' ,startRow-1, '
       ↪ ReturnOnError', false);
    fclose(fileID);

    fileID = fopen(file,'r');
    Line1 = fgetl(fileID);
    Line2 = fgets(fileID);
    Line3 = fgets(fileID);
    %data = textscan(test2,'%s%[^]i=]%[^]j=]','Delimiter',',');
    Grids = textscan(Line3,'%s%s%s','Delimiter',',');
    XGrid_New = char(Grids {1,2});
    YGrid_New = char(Grids {1,3});
    XGrid = XGrid_New(1,:);
    YGrid = YGrid_New(1,:);
    lenx = length(XGrid);
    leny = length(YGrid);
    xgrid(AP,1) = str2num(XGrid(3:lenx));
    ygrid(AP,1) = str2num(YGrid(3:leny));
    %data = textscan(fileID, formatSpec,1,'Delimiter', delimiter, '
       ↪ EmptyValue' ,NaN,'HeaderLines' ,startRow-2, '
       ↪ ReturnOnError', false);
    fclose(fileID);

 %% Initialize arrays for memory allocation

U_new = zeros(xgrid(AP,1),ygrid(AP,1));
V_new = zeros(xgrid(AP,1),ygrid(AP,1));
un = zeros(xgrid(AP,1),ygrid(AP,1));
vn = zeros(xgrid(AP,1),ygrid(AP,1));
uave = zeros(xgrid(AP,1),ygrid(AP,1));
vave = zeros(xgrid(AP,1),ygrid(AP,1));
dUdx = zeros(xgrid(AP,1),ygrid(AP,1));
dUdxn = zeros(xgrid(AP,1),ygrid(AP,1));
dUdy = zeros(xgrid(AP,1),ygrid(AP,1));
dUdyn = zeros(xgrid(AP,1),ygrid(AP,1));
dVdx = zeros(xgrid(AP,1),ygrid(AP,1));
dVdxn = zeros(xgrid(AP,1),ygrid(AP,1));
dVdy = zeros(xgrid(AP,1),ygrid(AP,1));
dVdyn = zeros(xgrid(AP,1),ygrid(AP,1));
w_z = zeros(xgrid(AP,1),ygrid(AP,1));
wn = zeros(xgrid(AP,1),ygrid(AP,1));
```

```
dUdxave = zeros(xgrid(AP,1),ygrid(AP,1));
dUdyave = zeros(xgrid(AP,1),ygrid(AP,1));
dVdxave = zeros(xgrid(AP,1),ygrid(AP,1));
dVdyave = zeros(xgrid(AP,1),ygrid(AP,1));
wave = zeros(xgrid(AP,1),ygrid(AP,1));

    %% Allocate data array to variables
    X = data{1,1}; %% X-coordinates
    Y = data{1,2}; %% Y-coordinates
    U = data{1,3}; %% X=component of velocity
    V = data{1,4}; %% Y-component of velocity

    %% Clear temporary variables
    clearvars file startRow formatSpec fileID data ans;

    %% Re-arrange all variables so that they are in X x Y format, Y
       ↪  not equal to 1
    X_new(1:xgrid(AP,1),1) = X(1:xgrid(AP,1),1);
    for ii=1:ygrid(AP,1)
        Y_new(ii,1) = Y((ii*xgrid(AP,1)),1);
    end
    U_new(1:xgrid(AP,1),1) = U(1:xgrid(AP,1),1);
    V_new(1:xgrid(AP,1),1) = V(1:xgrid(AP,1),1);

    for j=2:ygrid(AP,1)
        U_new(1:xgrid(AP,1),j) = U(((j-1)*xgrid(AP,1))+1:j*xgrid(AP
           ↪ ,1),1);
        V_new(1:xgrid(AP,1),j) = V(((j-1)*xgrid(AP,1))+1:j*xgrid(AP
           ↪ ,1),1);
    end

    Xn = reshape(X,xgrid(AP,1),ygrid(AP,1));
    Yn = reshape(Y,xgrid(AP,1),ygrid(AP,1));

    %% CALCULATING GRADIENTS AND WALL-NORMAL GRADIENTS
    for jj=2:xgrid(AP,1)-1
        for kk=2:ygrid(AP,1)-1
            dUdx(jj,kk) = (U_new(jj+1,kk)-U_new(jj-1,kk))/(Xn(jj+1,
               ↪ kk)-Xn(jj-1,kk));
            dUdy(jj,kk) = (U_new(jj,kk+1)-U_new(jj,kk-1))/(Yn(jj,kk
               ↪ +1)-Yn(jj,kk-1));
            dVdx(jj,kk) = (V_new(jj+1,kk)-V_new(jj-1,kk))/(Xn(jj+1,
               ↪ kk)-Xn(jj-1,kk));
            dVdy(jj,kk) = (V_new(jj,kk+1)-V_new(jj,kk-1))/(Yn(jj,kk
               ↪ +1)-Yn(jj,kk-1));
```

```
            w_z(jj,kk) = dVdx(jj,kk)-dUdy(jj,kk);
        end
    end

    %% Calculate vector SUM of velocity & vorticity components for
       ↪ cycle-averaging outside loop
    un = un + U_new;
    vn = vn + V_new;
    dUdxn = dUdxn + dUdx;
    dUdyn = dUdyn + dUdy;
    dVdxn = dVdxn + dVdx;
    dVdyn = dVdyn + dVdy;
    wn = wn + w_z;


%% CYCLE-AVERAGE THE VELOCITY, VELOCITY GRADIENT & VORTICITY
   ↪ FIELDS
uave = un/ncycles;
vave = vn/ncycles;

%%multiply all gradients and vorticity by 1000 for converting
   ↪ units from (m/s)/mm to (1/s)
dUdxave = 1000*(dUdxn/ncycles);
dUdyave = 1000*(dUdyn/ncycles);
dVdxave = 1000*(dVdxn/ncycles);
dVdyave = 1000*(dVdyn/ncycles);
wave = 1000*(wn/ncycles);

%% CYCLE-AVERAGED VELOCITY MAGNITUDE
vel_mag = sqrt(uave.^2+vave.^2);

%% WRITE OUTPUT FILE CONTAINING CYCLE-AVERAGED QUANTITIES!
tot = xgrid(AP,1)*ygrid(AP,1);
datafinal = zeros(tot,10);
datafinal(:,1) = X;
datafinal(:,2) = Y;
datafinal(:,3) = reshape(uave,tot,1);
datafinal(:,4) = reshape(vave,tot,1);
datafinal(:,5) = reshape(vel_mag,tot,1);
datafinal(:,6) = reshape(dUdxave,tot,1);
datafinal(:,7) = reshape(dUdyave,tot,1);
datafinal(:,8) = reshape(dVdxave,tot,1);
datafinal(:,9) = reshape(dVdyave,tot,1);
datafinal(:,10) = reshape(wave,tot,1);
```

```
  fnam = strcat ('AverageDatFiles','\',FolderNames(pj));
    if ~exist(fnam, 'dir' )
       mkdir (fnam);
    end

    %fnam = strcat (path,'Re',num2str(Re),'_',bag,'_',G_D(1,k),'\','
        ↪ Avg_Re',num2str(Re),'_',G_D(1,k),'_',bag,'_',num2str(AP(pj))
        ↪ ,'.csv');
    %fnampath = strcat (fnam,'\','Avg','_',FolderNames(pj),'_',num2str
        ↪ (AP),'.csv');
    %fprintf('%s%s\n','Writing file: ',fnampath{1});
    %csvwrite(fnampath{1},datafinal)

    %% Calculating the kinetic energy
    f = xgrid(AP,1)*ygrid(AP,1);
    for m=1:f
        velocity_square(m) = U(m).^2+V(m).^2;
    end
    %kin_enrgy(mm) = sum(velocity_square)/(2*f);

    % TECPLOT WRITEOUT ****NEEDS TROUBLESHOOTING!!****
    %fnam = strcat(path,'Re',num2str(Re),'_',bag,'_',G_D(1,k),'\','
        ↪ Avg_Re',num2str(Re),'_',G_D(1,k),'_',bag,'_',num2str(AP(pj))
        ↪ ,'.dat');
    fnampath = strcat (fnam,'\','Avg','_',FolderNames(pj),'_',num2str(
        ↪ AP),'.dat');
    fid6 = fopen(fnampath{1},'w');
    fprintf('%s%s\n','Writing file: ',fnampath{1});
    fprintf(fid6,'%s \n','TITLE = "B00001"');
    fprintf(fid6,'%s\n','VARIABLES = "x [mm]", "y [mm]", "u", "v", "
        ↪ velocity" , "du/dx", "du/dy", "dv/dx", "dv/dy", "vorticity
        ↪ "');
    fprintf(fid6,'%s%s %s%d%s %s%d\n','ZONE T="Fling"',',',',','I=',xgrid(
        ↪ AP,1),',',',','J=',ygrid(AP,1));
    for j=1:tot
        fprintf(fid6,'%8.4f %8.4f %8.4f %8.4f %8.4f %8.4f %8.4f %8.4f
            ↪ %8.4f %8.4f\n',datafinal(j,1),datafinal(j,2),datafinal(j
            ↪ ,3),datafinal(j,4),datafinal(j,5),datafinal(j,6),
            ↪ datafinal(j,7),datafinal(j,8),datafinal(j,9),datafinal(j
            ↪ ,10));
    end
    fclose(fid6);
end
end
```

```
% % break;
```

A.11 Procedure for force calculations

Step 1:

Calibrate the force brackets (all lift and drag brackets used) and the calibration data and the plot the data for calibration as shown in the image below:

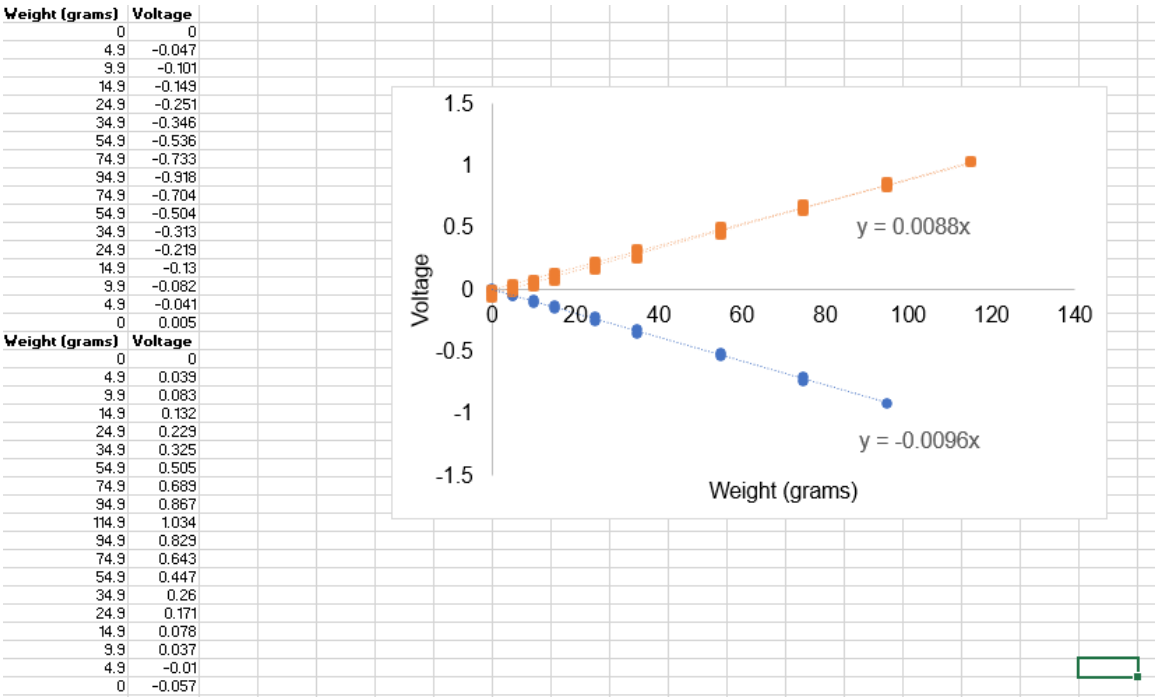

Weight (grams)	Voltage
0	0
4.9	-0.047
9.9	-0.101
14.9	-0.149
24.9	-0.251
34.9	-0.346
54.9	-0.536
74.9	-0.733
94.9	-0.918
74.9	-0.704
54.9	-0.504
34.9	-0.313
24.9	-0.219
14.9	-0.13
9.9	-0.082
4.9	-0.041
0	0.005
Weight (grams)	Voltage
0	0
4.9	0.039
9.9	0.083
14.9	0.132
24.9	0.229
34.9	0.325
54.9	0.505
74.9	0.689
94.9	0.867
114.9	1.034
94.9	0.829
74.9	0.643
54.9	0.447
34.9	0.26
24.9	0.171
14.9	0.078
9.9	0.037
4.9	-0.01
0	-0.057

Figure A.11. 0.1: Sample calibration plot showing positive and negative slopes for bracket used.

Step 2:

Filter the raw force data:

```
[DragForceRe10_Solid_Single_0percentpause,
    ↪ FD_DFRe10_Solid_Single_0percentpause] = Re10_forcevoltage('L:\
    ↪ ForceData_Pausetimes_Singlewing_BioinspRound1\ForceData_Drag\0
    ↪ percentpause_Single\DragForceDataRe10_Solid_0percentpause.xlsx
    ↪ ',22200);

%%%%%%%%%%%%%%%%%%%%%%%%%
MATLAB CODE for filtering
%%%%%%%%%%%%%%%%%%%%%%%%%

function [ImportedData,FilteredData] = Re10_forcevoltage(filename,
    ↪ sampleLength)
ImportedData = importData(filename,sampleLength);
FilteredData = filterdata(ImportedData);
```

```
end
function ImportedData = importData(filename,sampleLength)
ImportedData = zeros(sampleLength,30);
testlen = strcat('A',num2str(sampleLength+1));
range = strcat('A2:',testlen);
for n=2:31
    ImportedData(:,n-1) = xlsread(filename,n+5,range);
    disp(n)
end
end
function FilteredData = filterdata(ImportedData)
[b,a] = butter(3,0.0022); % the value of 0.0022 is based on cutoff
    ↪ frequency
[sos,g] = tf2sos(b,a);
FilteredData = filtfilt(sos,g,ImportedData);
end
```

Step 3:

A sample code for next steps in force data calculation with all related matlab functions are shown below:

```
% Import Zero force data
Zero_FDForce_Solid_Single_0percentpause = importdata('L:\
    ↪ ForceData_Pausetimes_Singlewing_BioinspRound1\ZeroDragForceData
    ↪ ');
Zero_AFDForce_Solid_Single_0percentpause = mean(
    ↪ Zero_FDForce_Solid_Single_0percentpause);

% Convert the raw filtered force data to force data in grams using the
    ↪  slopes from the calibration plots shown in step 1
FDForceArray_Solid_Single_0percentpause = convertToForceNoAvg(
    ↪ FD_DFRe10_Solid_Single_0percentpause,
    ↪ Zero_AFDForce_Solid_Single_0percentpause, 0.0088,-0.0096);

% Apply the angle to which the wing is rotated giving both horizontal
    ↪ (drag) and vertical (lift) components
[newFDForceArray_Solid_Single_0percentpause,
    ↪ D_newFLForceArray_Solid_Single_0percentpause] =
    ↪ useAngleNoAvg_All(FDForceArray_Solid_Single_0percentpause,
    ↪ DAngleRe10_0percentpause_c);

% Convert the force in grams to force coefficients
FDcoeffArray_Solid_Single_0percentpause = forceToCoefficientNoAvg(
    ↪ newFDForceArray_Solid_Single_0percentpause,
    ↪ 1261.5,0.1570078,0.045,0.081);
D_FLcoeffArray_Solid_Single_0percentpause = forceToCoefficientNoAvg(
```

```
    ↪ D_newFLForceArray_Solid_Single_0percentpause,
    ↪ 1261.5,0.1570078,0.045,0.081);

% Zero the initial force data where the wings start and calculate the
    ↪ standard deviations in time
for i = 1:30
FDcoeffArray_Solid_Single_0percentpause(:,i) =
    ↪ FDcoeffArray_Solid_Single_0percentpause(:,i) -
    ↪ FDcoeffArray_Solid_Single_0percentpause(1,i);
D_FLcoeffArray_Solid_Single_0percentpause(:,i) =
    ↪ D_FLcoeffArray_Solid_Single_0percentpause(:,i) -
    ↪ D_FLcoeffArray_Solid_Single_0percentpause(1,i);
newFDForceArray_Solid_Single_0percentpause(:,i) =
    ↪ newFDForceArray_Solid_Single_0percentpause(:,i)-
    ↪ newFDForceArray_Solid_Single_0percentpause(1,i);
D_newFLForceArray_Solid_Single_0percentpause(:,i) =
    ↪ D_newFLForceArray_Solid_Single_0percentpause(:,i)-
    ↪ D_newFLForceArray_Solid_Single_0percentpause(1,i);
end

FDcoeffArray_Solid_Single_P_0percentpause =
    ↪ FDcoeffArray_Solid_Single_0percentpause.*-1;
D_FLcoeffArray_Solid_Single_P_0percentpause =
    ↪ D_FLcoeffArray_Solid_Single_0percentpause.*-1;
newFDForceArray_Solid_Single_P_0percentpause =
    ↪ newFDForceArray_Solid_Single_0percentpause.*-1;
D_newFLForceArray_Solid_Single_P_0percentpause =
    ↪ D_newFLForceArray_Solid_Single_0percentpause.*-1;
SD_FDFRe10_Solid_Single_0percentpause = transpose(std(transpose(
    ↪ FDcoeffArray_Solid_Single_P_0percentpause)));
SD_D_FLcoeffArray_Solid_Single_0percentpause = transpose(std(transpose
    ↪ (D_FLcoeffArray_Solid_Single_P_0percentpause)));
SD_newFDForceArray_Solid_Single_0percentpause = transpose(std(
    ↪ transpose(newFDForceArray_Solid_Single_0percentpause)));
SD_D_newFLForceArray_Solid_Single_0percentpause = transpose(std(
    ↪ transpose(D_newFLForceArray_Solid_Single_0percentpause)));

%%%%%%%%%%%%%%%%%%%%%%%%%%%%%%%%%%%%%%%%%%%%%%%%%%%%%%%%%%%%%%%%
MATLAB code for converting filtered force data to force data in grams
    ↪ using the slopes from the calibration plots shown in step 1
%%%%%%%%%%%%%%%%%%%%%%%%%%%%%%%%%%%%%%%%%%%%%%%%%%%%%%%%%%%%%%%%

function ForceArray = convertToForceNoAvg(voltageArray, zeroAvg,
    ↪ posSlope,negSlope)
% voltageArray: averaged voltage sample
```

```
% zeroAvg: average voltage when the wing is idle
% posSlope: slope of the positive calibration
% negSlope: slope of negative calibration
ForceArray = zeros(length(voltageArray(:,1)),length(voltageArray(1,:))
   ↪ );
temp=voltageArray - zeroAvg;
  for j=1:length(voltageArray(1,:))
    for i=1:length(voltageArray(:,1))
      if temp(i,j) >= 0
        ForceArray(i,j) = temp(i,j)/posSlope;
      else
% This may need to be modified. If you plot the ForceArray and
% it never shows a negative value, add a negative sign to this
% calculation.
        ForceArray(i,j) = - temp(i,j)/ negSlope;
      end
    end
  end
end

%%%%%%%%%%%%%%%%%%%%%%%%%%%%%%%%%%%%%%%%%%%%%%%%%%%%%%%%%%%%%%%%%%%
MATLAB code for applying the angle to which the wing is rotated giving
   ↪  both horizontal (drag) and vertical (lift) components
%%%%%%%%%%%%%%%%%%%%%%%%%%%%%%%%%%%%%%%%%%%%%%%%%%%%%%%%%%%%%%%%%%%
function newForceArray = useAngleNoAvg(forceArray, angleArray)
newForceArray = zeros(length(forceArray(:,1)),length(forceArray(1,:)))
   ↪ ;
  for j=1:length(forceArray(1,:))
    for i=1:length(forceArray(:,1))
        WAngle(i,j) = angleArray(i,j)+45;
      newForceArray(i,j) = forceArray(i,j).*cosd(WAngle(i,j));
    end
  end
end

%%%%%%%%%%%%%%%%%%%%%%%%%%%%%%%%%%%%%%%%%%%%%%%%%%%%%%%%%%%%%%%%%%%
MATLAB code for converting the force in grams to force coefficients
%%%%%%%%%%%%%%%%%%%%%%%%%%%%%%%%%%%%%%%%%%%%%%%%%%%%%%%%%%%%%%%%%%%

function coeffArray = forceToCoefficientNoAvg(forceArray, density,
   ↪ velocity, chord, span)
coeffArray = zeros(length(forceArray(:,1)),length(forceArray(1,:)));
for j=1:length(forceArray(1,:))
 for i=1:length(forceArray(:,1))
    coeffArray(i,j) = (forceArray(i,j)*9.81/1000)/(0.5*density*(
```

```
        ↪ velocity^2)*chord*span);
 end
end
end
```

VITA

Vishwa Teja Kasoju

Candidate for the Degree of

Doctor of Philosophy

Dissertation: AERODYNAMICS OF ACTIVE AND PASSIVE DISPERSAL OF MINIATURE INSECTS WITH BRISTLED WINGS

Major Field: Mechanical and Aerospace Engineering

Biographical:

Personal Data: Born in Hyderabad, Telangana, India in September 1992.

Education:
Completed the requirements for Doctor of Philosophy with a major in Mechanical and Aerospace Engineering at Oklahoma State University, Stillwater, Oklahoma in July 2021.
Completed the requirements for Masters of Science in Mechanical and Aerospace Engineering at Oklahoma State University, Stillwater, Oklahoma in May 2017.
Completed the requirements for Bachelors of Engineering in Mechanical Engineering at M.V.S.R Engineering college, Osmania University, Hyderabad, India in June 2013.

Experience:
Graduate Teaching Assistant Jan 2015 – May 2021
Oklahoma State University
Graduate Research Assistant Aug 2015 – June 2021
Oklahoma State University

Professional Membership:
American Physical Society (APS)
Society for Integrative and Comparative Biology (SICB)
The American Institute of Aeronautics and Astronautics